

https://dspace.org/

Surface brillouin scattering study of radio frequency sputtered hard thin films

Kuria, Jonah Muiru

2018

https://hdl.handle.net/10539/27329

Kuria, Jonah Muir (2018) Surface brillouin scattering study of radio frequency sputtered hard thin films, University of the Witwatersrand, Johannesburg, https://hdl.handle.net/10539/27329

Downloaded from a DSpace repository. https://dspace.org/

SURFACE BRILLOUIN SCATTERING STUDY OF RADIO FREQUENCY SPUTTERED HARD THIN FILMS

Jonah Muiru Kuria

A Thesis submitted to the Faculty of Science, University of the Witwatersrand, Johannesburg, in fulfillment of the requirements for the degree of Doctor of Philosophy.

10 September 2018

DECLARATION

I declare that this Thesis is my own, unaided work. It is being submitted for the Degree of Doctor of Philosophy at the University of the Witwatersrand, Johannesburg. It has not been submitted before for any degree or examination at any other University.

_____

(Signature of candidate)

_____day of_____20____

Abstract

Surface Brillouin Scattering (SBS) is used to investigate the elastic properties of NbN, TaN, and ZrN thin films deposited on Si substrates using rf magnetron sputtering. Influence of sputter power and hence the ad-atom energy on the elastic properties of NbN has been established for the films deposited at sputter powers ranging from 75 W - 250 W. TaN and ZrN thin films have been deposited at sputter powers of 150 W and 200 W respectively. For each sputter power, a sample set of eight films of thickness ranging from 50 nm - 800 nm has been used for the investigations.

From the measured SBS spectra, the SAW phase velocities were calculated and used to obtain the velocity dispersion curves for all the sample sets. The surface elastodynamic Green's technique was used to simulate Brillouin spectra of the films. Theoretical SAW phase velocities and hence the velocity dispersion curves have been obtained from the simulations. In NbN and TaN films, the dominant RSAW is observed in all the sample sets with higher order peaks (Sezawa modes) emerging from film thicknesses of 150 nm above. For the ZrN thin films on Si, no guided modes are observed. Increasing film thickness for NbN and TaN leads to a stiffening of the acoustic modes. Elastic constants for the NbN films and TaN films have been determined from the velocity dispersion modes. A least square fitting procedure has been used to optimise the elastic constants obtained from the Green's function approach. The uncertainties of the elastic constants have also been calculated from the same procedure. Picosecond ultrasonic technique has been used as a complementary technique for the extraction of elastic constants of ZrN films.

Dedicated to

To my parents and my family

Acknowledgements

Glory be to God in the highest, creator of the heavens and the earth. Thus far He has brought me.

I would like to thank the people who have contributed to this work, through their assistance, support, and encouragement, making this PhD work a success.

I am deeply grateful to my supervisors Prof. Darrell Comins and Prof. Daniel Wamwangi for their patience, guidance, and support throughout the project. Their expertise and insights in Surface Brillouin Scattering and Thin films technology has contributed greatly to this work as well developing my academic and research capabilities.

At the mechanical workshop in the Physics department, several staff offered technical assistance in solving various problems in the laboratory. They include, Messrs Alban Mafemba, John Augustine, and Tsepo Mashoene. Many thanks to Prof. Mandla Msimanga for helping with the Heavy-Ion Elastic Recoil Detection Analysis measurements and useful discussions on the same. Prof. Arthur Every's assistance with the optimisation of the elastic constants is greatly appreciated. I am grateful to Prof. Bernard Perrin of CNRS, Paris for his assistance with picosecond acoustics measurements. Special thanks to fellow graduate students: Clemence Sumanya, Kudakwashe Jakata, Isaac Motochi, Maxwell Vhareta, and Fekadu Ayele for their friendship and support during the project. I appreciate the generous financial support of DST/NRF Center of Excellence in Strong Materials, African Laser Centre and the University of the Witwatersrand Post Graduate Merit Award. Lastly, special thanks to my wife Rosslyne and our children Ryan and Nathan for their patience and support throughout this project.

Contents

Abstract ..... **iii**

Acknowledgements ..... **v**

Contents ..... **vi**

List of Figures ..... **xi**

List of Tables ..... **xvii**

1. Introduction **1**

2. Theory of Brillouin Scattering **21**

2.1 Introduction 21

2.2 Surface Brillouin Scattering 23

2.2.1 Surface Brillouin Scattering Principles 24

2.3 Scattering Mechanisms of SBS 26

2.3.1 Elasto-optic mechanism 26

2.3.2 Surface ripple mechanism 28

2.4 Kinematics of Surface Brillouin scattering 29

2.5 Surface Brillouin scattering in opaque materials and thin films 31

2.6 Surface elastodynamic Green's function of a supported layer 36

3. Thin Film Deposition and Characterisation **43**

3.1 RF Magnetron Sputtering 44

3.2 Structure Zone Model 49

3.3 X-ray Reflectivity 51

3.3.1 Introduction 51

3.3.2 Reflection of X-rays at material surfaces 52
3.3.3 Structural Parameters of thin films from XRR 54
3.3.3.1 Film Density 55
3.3.3.2 Film Thickness 55
3.3.3.3 Film surface roughness 56
3.3.4 Experimental Details 57
3.4 Grazing Incidence X-ray Diffraction 57
3.4.1 Introduction 57
3.4.2 Grazing Incidence X-ray Diffraction Geometry 59
3.4.3 Experimental Details 60
3.5 Atomic Force Microscopy (AFM) 61
3.6 Scanning Electron Microscopy (SEM) 63
3.6.1 Description of the Technique 63
3.6.2 Experimental Details 65
3.7 Heavy Ion Elastic Recoil Detection Analysis (ERDA) 66
3.7.1 Introduction 66
3.7.2 Experimental Details 66

4. Experimental aspects of surface Brillouin scattering (SBS) 70

4.1 SBS experimental setup 70
4.2 The Laser 71
4.2.1 Spontaneous and Stimulated emissions 72
4.2.3 Amplification by stimulated emission 73
4.2.4 Population inversion with a three-level system 76
4.2.5 Population inversion with a four-level system 76
4.2.6 The Argon Ion Laser 77

4.3 The tandem Fabry-Pérot interferometer 78

5. Elastic Properties of Niobium Nitride Thin films 85

5.1 Introduction 85

5.2 Experimental Details 87

5.2.1 Sample preparation 87

5.2.2 Composition, morphology and microstructure of NbN thin films at various ad atom energies 88

5.3 Results and Discussion 90

5.3.1 Composition determination by Heavy ion-elastic recoil detection analysis (HI-ERDA) 90

5.3.2 Scanning electron microscopy (SEM) 93

5.3.3 Microstructural dependence on the adatom energies by X-ray Reflectivity (XRR) 98

5.3.4 Atomic force microscopy (AFM) 102

5.3.5 Grazing incidence X-ray diffraction (GIXRD) 105

5.4 Surface Brillouin Scattering in NbN films 107

5.4.1 Measured Spectra for NbN thin films 107

5.4.2 SAW Velocity Dispersion and Elastic Stiffness 112

5.5 Conclusions 121

6. Elastic Properties of Tantalum Nitride Thin films 122

6.1 Introduction 122

6.2 Sample preparation and characterisation 124

6.2.1 Thin film growth 124

6.2.2 Structural and Chemical properties of TaN thin films 125

6.3 Results and discussion 126

6.3.1 Thickness, deposition rate, and mass density by XRR 126

6.3.2 Morphology and microstructure by AFM and SEM 128

6.3.3 Crystalline structure by grazing incidence XRD 131

6.3.4 Composition determination by HI-ERDA and RBS 133

6.4 Surface Brillouin scattering (SBS) in TaN thin films 134

6.4.1 TaN measured SBS spectra 134

6.4.2 SAW Velocity Dispersion and Elastic Stiffness 136

6.5 Conclusions 140

7. Optimisation of Elastic Constants for Isotropic NbN and TaN thin films 141

7.1 Elastic constants of NbN thin films deposited at various sputter powers 143

7.2 Optimisation and analysis of the elastic constants of TaN thin films 150

7.3 Conclusions 152

8. Elastic Properties of Zirconium Nitride Thin films 153

8.1 Introduction 153

8.2 Sample preparation and characterisation 155

8.2.1 Thin film growth 155

8.2.2 Microstructure and composition of ZrN thin films 156

8.3 Results and discussion 157

8.3.1 XRR analysis 157

8.3.2 Morphology and microstructure of ZrN films 158

8.3.3 Grazing incidence XRD analysis 160

8.3.4 Chemical composition using HI-ERDA 161

8.4 Surface Brillouin scattering (SBS) in ZrN thin films 163

8.4.1 ZrN Measured SBS spectra 163

8.4.1 Picosecond laser ultrasonics 165

8.4.2 Results and discussion 169

8.5 Conclusions 172

9. Conclusion 173

9.1 Summary 173

9.2 Suggestions for future work 175

References 176

Publications 190

Conference presentations 190

List of Figures

Figure 2.1: Conventional scattering geometry of SBS..... 25
Figure 2.2: The anti-Stokes component of the SBS spectrum for the $VC_{0.75}$ (110) surface with $k_{||}$ in the [$1\bar{1}0$] direction [70]..... 26
Figure 2.3: Geometry defined for surface Brillouin scattering. Axis 3 is taken to be pointing outwards i.e. normal to the surface. 30
Figure 2.4: Light-scattering geometry for SBS from a thin supported film [115].37
Figure 2.5: Typical SBS spectrum for a thin supported film showing the Rayleigh surface acoustic wave (RSAW), Sezawa waves (SW), pseudo-Sezawa waves (pSW) and sharp resonances [142]. 42

Figure 3.1: Schematic of physical sputtering process [146]. 44
Figure 3.2: Typical set up for film deposition by sputtering (glow discharge) [147]. 45
Figure 3.3: Variations of sputter yield with incident ion energy [149]..... 47
Figure 3.4: A photograph of the RF sputtering equipment used in this work (Courtesy of School of Physics, University of the Witwatersrand). A - shows the chiller used to cool the magnetron during deposition, B - the RF chamber under high vacuum, C - turbo pump control unit, D - fore pump, E - RF generator, B - gas control unit, and G - linear amplifier. 48
Figure 3.5: Thornton structural zone diagram [152]..... 50
Figure 3.6: Information provided by X-ray reflectivity profile [155]..... 52
Figure 3.7: Reflection and refraction of X-rays on material surface [155]..... 53
Figure 3.8: Reflectivity curve of Si [155]. 53
Figure 3.9: Conditions for total external reflection of X-rays [155]..... 54
Figure 3.10: Schematic diagrams of (a) symmetric θ-2θ and (b) asymmetric grazing incidence XRD geometry[172]. 60
Figure 3.11: Schematic diagrams of the experimental setup. The wave vectors of the incident wave and scattered wave ($\boldsymbol{k}_i$ and $\boldsymbol{k}_f$ respectively), the corresponding scattering vector $\boldsymbol{q}$, and its in-plane and out-of-plane components ($\boldsymbol{q}_p$ and $\boldsymbol{q}_z$, respectively) as well as probed lattice planes are indicated [176]. 61

Figure 3.12: A block diagram of the atomic force microscope [179]. 62
Figure 3.13: Photographs of the Veeco Dimension 3100 atomic force microscope showing (a) the various parts of the equipment and (b) a close-up view of the AFM head [182]. 63
Figure 3.14: Schematic drawing showing types of electrons and photons produces when an electron beam interacts with a solid sample [183]..... 65
Figure 3.15: Schematic SEM components. Note that there are detectors for secondary electrons (<50eV) and for elastically backscattered electrons which have energies approximately equal to the incident electrons [183]. 65
Figure 3.16: Time of flight edge of 12.6 MeV ^{16}O surface recoils from an Al_2O_3 layer on Si substrate [187]..... 67
Figure 3. 17: ToF-Energy scatter plots of recoils (and forward scattered beam) from (a) the as-deposited and (b) annealed samples [187]. 68
Figure 3.18: A linear scatter plot of recoil ion energies from the as-deposited sample calculated from the measured ToF plotted as a function of the Si detector (trigger) response [187]. 69

Figure 4.1: Schematic diagram of a typical Brillouin scattering experiment in the transmission configuration [90]. 71
Figure 4.2: Schematic representation of (a) spontaneous and (b) stimulated emission [188]. 73
Figure 4.3: Amplification by stimulated emission [188]. 74
Figure 4.4: The three-level system. 76
Figure 4.5: Schematic diagram of a four-level system. 77
Figure 4.6: Schematic diagram of a multi-pass tandem Fabry-Pérot interferometer (*after Speziale et al.* [90])..... 82
Figure 4.7: Block diagram of the experimental SBS setup (*after Wittkowski* [190]). 83

Figure 5.1: ERDA spectra showing the composition as a function of depth profile (in the units of atoms cm^{-2}) of the NbN films deposited at (a) 75 W, (b) 100 W, (c) 150 W, (d) 200 W, and (e) 250 W..... 93

Figure 5.2: SEM micrographs of cross-sectional morphology of NbN films deposited at sputter powers of (a) 75 W, (b) 100 W, (c) 150 W, (d) 200 W, and (e) 250 W. The film thickness was kept constant for ease of comparison. From the structure zone model, (a) and (c) represent Zone I, (b) and (e) Zone III, and (d) Zone II. 96
Figure 5.3: SEM micrographs of surface morphology of NbN films deposited at sputter power of 200 W for (a) 9 mins, (b) 19 mins, and (c) 33 mins. Film (a) corresponds to Zone I, while (b) and (c) correspond to Zone III of the structure zone model. 98
Figure 5.4: X-ray reflectivity spectra of the niobium nitride films showing the raw and the fitted curves. A layer stack of Nb_2O_5/NbN/SiO_2/Si was used for fitting. 101
Figure 5.5: The 3D view of the morphology of the thin films of 50 nm thickness deposited at (a) 75 W, (b) 100 W, (c) 150 W, and (d) 200 W. 103
Figure 5. 6: The 3D view of the change in morphology of the thin films deposited at 250 W with thickness of (a) 100 nm, (b) 300 nm, (c) 600 nm, and (d) 800 nm. 104
Figure 5.7: Grazing incidence XRD pattern recorded from NbN films deposited at varying sputter powers. 105
Figure 5.8: Calculated lattice constants of NbN thin films deposited at various sputter powers. After 200 W the NaCl structure increases its lattice constant owing to the appearance of the hexagonal phase. 106
Figure 5.9: Measured SBS spectrum for a 150 nm ($k_{||}d = 3.48$) NbN/Si. Shown are the Stokes and anti-Stokes bands. 108
Figure 5.10: Measured Brillouin spectra at different thickness ($k_{||}d$) for NbN/Si deposited at 75 W. 109
Figure 5.11: Measured Brillouin spectra at different thickness ($k_{||}d$) for NbN/Si deposited at 100 W. 110
Figure 5.12: Measured Brillouin spectra at different thickness ($k_{||}d$) for NbN/Si deposited at 150 W. 110
Figure 5.13: Measured Brillouin spectra at different thickness ($k_{||}d$) for NbN/Si deposited at 200 W. 111

Figure 5.14: Measured Brillouin spectra at different thickness ($k_{||}d$) for NbN/Si deposited at 250 W. 111
Figure 5.15: Calculated Brillouin intensities compared to the measured intensities for NbN/Si deposited at (a) 75 W, (b) 100 W, (c) 150 W, (d) 200 W and (e) 250 W as a function of $k_{||}d$. The red circles represent the measured while the green profile represent the calculated velocities. The values of the elastic stiffness resulting from the best fit are shown in the table 5.7 115
Figure 5.16: Measured and calculated anti-Stokes SBS spectra for 300 nm NbN/Si films deposited at (a) 75 W, (b) 100 W, (c) 150 W, (d) 200 W, and (e) 250 W. 118

Figure 6.1: XRR measured (raw) and simulated spectra for a TaN film deposited at 150 W. 126
Figure 6.2: Deposition rate of TaN films deposited at 150 W. 127
Figure 6.3: The 3D view AFM images for TaN films deposited at 150 W with thickness ranging from ~50 nm – 800 nm. 129
Figure 6.4: Cross-sectional field emission scanning electron microscope image of a 600 nm TaN film deposited at 150 W. The image depicts very fine grains in the film. It should be noted that the SEM image presents a continuous and homogeneous cross-section of the TaN film. 131
Figure 6.5: Glancing angle X-ray diffraction of TaN on (001) Si. 132
Figure 6.6: ERDA spectra of TaN deposited at 150 W showing the composition as a function of the depth profile. 133
Figure 6.7: Measured SBS spectra for TaN films deposited at 150 W of varying thickness and $k_{||}d$. 135
Figure 6.8: Surface Brillouin intensities compared to measured results for the TaN/Si system. Stiffnesses obtained from the best fit are $C_{11} = 288$ GPa, $C_{12} = 128$ GPa, and $C_{44} = 80$ GPa. 136
Figure 6.9: Calculated and measured SBS spectra for TaN of 50 nm thickness. 137
Figure 6.10: Calculated and measured SBS spectra for TaN of 100 nm thickness. 137
Figure 6.11: Calculated and measured spectra for a TaN film of 150 nm thickness. 138

Figure 6.12: Calculated and measured spectra for a TaN film of 300 nm thickness. 138
Figure 6.13: Calculated and measured spectra for a TaN film of 450nm thickness. 139

Figure 7.1: Contour plots of the minimised χ^2 values to establish the optimum elastic constants of NbN thin films deposited on (001) Si at (a) 75 W, (b) 100 W, (c) 150 W, (d) 200W, and (e) 250 W. The colour scheme corresponds to the χ^2 values for the sets of C_{11} and C_{44} values..... 146
Figure 7.2: Measured and optimised calculated anti-Stokes SBS spectra for 300 nm NbN/Si films deposited at (a) 75 W, (b) 100 W, (c) 150 W, (d) 200 W, and (e) 250 W. 149
Figure 7.3: Optimised elastic constant values of isotropic TaN thin film, the color scheme represents the upper limits of χ^2 values..... 151
Figure 7.4: Measured and optimised calculated SBS spectra of a 300 nm TaN film on (001) Si. 152

Figure 8.1: XRR measured and simulated spectra for ZrN thin film deposited at 200 W for 4 minutes. A layer stack of ZrN/SiO_2/Si was used for fitting. 157
Figure 8.2: Surface morphology of ZrN films deposited at 200 W with increasing thickness ranging from ~50 nm – 800 nm. The AFM images show larger grains formed with increasing thickness. 159
Figure 8.3: The cross-sectional SEM image of a 600 nm thick ZrN coating..... 160
Figure 8.4: Glancing angle X-ray diffraction of ZrN on (001) Si. 161
Figure 8.5: ERDA spectra of ZrN deposited at 200 W showing the relative atomic fraction as a function of depth profile. 162
Figure 8.6: Measured SBS spectra for ZrN thin films deposited at 200 W and varying thickness and $k_{||}d$. 163
Figure 8.7: Measured velocity dispersion curve of the Rayleigh surface wave for varying $k_{||}d$ values. 164
Figure 8.8: Illustration of the picosecond ultrasonic measurements on ZrN/Si thin films [239]. 167

Figure 8.9: Experimental setup for the picosecond ultrasonic measurement [239]. 167
Figure 8.10: Real (reflectometry) and imaginary (interferometry) parts of the change of the complex reflectivity coefficient as a function of time. 170
Figure 8.11: Reflectivity coefficient of ZrN on Si as a function of time after thermal background subtraction. 171

List of Tables

Table 3.1: Deposition conditions used in films deposition. 49

Table 5.1: The composition of the NbN thin films as a function of sputter power. 90

Table 5.2: The average mass density and deposition rate of the samples as a function of sputter power measured by XRR. 100

Table 5.3: The surface roughness of the samples as measured by XRR for deposition rate determination. 101

Table 5. 4: The rms surface roughness of the niobium nitride films of varying thickness deposited at varying sputter powers. 104

Table 5.5: The calculated and measured densities of NbN thin films as a function of sputter. 107

Table 5.6: Showing the film thickness and the corresponding $k_{||}d$ values. 108

Table 5.7: Elastic constants of NbN in GPa deposited at varying sputter power. 115

Table 5.8: Moduli of NbN thin films deposited at varying sputter power 120

Table 6.1: The rms surface roughness of TaN films deposited at 150 W. 130

Table 6.2: TaN Bragg reflexes. 132

Table 7.1: Initial elastic constants values of the transition metal nitride thin films on (001) Si obtained from Green's function. 143

Table 7.2: Summary of the optimised elastic constants of transition metal nitride thin films. 151

Table 8.1: Root mean-square surface roughness of ZrN films deposited at 200 W. 158

Chapter 1

Introduction

Transition metal nitride thin films have been used as coatings for several purposes; to protect mechanical cutting tools such as bits and drills, to provide biocompatibility to steel, as decorative layers [1] and biomedical implants [2–4]. The unique combination of chemical and physical properties such as high melting points, superior hardness, high corrosion resistance, chemical inertness, resistance to oxidation (thermal stability), high electrical conductivity, and metallic appearance have seen thin films and coatings of binary nitrides MN (M = Ti, Zr, Hf, V, Nb, Ta, Cr, Mo, W) being utilized in many applications under extreme environments. A unique application constitutes their use as diffusion barrier materials due to their good thermal stability and conductivity in Cu metallization schemes in ultra-large-scale integration (ULSI) devices. Besides diffusion barrier layers, transition metal nitrides and metal-silicon nitrides are promising gate electrodes for complementary metal oxide semiconductor (CMOS) devices [5].

Of the transition metal nitride thin films, titanium nitride (TiN) has been found to be the technologically most important nitride of this class of materials, due to superior electrical conductivity (40 $k\Omega^{-1}cm^{-1}$), high hardness (closer to that of diamond) which exceeds all elemental metals, and high melting points (T_m ~ 3000ºC) [5].

The work presented in this thesis, focuses on the synthesis, characterization, and elastic constants of transition metal nitride thin films of niobium (NbN), zirconium (ZrN), and tantalum (TaN). Nb and Ta are transition

metals with similar valence electron and ionic radii R_{Nb+} (0.64 Å) and R_{Ta+} (0.64 Å). However, their bond enthalpies with N varied and thus lead to the formation of transition metal nitrides with varying properties. On the other hand, Zr lies in the same group as Nb but with one electron less than Nb. It is thus expected that the mechanical properties of these materials are dependent on their electronic properties.

Niobium nitride (NbN) thin films were in the initial years investigated more frequently because of their superconducting properties rather than their mechanical properties [6]. Because of their transition temperature, one of the superconducting properties at 16 – 17 K made them find wide applications in superconducting microelectronics [7].

In the recent years, NbN thin films have become increasingly popular due to their high hardness, high melting point, wear resistance [8], chemical inertness [9], and thermal stability [10]. Due to these unique properties, niobium nitride films have been used in various cryogenic devices such as high-resolution X-ray and electromagnetic radiation detectors ranging from millimeter wavelengths to visible light [11–13], diffusion barriers in Josephson junctions [14], protective coatings [15], and field emission cathodes among others [16].

Various researchers have extensively studied the structural and mechanical properties of NbN coatings deposited using different techniques. Zhitomirsky [17] studied the structure and properties of NbN and NbN-based multi-component and multilayer coatings deposited using two different vacuum arc deposition (VAD) systems: with and without magnetic guiding of the metal plasma flow. Nb-N coatings were fabricated Nb-N with the deposition of the metal plasma produced from a Nb cathode in a background of reactive nitrogen gas at different pressures.

For the binary Nb-N coatings fabricated using deposition systems, the phase composition, the Vickers hardness (HV), and the critical load strongly depended on the deposition pressure. The maximum value of measured HV of ~42 GPa was obtained for coatings deposited at low pressure using VAD with magnetic plasma guiding. The coatings had a relatively low critical load and comprised of a hexagonal Nb_2N phase. Depositing the coatings at a higher nitrogen pressure resulted in single phase NaCl-type cubic NbN structured films with the highest critical load and HV ~38GPa. A similar correlation between the properties of Nb-N and deposition pressure for the coatings deposited using VAD without magnetic plasma was established, but their hardnesses were lower.

Zhitomirsky *et al.* [18] investigated the influence of nitrogen pressure on the chemical composition and mechanical properties of NbN coatings deposited on cemented carbide using vacuum arc deposition with a bias voltage of –40 V. It was shown that for nitrogen pressures ranging from 0.13 – 0.4 Pa the coatings were composed of a mixture of two phases: hexagonal Nb_2N and cubic NbN, whereas at pressures of 0.67 Pa and above single-phase cubic NbN with a NaCl type structure was obtained. Kawakami *et al.* [19] fabricated Josephson junctions having an epitaxial NbN/MgO/NbN microstrip resonator to evaluate the RF performance of the trilayers. Using X-ray analysis, they confirmed that all of the NbN and the MgO layers that formed the junctions and the resonators were epitaxial growth. The work of Alfonso *et al.* [20] on the influence of substrate temperature, sputter power and additional N_2 flux in the preparation chamber on the crystallization, microstructure and surface composition of NbN thin films deposited using RF magnetron sputtering showed that films grown at a substrate temperature of 573 K and RF power of 300 W presented the same crystalline

structure as that of the target. However, the films grown at the same temperature and power conditions plus the additional presence of N_2 during fabrication grew highly textured along the plane (200). Kim *et al.* [21] studied the influence of the N_2/Ar gas ratio of the inlet gases, deposition temperature, and substrate bias potential on the mechanical and structural properties of films prepared using the DC magnetron sputtering process. It was observed that cubic NbN was formed at a low N_2/Ar ratio while increasing the N_2/Ar ratio led to the formation of hexagonal NbN resulting in a mixture of cubic NbN and hexagonal NbN. It was further reported that the hardness of the films increased with an increase in the deposition temperature up to 300 ºC while the adhesion of the films decreased with an increase in deposition temperature. The films' hardness was reported to reach a maximum level at the bias potential of –200 V and decreased with a further increase of the bias potential. It was also established that the films deposited at the substrate bias potential range from –50 to –150V exhibited relatively high adhesion. Xin-kang *et al.* [22] carried out some fundamental studies on the preparation, structure and optical properties of NbN. They deposited the films using DC reactive magnetron sputtering at different N_2 partial pressures and different substrate temperatures ranging from –50 ºC to 600 ºC. They observed that, with the increase in the N_2 partial pressure, cubic NbN phase structure formed and the grain size and the lattice constant of the cubic NbN increased. The transmittance of the films was reported to decrease with the increase in temperature for the films of the same thickness. A comparative study of NbN coatings deposited by balanced and unbalanced magnetron sputtering carried out by Olaya *et al.* [14] demonstrated the strong effect of magnetic field configuration on the ion bombardment, and the resultant coating characteristics.

Havey *et al.* [23] investigated the structural and tribological properties of NbN films deposited onto 440C stainless steel substrates using magnetron sputtering. They varied the nitrogen partial pressure (PN_2) to change the crystal structure of the films. It was observed that at 4×10^{-4} torr, the films were cubic and as the partial pressure of the gas increased, an increasing fraction of hexagonal NbN appeared. The films had friction coefficients of approximately 0.6 and 0.7 when slid against Si_3N_4 and stainless steel balls respectively.

Cansever [24] deposited NbN coatings on a high speed steel substrate by cathodic arc physical vapour deposition using –150 V, –200 V and –200 V bias voltages at 1 Pa nitrogen pressure. Using XRD data, it was shown that hexagonal niobium nitride was formed for all bias voltages. Existence of the transition zone in all coatings was revealed by fracture cross-sections. A maximum hardness of 39 GPa was reported. Rockwell C adhesion and scratch tests were employed to compare adhesion properties. The best adhesion was achieved at –150 V and in the scratch test the cracks occurred at approximately 3–5 Ns. Sandu *et al.* [25] investigated the morphological, structural and mechanical properties of NbN thin films deposited by reactive magnetron sputtering. A systematic study exploring the effect of important process variables on the composition and structure of niobium nitride thin films synthesised by reactive pulsed laser deposition through ablation of high purity niobium targets in the presence of low pressure nitrogen gas has been presented by Krishnan *et al.* [26]. Wen *et al.* [27] explored the effects of nitrogen flow rate on the preferred orientation, phase transition and mechanical properties of NbN films deposited on Si (100) substrates using dc reactive magnetron sputtering. An evaluation of niobium nitride coatings deposited on stainless steel substrates as possible biocompatible surfaces that

might improve the biocompatibility and extended lifetime of stainless steel dental implants has been done by Ramírez *et al.* [28]. Benkahoul *et al.* [29] incorporated Si into NbN films deposited by reactive magnetron sputtering and studied the influence it had on the structure and mechanical properties of the films. Singh *et al.* [6] investigated the effects of N_2 flow and substrate bias on the deposition rate, crystal structure, surface hardness, adhesion and tribology of NbN thin films deposited on mild steel (MS), stainless steel (SS) and high speed steel (HSS) substrates using reactive DC magnetron sputtering. An investigation of the structural, electronic, and nanomechanical properties of cubic niobium nitride thin films deposited on Si (100) using reactive pulsed laser deposition has been reported by Ufktepe *et al.* [30].

The fourth column transition metal mononitrides have interesting properties resulting from their exhibition of both metallic and covalent bonding characteristics. The covalent crystalline properties are: high melting points; extreme hardness and brittleness; and excellent thermal and chemical inertness. The metallic characteristics are electrical conductivity and the metallic reflectance. A gold-like appearance results from high reflectance of the materials at the red-end of the visible spectrum with low reflectance near the ultraviolet region [31]. Zirconium nitrides (ZrN) and titanium nitrides (TiN) belong to this group of materials and have been the most successful in industrial applications as decorative coatings. For decorative purposes, due to their gold-like colour, TiN and ZrN are employed as a replacement for gold coating, which is less abrasion resistant. In the last two decades, ZrN films have been attracting attention because of their better corrosion resistance, lower resistivity, higher mechanical properties, and warmer golden colour than the corresponding properties of TiN films [32].

However, zirconium has a higher melting point, a lower vapour pressure and higher susceptibility to contamination by oxygen and carbon; thus it is more difficult to deposit ZrN films than TiN or CrN [33]. The properties of ZrN films depend on the deposition techniques and processing parameters [34]. Thin films of zirconium and its nitrides are important to the electronics and optical communities [35]. With ZrN stoichiometry, the nitride is metallic-like with a gold yellow colour and its optical index N is of about $N = 0.5 - i3.2$ at 633 nm. This is the thermodynamically stable phase of the zirconium nitride. On the contrary Zr_3N_4 is a metastable phase; this compound is an insulator almost transparent with $\mathrm{N} = 3.2 - i0.2$ at 633 nm [36].

Various studies on properties of ZrN thin films deposited using varying techniques have been reported by different researchers. Ma *et al.* [37] carried out a study of the preferred orientation of ZrN coatings deposited on silicon substrates using ion beam assisted deposition (IBAD). In their investigation, the substrate temperature (150, 300, and 500°C), nitrogen ion beam energy (150-1000 eV) and incident angle (45 and 0 °) were chosen as the processing variables. They observed a change in the preferred orientation of the ZrN films from (111) to (200) at a 300 °C growth temperature with normal ion-beam energy of 750 V. A systematic study of the effect of varying the nitrogen partial pressure on the structural, electrical, and optical properties of ZrN films deposited by a DC reactive magnetron was reported by Bhuvaneswari *et al.* [38]. The films were deposited on silicon substrates at room temperature. They varied the nitrogen partial pressure from 4×10^{-5} to 10×10^{-5} mbar. It was found that the films formed at a nitrogen pressure of 6×10^{-5} mbar showed a low electrical resistivity of 1.726×10^{-3} Ω.cm. The films were reported to be crystalline with a refractive

index and an extinction coefficient of 1.95 and 0.4352 respectively. In their study of insulating zirconium and hafnium nitrides, Becker *et al.* [39] used atomic layer deposition to produce higher nitrides of zirconium and hafnium from homoleptic tetrakis(dialkylamido)-metal(IV) complexes and ammonia at low substrate temperatures (150-250 °C). The precursor vapours were alternately pulsed into a heated reactor, yielding 1.15-1.20 Å of metal nitride film for every cycle. They successfully deposited the films on silicon, glass quartz, and glassy carbon. All the films were reported to have shown good adhesion to the substrates, were chemically resistant and did not oxidise over time. X-ray diffraction and transmission electron microscopy results showed that the films were amorphous. In contrast to the well-known mononitrides, which are shiny, gold-coloured, and highly conducting, these films are insulating, transparent and coloured. The work of Benia *et al.* [40] on non-stoichiometric zirconium nitrides details an investigation of the effect of varying the nitrogen flow on the structural, optical and electrical properties of the films prepared by dc magnetron sputtering. They combined Rutherford back scattering (RBS), X-ray diffraction (XRD), reflectometry and a four-point probe method to characterise their films. They found that the deposition rate decreased with the increase in the nitrogen flow. Stoichiometric zirconium nitride films (ZrN) were reported at nitrogen flow of 4 sccm. This film had a rock-salt structure and presented a minimum of resistivity and a gold-like colour. As the nitrogen flow was increased, the films became more and more amorphous, semi-transparent and electrically resistive. At a nitrogen flow of 9 sccm, they reported a nitrogen to zirconium ratio of near 1.33 with the film exhibiting properties close to those of a Zr_3N_4 phase. Studies of oxidation of nitrides or oxynitrides compounds are important since their electrical, thermal,

catalytic and reactional properties are drastically modified by the oxidation layer encountered on top of these ceramics. Wiame *et al.* [41] presented a study on the thermal oxidation of ZrN under O_2. By analysing the gas reaction products during oxidation and with the results from XPS and DRIFTS, they reported the formation of a stable Zr-N-N-O-Zr intermediate. A study of the effect of bias on the microstructure and properties of zirconium nitride deposited on Si (100) and AISI stainless steel 304 was carried out by Huang *et al.* [34]. Hollow cathode discharge ion plating (HDC-IP) technique was used to deposit the ZrN thin films. The Taguchi experimental method was used to determine the optimum coating conditions. It was shown that the columnar structure of the ZrN film became denser with increasing bias. XRD results showed that all the coatings they deposited exhibited (111) preferred orientation both on Si and on SS304 substrates. Nano-indentation results showed that the hardness ranged between 27 - 30 GPa and 32.5 - 40.8 GPa for the films deposited on Si and stainless steel 304 respectively. The surface roughness of the films deposited on stainless steels was reported to be in the range between 1.1 - 3.9 nm. Using X-ray photo-electron spectrometry (XPS) it was established that the films were almost stoichiometric. The resistivity of the films decreased gradually with increasing bias until -120 V and then abruptly increased. The corrosion resistance of ZrN-coated stainless steel was evaluated using standard salt spray test and potentiodynamic scanning in two kinds of solution environments: 5% NaCl and 1N H_2SO_4+0.05M KSCN, respectively. The results showed a consistent trend between the salt spray test and potentiodynamic scanning. They reported an increase in corrosion resistance with the increase in bias ranging from 0 to -90V, then an abrupt decrease at -120V, and finally an increase again at -150V. Cathodic arc sputtered polycrystalline ZrN thin

films have been characterised by Gruss *et al.* [42]. The films were deposited onto Incoloy 825, Hastelloy C22 and Titanium Grade 12 metal substrates. The presence of 1 - 8 µm macroparticles composed of ZrN metal was revealed by analysing the coatings using scanning electron microscopy and Auger electron microscopy. The composition of the films was determined to be 58.41 % Zr and 41.59 % N. Using X-ray diffraction, compressive stresses of 4.06, 3.88 and 2.69 GPa in the coatings deposited on Incoloy 825, Hastelloy C22 and Titanium Grade 12 substrates respectively were measured. Young's modulus and hardness values of 458 and 27.65 GPa respectively were obtained using nano-indentation. Chemically abrupt interfaces and good compositional uniformity throughout the thickness of the zirconium nitride coatings was revealed by Auger electron microscopy and transmission electron microscopy. Optical and electrical characterisation of non-stoichiometric dc magnetron sputtered ZrN films on silicon has been done by Benia *et al.* [43] using spectral reflectance measurements and a four-point probe method respectively. The nitrogen flow was varied from 1 - 11 sccm. A strong dependence of the reflectivity and electrical resistivity on nitrogen flow was revealed by the experimental results. By using Drude's model to fit the reflectance spectra of the films with a metallic behaviour and an extended model for the films with an insulating behaviour, the optical constants of the various ZrN films were determined. A comparison between the electrical resistivity obtained by the four- probe method and the optical resistivity derived from the optical constants at frequency $\omega = 0$ showed good agreement. Hu *et al.* [44] studied the influence of substrate temperature and N_2: (N_2 + Ar) flow ratio on the properties zirconium nitride films. The films were deposited on glass substrates using reactive dc magnetron sputtering. It was established that in a wide

range of *F* (N2) (4-24%), the films showed fcc NaCl structure whereas for *F* (N2) in the ranges of 5-12, 12-24 and > 24%, the films showed (111) / (200), (111) only and amorphous structures respectively. ZrN films deposited on Si (100) substrates using the hollow cathode ion-plated (HCD-IP) technique have been studied by Chou *et al.* [32]. The deposition conditions were chosen in such a way as to deposit stoichiometric films. Substrate bias was used as a controlling parameter ranging from floating to -300V. It was shown that (111) was the dominant preferred orientation in the ZrN films deposited at the bias voltage ranging from 0 to -250 V. At a bias voltage of -300 V, the (200) orientation became the preferred orientation of the films. Hardness of the films was reported to range between 22 - 32 GPa while the optimum condition of negative bias was close to 50 V. It was shown at this condition that the films showed the lowest resistivity of 56 μΩ.cm, highest packing factor of 0.99, the lowest roughness of 0.66 nm, the highest brilliance of 87.2, and a relatively high hardness of 30.63 GPa. Resistivity increased with increasing bias and with decreasing packing factor while the brilliance increased linearly with increasing packing factor. Variation of colour in zirconium nitride decorative thin films with respect to the atomic ratio between nitrogen and zirconium and with oxygen as a contaminant was investigated by Niyomsoan *et al.* [31]. Cathodic arc evaporation was used to deposit the films. The stoichiometry of the films was controlled by varying the nitrogen flow rate and total pressure in the chamber. A correlation of the oxygen content in the films to the colour was established by measuring the reflectivity spectra of the films in the visible region of the spectrum and quantifying the colour in the International Commision on Illumination (*Commission internationale de l'éclairage*) colour space. Increase in the atomic ratio of nitrogen

to zirconium caused the overall reflectivity of the gold-like colour to decrease and the yellowness to increase. It was also established that the variation in oxygen content resulted in colour change in the same direction as that of the variation of nitrogen content. Larijani *et al.* [33] have investigated the influence of varying N_2/Ar ratio and substrate temperature on the structural and mechanical properties of ZrN films. The films were deposited on stainless steel 304 substrates using ion beam sputtering technique and introducing a mixture of (Ar + N_2) gases into the chamber. Characterisation of the phase and morphology of the films was done using X-ray diffraction (XRD) and scanning electron microscopy (SEM) respectively; the composition depth profile was obtained using secondary ion mass spectroscopy (SIMS). It was observed that in a wide range of flow ratio $F(N_2)$ (10-54%), the intensity of the preferred orientation (111) peak increased, while for $F(N_2)$ more than 54% the ZrN peak intensity decreased and amorphous structure was formed at 95%. A texture change due to the variation of the processing temperature (200-250 °C) was established using the XRD patterns. The (111) crystalline plane intensity at 400 °C was higher than the others leading to the presence of a preference for this orientation. Vickers micro-hardness tester with a load of 25 g was used to measure the hardness of the films. It was confirmed that the structural and mechanical properties were strongly influenced by the nitrogen ratio and the substrate temperature. Pichon *et al.* [36] studied the physical properties and growth modelling of ZrN thin films deposited using dual ion beam sputtering. Ramos *et al.* [45] deposited ZrN films on copper substrates using a multi-cusp plasma sputter-type negative ion source to investigate their structural and electrical properties and determine the optimum conditions for the synthesis of the films.

Tantalum nitride (TaN) has been widely used in aviation aerospace, microelectronics, biomedical, power machinery and other fields due to its unique properties including high melting point, high anti-wear ability and low temperature coefficient of resistance. Besides these properties TaN exhibits exceptional chemical stability under harsh chemical and radiation environments [46]. Recently, TaN thin films are attracting increasing attention for thin film resistors, and as diffusion barriers in the microelectronics industry. These applications have prompted investigations of the mechanical properties of TaN thus highlighting its potential in hard coating applications [47]. Ta and Ta-based compounds have been investigated in the past as thin film resistor materials with low temperature coefficient resistivity and as a stable contact materials to Si [48]. In silicon technology, copper has drawn much attention as a new interconnecting material for deep submicron integrated circuits as a replacement for aluminium and its alloys. However, copper is known to diffuse into either Si or SiO_2 layers during processing, and this problem is addressed by employing a suitable diffusion barrier layer between the copper overlayer and the silicon substrate. In this direction, TaN and Ta_2N compounds have been investigated [49–52] and found to be promising materials to serve as diffusion barriers because TaN-based materials can withstand high temperatures. TaN has good adhesion to GaAs and has been used as thin film resistors in the fabrication of power amplifiers [53]. TaN films have been deposited by physical and chemical deposition (PVD and CVD) techniques [51,54,55]. Very little work has been done on the application of TaN films in hard wear-resistant coatings [56]. However, there is considerable literature on the deposition and characterisation of TaN thin films.

Liu *et al.* [47] investigated the effects of deposition and annealing temperature on mechanical properties of TaN films. The films were synthesised by electron cyclotron resonance direct current (ECR-DC) sputtering. Scanning electron microscopy (SEM), X-ray diffraction (XRD) and X-ray photoelectron spectroscopy (XPS) were used to characterise the cross-section pattern, microstructure and binding energy respectively. Using nano-indentation, it was shown that the maximum hardness value of approximately 40 GPa was achieved at deposition temperature of 573 K. The hardness, modulus and adhesion of the TaN films decreased with a decrease in the deposition temperature. Hardness and modulus also increased with an increase in the annealing temperature. Maximum adhesion strength of 40 N was achieved at an annealing temperature of 448 K. A study of the electrical and mechanical properties of TaN films deposited on ceramic substrates by reactive sputtering was done by Kim *et al.* [57]. Variation in the nitrogen/argon gas flow ratio (defined as *R*), caused an unusually wide variation in resistivity (10^7 orders) from metal to insulator. It was reported that such an increase in resistivity could be attributed to the theoretically predicted Ta vacancies and anti-site defects (excess N atoms occupying Ta sites) or thermodynamically stable N-rich phase formation under N-rich conditions. The hardness of two TaN films (R = 1 and 2) were found to be similar and in the range between 600 and 1600 kg/mm^2. There was no much change in the hardness of the films with an increase in the N content, which seemed to indicate that a N-rich thermodynamic phase such as tetragonal Ta_4N_5 or orthorhombic Ta_3N_5 were formed as the N content increased (rather than a TaN film with anti-site defects). Shen and Ramanathan [53] fabricated a low resistivity (~ 80 μΩ-cm) tantalum nitride thin film using reactive ion DC sputtering. The film was more stable when

compared with high resistivity films with high nitrogen flow rates. Low angle X-ray diffraction results showed that the low resistivity TaN film was highly crystallised in comparison with that of each individual film deposited in the bilayer design. The crystalline structure and the film resistivity of the bilayer TaN film remained unchanged even when there was a change of thickness of each layer, indicating the large process window that is critical to high volume manufacturing. The structural and mechanical properties of TaN thin films deposited on SiO_2 (600 nm)/Si substrates using dc magnetron sputtering were investigated by Coung *et al.* [58]. They varied the nitrogen/argon ratio as well the deposition temperature to establish the effect of these parameters on the properties of the films. As the nitrogen/ratio increased from 3 to 25 %, a phase change as Ta_2N or TaN was observed. They associated the phase changes with a change in the resistivity and TCR (temperature coefficient of resistance) of the films. TCR values of the films deposited at room temperature and different nitrogen contents were negative, and strongly decreased with the increase in nitrogen/argon ratio. The Ta_2N films deposited at a nitrogen/argon ratio of 3 % and a temperature of 200 °C showed a TCR value of -47 ppm/K, which was close to near-zero TCR in the range of the deposition temperature. Riekkien *et al.* [59] evaluated tantalum nitride films fabricated using reactive sputtering by adjusting the deposition parameters. Si wafers substrates were used to deposit the films at varying N_2/Ar gas ratios. The phases of the as-deposited films were identified as β-Ta, Ta_2N (5% N_2-flow), hexagonal TaN (10% N_2-flow) and f.c.c.-TaN (15% N_2-flow) with resistivities of 166 μΩ cm, 234 μΩ cm, 505 μΩ cm and 531 μΩ cm, respectively as the amount of nitrogen was increased. Only the phase obtained at 5% N_2-flow showed a reasonable uniformity over the wafer suggesting suitability as thin film

resistors. A value of - 103 ppm/°C TCR was determined for the Ta_2N thin film resistor. Dalili *et al.* [60] investigated the thermal and electrical stability of TaN_x films applied as diffusion barriers for Cu metallisation. They deposited amorphous TaN_x thin films (14 and 62 nm) on Si substrates using reactive sputtering. Amorphous TaN_x thin films crystallised at 600 °C to hexagonal Ta_2N by a polymorphous transformation. Aryasomayajula *et al.* [61] investigated pulsed DC magnetron sputtered tantalum nitride hard coatings for tribological applications. Ibidunni [62] studied the oxidation of reactively sputtered tantalum nitride films. Palacio *et al.* [63] employed Auger electron spectroscopy to study the preferential enrichment of tantalum in the surface of TaN films deposited using reactive sputtering. Studies of TaN based films synthesised by atomic layer deposition from cyclopentadienyl (C_5H_5) type precursor has been reported by Anacleto *et al.* [64]. Sun *et al.* [65] studied the properties of reactively sputtered TaN thin films.

The characterisation of the mechanical properties of metal nitride films is an important and a challenging problem. There are well-established ultrasonic techniques for measuring the elastic properties of bulk solids and thick coatings. These techniques are; however of limited usefulness particularly for thin films with thicknesses lower than 1 μm [66]. In most earlier studies on the elastic properties of transition metal nitride thin films, X-ray techniques [67–69] have been employed to study the elastic properties. Laser-generated surface acoustic waves (LSAW) and acoustic microscopy (AM) techniques [70] have also been used to measure the elastic properties of solids and thin supported films. Kim *et al.* [71,72] have used line focus acoustic microscopy (LFAM) technique to determine the elastic constants of single crystal TiN. It is an accurate

nondestructive technique capable of measuring the elastic properties of layers of thickness from some hundreds of nanometers to tens of microns.

Surface Brillouin scattering (SBS) is a powerful means of characterising the elastic behaviour of thin solid films and multilayers at both ambient [73,74] and high temperatures [75]. It is a contactless non-destructive technique that can be applied to samples as small as 1 mm on edge [66]. The elastic constants determined this way using SBS can be related to engineering moduli. SBS on opaque materials is caused by thermally excited phonons in the GHz frequency range, mediated principally by surface ripple mechanism. Film grown by RF magnetron sputtering are in general, nanocrystalline or amorphous and do not exhibit single crystal properties. Their elastic constants need to be determined experimentally because they depend strongly on the deposition conditions and can in general not be derived from theoretical considerations. SBS is a well-established technique to obtain information on the elastic properties of thin films by measuring the frequency shift of light scattered inelastically from phonons [76]. Surface Brillouin scattering in bulk media has been used in the past to study solids and liquids (Fleury 1970, Sandercock 1975), thin films (Rowell *et al.* 1978), supported transparent films (Bortolani *et al.* 1982) [77], vanadium carbides in a range of carbon to metal ratio (Zhang *et al.* 1998) [78], opaque solids and thin supported films (Comins *et al.* 2000) [79], and more recently; spherical nanoparticles (Montagna, 2008) [80], cellulose nanocrystal films (Sui *et al.* 2010) [81], nanoscale permalloy stripes (Nguyen *et al.* 2009) [82], carbon films (Salas *et al.* 2010) [83], thin single silicon layers (Lou *et al.* 2010) [84], planar magnonic crystals (Gubbiotti *et al.* 2010) [85], aqueous mixtures of polyethylene glycol polymer (Pochylski *et al.* 2010) [86], sodium silicate glasses (Zhao *et al.* 2011)

[87], single crystal indium arsenide antimonide (Kotane *et al.* 2011) [88], gallium nitride layers (Jiménez-Riobóo *et al.* 2012) [89]. Speziale and Marquardt [90] have presented a study of application of SBS and its applications in geosciences. A comprehensive treatment of the theoretical aspects of SBS can be found in [77,91–94]. SBS work on thin films has been carried out by several researchers, Elmiger *et al.* [95] measurements on single crystals of Ge and Si, thin films of $CoSi_2$ and epitaxially grown $CoSi_2$/Si superlattices on Si(111) determined the elastic constant tensor using the angular dispersion of the hypersonic surface wave localized at the surface. Carlotti *et al.* [74] determined the dispersion curves of guided acoustic modes propagating along piezoelectric ZnO films. Investigations by Wittkowski *et al.* [96] on hexagonal (sp^2-bonded) boron nitride, cubic (sp3-bonded) boron nitride and films consisting of layers of both crystallographic phases, determined from acoustic phonon dispersion several independent components of the stiffness tensor (for h-BN $C_{11} = 750$ GPa, $C_{33} = 18.7$ GPa and c-BN $C_{11} = 820$ GPa, $C_{44} = 480$ GPa). These values are comparable to the hardest material known (diamond $C_{11} = 1084.4$ GPa, $C_{44} = 587$ GPa Chandrasekharan *et al.* [97]) however, their closeness to those of diamond indicates a high hardness in the BN. The work of Every *et al.* [66] on TiN films deposited on high-speed steel (HSS) inferred that the elastic constants of TiN played a crucial role in the acoustic behavior of TiN/HSS. A comparison between the measured and the calculated dispersion relations showed that the effective elastic moduli of TiN for film thickness d < 500 nm were about 25% smaller than that of bulk TiN. The low elastic moduli of the thinner films were attributed to the difference in the composition variations at the TiN-HSS interface. Gump *et al.* [98] investigated the elastic constants of face-centred-cubic cobalt films. Using

the dispersion of the mode velocities they were able to determine the independent elastic constants of the cubic phase of cobalt. Zinin *et al.* [99] used SBS to determine the elastic constants of cubic boron nitride films deposited on silicon by mass selected ion beam deposition. Beghi *et al.* [100] studied the elastic properties of a thin isotropic gold film alloyed with Cu and Ni deposited on Si(001) using magnetron sputtering. Crowhurst *et al.* used SBS to examine the elastic properties of a supported gold film on a glass substrate at high pressure using a modified miniature Merrill-Bassett cell with cubic zirconia anvils. Other SBS measurements on thin films involved the work due Mirkarimi *et al.* [101] which established the independence of the superlattice wavelength from measured wave velocities over the entire range (1.5-30 nm).

In the present work, thin films of transition metal nitrides (NbN, ZrN and TaN) have been deposited on Si (100) at room temperature using RF magnetron sputtering. The argon flow was maintained at 13 sccm and working gas pressure at 8.5 x 10^{-4} mbar while sputter power was varied from 75 - 250 W. X-ray reflectivity (XRR) was used to determine the variation of film mass density and deposition rates for the sputter powers used. Atomic force microscopy (AFM) was used to establish the surface roughness of the films. Grazing incidence X-ray diffraction (GIXRD) was employed to determine the crystalline structure of the films. Heavy ion elastic recoil detection analysis (HI-ERDA) was used to establish the composition of the thin films. The films growth mode was identified using scanning electron microscopy (SEM). A combination of SBS and theoretical calculations based on the surface Green's function was used to extract the elastic constants of the films. The influence of the variation of sputter power on the morphology, microstructure and elastic constants of the films is presented.

In the first chapter of this thesis, an overview of the properties and applications of transition metals nitrides has been presented. A review of the work done on transitional metal nitrides of niobium, zirconium and tantalum is also presented. The theoretical formalism of surface Brillouin scattering is discussed in detail for bulk media and thin solid films in Chapter 2. Chapter 3 describes the deposition and characterisation methods of thin films. RF magnetron sputtering is described here as the thin film fabrication technique. Additionally, the characterisation techniques used to establish the film properties are presented in detail in this chapter. To this end, the principles of X-ray reflectivity (XRR), grazing incidence X-Ray diffraction (GIXRD), atomic force microscopy (AFM), scanning electron microscopy (SEM), and heavy-ion elastic recoil detection analysis (HI-ERDA) are briefly highlighted. The experimental aspects of SBS are presented in Chapter 4. Experimental results for NbN are presented in Chapter 5, TaN in Chapter 6 and ZrN in chapter 8. A discussion of the optimisation of the elastic constants for NbN and TaN films is given in Chapter 7. Finally, the thesis is concluded in Chapter 9.

Chapter 2

Theory of Brillouin Scattering

2.1 Introduction

Brillouin light scattering is the inelastic scattering of light by thermally generated acoustic vibrations (phonons) [74]. The interaction between thermally excited acoustic phonons was first predicted and investigated by Léon Brillouin in 1922 [102] and then by Mandelstam in 1926 [103]. Through their independent investigations of light scattering by density fluctuations associated with acoustic waves in a homogeneous medium, both Brillouin and Mandelstam proposed that light scattered by thermally excited waves in a medium should be frequency shifted with respect to the incident light by an amount equal to the frequency of the scattering fluctuations.

Following the work of Brillouin and Mandelstam, Gross experimentally confirmed their prediction in liquids and crystals in 1930 [104,105]. Initially the measurement of Brillouin light scattering was limited to compressed gases and fluids plus a handful of some transparent solids [106]. Although some aspects of the theory were later verified using Raman scattering techniques, the subject generally received little attention until the advent of the laser. Then it was shown in some elegant experiments that Brillouin scattering is an excellent means of investigating the elastic and photo-elastic properties of materials [107], particularly in the neighbourhood of phase transitions [108,109], allowing measurements on small and even opaque samples .

There are usually two distinct aspects of the said inelastic scattering of light by thermally activated phonons. Light scattering by bulk elastic waves which allows for the determination of the elastic properties of near transparent materials is termed as Brillouin Scattering (BS). Conversely, determination of the elastic properties of opaque and near opaque materials involves light scattering from thermally induced long-wavelength surface acoustic waves with frequencies to about 150 GHz, a branch of the subject known as Surface Brillouin Scattering (SBS) [110]. This was only made possible after the introduction of the high-contrast multi-pass tandem Fabry-Pérot interferometer by Sandercock [111] and high sensitivity, low-noise detectors.

SBS is a non-contact technique having the advantage that small samples can be used and is one of the very few techniques available for the study of thin supported films of thickness of less than 1000nm [79]. The technique also allows for the experimental determination of the dispersion curves of the acoustic modes naturally present in a wide range of acoustic wavenumber and angular frequencies. Analysing these curves provides direct insight into the elastic properties of the film and their dependence on film thickness, mass density, substrate material and interface effects [74]. Another advantage of SBS makes it possible for the technique to be used on samples at high pressure and at elevated temperatures [66].

Several workers have developed the theory of Brillouin scattering from surface acoustic phonons in opaque bulk materials. Loudon used the Green's function approach in 1978 [92], Marvin *et. al.* [77] used a direct matching of the electromagnetic field at the surface. The work of Bortolani *et. al*. [91] extended the latter's theory to the supported films whilst incorporating various scattering

mechanisms, i.e. the scattering from the surface and interface ripples and elasto-optic coupling in the film and the substrate. In this chapter the basic theory of Brillouin scattering in opaque and transparent material is presented. The Green's function approach for the theory of Brillouin scattering from the surface of a supported layer is also discussed. The latter has been used to study the elastic properties of transition metal nitrides thin films in this work.

2.2 Surface Brillouin Scattering

Surface Brillouin Scattering (SBS) is a powerful technique in the study of thermally induced surface acoustic excitations in the GHz frequency range and the elastic properties of opaque solids and thin supported layers [79]. In this case, the surface ripple mechanism mediates the light scattering and dominates that of the elasto-optic coupling mechanism being predominant in transparent media. The scattering mechanisms of SBS are discussed in section 2.3. SBS is a non-contact technique applicable to small samples (<1000nm) under controllable conditions of temperature and pressure [70]. A laser beam is used to probe thermally excited dynamic fluctuations in the surface profile and sub-surface strain field. The laser itself does not cause these surface vibrations since it is of moderately low power thus produces minimal heating. The inelastically scattering light, which is a tiny fraction of the incident intensity provides information about the surface dynamics. The combination of the overlayer and the substrate determines the types of observed acoustic excitations localised near the surface in case of thin layers. The development of the high contrast ($\sim 10^7$), multi-pass Fabry-Pérot interferometer and low-noise high-sensitivity detectors [111] has greatly facilitated progress in SBS.

With SBS it is possible to determine the velocities of Rayleigh waves and pseudo-surface waves, as well as the continuum of excitations resulting from the surface displacements of bulk waves (Lamb shoulder). A major application of surface Brillouin scattering is in the analysis of acoustic excitations in thin opaque layers in the range of 20 – 1000 nm. These excitations may include Rayleigh waves, pre-Rayleigh waves, pseudo-surface acoustic waves, Sezawa and pseudo-Sezawa waves, Love waves, the Lamb shoulder, and various interface waves depending on the physical and experimental parameters. One can determine the elastic constants of thin film materials by analysing their behaviour. In the present work, the elastic properties of transition metal nitrides have been investigated.

2.2.1 Surface Brillouin Scattering Principles

The principles of SBS have been discussed in [70] and are shown in Figure 2.1. A laser beam (e.g. Ar^+ ion or Nd-YAG) of angular frequency ω_i and wavevector k_i is incident on the highly polished surface of a sample at angle θ to the normal. Most of this light is specularly reflected or absorbed. However, as a result of thermally excited dynamic surface corrugations and fluctuaions in the subsurface strain field, a small fraction of the light is inelastically scattered with a frequency shift which depends on the nature of the scattering process.

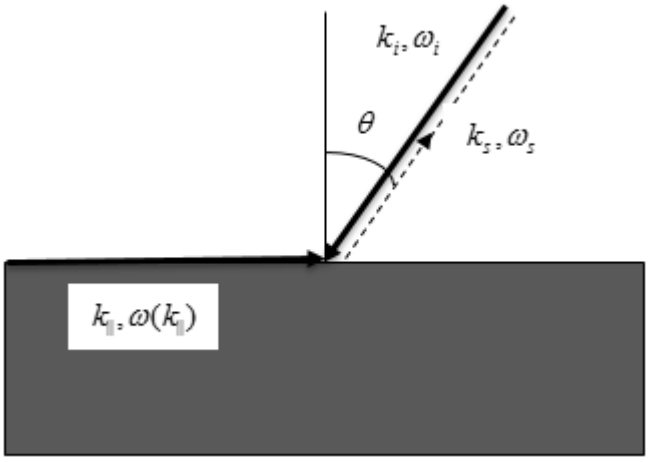

Figure 2.1: Conventional scattering geometry of SBS.

In the usual implementation of SBS, the backscattered light of frequency ω_s, and wavevector k_s in a small cone around k_i, is collected and analysed using a Sandercock-type Fabry-Pérot interferometer [111–114]. The change in frequency of the light on being scattered $|\omega| = |\omega_s - \omega_i| \ll \omega_i$, and so $|k_s| \approx |k_i|$. The surface mode involved in the scattering for detection in the backscattering direction thus has surface wavevector

$$k_{||} = 2k_i sin\theta. \tag{2.1}$$

As an example, Figure 2.2 shows the anti-Stokes (frequency-upshifted) component of the SBS spectrum of the (110) surface of the cubic crystal $VC_{0.75}$ for $k_{||}$ in the $[1\,\bar{1}\,0]$ direction obtained by Zhang *et. al*. [78]. Only that part of the spectrum well away from the intense central peak of elastically scattered light is shown.

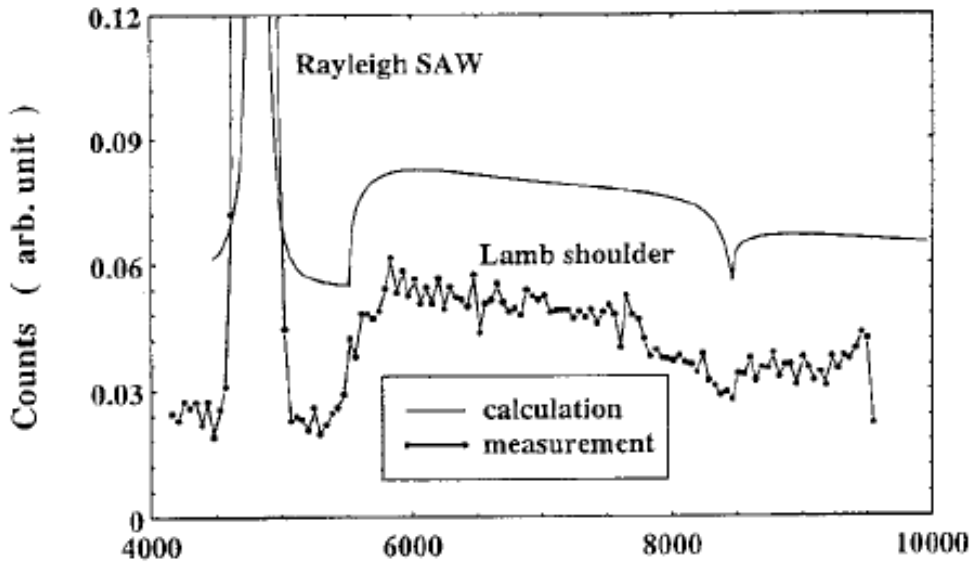

Figure 2.2: The anti-Stokes component of the SBS spectrum for the $VC_{0.75}$ (110) surface with $k_{||}$ in the [$1\bar{1}0$] direction [70].

2.3 Scattering Mechanisms of SBS

Several authors have published the theoretical treatments of SBS [77,92,115–122]. Two principal scattering mechanisms mediate the scattering, i.e. elasto-optic and surface ripple scattering. These mechanisms are explained in sections 2.3.1 and 2.3.2 below which appear in [70].

2.3.1 Elasto-optic mechanism

The elasto-optic effect mediates the scattering in this case, whereby the dynamic fluctuations in the strain field bring about fluctuations in the dielectric constant, which in turn translate into fluctuations in the refractive index. These fluctuating inhomogeneities result in inelastic scattering of the light as it passes through the solid. The phonons present inside a solid move in thermal equilibrium with very small amplitudes creating fluctuations in the dielectric constant, which is viewed as a moving diffraction grating by an incident light wave. The Brillouin spectrum

for the case of highly transparent solids is dominated by scattering from bulk Longitudinal (L) and Transverse (T) waves, for which the scattering selection rule involves conservation of all three components of the wavevector. There are sharp peaks in the spectrum, having frequency shifts for backscattering given by

$$\omega = 2nk_i v \tag{2.2}$$

where n is the refractive index of the medium, and v is the bulk L or T velocity for a particular direction. These peaks thus yield bulk wave velocities from which individual elastic constants or combinations of constants can be determined [123]. The factors n, k_i and v in equation (2.2) are such that the frequency shifts in bulk wave scattering (up to 150 GHz or so) are much larger than for surface wave scattering (typically up to about 30 GHz). In the determination of elastic constants using SBS, the presence of bulk wave peaks, well separated from surface wave scattering is advantageous.

A number of authors [77,119–122] have discussed the treatment of the intermediate situation of a semi-transparent layer on a solid. The full calculation requires a knowledge of the complex refractive indices and elasto-optic constants of the layer and substrate (which are not always readily available) and the near surface dynamics, and takes into account the interference between ripple and elasto-optic scattering [124]. SBS spectra can often be semi-quantitatively understood with just a knowledge of surface dynamic response in a case where elasto-optic scattering plays a minor or subsidiary role. Specifically, the positions (but not the intensities) of the Rayleigh wave and Sezawa peaks are independent of the scattering mechanism. It is interesting to note that when elasto-optic

scattering predominates, the dip in the Lamb shoulder at the longitudinal (L) threshold reverses, and becomes a peak very close to the L threshold, called the L guided mode [125].

2.3.2 Surface ripple mechanism

Unlike the elasto-optic effect, this mechanism occurs at the surface rather than in the bulk of the specimen [112]. The light is scattered by dynamic corrugations in the surface of the profile [92,126]. The phonons present at the surface of the sample move in thermal equilibrium with very small amplitudes creating corrugation of the surface, which can diffract incident light. The surface ripple mechanism is the dominant scattering mechanism in opaque solids, and the inelastic component of Brillouin spectrum displays prominent Stokes and anti-Stokes peaks frequency shifted from ω_i by

$$\omega = \pm v_R k_{||} \tag{2.3}$$

The effect can be viewed as a diffraction with an accompanying Doppler frequency shift brought about by the Rayleigh wave (RW) acting as a grating travelling in the reverse (+) or forward (-) directions at velocity v_R. The effect is interpreted as a phonon creation or annihilation from a quantum mechanical point of view, a process in which the phonon loses or gains the energy of the phonon.

Dynamic surface corrugations can also be caused by bulk acoustic waves incident on the surface, which will be detected if the component of their wavevector in the surface is equal to $k_{||}$. The wavevectors of these bulk waves take on a continuum when combined with their normal component, giving rise to

a broad continuum in the Brillouin spectrum extending from the bulk transverse wave threshold to high frequencies. This is the broad band to the right of the RW peak in Figure 2.2 and is known as the Lamb shoulder.

For the temperature at which most SBS experiments are conducted, $\omega \ll K_B T / \hbar$, where k_B is Boltzmann's constant and $\hbar$ is Planck's constant, and the classical approach described below is adequate for calculating the spectrum. A quantum mechanical approach is only necessary at very low temperatures $T < \hbar\omega / k_B$. It can be shown that in the classical regime, the cross-section for scattering of light with frequency ω and surface wavevector $k_{||}$ is given by [110,121],

$$\frac{d^2\sigma}{d\Omega d\omega} = \frac{AT}{\omega} ImG_{33}(k_{||}, \omega), \tag{2.4}$$

where A is a constant that depends on the scattering geometry, the frequency and polarization of the incident light, and the optical properties of the medium.

2.4 Kinematics of Surface Brillouin scattering

The typical geometry for SBS experiments is shown if Figure 2.3. The realistic situation of a relatively large collection aperture for the scattered light is considered; it is necessary to achieve relatively short data acquisition times since the light intensity is rather low in SBS [110]. Therefore, the incident and scattered wavevectors, $\boldsymbol{k}_i$ and $\boldsymbol{k}_s$ respectively do not lie in the sagittal plane (the 1-3 plane containing the incident wavevector). The incident angle is θ_i, while θ_s is the angle between the 3-axis and the wavevector $\boldsymbol{k}_s$ of the scattered light. The angle φ

separates the projections of $\boldsymbol{k}_i$ and $\boldsymbol{k}_s$ on the sample surface, such that $\phi = 180 - \varphi$, where φ is the azimuthal angle.

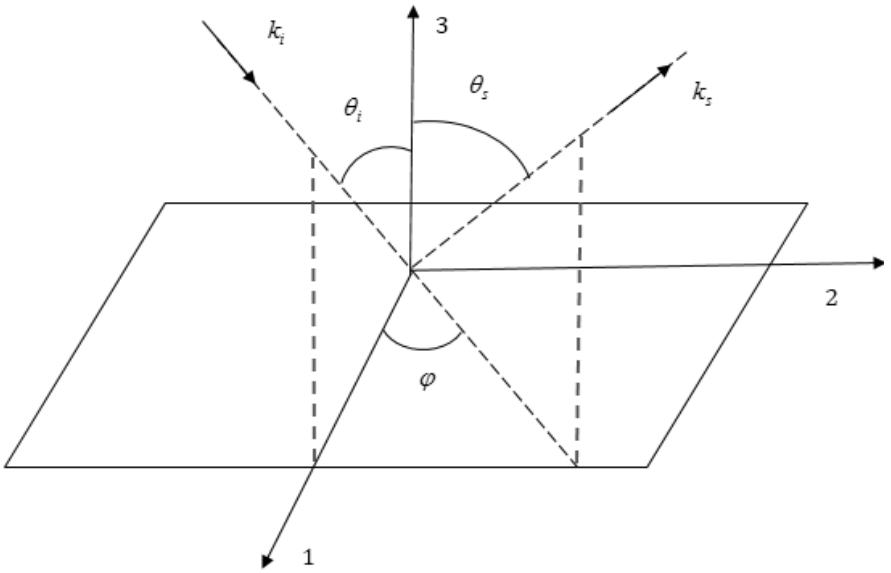

.

Figure 2.3: Geometry defined for surface Brillouin scattering. Axis 3 is taken to be pointing outwards i.e. normal to the surface.

For the geometry shown in figure 2.3, the components of the wavevector $q_{||}$ are

$$q_1 = k_i sin\theta_i + k_s sin\theta_s cos\varphi \tag{2.5}$$

$$q_2 = k_s sin\theta_s sin\phi \tag{2.6}$$

$k_s = k_i$ since the velocity of light is much greater than the phonon velocity. By summing up the components of the wavevector $q_{||}$ the following is obtained:

$$q_{||} = k_i[sin^2\theta_i + 2sin\theta_i sin\theta_s cos\phi + sin^2\theta_s]^{1/2}. \tag{2.7}$$

For the back-scattering geometry, which is normally used for SBS experiments, it is common to make the approximation that $\phi = 0°$ and $\theta_s = \theta_i$. Consequently, Eq. (2.7) becomes

$$q_{||} = 2k_i sin\theta_i \tag{2.8}$$

giving the phonon velocity as

$$V = \frac{\omega}{q_{||}} \tag{2.9}$$

where ω is the angular frequency of the surface acoustic phonon and is measured by the frequency shift of the scattered light. Eq. 2.9 expresses the result used in the current SBS work to determine the velocity of surface acoustic waves in thin films using the backscattering geometry. It is worth noting that the velocity thus determined is independent of the refractive index of the material.

2.5 Surface Brillouin scattering in opaque materials and thin films

Brillouin scattering studies on opaque materials has been a subject of interest since the 1970s [110,127]. The scattering process is limited to a very shallow region near the surface due to the optical opacity of the sample and hence the technique is generally referred to as surface Brillouin scattering (e.g., [79]). Generally, surface Brillouin scattering is not observed in transparent materials where bulk effects dominate the scattered intensity. SBS as a technique of choice has been used to study acoustic wave velocities in opaque solids including thin films [78,79,99], metals [128–130] and metallic liquids [131] and of metals at high pressure [132].

The opacity of the material determines the dominant scattering mechanism (see section 2.3). Elasto-optic coupling will be the dominant process in an isotropic solid with a complex refractive index $n = \eta + i\kappa$ and $\kappa < \eta$ (semi-opaque material), where η and κ are the real and complex part of the complex refractive index of the solid. Due to the small penetration of light in materials with $\kappa \approx \eta$, scattering will be mostly through surface ripples caused by phonons that propagate in thermal equilibrium and does not involve coupling of light with phonon-induced modulations of the dielectric constant of the sample material. Additional spectral features are produced when the two mechanisms coexist in the same system due to degeneracies of surface excitations with bulk ones. Scattering caused by interfacial waves between a thin opaque layer and substrate can also give rise to additional spectral features. They are observed when the thickness of the layer is comparable or smaller than the wavelength of the scattering acoustic mode [70,111].

The case of isotropic materials will be considered first. The general features of the surface modes involved Brillouin scattering from opaque materials, thin films and multilayered materials can be identified by comparing them with the simple case of transverse resonance in an isotropic plate of thickness H [133]. For the case of shear waves with polarisation on the surface of the plate (SH), the solution fulfils the required boundary conditions and symmetry of the plate forms a continuum with a lower cut off at $\omega = \pi v_t / H$ (where v_t is the shear velocity). The SH waves in the free space correspond to a limiting case of Love waves [134], which are defined for thin plates on a semi-infinite substrate. In addition to a shear vertical (SV) component, a longitudinal (L) component can be produced by reflection at the plate boundaries for shear waves with a general polarisation.

Four plane wave solutions satisfy the boundary conditions, and the frequency spectrum will be characterised by three regimes: (I) $\omega / q < v_t$ (where q is the plate normal mode wavevector and v_t is the shear velocity of the bulk sample) in which all the transverse and longitudinal modes are dissipative (their q are imaginary) and localised at the surface and are related to the Rayleigh mode of a semi-infinite solid; (II) $v_t < \omega / q < v_l$ (where v_l is the bulk longitudinal velocity of the plate) where the solutions are the combinations of transverse and longitudinal modes and are referred to as Lamb waves; (III) $\omega / q > v_l$ where all the solutions are real and are bulk normal modes. In the case of a semi-infinite medium (corresponding to the limit $H_q \rightarrow \infty$) the low order solutions (I) give rise to the Rayleigh surface mode and the SH and the Lamb wave solutions form continua that are indistinguishable from the bulk shear modes. Only the Lamb waves have a longitudinal component localised at the surface.

Secondly, in the case of anisotropic extended opaque media, SBS spectra present peaks arising from both pure surface transverse modes (surface acoustic waves, SAW) or their combinations with transverse bulk normal modes of the material (pseudo-SAW; e.g., [70]). Depending on the relative magnitudes of the acoustic velocity of the film and substrate, the most important features detected by SBS from anisotropic thin films supported by thick substrates and multi-layered composites can be summarised into two basic cases:

(I) In the low frequency regime ($\omega / q < v_t^{layer}$), it is possible to observe a SAW whose velocity approaches (at large film thickness) the bulk Rayleigh velocity for a supported thin layer of lower acoustic velocity than the semi-infinite substrate; Lamb waves and Sezawa waves (localised waves supported by the film layer whose displacement field decays towards the substrate) are

observed in the frequency regime $v_s^{layer} < \omega / q < v_t^{substrate}$. Combinations of Sezawa waves and bulk modes of the substrate can be finally observed at frequencies such that $\omega / q > v_t^{substrate}$. (II) For a supported thin layer with a high acoustic velocity than the substrate at very low layer thickness, the Rayleigh wave of the substrate dominates the spectrum. At increasing thickness, the Rayleigh wave transforms into a SAW reaching the bulk shear wave threshold of the substrate. As the thickness increases further, the SAW of the layer becomes detectable and merges the Rayleigh wave velocity at the limit at which the thin layer becomes effectively a semi-infinite layer. In case of thick semi-transparent layers with appropriate matching elastic and elasto-optic properties of both layer and substrate, localised interfacial waves known as Stoneley waves can also be observed [70,135]. It is worth noting that Brillouin scattering from SH waves can only take place by the elasto-optic coupling mechanism since they do not contribute to surface ripples (a theoretical analysis of the associated spectral intensity is given in [136]). The detection of Brillouin scattering from SH waves is limited to transparent materials [136,137]. It is necessary to take advantage of the penetration through the interface between metals films and transparent substrates of the displacement field associated with SH waves of the substrate in order to detect Brillouin scattering from SH waves in metals [138].

A theoretical interpretation of SBS spectral intensity is important in the determination of the elastic properties of the material under study. The work of several researchers on the subject over the past years has resulted in to two main approaches: (a) the elastodynamic Green's function approach (b) the direct calculation of the surface scattered electromagnetic field intensity. A summary of

the two approaches is given below as presented in [90]. Later in section 2.6, the theory of the elastodynamic Green's function is discussed further.

(a) In [70], as an example of the first approach, for a layer supported by a substrate the appropriate surface elastodynamic Green's function (in the frequency domain) is $G_{33}(k_{||}; x = 0; \omega)$, which describes the (surface-)normal component of displacement of the free surface ($x = 0$) of a supported layer or semi-infinite solid in response to periodic forces acting on the same surface and having spatial frequency $k_{||}$ and time frequency ω. The imaginary part of the function, (in the limit of $\omega \ll k_B T \,/\, \hbar$ where k_B is Boltzmann's constant and $\hbar = h \,/\, 2\pi$ is the reduced Planck's constant), can be related to the surface displacement power spectrum that is proportional to the scattering efficiency and gives information about the relevant surface modes that contribute to the measured Brillouin signal [115,139]

$$I(\omega) = D\frac{T}{\omega} Im\{G_{33}(k_{||}; x = 0; \omega)\} \tag{2.10}$$

where $I(\omega)$ is the scattering efficiency and D is a factor that depends on the properties of the sample, the scattering geometry, and the frequency and polarisation of the incident light. The density and elastic constants of the material (or materials in case of supported thin films) determine the appropriate Green's function of the system under study. The calculated scattering efficiency will include terms describing the elasto-optic coupling (Pockel's coefficients) of the scattering material if the model includes the surface modified bulk fluctuations of

the dielectric constant of the material (elasto-optic contribution to the scattering) [116].

(b) Calculation of the scattered magnetic field in the bulk system which is specialised for the case of surface scattering constitutes the second approach. The scattering cross-section is then calculated from the Poynting vector of the scattered field. A more direct identification of the modes that contribute to the scattering cross-section is made possible by this approach [77]. The inclusion of both ripple and elasto-optic contributions to both the elastodynamic Green's function and direct calculation of the scattered electromagnetic field allows for the interpretation of the experimental spectra and the dispersion curves both in terms of elastic constants and of photo-elastic coefficients of the investigated materials.

The theory of Brillouin scattering in isotropic and anisotropic semi-infinite media and in supported or unsupported plates has been developed in several studies [91,119]. The prevalence of the ripple scattering mechanism in the highly opaque systems has been confirmed by a comparison between theoretical and available experimental results [78]. The importance of adding the elasto-optic contribution to fully interpret the observed spectral features has been confirmed by experimental studies carried out on semiconductor layers supported by metals [121,140].

2.6 Surface elastodynamic Green's function of a supported layer

Based on the work of several authors [70,110,115], the following section discusses the surface elastodynamic Green's function approach to the

interpretation of the SBS spectra for opaque thin films perfectly bonded on a substrate.

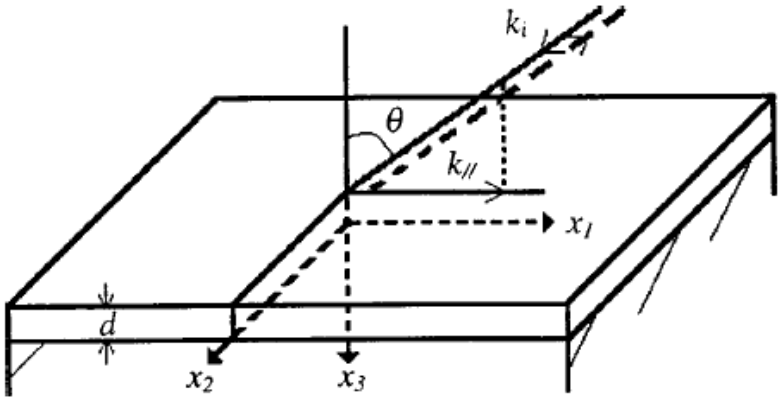

Figure 2.4: Light-scattering geometry for SBS from a thin supported film [115].

For the calculation of the elastodynamic Green's function for a thin supported film, the geometry shown in figure 2.4 is chosen. x_3 is defined as an outward normal to the traction free surface of the layer which occupies the half space $x_3 < 0$.

The evaluation of $G_{33}(k_{||}, x_3 = -d, \omega)$ is required for the case of an opaque layer where the scattering occurs at the surface of the layer. $G_{33}(k_{||}, x_3 = -d, \omega)$ is the (x_3, x_3) component of the Fourier-domain Green's tensor of the system for force and displacement response at the surface of the layer. Continuity of the stress components (traction forces) $\sigma_{l3}(k_{||}, x_3 = -d, \omega)$ and displacement field $\boldsymbol{u}$ at the interface are the boundary conditions in evaluating the response with

$$\sigma_{l3}(k_{||}, x_3 = -d, \omega) = -\delta_{l3} \tag{2.11}$$

at the surface. For a homogeneous elastic continuum, the displacement field must satisfy the equations of motion

$$\rho \frac{\partial^2 u_i}{\partial t^2} = C_{ijkl} \frac{\partial^2 u_l}{\partial x_i \partial x_k}, \tag{2.12}$$

where C_{ijkl} is the elastic-modulus tensor, ρ the mass density, and u_i the particle displacement components in the individual media. Eq. (2.12) admits six plane-wave solutions for each value of $k_{||}$ and ω in which the third component k_3^n, n = $1, \ldots 6$ of $\boldsymbol{k}$ is obtained as a real or complex root of the sextic Christoffel characteristic equation

$$\left| C_{ijkl} k_j k_k - \delta_{il} \rho \omega^2 \right| = 0, \tag{2.13}$$

with the associated polarisation vector U_i being obtained from

$$\left(C_{ijkl} k_j k_k - \delta_{il} \rho \omega^2 \right) U_i = 0. \tag{2.14}$$

All six waves $k_3^{(n)}, n = 1, \ldots 6$ are used for the layer; while for the substrate only the three outgoing waves ($n = 7,8,9$) are retained and three incoming waves discarded as discussed in [141]. The outgoing waves are either homogeneous, with $k_3^{(n)}$ real and with ray vectors $\boldsymbol{v} = \partial\omega / \partial \boldsymbol{k}$ directed into the interior of the substrate, or evanescent waves with $Im\left(k_3^{(n)} > 0\right)$, so that their amplitudes fall off into the interior.

The solution that satisfies the boundary conditions in the layer takes the form of a superposition of the six plane waves ($n = 1,2, \ldots, 6$):

$$u_i^-\left(k_{||}, x_3, \omega\right) = \sum_{n=1}^{6} A_3^{(n)} U_i^{(n)} exp\left\{ik_3^{(n)}\right\}, \tag{2.15}$$

and in the half space of the three outgoing plane waves $n = 1,2,\ldots,6$:

$$u_i^+\left(k_{||}, x_3, \omega\right) = \sum_{n=7}^{9} A_3^{(n)} U_i^{(n)} exp\left\{ik_3^{(n)} x_3\right\}. \tag{2.16}$$

From the stress-strain relationship, $\sigma_{lm} = C_{lmpq}\partial u_p \,/\, \partial x_q$ for the layer and Eq. (2.15) it follows that the surface tractions are given by

$$\sigma_{l3}\left(k_{||}, x_3 = -d, \omega\right) = i\omega \sum_{n=1}^{6} A_3^{(n)} B_l^{(n)}, \tag{2.17}$$

where

$$n = 1,2,\ldots,6, \quad l = 1,2,3. \tag{2.18}$$

Comparing Eqs. (2.11) and (2.17), a set of three linear equations for the amplitudes $A_3^{(n)}$ are obtained as

$$\sum_{n=1}^{6} B_l^{(n)} A_3^{(n)} = \begin{cases} \dfrac{i}{\omega}\delta_{3l}, & l = 1,2,3 \\ 0, & \end{cases} \tag{2.19}$$

for the surface and interface Green's functions, respectively.

Another set of three equations for the partial wave amplitudes arise from the stress conditions at the interface, which yield

$$\sum_{n=1}^{9} B_l^{(n)} A_3^{(n)} = \begin{cases} \frac{i}{\omega} \delta_{3l}, \\ 0, \end{cases} \quad l = 4,5,6 \tag{2.20}$$

for the surface and interface Green's function respectively, where

$$B_l^{(n)} = \sum_{pq} C^{+}_{3(l-3)pq} \, U_p^{(n)} k_q^{(n)} \, / \, \omega, \qquad l = 4,5,6, \qquad n = 7,8,9 \tag{2.21}$$

$$B_l^{(n)} = -\sum_{pq} C^{-}_{3(l-3)pq} \, U_p^{(n)} k_q^{(n)} \, / \, \omega, \qquad l = 4,5,6 \;\; n = 1,2,\ldots,6 \tag{2.22}$$

Finally, there are three equations for the partial wave amplitudes arising from continuity of the displacement field at the interface, which yield

$$\sum_{n=1}^{9} B_l^{(n)} A_j^{(n)} = 0, \qquad l = 7,8,9 \tag{2.23}$$

where

$$B_l^{(n)} = U_{l-6}^{(n)}, \qquad l = 7,8,9, \qquad n = 7,8,9, \tag{2.24}$$

and

$$B_l^{(n)} = -U_{l-6}^{(n)}, \;\; l = 7,8,9, \;\; n = 1,2,\ldots,6. \tag{2.25}$$

The solution of the nine equations for $A_3^{(n)}$ above takes the form

$$A_3^{(n)} = \frac{i}{\omega}(B^{-1})_3^{(n)}. \tag{2.26}$$

By substituting these results for $A_3^{(n)}$ into Eq. (2.15), the displacement Green's function for the free surface of the layer is obtained, i.e.

$$G_{33}\left(k_{||}, x_3 = -d, \omega\right) = \sum_{n=1}^{6} \frac{i}{\omega}(B^{-1})_3^{(n)} U_3^{(n)} exp\left\{-ik_3^{(n)} d\right\}, \tag{2.27}$$

and that for the interface is

$$G_{33}\left(k_{||}, x_3 = 0, \omega\right) = \sum_{n=1}^{6} \frac{i}{\omega}(B^{-1})_3^{(n)} U_3^{(n)}. \tag{2.28}$$

Eq. (2.27) determines the SBS spectrum for the free surface of the layer, where $U_3^{(n)}$ and $k_3^{(n)}$ are the components of the mode polarisation and the frequency dependent wavevector perpendicular to the film plane, respectively, B is the boundary condition matrix, d is the film thickness while $n = 1,\ldots,6$ refers to partial waves in the layer and $n = 7,8,9$ to the outgoing partial waves in the substrate.

The experimental arrangement and the scattering geometry normally determine $k_{||}$ in a surface Brillouin scattering experiment. The imaginary part of the Green's function $Im\{G_{33}(k_{||}, x_3 = -d; \omega + i0)\}$, determines the scattering efficiency $I(\omega)$ (Eq. (2.10)) which is a function of the angular-frequency shift in the measured spectrum. When the boundary matrix B^{-1} becomes singular, a true

surface wave (RSAW) becomes apparent with a sharp line in the spectrum visible. The combination of the overlayer and the substrate determines the nature and type of the excitations observed in thin supported films. For some of the films in this work, Sezawa modes are observed in a system commonly referred to as a slow on a fast system. These and other spectral features are discussed in the results chapters 5, 6, and 7.

As an example, Figure 2.5 shows a typical SBS spectrum for an opaque thin film calculated from the surface Green's function. The extraction of the elastic constants for thin films is done by simultaneously fitting the dispersion curves for the observed modes (Rayleigh and Sezawa) as a function of the product of the phonon wavevector parallel to the surface and layer thickness (i.e. $\boldsymbol{v}$ vs $k_{||}d$).

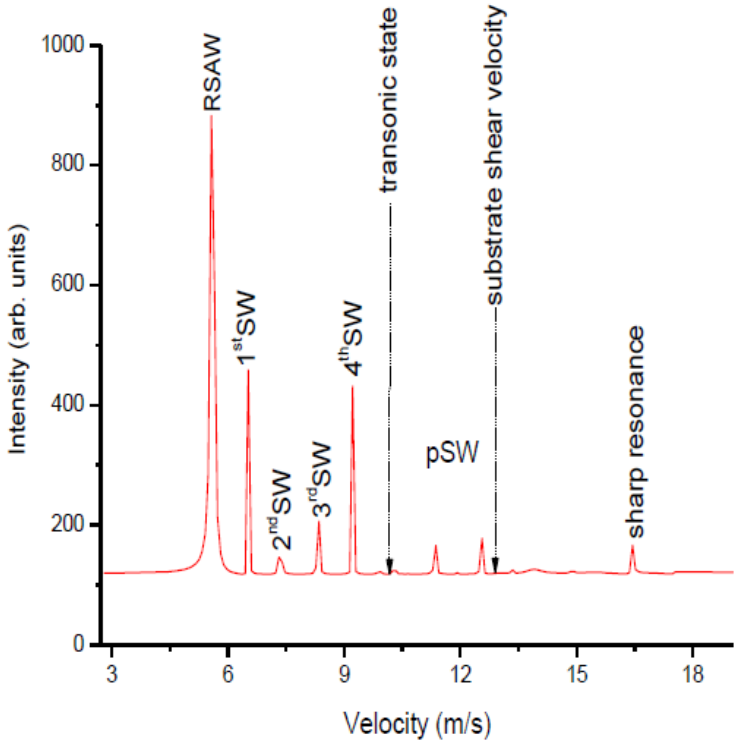

Figure 2.5: Typical SBS spectrum for a thin supported film showing the Rayleigh surface acoustic wave (RSAW), Sezawa waves (SW), pseudo-Sezawa waves (pSW) and sharp resonances [142].

Chapter 3

Thin Film Deposition and Characterisation

Physical vapour deposition (PVD) methods have been widely applied to deposit transition metal nitride films [143]. PVD is normally divided into three categories: evaporation, sputtering, and hybrid PVD processes (ion plating, reactive evaporation and ion-beam assisted deposition, etc.) [32]. Evaporation involves the removal of atoms from the source by thermal means, whereas sputtering involves the removal of atoms from the target material by the interaction of incident particles and ions of a gas. The films studied in the present work have been prepared using RF magnetron sputtering. This chapter gives a description of the techniques, tools and processes used in the deposition and characterisation of thin films studied in this work. Section 3.1 gives a description of RF magnetron sputtering process and the equipment used in this work. In Section 3.2, a brief discussion of the structure zone model is given. Section 3.3 presents thin films thickness analysis using X-ray reflectivity (XRR). In section 3.4, grazing incidence X-ray diffraction (GIXRD) is discussed as applied for phase identification of the films. Surface roughness characterization of the films using atomic force microscopy (AFM) is discussed in section 3.5. Section 3.6 looks into the microstructure and growth mode identification using scanning electron microscopy (SEM). Composition determination of the thin films using heavy-ion elastic recoil detection analysis (HI-ERDA) is discussed in section 3.7.

3.1 RF Magnetron Sputtering

Inert gas ions of energies in excess of about 30 eV eject materials upon impacting on a target's surface via a knock-on effect [144]. This process is termed as sputtering. The sputtering process was first reported in 1852 by Grove [145]. Since then the basic level of understanding of sputtering phenomena has been refined paving way for it to be used to deposit films on architectural glass, integrated circuits, hard drive platters, and a plethora of other applications. Sputtering deposition and sputtering etching have become common manufacturing processes for a wide variety of industries.

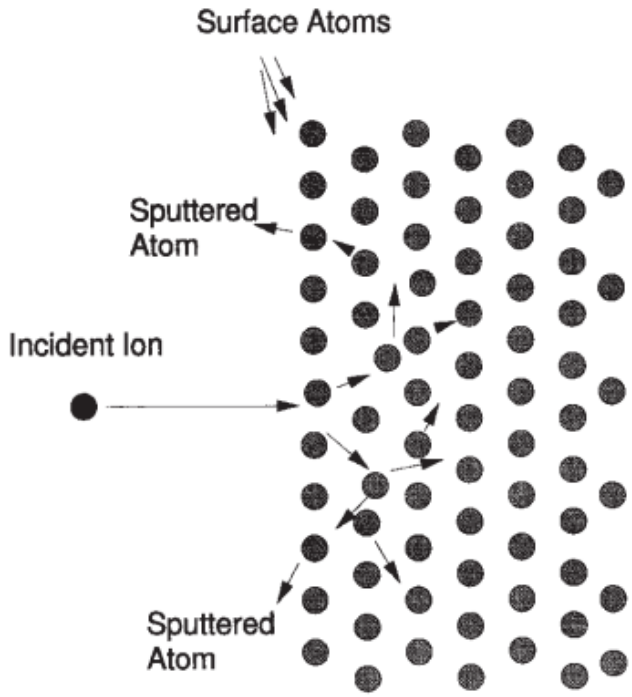

Figure 3.1: Schematic of physical sputtering process [146].

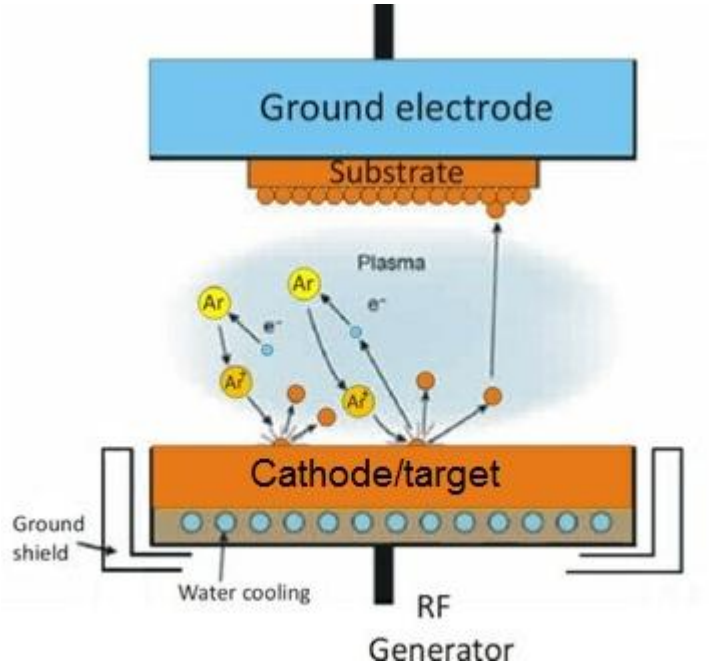

Figure 3.2: Typical set up for film deposition by sputtering (glow discharge) [147].

The sputtering process is a glow discharge or a plasma process, in which ionised gas atoms/molecules accelerate in an electric field to erode material from the source (target), which then condenses on a work piece (substrate). The cathode (RF magnetron) is driven by an RF power source, to generate sustained plasma between the two electrodes by continuous ionisation of argon gas through impact ionisation (Figure 3.2).

A negative DC potential is used to drive the ions towards the target surface causing atoms to knock off the target atoms to condense on the substrate surface. A strong magnetic field confines the electrons spirally on the surface of the target hence sustaining the plasma in that location. A high electron density increases the deposition rate. Sputtering occurs whenever any particle strikes a surface with enough energy to dislodge an atom from the surface. The erosion of the target is a momentum transfer process [148], the efficiency of which is termed as the sputter

yield (S atoms/ion). The sputter yield, *S*, which is the removal rate of surface atoms due to ion bombardment, is defined as the number of atoms removed from the surface of a solid per incident ion and is given by equation 3.1 [149].

$$S = \frac{\text{atoms removed}}{\text{incident ions}} \tag{3.1}$$

Several authors have derived equations describing the sputter yield as a function of energy and projectile-target combinations. According to the theory of Sigmund [150], the sputter yield near threshold, i.e. at low ion energy is given by

$$Y = \frac{3}{4\pi^2}\alpha\frac{4M_1M_2}{(M_1+M_2)^2}\frac{E}{U_s} \tag{3.2}$$

with E the energy of the projectile, and $M_1$and M_2 the masses of the projectile and the target atom (in amu). U_s is the surface binding energy and α a dimensionless parameter depending on the mass ratio and the ion energy. At low energy, and mass ratios $M_2 \,/\, M_1$ lower than 1, α is of the order 0.2. This equation can be understood as follows. An incoming ion transfers its momentum to the target atoms which explains the term $4M_1M_2 \,/\, (M_1+M_2)^2$ with a maximum when $M_1 = M_2$. To sputter an atom from the target, momentum transfer from the ion-induced collision must overcome the surface barrier, given by the surface binding energyU_s. The sputter yield will be influenced by the following factors [149]:

- Energy of the incident particles
- Target materials
- Incident angles of particles

- Crystal structure of the target surface

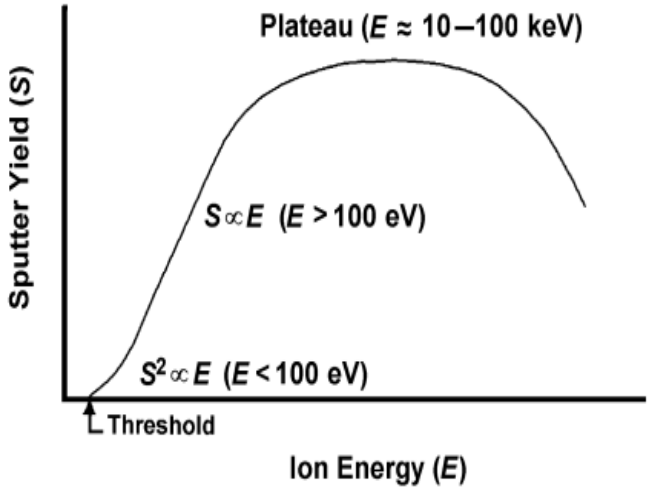

Figure 3.3: Variations of sputter yield with incident ion energy [149].

RF magnetron sputtering can be used to deposit material from insulating targets. Power from an RF generator typically operating at 13.56 MHz is transmitted to a matching network via a 50 Ω coaxial cable. The matching network consists of a variable capacitor and inductor and is needed to match the impedance of capacitive discharge plasma to the 50 Ω output impedance of the generator. The applied RF field would normally tend to just oscillate charged particles and therefore not generate any sputter deposition. However, due to a large difference in mass between ions and electrons, oscillations of the electrons are large enough that a significant portion impinges on the target and the chamber, whereas the ions are basically static. Since the chamber walls are grounded, and the target is electrically floated on capacitors, the target tends to build up negative charge over time, i.e. develops a negative bias.

Mechanical and electrical properties are similar to bulk values. The growth mechanism of RF sputtered thin films can be explained by the island growth mode

(or Volmer-Weber, VW) and the layer-plus-island growth mode (or Stransky-Krastanov, SK) [144]. Use of RF power source in sputtering alleviates the necessity to employ conductors as targets. In RF magnetron sputtering, at low pressures (5 - 15 mtorr), a self-sustaining discharge is maintained when RF supplies power to the electrodes. The RF magnetron used to deposit the films in the present work is shown in Figure 3.4.

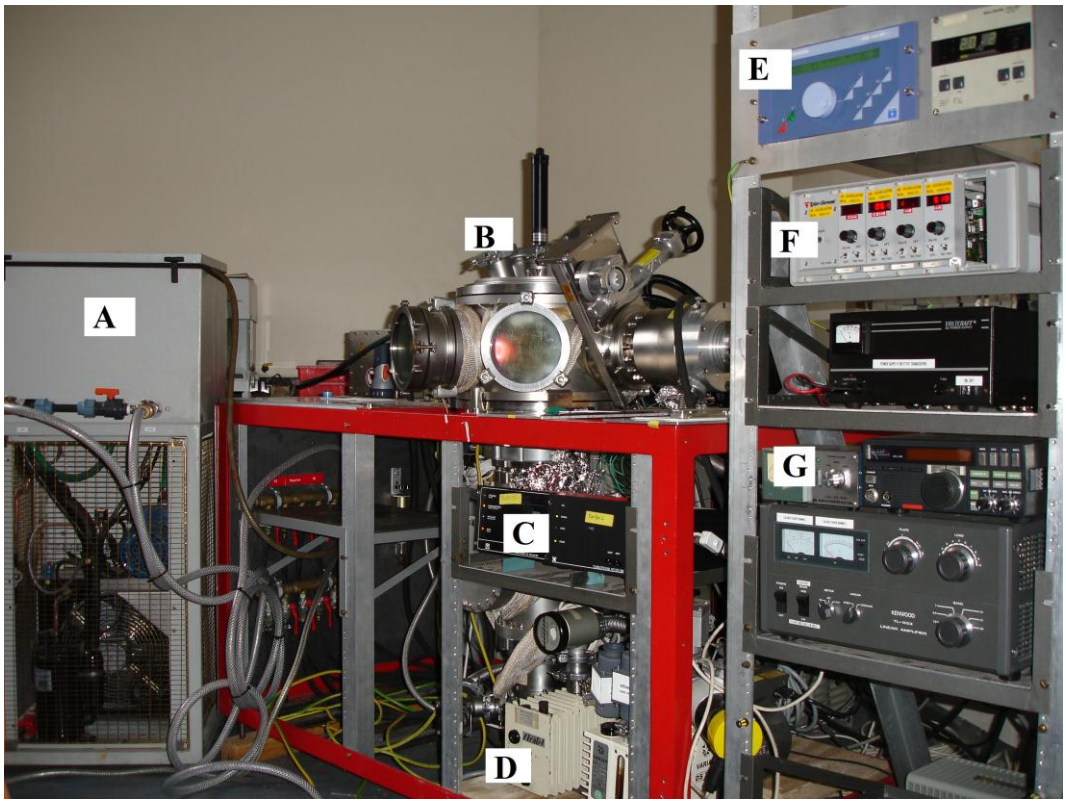

Figure 3.4: A photograph of the RF sputtering equipment used in this work (Courtesy of School of Physics, University of the Witwatersrand). A - shows the chiller used to cool the magnetron during deposition, B - the RF chamber under high vacuum, C - turbo pump control unit, D - fore pump, E - RF generator, B - gas control unit, and G - linear amplifier.

Thin films of NbN, ZrN, and TaN were deposited on Si (100) single crystal substrates (1.5cm × 1.5 cm). Film deposition was carried out using 99.9% pure, 76 mm diameter × 6mm thick NbN, ZrN and TaN targets (Semiconductor Wafer Inc.) respectively at a fixed sample distance of 6 cm. The substrates were cleaned

with successive rinses in ultrasonic baths of acetone and ethanol and then blow dried with N_2 before deposition. Prior to the deposition, the chamber was evacuated with fore- and turbo-pumps to a base pressure of 2.4×10^{-5} mbar. A high vacuum is essential to ensure there is no target poisoning or contamination or formation of an oxide monolayer during deposition. The targets were pre-sputtered in argon ions at sputter power of 100 W for 15 minutes to remove impurities on the target surface. Prior to deposition, the silicon substrates were sputter etched in Ar at a sputter power of 40 W for 5 minutes to remove the native oxide layer from the substrate surface. For XRR samples, the substrates were not sputter etched, the native oxide layer being important in XRR simulations (see section 3.3). Table 3.1 shows the deposition conditions used for the films.

Table 3.1: Deposition conditions used in films deposition.

Base pressure (mbar)	2.4×10^{-5}
Working gas pressure (mbar)	8.5×10^{-5}
Ar flow rate (sccm)	13
Target voltage (V)	0
Magnetic field (T)	0.3
Sputter power (W)	75 - 250

3.2 Structure Zone Model

Several authors have attempted to summarise the influence of deposition parameters on thin film morphology and microstructure in a single diagram. These diagrams are known as structural zone models (SZMs) [146]. The Thornton

[151] model is a structural zone model relating substrate pressure and temperature to the morphology of the film.

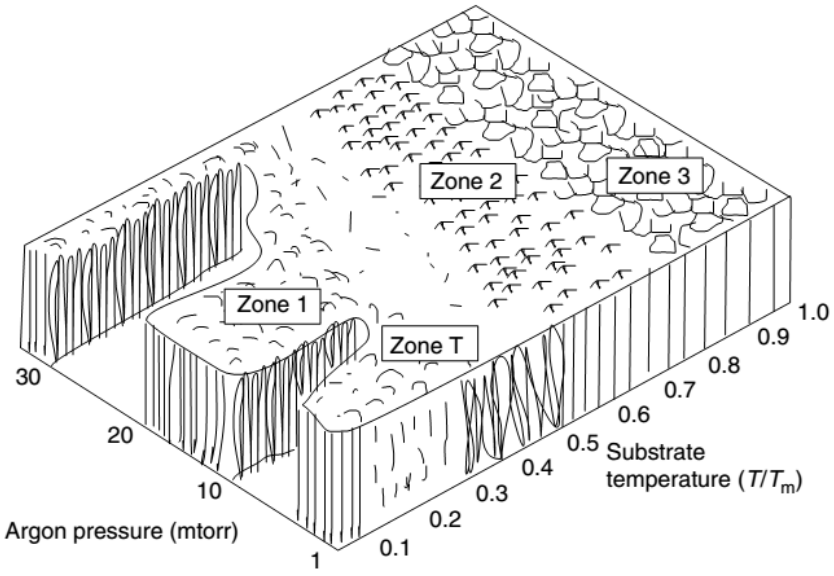

Figure 3.5: Thornton structural zone diagram [152]

The four basic zones are shown in Figure 3.4 above. Zone I is characterised by a columnar grain structure with significant porosity between the grains, and large defect concentrations within the grains. Films with a Zone T microstructure are formed as the pressure decreases and/or the temperature of the substrate increases. The porosity between the fine columnar grains diminishes, which increases film density. Higher temperatures are needed to achieve Zone II, which has a large grain columnar structure, possibly a faceted surface, and properties are nearly those of bulk materials. Zone III morphology occurs for temperatures near the melting temperature of the deposited material and has large equiaxed grains due to impurity induced re-nucleation.

3.3 X-ray Reflectivity

3.3.1 Introduction

X-ray reflectivity is a non-destructive technique which finds many applications in the analysis of thin films, as it provides information about thickness, density, and surface roughness of single- and multilayered samples [153]. Like electromagnetic radiation in the visible region, X-rays can be reflected specularly by planar surfaces; in fact, at their characteristic wavelengths the diffraction index of the material is less than one, which makes it possible to obtain total reflection at the air-material interface when the incidence angle is lower than $0.2 - 0.5°$ (for wavelength of ~Å). Above this value, a sharp drop of the reflected intensity is observed, along with oscillations in the signal (Kiessig fringes [154]), due to the interference between the X-ray reflected from the surface and the interface. The visibility of these interference effects in the XRR spectra depends essentially on the density ratio between film and substrate. The angle at which the reflected intensity reaches half the value observed in the total reflection region is defined as the critical angle, and it depends basically on the density of the material. The spacing between the maxima of the oscillations is related to the film thickness. Information on the surface roughness is basically contained in the degree of contrast among interference fringes. By measuring the total reflection intensity (reflectivity) as a function of the incident angle with respect to the thin film surface, a profile such as one shown in Figure 3.6 can be obtained, and structural parameters such as density, thickness and roughness of each layer of the thin film can be evaluated non-destructively.

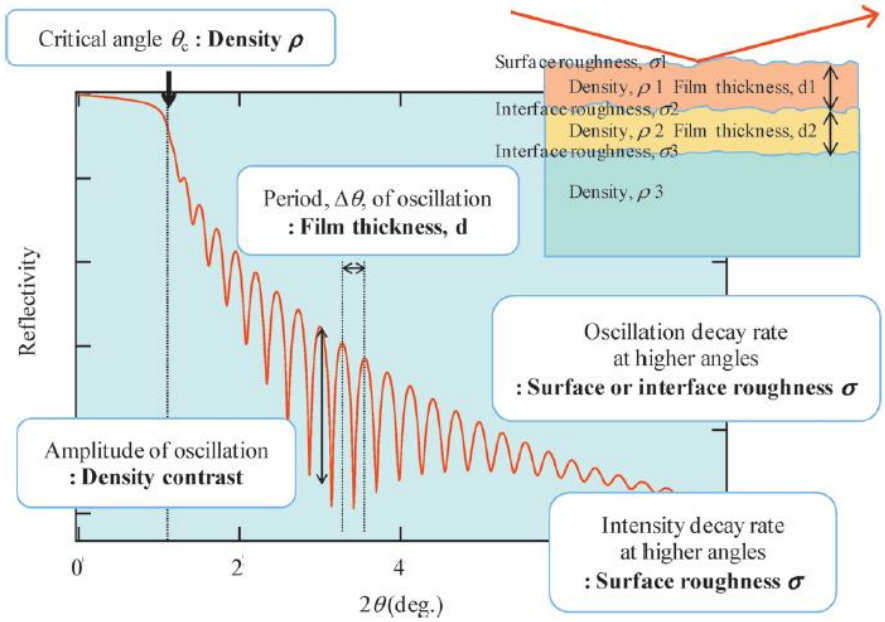

Figure 3.6: Information provided by X-ray reflectivity profile [155].

An extensive discussion of the XRR principle can be found elsewhere [156–159].

3.3.2 Reflection of X-rays at material surfaces

This section discusses the interaction of X-ray and material surfaces and closely follows the discussion of X-rays involving thin film measurement techniques by Miho Yasaka [155]. When electromagnetic waves including visible wavelengths are incident onto a sample surface, these electromagnetic waves are reflected from the surface. The incident electromagnetic waves generate a specularly reflected wave, a refracted wave and diffused reflections as shown in Figure 3.7. In the case of X-rays, which are incident electromagnetic waves, the refractive index of a material is slightly less than 1.

Therefore, the X-rays undergo total reflection when incident on a flat surface of a material at a grazing angle that is smaller than the critical angle for total reflection (θ_c).

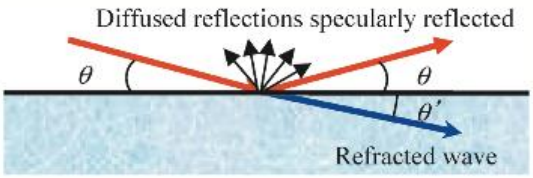

Figure 3.7: Reflection and refraction of X-rays on material surface [155].

Thus, X-ray reflectivity is related to the values of the refractive index and X-ray wavelength.

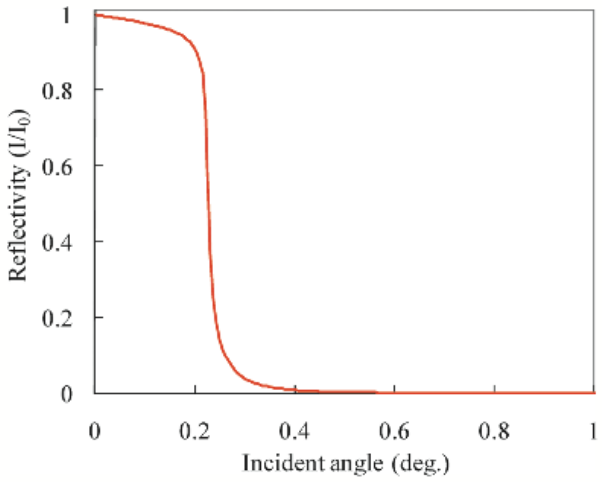

Figure 3.8: Reflectivity curve of Si [155].

In Figure 3.8, a calculated X-ray reflectivity curve of bulk Si is shown while figure 2.10 shows the X-ray optics for the cases of the incident angles smaller, equal to, and greater than the critical angle for total reflection, θ_c. As shown in Figure 3.8, when an X-ray beam is impinged at a grazing angle onto an ideal surface of a material, total reflection occurs below the incident angle θ_c, and the incident X-rays do not penetrate the material. X-ray reflectivity decreases rapidly

with increasing incident angle θ above θ_c. The ratio of specularly reflected X-ray decreases proportionally to θ^4.

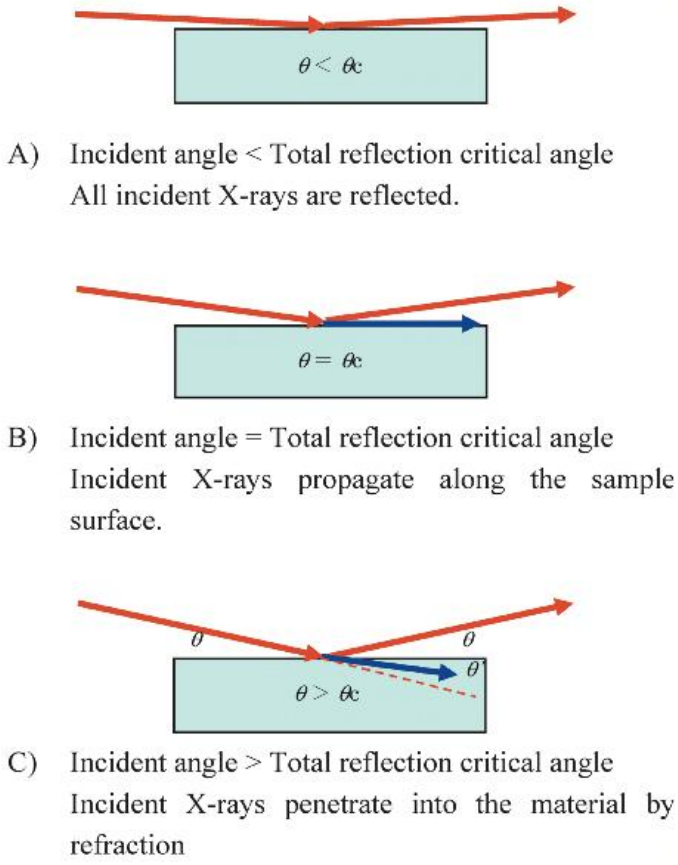

Figure 3.9: Conditions for total external reflection of X-rays [155].

3.3.3 Structural Parameters of thin films from XRR

By analysing the resulting X-ray reflectivity curves, information on the structural properties such as film thickness, density and roughness are obtained. The following sections give descriptions of how these parameters are obtained based on the treatment of Tolan *et al.* [160], Holý *et al.* [161], and Als-Nielsen *et al.* [162]. When an X-ray beam impinges on the surface of a sample, similar conditions apply as for optics with the visible light, i.e. the index of refraction n is the relevant parameter.

For X-rays, i.e. electromagnetic radiation with a wavelength λ around 1 Å, the following is found:

$$n = 1 - \delta - i\beta, \tag{3.3}$$

with

$$\delta = \frac{\lambda^2}{2\pi} r_e \rho_e \tag{3.4}$$

and

$$\beta = \frac{\mu\lambda}{4\pi} \tag{3.5}$$

ρ_e is the electron density, $r_e = 2.818 \times 10^{-15} m$ is the classical electron radius and μ is the linear absorption coefficient.

3.3.3.1 Film Density

From the measurement of the critical angle, the density can be estimated by the formula

$$\theta_c = \sqrt{2\delta} = \lambda\sqrt{\frac{r_e}{\pi}} \tag{3.6}$$

3.3.3.2 Film Thickness

For incident angles greater than $\theta_c (\theta_R > \theta_c)$ the X-ray beam penetrates inside the film. Reflection will therefore occur at the top and bottom surfaces of the film. The interference between the rays reflected from the top and the bottom of the film surfaces results in interference fringes. For intensity maxima, the path

difference between the reflected waves should be an integral multiple of the incident wavelength,

$$m\lambda \approx 2d\sqrt{sin^2\theta_m - sin^2\theta_c} \tag{3.7}$$

where m is an integer.

Since the angles are small, the equation above can be expressed as

$$m\lambda \approx 2d\sqrt{\theta_c^2 - \theta_c^2}. \tag{3.8}$$

The layer thickness is therefore given by

$$d = \frac{1}{2}m\lambda\frac{1}{\sqrt{\theta_m^2 - \theta_c^2}}, \tag{3.9}$$

3.3.3.3 Film surface roughness

Another important quantity determined from XRR measurements is the surface and interface-roughness. Roughness gives rise to diffuse scattering, resulting to a lower intensity in the specularly reflected beam. In one of the formalisms, Névot and Croce [163] considered roughness by assuming non-homogeneous thickness. They assumed that the thickness has a Gaussian distribution with a mean d and a standard deviation σ. With this assumption, they corrected the Fresnel coefficients of reflection $\rho_{v,h}$ as

$$\rho_{v,h}.exp\left(-\frac{d}{2\sigma^2}\right) \tag{3.10}$$

3.3.4 Experimental Details

XRR was used to determine the films thickness, surface roughness and mass density of selected films. The measurements were carried out using a D8 Discover high resolution X-ray diffractometer (Bruker AXS GmbH) coupled to Cu Goebel mirror and Ge (004) crystal to yield a highly collimated monochromatic Cu Kα beam at 8.0 keV. A series of manual and programmable detector slits of 0.1 mm were used to further collimate the incident and secondary X-ray beams. All XRR measurements were carried out in the 2θ-ω geometry up to 6° in 2θ. The measured XRR spectra were subsequently simulated using "leptos" software (Bruker AXS GmbH) software for the extraction of film density, surface roughness and film thickness.

3.4 Grazing Incidence X-ray Diffraction

3.4.1 Introduction

X-rays have been used for decades to study the structure of bulk crystalline materials. They interact weakly with matter compared to electrons. This gives them a number of advantages [164] :

- Multiple scattering can often be neglected unlike electrons and X-rays penetrate significant distances, typically on the order of 0.1 to 10 mm depending on the material and the X-ray energy. These points allow them to provide microstructural information averaged over a large ensemble of atoms or molecules. This distinguishes X-ray techniques from imaging techniques such as scanning electron microscopy or transmission electron microscopy: the latter is restricted to small areas a few hundreds of

nanometers thick, depending on the material while the former is a purely surface probe.

- Even if X-ray diffraction is not intrinsically a surface selective tool, the grazing incidence X-ray diffraction technique provides the opportunity to probe the structural evolution of solids near the surface. This is thanks to the fact that the refractive index is slightly less than 1 for X-rays. As pointed out by many authors[165,166], the refractive index is a function of the electron density in the material and thus of the chemical composition [166,167].

The scattering of X-rays at long range ordered periodic systems is in general called X-ray diffraction. These systems are typically crystals. The scattering of these periodic structures causes constructive and destructive interference of the scattered waves resulting in spots of high intensity. These peaks are called Bragg peaks or Bragg reflections.

X-ray diffraction is a powerful tool for probing material structures in the atomic scale. The conventional Bragg diffraction, sometimes called two-beam diffraction, is used to determine the crystallographic orientation, morphology, particle size and lattice parameters of thin films and the lattice mismatches and strain between the thin films and substrates [168]. The phenomena of X-ray diffraction in single crystals was first discovered and theoretically described by Laue [169] and Bragg [170] in 1912 and 1913 respectively.

3.4.2 Grazing Incidence X-ray Diffraction Geometry

The conventional Bragg-Brentano (also called θ-2θ) (Figure 3.10 (a)) X-ray diffraction geometry is not useful for the study of ultra-thin, graded composition and multi-layered thin films, partly because of poor sensitivity and partly because of the presence of interfering effect of the substrate [171]. X-rays with large glancing angles of incidence will go through a few to several hundred micrometers inside the material under investigation, depending on its "radiation" density, so that when it comes to thin film analysis the penetration depth may be much greater than the sample thickness [172].

To limit the incident X-ray beam to the surface, grazing incidence X-rays are needed [173]. At an incident angle slightly lower than the critical angle for total reflection, the incident beam is evanescent and penetrates only the top 1000 Å or less into the surface [174,175]. There is also an enhancement in the intensities at the surface [173]. At incident angles near to the critical angle, X-rays are enhanced by 2-4 times at the surface over the intensities in the bulk [175].

The following description of the grazing incidence is given by Bouroushian et al [172]. In the grazing XRD, the Bragg-Brentano geometry is modified to provide an "asymmetric" diffraction result, which allows access to small depths in the sample by lowering the angle of incidence. A parallel mono-chromatic X-ray beam falls on the sample surface at a fixed, low glancing angle α (larger than the critical angle for total reflection, α_c , but usually smaller than 10°) and the diffraction profile is recorded by the detector-scan only (Figure 3.10 (b); non-rotating sample).

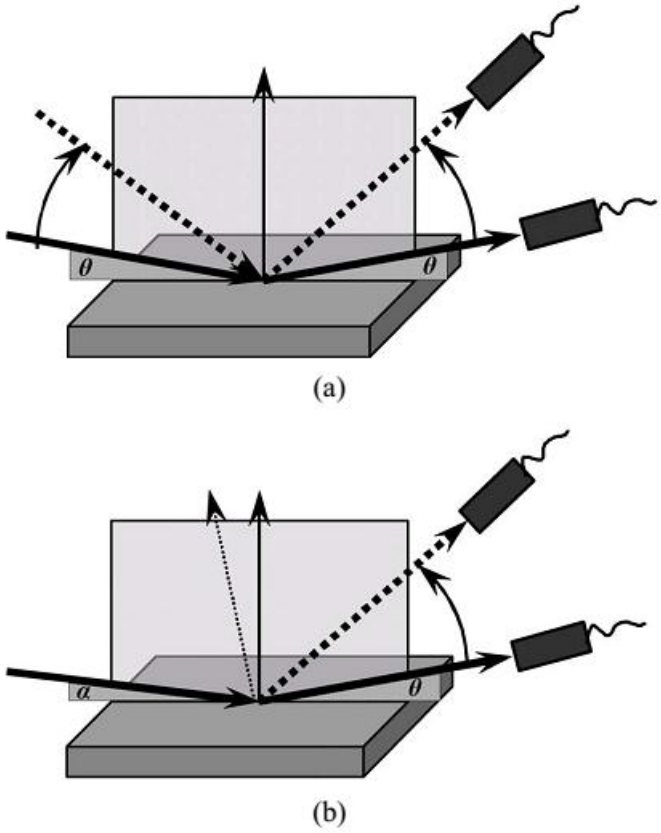

Figure 3.10: Schematic diagrams of (a) symmetric θ-2θ and (b) asymmetric grazing incidence XRD geometry[172].

3.4.3 Experimental Details

All the samples in the present project were measured using a commercial four-circle D8 Discover X-ray diffractometer (Bruker AXS GmbH). The angle of incidence was set at 0.7°. A conventional 2.2 kW water-cooled X-ray tube with a copper anode in line-focus mode is used as the X-ray source. The divergent X-ray beam emitted from the line-shaped source and collimated by a 2.5° Soller slit coupled with a 0.1 primary divergent slit were used. These measurements were carried out in the 2Theta geometry ranging between $20° < 2\theta < 80°$. A schematic diagram of the experimental setup is shown in Figure 3.11.

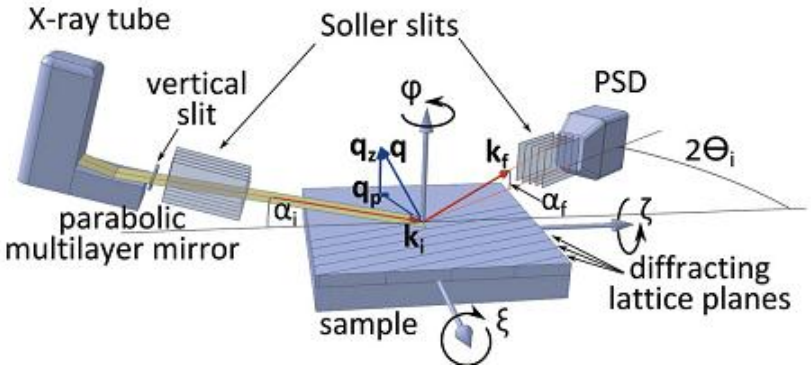

Figure 3.11: Schematic diagrams of the experimental setup. The wave vectors of the incident wave and scattered wave ($\boldsymbol{k}_i$ and $\boldsymbol{k}_f$ respectively), the corresponding scattering vector $\boldsymbol{q}$, and its in-plane and out-of-plane components ($\boldsymbol{q}_p$ and $\boldsymbol{q}_z$, respectively) as well as probed lattice planes are indicated [176].

3.5 Atomic Force Microscopy (AFM)

One of the essential methods for controlling surface roughness of thin films at nanometer scale is AFM. Solookinejad *et al.* [177], Schmitz *et al.* [178] have provided the following description of the AFM technique. The method gives information about the statistical characteristics of the surface due to the difference in nature of the AFM probe. In the tapping mode AFM, the tip is not in permanent contact with the sample surface as in the case of contact mode. To sense the surface, a vibrating tip strikes the surface only in the lower part of each oscillation cycle. The vibrating tip has enough kinetic energy to escape out of the water layer which is present on surfaces under ambient conditions. A feedback loop is employed to manage the vertical position of the sample mounted on a piezoelectric tube, maintaining the constant force between the tip and the sample surface topography. The vertical space travelled by the scanner at each x and y data point is stored by the computer to form the topographic image of the sample surface. Because of high lateral resolution of this procedure and its potential of

gaining quantitative three-dimensional information concerning surface topography, roughness, height and the tilt angle of topographic structures, this procedure is appropriate for the investigation of thin films.

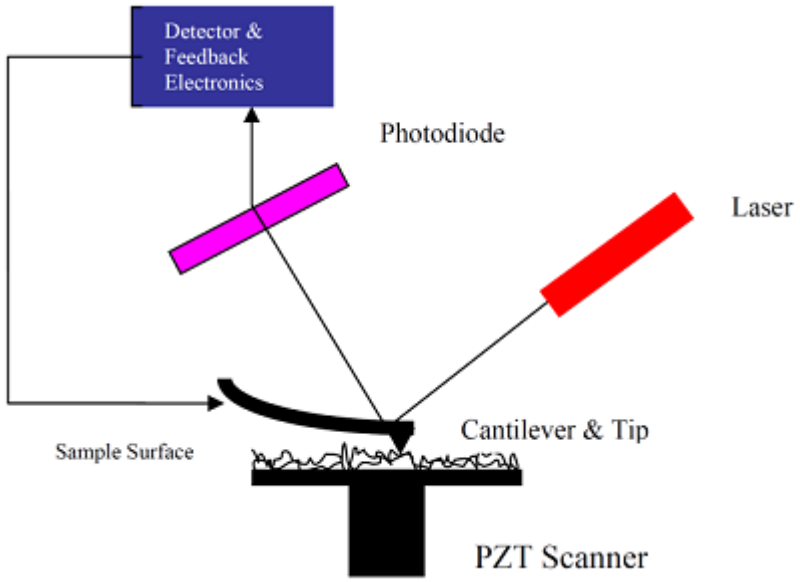

Figure 3.12: A block diagram of the atomic force microscope [179].

The microstructure of amorphous and polycrystalline thin films tends to be columnar, leading to microscopically rough surfaces that can be difficult to observe using traditional electron microscopy techniques [180]. Therefore, AFM is an instrument of choice to study the surface roughness of sputtered thin films. To investigate surface roughness of the thin films used in this project, a Veeco Dimension 3100 (Bruker) atomic force microscope was used. The instrument was operated in tapping mode with a scan size of 1 μm^2 and scan rate of 1.51 Hz. Gwyddion [181] software was used to analyze the AFM data.

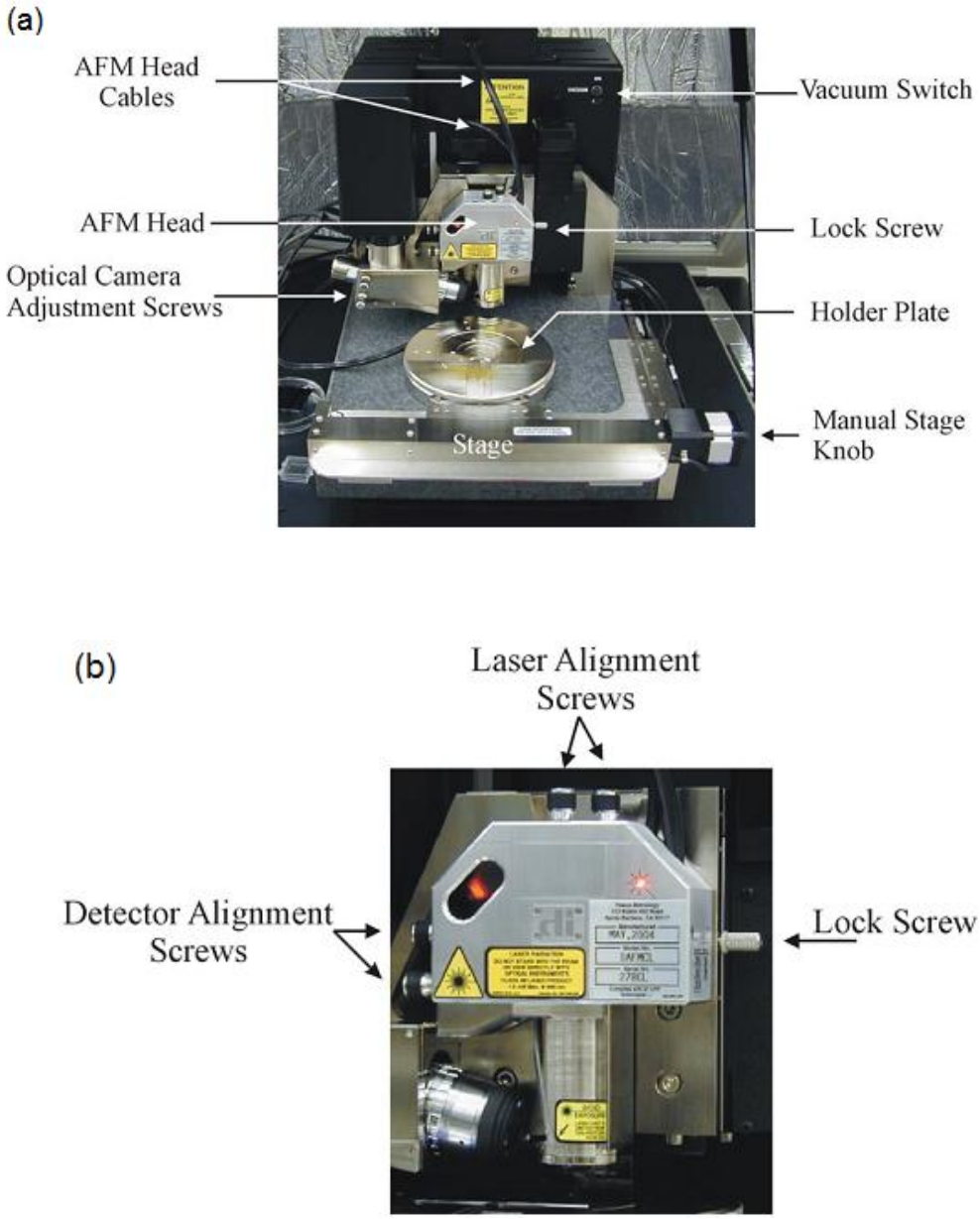

Figure 3.13: Photographs of the Veeco Dimension 3100 atomic force microscope showing (a) the various parts of the equipment and (b) a close-up view of the AFM head [182].

3.6 Scanning Electron Microscopy (SEM)

3.6.1 Description of the Technique

The following discussion of the SEM technique follows the description on chapter 16 of the Handbook of Deposition Technologies for Films and coatings (Third Edition) [183]. A scanning electron microscope images the topography and

structure of a sample by collecting secondary or backscattered electrons created by scanning the sample with a focused electron beam. The energy ranges from 100 eV to 30 keV. The resulting images can be collected at very high magnification to provide a great deal of information about the surface topography. The incident beam also excites characteristic X-rays which can be used to collect elemental information about the sample using energy or wavelength dispersive X-ray detectors.

When an electron strikes the surface, some electrons are backscattered (and have energies similar to the incident beam), some lower energy secondary electrons are excited ($< 50eV$), a few Auger electrons are produced, and characteristic X-rays are excited (Figure 3.14). Using different type of detectors each of these types of electrons or photons can be used to create images or determine the information about samples. A simplified diagram showing components of a scanning microscope is shown in Figure 3.15. Secondary electron imaging shows the topography of surface features a few nm across. Films as thin as 2 nm produce images with adequate contrast. Materials are viewed at useful magnifications up to $800000\times$ without the need for extensive sample preparation and without damaging the sample. Thickness of thin films can be determined using SEM micrographs.

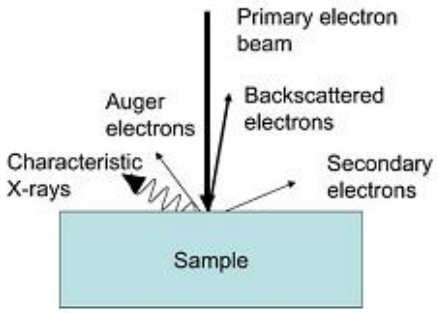

Figure 3.14: Schematic drawing showing types of electrons and photons produces when an electron beam interacts with a solid sample [183].

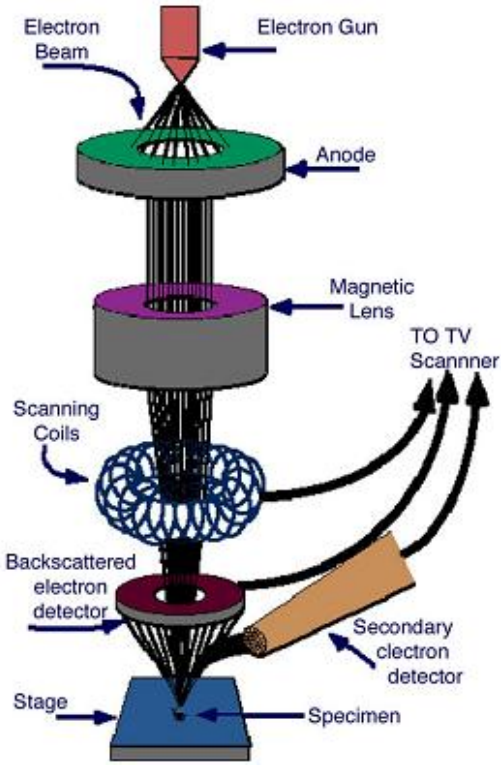

Figure 3.15: Schematic SEM components. Note that there are detectors for secondary electrons (<50eV) and for elastically backscattered electrons which have energies approximately equal to the incident electrons [183].

3.6.2 Experimental Details

In this work a Jeol JSM-7001F high-resolution scanning electron microscope (SEM) was used to investigate the cross-sectional morphology of the films to establish the nature of the film growth mode based on the structural zone model.

3.7 Heavy Ion Elastic Recoil Detection Analysis (ERDA)

3.7.1 Introduction

It is possible to carry out composition analysis of thin films including light elements (such as hydrogen) using high energy ion beam scattering spectrometry, of which one of the technique is elastic recoil detection analysis (ERDA) [184]. ERDA has been widely used for depth profiling of hydrogen involved in thin films or subsurface regions of solids [185]. It is a technique in which the observation of recoiled target atoms provides the most direct information about target composition [186]. Stopping foils are used to separate the recoiling atoms of different elements in conventional ERDA. However, the foils cause energy straggling making it hard to use when several elements need to be separated. As a result, Time-of-flight (ToF-ERDA) is employed to separate the elements by measuring the time-of-flight over a known distance for each atom. The mass of each detected atom can then be calculated from the classical formula for kinetic energy.

3.7.2 Experimental Details

The description of the ERDA setup used for characterising the films used in this thesis follows the detailed explanation given in [187]. Heavy Ion ERDA consists in the detection of recoil atoms knocked off the first few 100 nm of a target sample surface by a projectile beam coming in at a grazing incidence angle to the surface. The setup is centred on a 6 MV tandem accelerator. The ion source used for heavy ion production is an 860 C sputter source with caesium gas as the source of sputtering ions. Energy calibration of the 6 MV accelerator was carried

out using two different reactions from which a weighted average of the 90° bending magnet constant (K) was obtained. At the core of the heavy ion ERDA setup is a massive dispersive time of flight (ToF) spectrometer consisting of two carbon foil based Microchannel Plate (MCP) time detectors 0.6 m apart, and a passive implanted planar silicon (PIPS) semiconductor energy detector at the end of the flight path just behind the second time detector. The spectrometer sits 30° to the incident beam direction. The total timing resolution of the spectrometer is typically less than 1.0 ns as shown in Figure 3.16 for 12.6 MeV ^{16}O recoils, where the resolution is 0.54 ns.

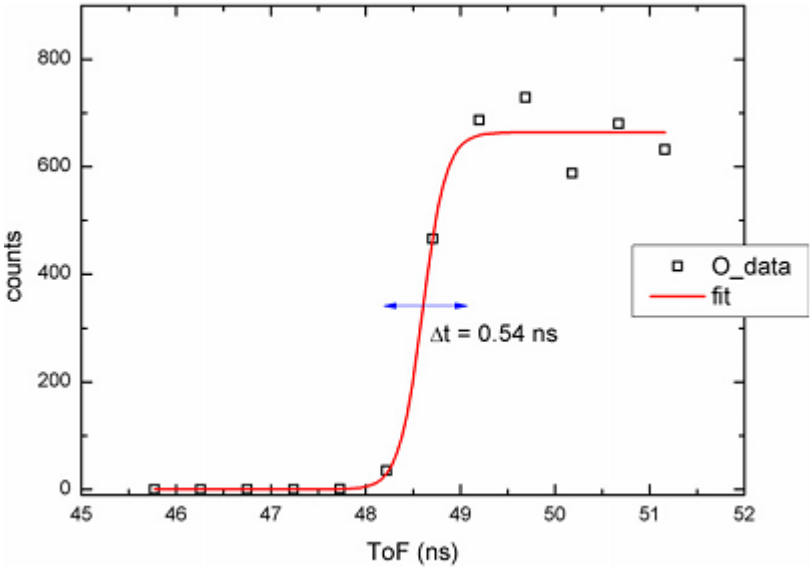

Figure 3.16: Time of flight edge of 12.6 MeV ^{16}O surface recoils from an Al_2O_3 layer on Si substrate [187].

The signal processing electronics are made up of standard Nuclear Instruments Modules that include Constant Fraction Discriminators for fast timing, a Time to Digital converter and an Analogue to Digital Converter for the PIPS signal. The data acquisition system is based on the freely available maximum integration data acquisition (MIDAS) platform, which was customised in-house for this setup.

Coincidence measurement of the Time of Flight (ToF) and energy of the recoil atoms, with the PIPS detector providing the trigger signal, leads to elemental separation according to the mass. This results in 2-D scatter plots showing different curves (see an example in Figure 3.17), each corresponding to a particular atomic mass, from which elemental energy spectra can be extracted. The energy spectra are obtained through conversion of the ToF axis into a linear energy axis through re-binning of event energies calculated using the measured ToF for each event as illustrated in Figure 3.18

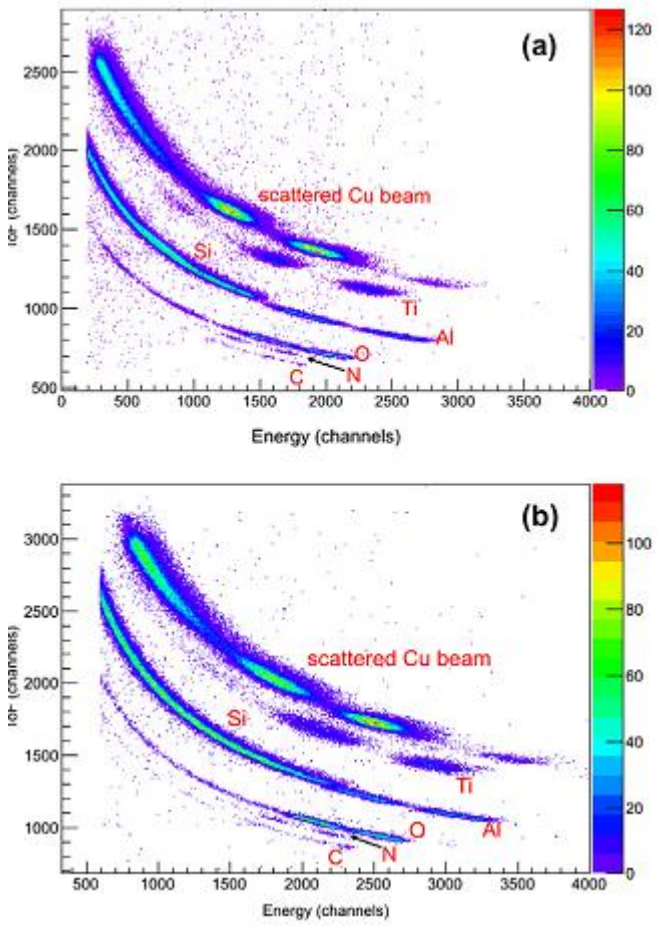

Figure 3.17: ToF-Energy scatter plots of recoils (and forward scattered beam) from (a) the as-deposited and (b) annealed samples [187].

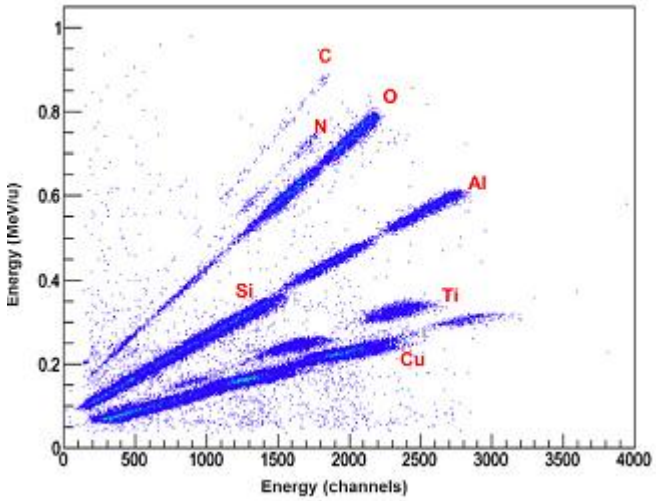

Figure 3.18: A linear scatter plot of recoil ion energies from the as-deposited sample calculated from the measured ToF plotted as a function of the Si detector (trigger) response [187].

For depth analysis, elemental depth profiles are obtained through both direct using KONZERD code, and through iterative simulation of elemental ToF spectra using the Monte Carlo based code CORTEO.

A 26.10 MeV $^{63}Cu^{7+}$ beam at a grazing incidence of 14° to the sample surface was used for the ERDA measurements in this work. The beam current was set below 10 nA for a runtime of about 40 min. NbN and ZrN samples used were deposited at powers ranging from 75 - 250W while the TaN samples were deposited at sputter power of 150W.

Chapter 4

Experimental aspects of surface Brillouin scattering (SBS)

The experimental arrangement for surface Brillouin scattering (SBS) measurements are discussed in this chapter. In section 4.1, details of the experimental setup for SBS experiments are presented. Then in section 4.2, the light source requirements and principles of operation are discussed. In section 4.3, scattering geometry details are presented. Section 4.4 concludes the chapter with a discussion of the spectrometer.

4.1 SBS experimental setup

Brillouin scattering measurements can be carried out in either of two configurations depending on the scattering mechanisms and the optical properties of the material. The transmission configuration is used for transparent materials, whereas the backscattering configuration is used for opaque materials. The backscattering configuration (Figure 4.7) used in this work is discussed in Section 4.3. An illustration of the basic setup for SBS measurements in a transmission configuration is shown in Figure 4.1. In Figure 4.1, L1, L2, and L3 are lenses for guiding the light from the light source through the sample to the spectrometer.

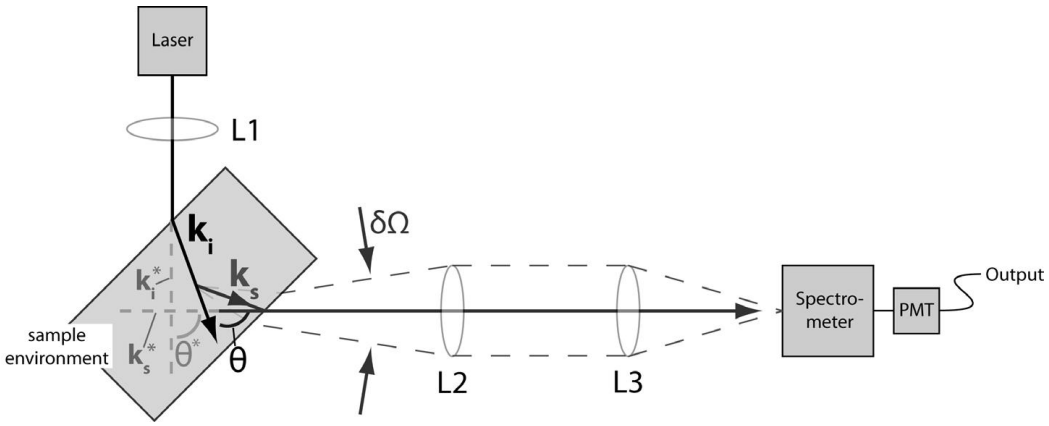

Figure 4.1: Schematic diagram of a typical Brillouin scattering experiment in the transmission configuration [90].

Light from a laser is focused with a lens L1 on to the surface of the sample, consequently designating a scattering volume V and an incident wavevector, k_i^*. L2 which defines the external scattered wavevector, k_s^* parallel to the direction of observation, the external scattering angle θ^*, collects the scattered light in a selected direction. The solid angle $\delta\Omega$ around the direction of observation is determined by the numerical aperture of the collecting lens. The lens L3 then focuses the collimated light from lens L2 on the entrance of the spectrometer. A solid-state detector (EG&G Optoelectronics Canada SPCM-200-PQ) then detects the light after passing through the spectrometer. Finally, a multichannel analyser records the light and assigns the measured signals containing the in-elastically scattered light and the instrumental artifacts (ghosts) in respective channels amongst the 512 channels used.

4.2 The Laser

In SBS experiments, signals produced by the inelastic scattering of light by thermally activated acoustic phonons are detected by light. To avoid ambiguities

in the spectra that would make it impossible to assign the observed peaks, a strictly monochromatic light source is required. Laser light is monochromatic, highly polarised, and highly collimated and hence suitable for SBS measurements. Green and blue lasers are the most commonly used in SBS measurements due to the λ^{-4} dependency of the intensity of the scattered light.

4.2.1 Spontaneous and Stimulated emissions

Lasers are devices that emit intense beams of light which are monochromatic, coherent and highly collimated through an optical amplification process based on the stimulated emission of electromagnetic radiation. They derive their name from their working principle: the term "laser" is an acronym for light amplification by stimulated emission of radiation. Laser light typically differs from other light sources in that it is coherent whereby all the photons (energy) that make up the laser beam have a fixed phase relationship (coherence) with respect to one another. Another characteristic feature of laser light is its low divergence enabling the light to travel over long distances or be focused to a very small spot. For these reasons, lasers have been used in wide range of applications in various fields.

Generally, an electron in an excited state eventually decays to a lower energy level, giving off a photon of radiation. The decay occurs without external influence and the photon is emitted in a random direction and a random phase in a process known as spontaneous emission. The time constant for spontaneous emission τ is defined as the average time taken by an electron to decay. Conversely, if an electron in energy state E_2 interacts with an incoming photon before it has a chance to spontaneously decay, the electron might decay in such a manner that a photon with the same wavelength, phase, and direction of travel is

emitted. If the energy of the incoming photon is $h\upsilon = E_2 - E_1$, the process is known as stimulated emission. These two processes have been depicted in Figure 4.2. Notice in the figure, that the latter processes involve the creation of a new photon. Stimulated emission is the processes by which lasers function as discussed in the section that follows on the amplification by stimulated emission.

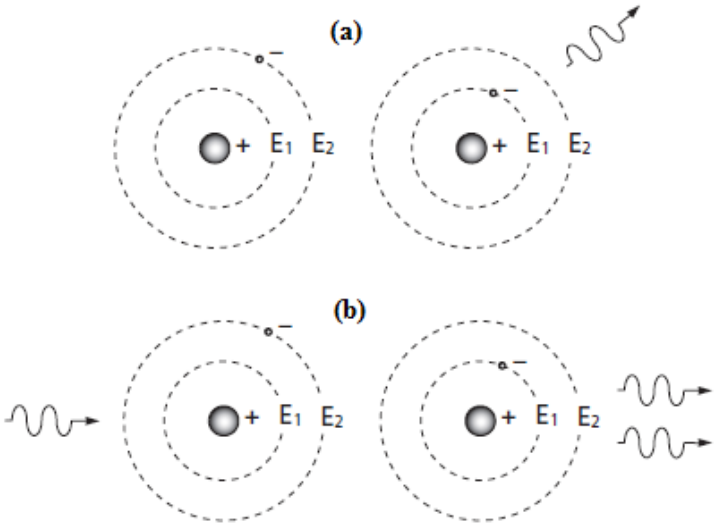

Figure 4.2: Schematic representation of (a) spontaneous and (b) stimulated emission [188].

4.2.3 Amplification by stimulated emission

Consider a group of atoms shown in figure 4.3 below: they start in the same excited state with most of them effectively within the stimulation range of a passing photon.

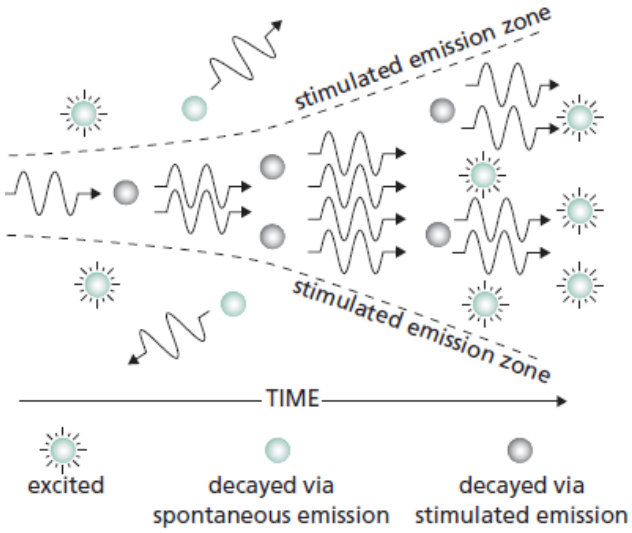

Figure 4.3: Amplification by stimulated emission [188].

Assuming that τ is very long, and that the probability for stimulated emission is 100%, the incoming (stimulating) photon interacts with the first atom, causing stimulated emission of a coherent photon; these two photons then interact with the next two atoms in line, resulting into four coherent atoms down the line. When the process is complete, there will be eleven coherent photons, all with the same phases and travelling in the same direction. Consequently, the original photon has been "amplified" by a factor of eleven. The energy required to put these atoms in excited states is supplied via an external source of energy usually referred to as the "pump" source.

The probability for stimulated emission is normally quite small in any real population of atoms. Moreover, most of the atoms are usually in the ground state and not in the excited state. From Boltzmann's principle, the relative population of any two energy levels of a collection of atoms at thermal equilibrium is given by

$$\frac{N_1}{N_2} = exp\left(-\frac{E_2 - E_1}{kT}\right) \tag{4.1}$$

where N_1 and N_2 are the populations of the upper and lower energy states, respectively, T is the equilibrium temperature, and k is the Boltzmann's constant. Substituting $h\upsilon$ for $E_2 - E_1$ yields

$$\Delta N = N_1 - N_2 = \left(1 - e^{-h\upsilon/kT}\right)N_1 \tag{4.2}$$

There will always be more atoms in the lower energy levels in comparison with the upper ones for a normal population of atoms. Considering that the probability of an individual atom to absorb a photon is equal to the probability of an excited atom to emit a photon via stimulated emission, the collection of real atoms will be a net absorber, not a net emitter, hence amplification will not occur. For amplification to occur and make a laser, a "population inversion" is required. Population inversion occurs when there are more atoms in the excited state than in the ground state.

4.2.4 Population inversion with a three-level system

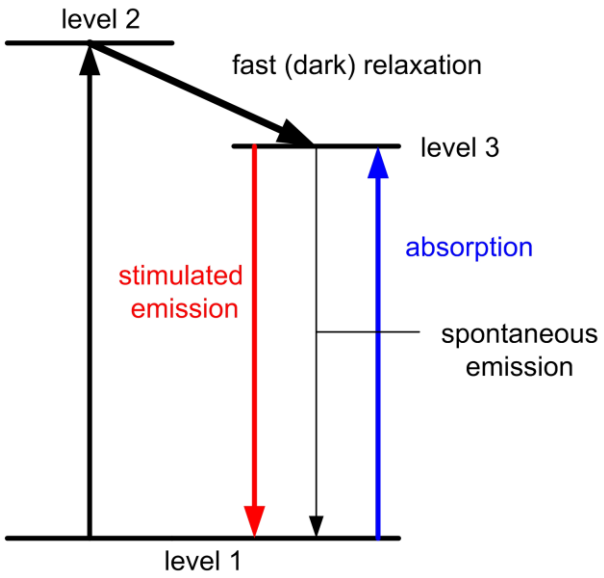

Figure 4.4: The three-level system.

State level 2 (Figure 4.4) is excited from the ground state either optically, electrically, or through a chemical reaction. The upper state level 2 relaxes quickly to the upper laser state level 3 (generally through nonradiative radiation). The upper laser state level 3 has a long lifetime and relaxes to the ground state level 1 via spontaneous and stimulated emission. Consequently, the population of state 3 is accumulated until inversion is achieved. For a three-level system, the ground level is spontaneous and predominantly by stimulated emission leading to a reduction of the inversion and therefore to a reduction of the optical amplification process. This limitation is overcome by using a four-level system.

4.2.5 Population inversion with a four-level system

Similar to the three-level system, the state level 2 is excited from the ground state using one of the three means: optical, electrical or chemical reaction. There is fast and nonradiative relaxation to upper state level 3. The upper state 3 has a long

lifetime and relaxes to lower state 4 via spontaneous and stimulated emission. State 4 relaxes quickly and without radiation to the ground state level 1. The inversion process of a four-level system is illustrated by Figure 4.5.

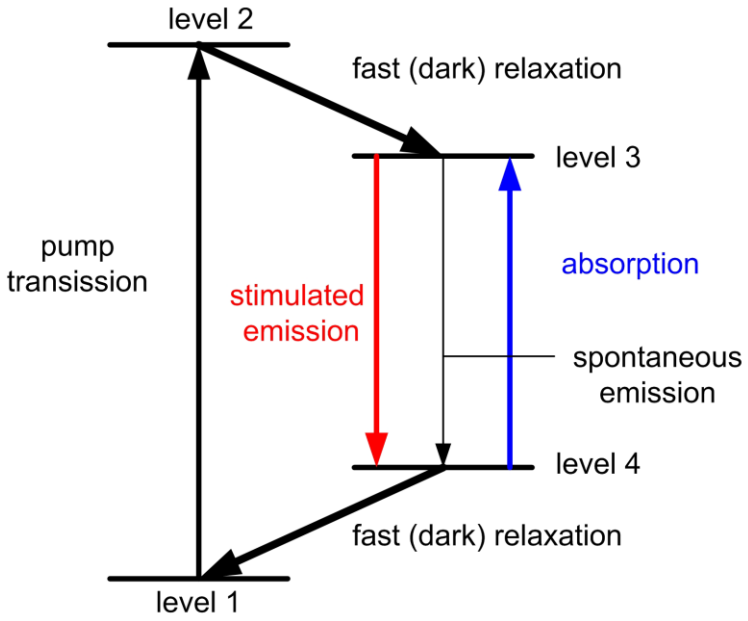

Figure 4.5: Schematic diagram of a four-level system.

State 4 is permanently depopulated and therefore the inversion is determined only by the population of the upper laser state and is higher with given pump rate than with a three-level system.

4.2.6 The Argon Ion Laser

The Argon ion (Ar^+) laser is one of the most widely used ion gas lasers, which typically generates several watts power of a green or blue high quality output beam [189]. A considerable amount of energy is supplied to the argon in order to singly ionize argon atoms in a four-level system explained in the section 4.2.2 above. In the present work, the SBS measurements were carried out using an Ar^+ laser (Coherent Innova 300). The laser uses a temperature stabilised intra-cavity

etalon to select a single longitudinal mode with ~ 3 MHz width from the laser gain profile. This is necessary for the SBS measurements which require an extremely narrow laser width. In this work, SBS spectra for all the samples were gathered using the 514.5 nm line from an argon-ion (Ar^+) laser operated in a single axial mode. The power of the laser reaching the samples was about 70 mW.

4.3 The tandem Fabry-Pérot interferometer

The Fabry-Pérot (FP) interferometer is the instrument of choice used for Brillouin scattering measurements to separate the spectral components of light due to the very small frequency shifts of the thermal acoustic phonons. It consists of two flat mirrors plates with faces very parallel to each other and a separating distance *L*. An incident beam is subject to multiple reflections at the surfaces of the opposing mirrors. Light of wavelength λ is transmitted only if the interference condition is satisfied:

$$m\lambda = 2nLcos\alpha \tag{4.3}$$

where m is an integer, n is the refractive index of the medium between the two mirrors of the interferometer, L is the mirror spacing and α is the angle of incidence (usually 0°). The frequency interval (in wavenumbers) corresponding to the difference between two wavelengths that are simultaneously transmitted by adjacent interference orders is defined as the free spectral range Δk defined as

$$\Delta k = \frac{1}{\Delta\lambda} = \frac{1}{2nL}\ , \qquad for\ \lambda \ll L. \tag{4.4}$$

For a single Fabry-Pérot interferometer, the instrumental function is determined by the convolution of three factors that depend on the non-perfect reflectivity and parallelism of the mirrors as well as the finite range of angles incident on the Fabry-Pérot. The Airy function expresses the ratio of the transmitted light to the incident light as:

$$A(\lambda, L, \alpha) = \frac{T}{1 + 4\left(\frac{F^2}{\pi^2}\right) sin^2\left[\left(\frac{2\pi nL}{\lambda}\right) cos\alpha\right]} \tag{4.5}$$

where T is the maximum transmitted intensity and F the effective finesse, which is related to the free spectral range and the width $\delta\lambda$ of a given transmission peak by

$$F = \frac{\Delta\lambda}{\delta\lambda} \tag{4.6}$$

The maximum number of features that can be resolved within a given free spectral range are determined by the finesse. The mirror surfaces imperfections in turn largely affect the effective finesse. For two mirror surfaces matching each within λ / m, the effective finesse does not exceed $m / 2$. On the other hand, the effective finesse for high quality mirror surfaces is $F \approx\sim 10^2$. There is normally a trade-off between finesse and throughput. The latter is controlled by geometric parameters of the external optical systems (lenses, focal lenses, mirrors, aperture, maximum angular spread of the beam) that determine the minimum achievable spectral range, which for a single Fabry-Pérot interferometer is in the order of $0.5 \times 10^{-2} cm^{-1}$. The spectral contrast C is defined as the ratio of the maximum and minimum transmission:

$$C = 1 + \frac{4F^2}{\pi^2} \tag{4.7}$$

Low spectral contrast and overlapping of transmission from different interference orders limit the use of a single Fabry-Pérot interferometer in Brillouin scattering measurements. In the presence of very intense elastic scattering from the surface of a material (as in the case of opaque materials), a single Fabry-Pérot interferometer lacks sufficient contrast to measure the Brillouin scattered light. This limitation can be overcome by multi-passing a single Fabry-Pérot or using multiple interferometers operated in series which increases the spectral contrast as $C_n = (C)^n$ where C^n is the overall contrast and C is the contrast of the single interferometer. Multi-passing a single interferometer guarantees higher stability and performance as opposed to systems based on multiple interferometers in series which suffer from imperfect synchronisation of the interferometer scans. Studies on the design and performance of multi-pass Fabry-Pérot systems for Brillouin scattering show that 5-passes through the same interferometer increase the contrast C from 10^4 to $10^9 - 10^{10}$ while maintaining a finesse that is comparable with that of a single-pass system (50 – 100). To allow one to resolve low-frequency spectral features generally related to shear acoustic modes, the spectral resolution is increased by reducing the free spectral range at a constant effective spectral finesse. However, when the free spectral range is reduced to below twice the highest frequency Brillouin peak, the adjacent orders of interference of the Brillouin components can partially overlap making the identification and attribution of the observed features to be ambiguous.

An alternative way to expand the free spectral range combining two FP of different mirror spacings L_1 and L_2 in series. This results in an increased free spectral range at a constant resolution. From equation 4.1, the transmission conditions ($\alpha - 0, \lambda_1 = \lambda_2$) for the tandem design yields:

$$L_1 = \frac{1}{2} m\lambda, \qquad L_2 = \frac{1}{2} n\lambda, \tag{4.8}$$

where m and n are integers. The effective result is increase of the FSP by a factor of few tens. For such a combination of interferometers to be effectively used, their scanning needs to be precisely synchronised such that the increments of the mirror distances for the FP1 and FP2, δL_1 and δL_2, satisfy the condition:

$$\frac{\delta L_1}{\delta L_2} = \frac{L_1}{L_2} \tag{4.9}$$

It has been observed that by multi-passing, a contrast of greater than 10^9 can be achieved, that is, five or six orders of magnitude greater than that of a single interferometer. Figure 4.6 shows a schematic diagram of the tandem FP interferometer implementation by Sandercock.

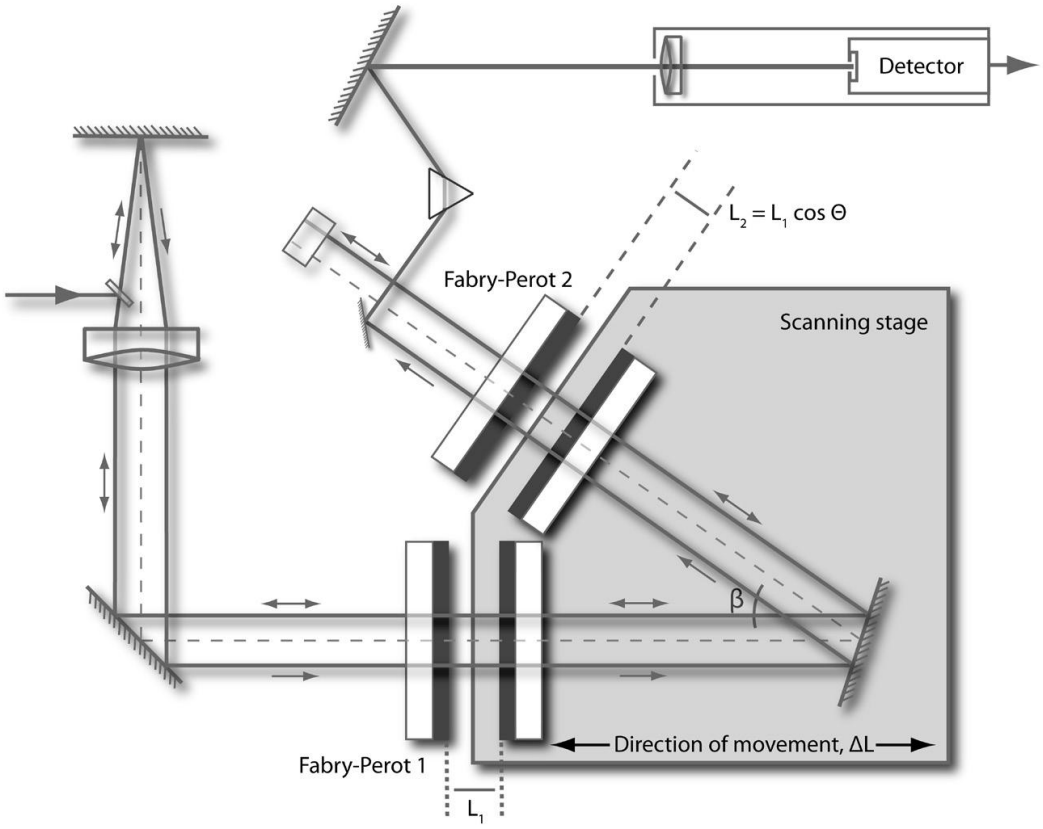

Figure 4.6: Schematic diagram of a multi-pass tandem Fabry-Pérot interferometer (*after Speziale et al.* [90]).

In the present work, a Sandercock (JRS Scientific instruments) 3 + 3 pass tandem interferometer is used. To isolate the interferometer from external vibrations, a dynamic isolation system is employed. The tandem interferometer is mounted on two dynamic isolation mounts (JRS Scientific instruments, Vibration Isolation System MOD-2), while the optical components of are mounted directly on the optical table. The SBS arrangement used in the present work is shown in Figure 4.7

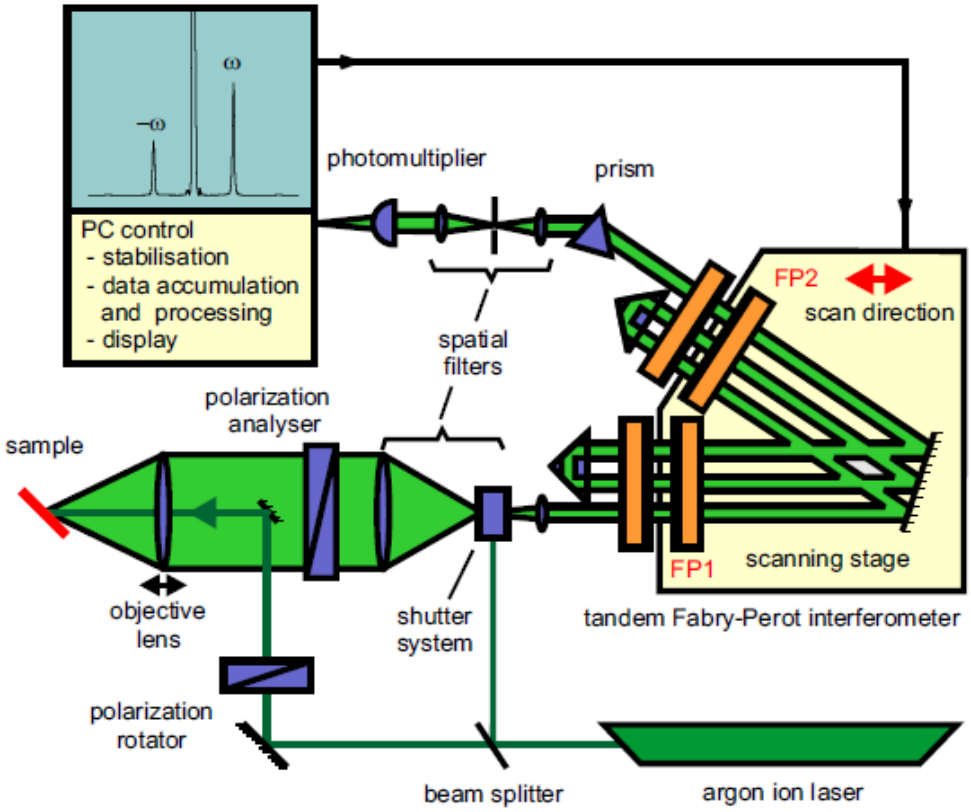

Figure 4.7: Block diagram of the experimental SBS setup (*after Wittkowski* [190]).

An elliptical dielectric coated mirror M_1 with a central 2 mm hole collects the scattered light which circumvents spectral distortions resulting from the use of the usual steering mirror together with its supporting arm to direct the laser beam onto the sample. A shutter system (JRS Scientific Instruments) protects the detector from possible overload from the strong elastically scattered light by preventing the light from entering the detector during each scan. The acousto-optic modulator (AOM) protects the detector from excessive light from the intense elastic peak by allowing continuous varying of the laser power on the sample without affecting the control signal. A high efficiency silicon avalanche photo-diode detector (EG&G Optoelectronics Canada SPCM-200-PQ) with a dark count of 1 per second detects the analysed light from the tandem interferometer. A detailed

discussion of the multi-pass tandem Fabry-Pérot interferometer setup used for this work is given in the operator manual [191].

Chapter 5

Elastic Properties of Niobium Nitride Thin films

In the present chapter, the results of the characterisation of rf magnetron sputtered niobium nitride (NbN) thin films using various techniques are presented and discussed. These results include the determination of the density and deposition rates using X-ray Reflectivity. The linearity between film thickness and deposition time at a fixed power is used to extrapolate film thickness values required for surface phonon dispersion at large $k_{||}d$ values. The dynamics of the surface acoustic waves (SAWs) determined from the measurement of the inelastically scattered light using surface phonons is presented through the surface Brillouin scattering study of NbN thin films. Finally, the numerical simulation approaches to extract the elastic constants by least square fitting of the velocity dispersion curves of surface phonons determined through variation of film thickness and the incidence angle of the backscattering geometry is presented. The elastodynamic Green's function method is also presented to exhibit the self-consistency and "inverse problem" to establish accurate values of the elements of the elastic constant tensor.

5.1 Introduction

In the past years, thin films of transition metal nitrides have been extensively and successfully used as protective coatings and decorative coatings [31,192–195], diffusion barriers [50,55], and biomedical implants [2–4]. Of these films, NbN

thin films were primarily investigated due to their superconducting properties rather than their mechanical properties [21]. Consequently, early studies were dedicated towards fabricating NbN thin films with increased superconducting transition temperatures (~17 K) [196–198]. Nevertheless, NbN thin films are suitable for wear applications too since their good thermal expansion matches with a wide range of tools. A unique combination of characteristics such as high hardness, high melting point, wear resistance [8], chemical inertness [9], thermal stability [10], and high electrical conductivity make them suitable materials for protective coatings [15], field emission cathode [16] and diffusion barrier in microelectronic devices [14].

Deposition of NbN thin films using sputtering techniques began in the late 1960s with the aim of manufacturing high-temperature semiconductors [199]. Investigations into the use of NbN as a wear-resistant coating begun later in the 1980s and with the introduction of superlattice coatings in 1990s, NbN was used as one of the component of the superlattice [200]. Thus, numerous examples of superlattice coatings of CrN/NbN, TiN/NbN, W/NbN and NbN/VN were investigated in corrosion protective and wear resistant applications. These coatings are known to exhibit very high hardness, up to twice that of the individual layers. Recently, single layers of NbN coatings have been investigated for various applications [18, 22, 23, 198, 199].

Several authors have established that fabrication parameters such as substrate temperature, rf power, substrate biasing, and N_2 influence crystallisation, microstructure, chemical composition and mechanical properties of NbN thin films [15,20,21,23,27]. In the present chapter, the effect of rf power and hence ad-atom energy on the film growth and surface phonon propagation in NbN films is

investigated. Ad-atom energy depends on the deposition process and source of atoms and is a critical factor in microstructure and morphology determination of thin films [203].

Determination of the elastic constants of thin films has been investigated in recent decades [70, 72, 201, 202], due to the growing importance of such materials in various applications as well as theoretical studies. Besides having practical importance in the calculation of engineering moduli, elastic properties are a valuable source of information on atomic potentials used in computational modelling of novel materials with unique qualities [78]. Since the thickness of thin films commonly ranges from a few tens of nanometers to one micron, the problem of characterising their elastic properties is challenging [99]. Several methods have been used over the years to measure the elastic properties of thin film materials, especially the elastic stiffness from which the engineering moduli can be determined. For example, line-focus acoustic microscopy [72], X-ray diffraction [203, 204], nanoindentation [208], resonance ultrasound spectroscopy [209], and laser-generated surface acoustic waves [210] among others.

5.2 Experimental Details

5.2.1 Sample preparation

NbN coatings were deposited on (1.5 × 1.5 cm^2) (100) Si substrates at room temperature using rf magnetron sputtering with an unbalanced magnetron. A 99.9% pure, 76mm diameter × 6 mm thick NbN target (Semiconductor Wafer) at a fixed sample to target distance of 6 cm and in Ar ambient was used for film deposition. The substrates were pre-cleaned with successive rinses in ultrasonic baths of acetone and ethanol and then blow dried with N_2 before deposition. Prior

to the deposition, the chamber was evacuated to a base pressure of 2.4×10^{-5} mbar. The NbN target was then pre-sputtered using Ar^+ at a sputter power of 100W for 15 minutes to remove impurities or adsorbents on the target surface. Thin film samples for X-ray reflectivity were deposited on Si (100) substrates at varied sputter power (75W - 250W) and deposition times (1.5 min - 5 min). Using the deposition rates extracted from the film thickness measured by XRR, the film thickness and microstructure was controlled by depositing the samples at varying times for investigation of the elastic properties of thin NbN films of thickness between ~50 - 450 nm and at room temperature.

5.2.2 Composition, morphology and microstructure of NbN thin films at various ad atom energies

The composition of thin films is dependent on the methods and process of deposition. In this respect, the ad-atom energy is strongly dependent on the nature of sputter gas, the kinetic energy dissipated on the surface of the target, the nature of the inert gas ions in the plasma and the surface binding energy of the target. Thus, the ad-atom energy can lead to variations in film composition and possible crystal structure of the resulting film. The ad-atom energy is also dependent on the sputter power and substrate temperature. The former process parameter was varied while the latter was kept constant during the deposition process. The composition of the films was determined by heavy ion-elastic recoil detection analysis (HI-ERDA).

A Jeol JSM-7001F high-resolution scanning electron microscope (SEM) was used to investigate the cross-sectional morphology of the films and thus establish the dependence of film growth mode based on the structural zone model on the ad-atom energies of the plasma species.

X-ray Reflectivity (XRR) is sensitive to microstructural changes through measurement of mass density. It has been used to determine film thickness from the interference patterns of the film-air and film-substrate interfaces; in addition, the surface roughness of NbN thin films at various RF sputter powers and thermal history was also measured. These measurements were carried out by a D8 Discover high resolution X-ray diffractometer (Bruker AXS GmbH) coupled to Cu Goebel mirror and Ge (004) crystal to yield a highly collimated monochromatic Cu Kα beam at 8.0 keV. A series of manual and programmable detector slits of 0.1 mm were used to further collimate the incident and secondary X-ray beams and provide a symmetric alignment of the primary and secondary X-ray beams. All XRR measurements were carried out in the 2Theta-Omega geometry up to 6° in 2θ. The measured XRR spectra were subsequently simulated for film density, thickness and roughness using Leptos (Bruker AXS GmbH) software. The simulation used a layer stack of $Si/SiO_2/NbN/Nb_2O_5$ in that order to generate the simulated spectra which was matched to the measured spectra (Figure 5.4).

To investigate the lateral surface roughness of NbN thin films, a Veeco Dimension 3100 atomic force microscope was used. The instrument was operated in tapping mode with a scan size of 1 μm^2 and scan rate of 1.51 Hz. Gwyddion software [181] was used to analyse the AFM data.

Information on the microstructure parameters such as grain size, structural phase amongst others can be derived from the surface sensitive Grazing incidence X-ray diffraction (GIXRD) measurements. These were performed on a D8 Discover X-ray diffractometer (Bruker AXS GmbH) at 0.7° incidence angle beyond the critical angle for total external reflection. To collimate the primary

beam and minimise sample footprints and axial divergence of the beam, a 2.5° Soller slit coupled with a 0.1 primary divergent slit was used. These measurements were carried out in the 2Theta geometry ranging between $20 < 2\theta < 80°$.

5.3 Results and Discussion

5.3.1 Composition determination by Heavy ion-elastic recoil detection analysis (HI-ERDA)

Figure. 5.1 shows representative ERDA depth profiles for the NbN film deposited at the sputter powers of interest. The composition of the films is significantly constant throughout the film thickness as shown by these depth profiles. ERDA results shown in Table 5.1 below indicate that the films deposited at sputter powers of 75 - 150 W and 250 W were sub-stoichiometric but those deposited at sputter power of 200 W were stoichiometric.

Table 5.1: The composition of the NbN thin films as a function of sputter power.

Sputter Power (W)	Nb atomic fraction (±0.003)	N atomic fraction (±0.003)
75	0.46	0.54
100	0.34	0.66
150	0.56	0.44
200	0.50	0.50
250	0.43	0.57

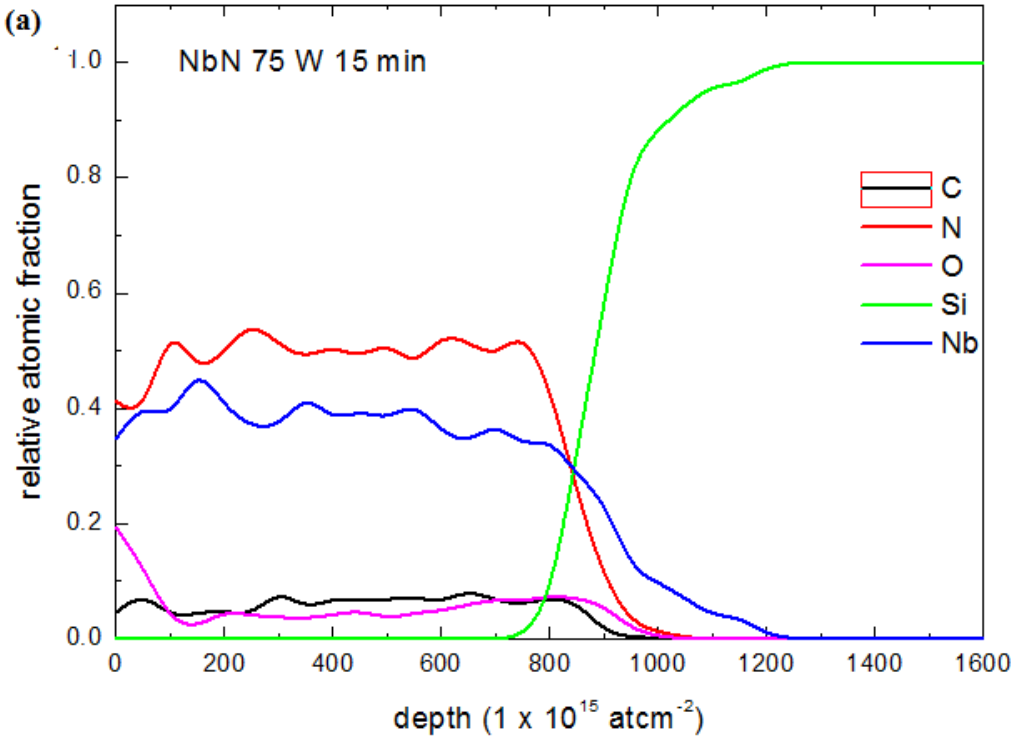
(a)
NbN 75 W 15 min
relative atomic fraction
depth (1 x 10^15 atcm^-2)
C
N
O
Si
Nb

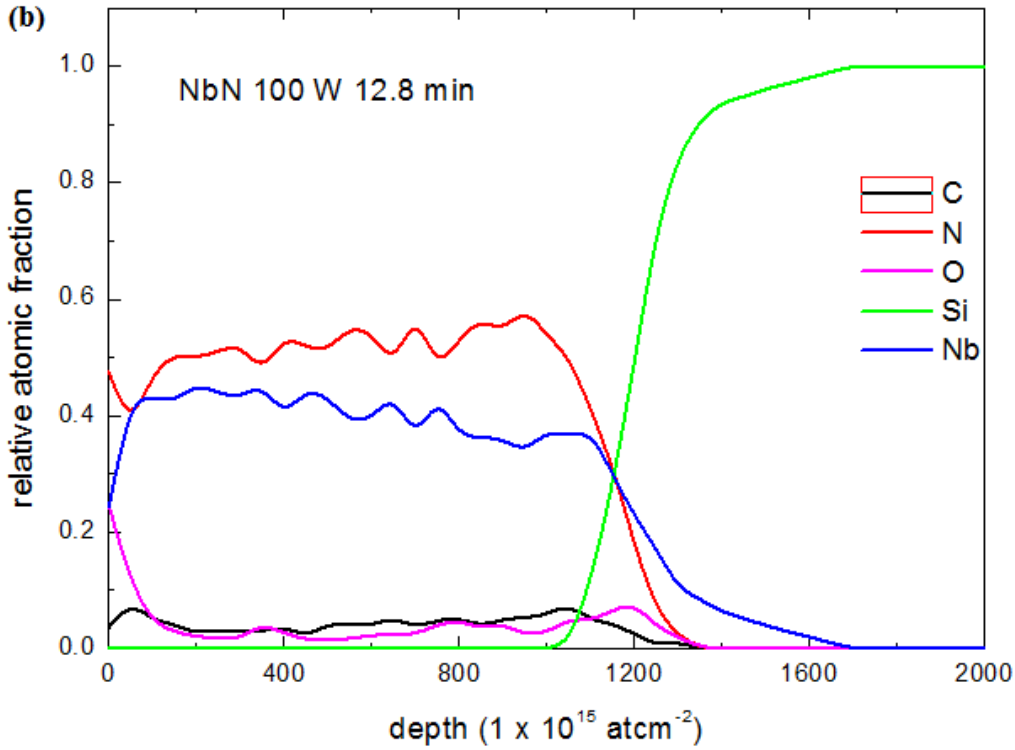
(b)
NbN 100 W 12.8 min
relative atomic fraction
depth (1 x 10^15 atcm^-2)
C
N
O
Si
Nb

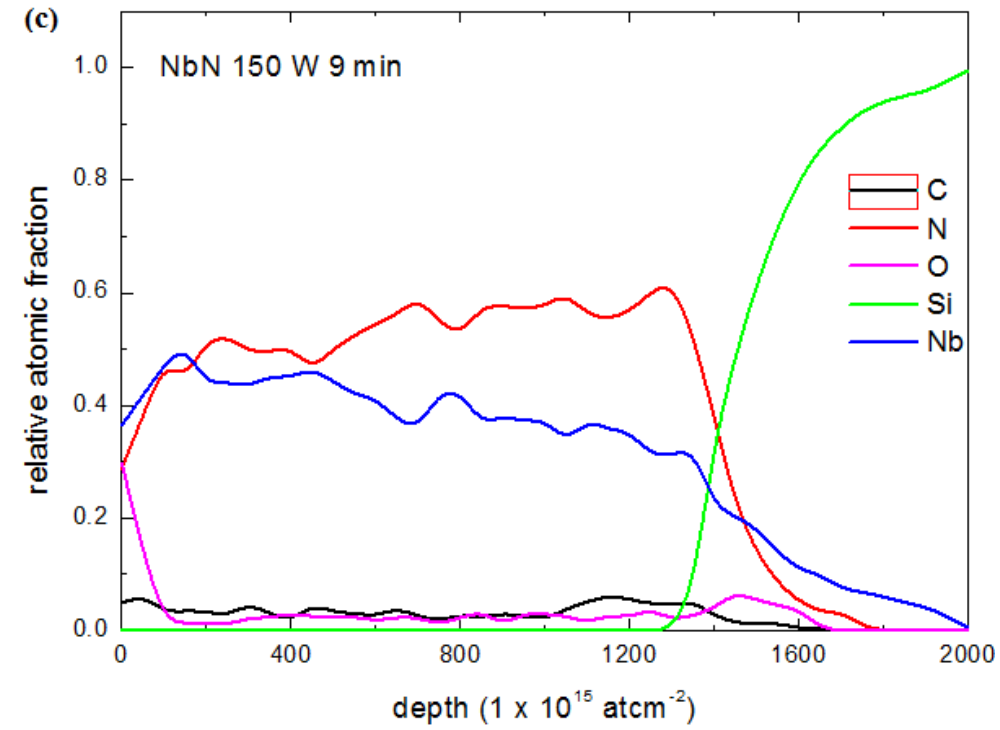
(c)
NbN 150 W 9 min
relative atomic fraction
depth (1 x 10^15 atcm^-2)
C
N
O
Si
Nb

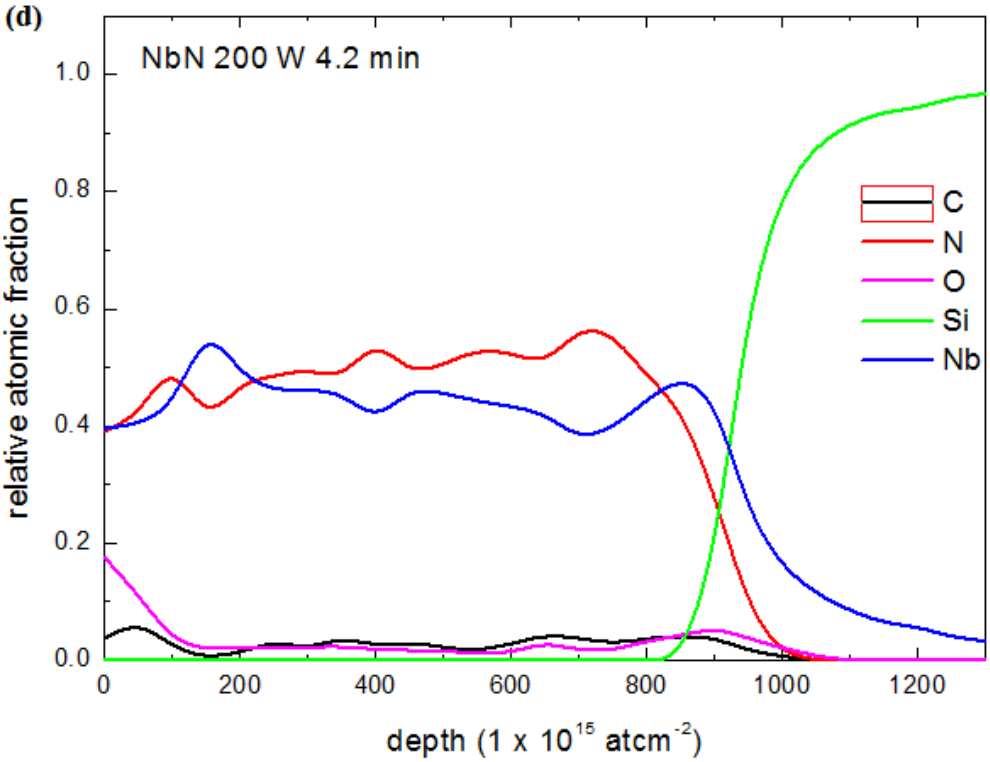
(d)
NbN 200 W 4.2 min
relative atomic fraction
depth (1 x 10^15 atcm^-2)
C
N
O
Si
Nb

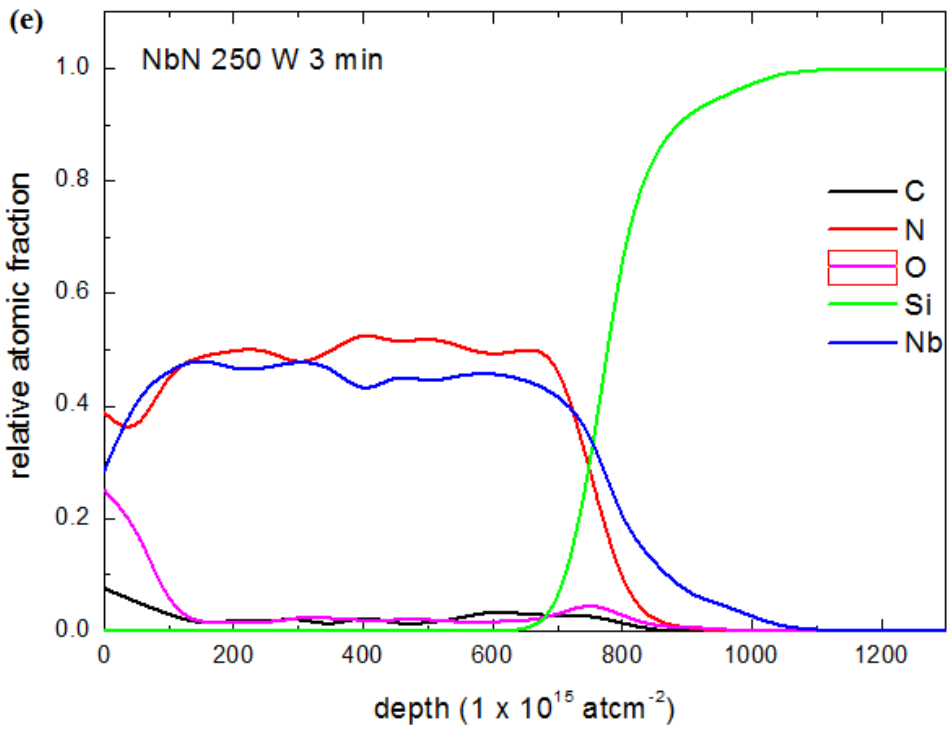

Figure 5.1: ERDA spectra showing the composition as a function of depth profile (in the units of atoms cm^{-2}) of the NbN films deposited at (a) 75 W, (b) 100 W, (c) 150 W, (d) 200 W, and (e) 250 W.

5.3.2 Scanning electron microscopy (SEM)

Scanning Electron Microscopy (SEM) analysis was carried out to establish dependence of film morphology with the RF sputter power and also on the contributions of thermal effects at constant sputter power on the film morphology. Figure 5.2. shows the SEM micrographs of a cross sectional cut of the samples prepared at varying sputter powers (75 W - 150 W) but a constant film thickness. All the films present diverse columnar micro-structure with varying film growth zones. The microstructures of the films deposited beyond RF powers of 150 W are compact in form (Figure 5.2 (c-e)). From the figure, it can be seen that the grain size of the films increases with increasing sputter power from 75 – 150 W.

This was later confirmed by X-ray diffraction measurements on NbN thin films at the deposition powers of interest.

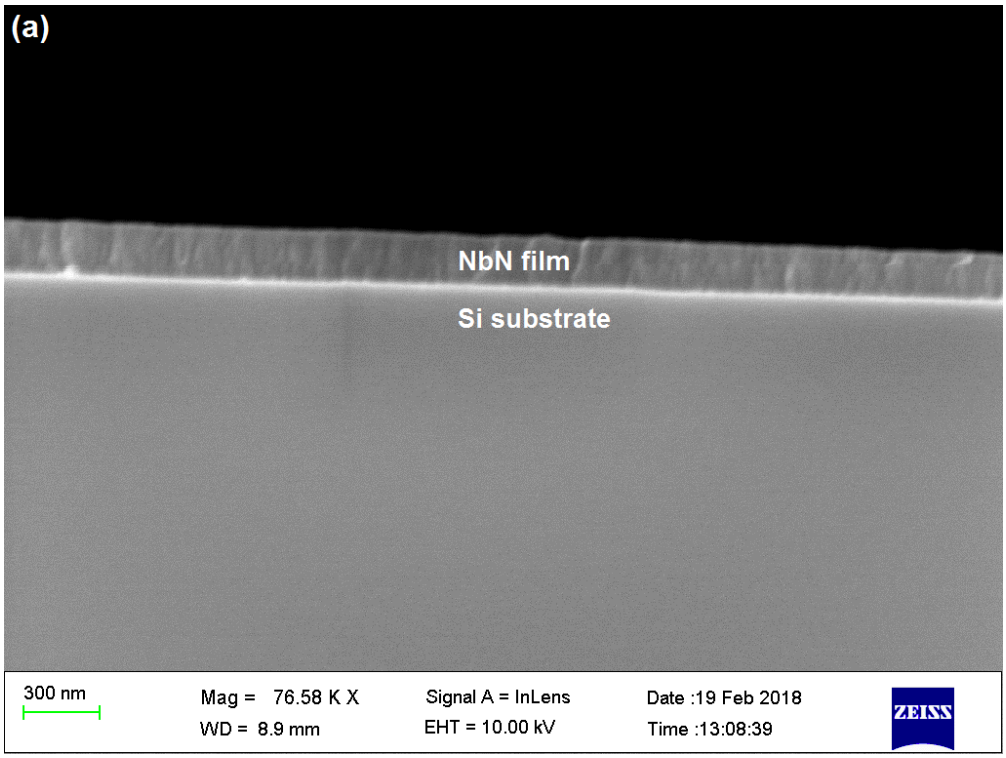

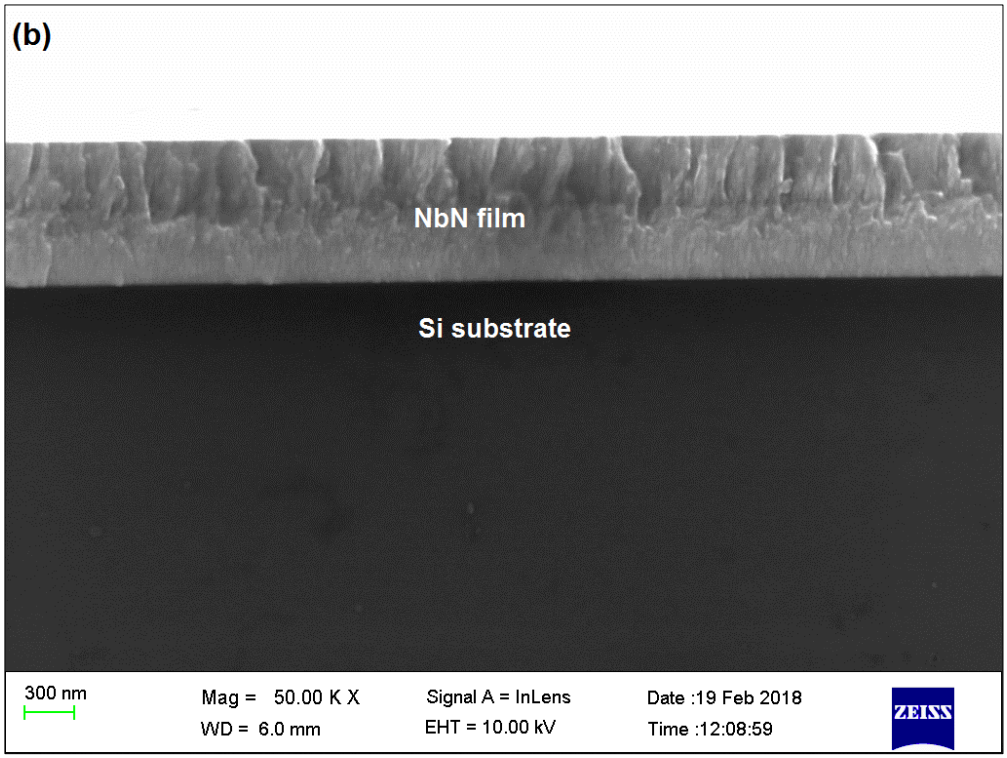

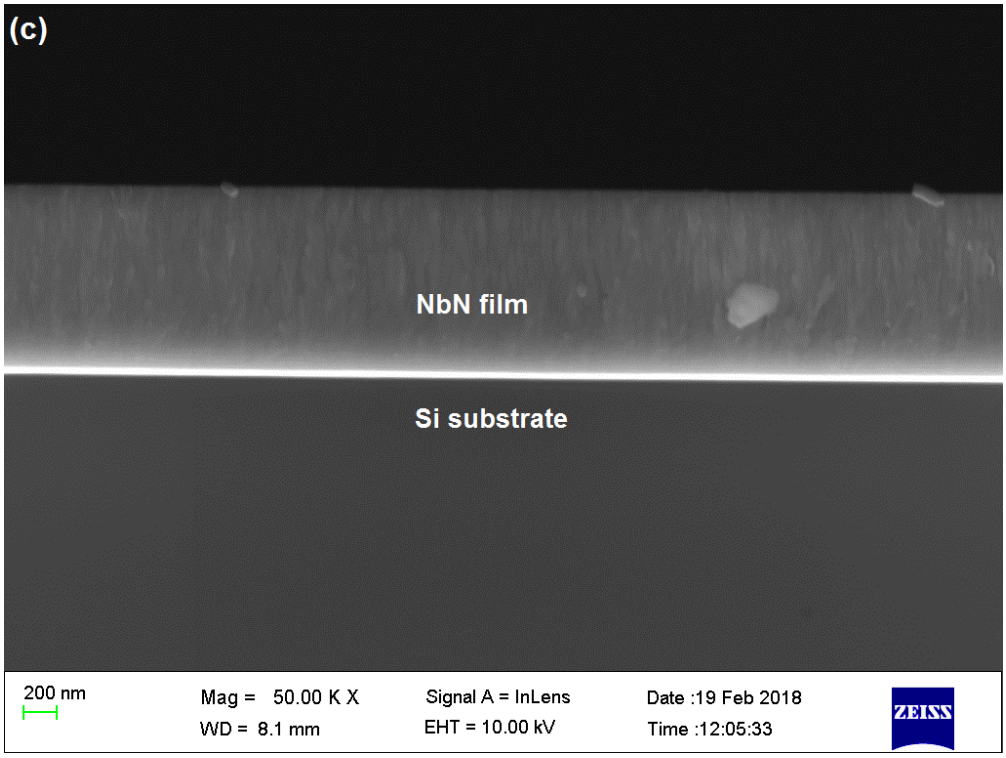
(c)
NbN film
Si substrate
200 nm
Mag = 50.00 K X
WD = 8.1 mm
Signal A = InLens
EHT = 10.00 kV
Date :19 Feb 2018
Time :12:05:33
ZEISS

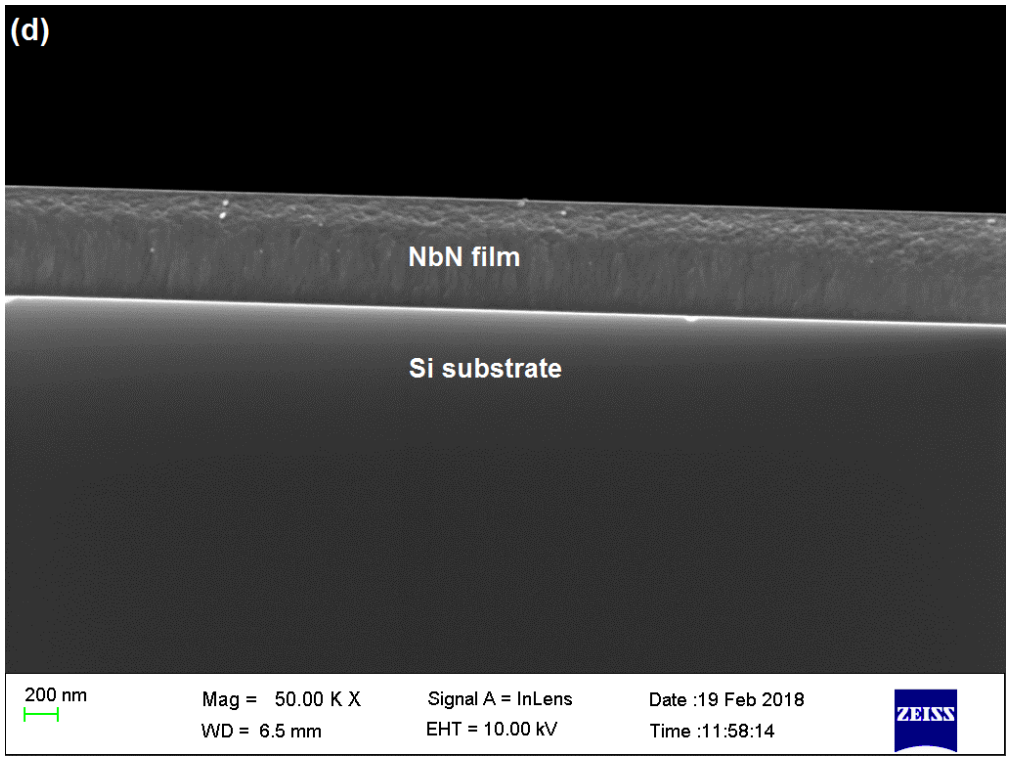
(d)
NbN film
Si substrate
200 nm
Mag = 50.00 K X
WD = 6.5 mm
Signal A = InLens
EHT = 10.00 kV
Date :19 Feb 2018
Time :11:58:14
ZEISS

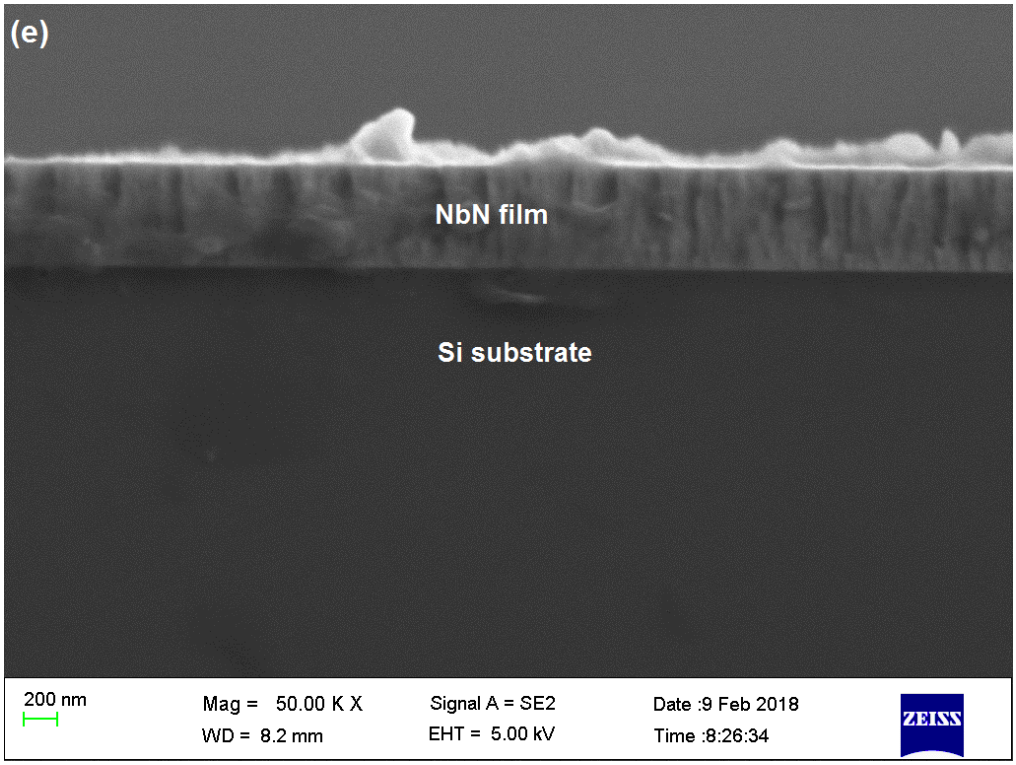

Figure 5.2: SEM micrographs of cross-sectional morphology of NbN films deposited at sputter powers of (a) 75 W, (b) 100 W, (c) 150 W, (d) 200 W, and (e) 250 W. The film thickness was kept constant for ease of comparison. From the structure zone model, (a) and (c) represent Zone I, (b) and (e) Zone III, and (d) Zone II.

During film deposition the ad-atoms can transfer their kinetic energies to the film, the dissipation of the kinetic energy of the ad-atoms through ad-atom stopping at the film surface produces thermalisation effects. This corresponds to insitu heating and can result in the changes of the microstructure above some threshold temperature in conformity to the structural zone model. To establish the dependence of elastic constants on the microstructure, NbN films grown at constant power and varying deposition times were evaluated for cross-sectional morphology as shown in Figure 5.3 (a,b,c). It is seen from the SEM images that the columnar growth microstructure does not change significantly with deposition times. Therefore the effect of ad-atom energy through changes in the sputter

power provides an avenue to study the correlation between microstructure and the elastic constants.

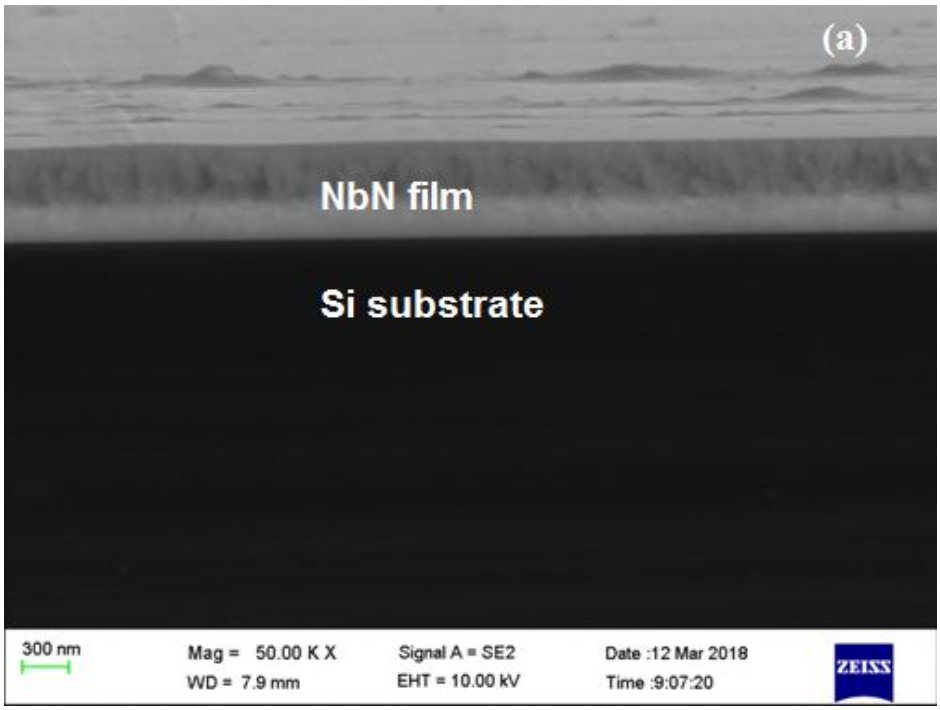

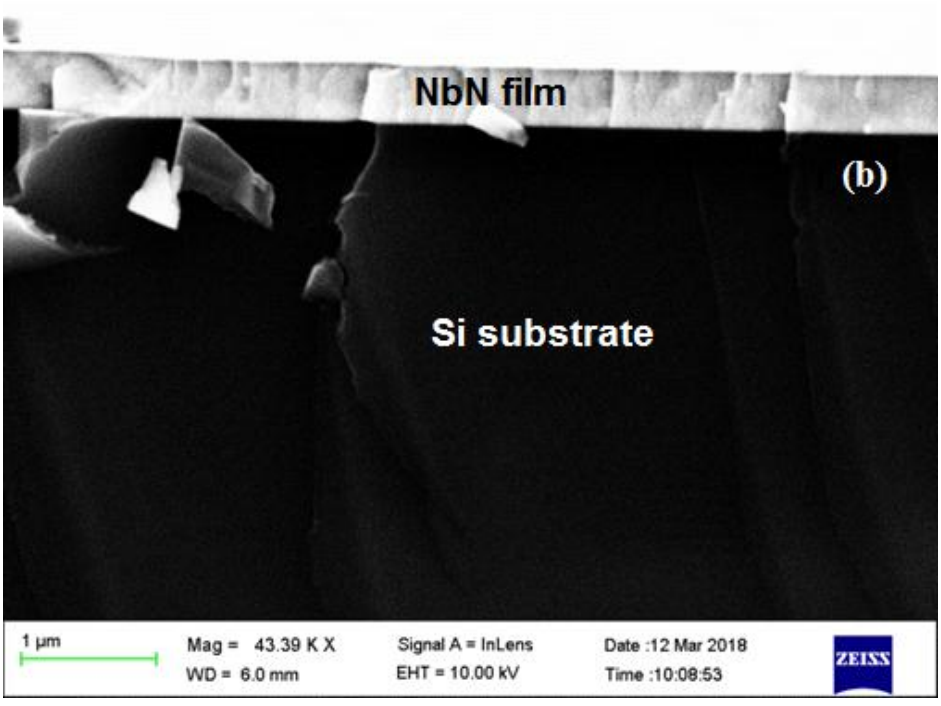

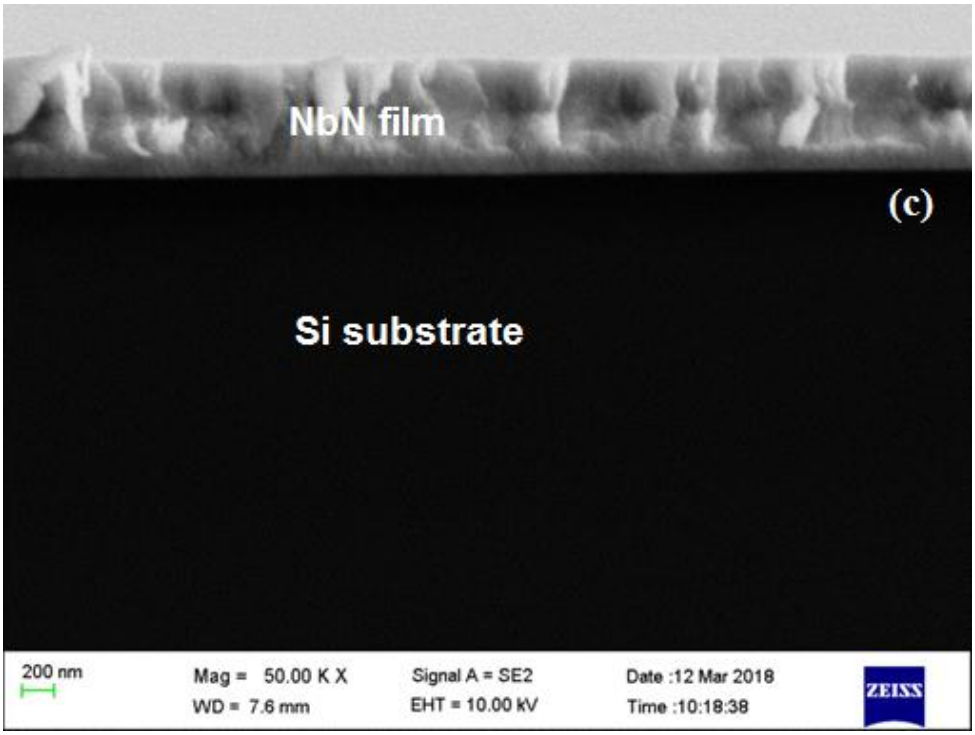

Figure 5.3: SEM micrographs of surface morphology of NbN films deposited at sputter power of 200 W for (a) 9 mins, (b) 19 mins, and (c) 33 mins. Film (a) corresponds to Zone I, while (b) and (c) correspond to Zone III of the structure zone model.

5.3.3 Microstructural dependence on the adatom energies by X-ray Reflectivity (XRR)

The measured and the simulated spectra for a NbN thin film on (100) Si substrate are shown in Figure 5.4. Above the critical angle of total external reflection, a gradual drop in intensity coupled with interference oscillations (Kiessig fringes) is observed. The spacing between the maxima of these oscillations provides thickness information as related by the modified Bragg equation [15]:

$$sin^2\theta_i = \theta_c^2 + (n_i + \Delta n)^2\lambda^2 \,/\, 4t^2 \qquad (5.1)$$

where θ_i is the observed position of the maximum or minimum of the ith fringe, θ_c the critical angle for total reflection, n_i is an integer, $\Delta n = 1 / 2$ and 0 for the maximum and minimum, respectively, λ is the wavelength and t is the film thickness.

The mass density values extracted from the X-ray reflectivity measurements were up to 97% of the bulk density value (8.47 g/cm^3). The presence of structural defects, stoichiometric variations and voids in the films especially at low sputter powers could lead to low density (7.74 g/cm^3, 7.89 g/cm^3 at 75 W and 100 W respectively). However, the microstructure changes with high sputter powers due to the subsequent densification of the film upon ad-atom condensation on the substrate. At high sputter powers, there is increased bombardment of the target by energetic Ar ions. This knock-on effect increases the kinetic energy of ad-atoms on the substrate. In addition, the bombardment may also lead to atomic peening effect due to momentum transfer from bombarding ions to the ad-atoms. As a result denser films are obtained [211]. In the films created in the present work this is observed for those deposited between 150 W and 250 W, whose mass density values are higher than those deposited at 75 W and 100 W.

The surface roughness values obtained from AFM also increased with increase in RF power. This could be attributed to increase in bombardment of ions and the competition between deposition rate and the adatoms energy. Larger grains are formed at such higher ad-atoms energy resulting to an increase in surface roughness [212]. There was also a significant difference between the surface roughness values obtained using AFM and those obtained using XRR. The values obtained using XRR were higher than those obtained using AFM for

select films. This difference is attributed to the inherent differences between the two techniques. AFM description of the roughness is limited to very low lateral length scales in comparison to XRR [213]. The XRR method is based on the fact that a short wavelength radiation is scattered effectively by a small-scale surface roughness. The angular dependences of specular and diffuse scattered radiation intensities contain the information about the average geometrical characteristics of roughness. On the other hand, AFM provides a direct measurement of the topography of the surface with extremely high lateral and vertical resolution [214].

XRR measurements indicated that NbN thin films were less dense than the bulk NbN. The mass density values for the films were in the range of 7.74 - 8.22 g/cm^3 (± 0.05 g/cm^3) as depicted in Table 5.2 which shows a correspondence between density and sputter power. The thickness obtained using XRR were used to calculate the deposition rates also shown in Table 5.2. The deposition rates increased with increase in sputter power and were between 6.67 - 33.3 nm/min. The increase in rf power enhances the argon ion energy which increases the number of molecules ejected from the surface of the NbN target hence the increase in the deposition rate [215].

Table 5.2: The average mass density and deposition rate of the samples as a function of sputter power measured by XRR.

Sputter Power (W)	**Average Mass density (g/cm^3) ±0.05**	**Deposition rate (nm/min)**
75	7.74	6.67
100	7.89	7.80
150	8.22	11.0
200	7.89	23.6
250	8.14	33.3

Table 5.3: The surface roughness of the samples as measured by XRR for deposition rate determination.

Sputter Power (W)	Thickness (nm)	Surface roughness (nm)
75	50	0.41
100	50	0.31
150	50	0.26
200	50	0.34
250	100	0.33

A typical X-ray reflectivity spectrum is shown in Figures 5.4 below.

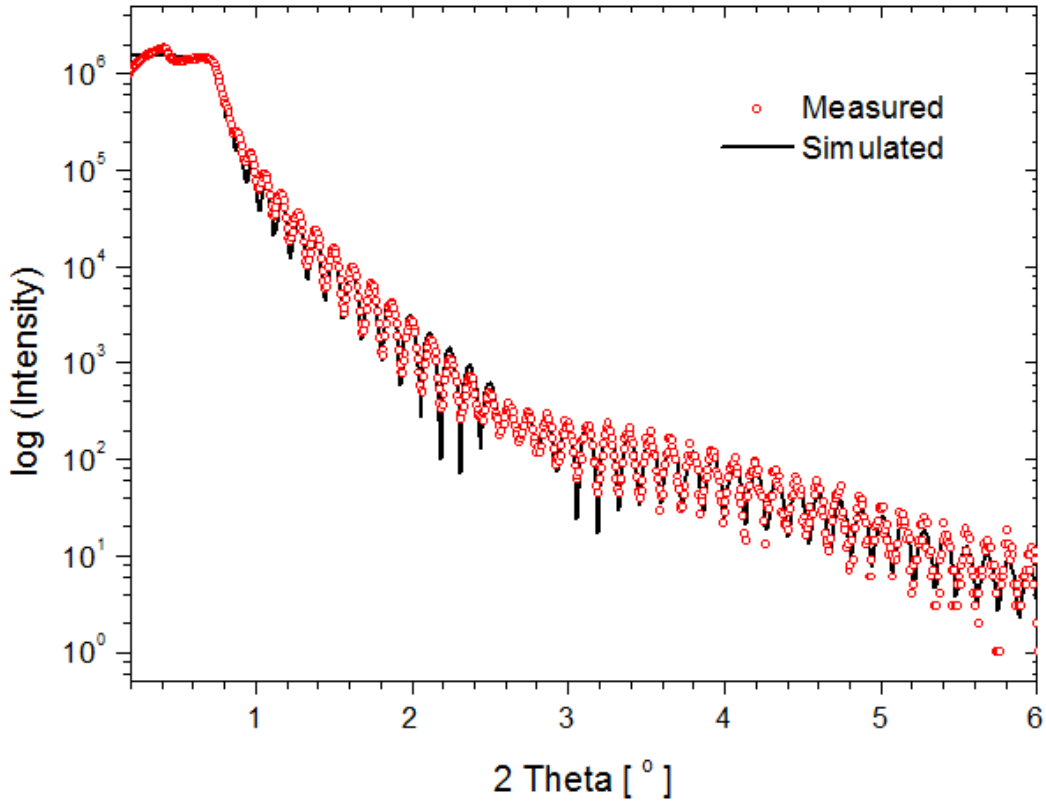

Figure 5.4: X-ray reflectivity spectra of the niobium nitride films showing the raw and the fitted curves. A layer stack of Nb_2O_5/NbN/SiO_2/Si was used for fitting.

5.3.4 Atomic force microscopy (AFM)

Studies have shown that sputter power, substrate temperature, and pressure are some of the parameters that affect morphological and structural properties of thin films [216,217]. In this study, rf power has been varied between 75 - 250 W to vary the T_{sub} / T_m ratio in the range 0.3 – 0.5 based on the structural zone model. The typical images are shown in Figure 5.5. The film surfaces show a nanostructured nature of the films. However, it was observed that with changing deposition times and hence in film thickness, the surface morphology changed substantially from large grains to smaller fine grains (see Figure. 5.5). The small particle-like clusters coalesce to larger clusters. This could be attributed to thermal effects that lead to an increase in ad-atom mobility within the surface of the film as a result of continuous dissipation of kinetic energy on the surface of the film.

The surface roughness of the films generally increases with increasing sputter power and also with increase in deposition rate as indicated in Table 5.4. Increase in sputter power helps to increase the surface mobility of ad-atoms which leads to formation of larger grains and hence increase in surface roughness [212]. Increasing sputter power also increases the deposition rate due to the increase in the number of sputtered NbN particles at the target following enhanced bombardment by the Ar^+ ions [218]. There are three basic modes of film growth based on the principle of interactions between substrate atoms and the deposited atoms, namely;

- Volmer-Weber's 3D island growth,
- Frank-van der Merwe's layer by layer growth,
- Stranski-Krastanov's layer plus island growth [212].

At low sputter powers, the films exhibit island growth mode while increase in sputter powers results in the films growth mode changing to layer-plus-island growth (Stranski-Krastanov) [144]. The root mean-square (rms) surface roughness of the films ranged from 0.17 - 1.50 nm. The surface roughness values are shown in Table 5.4. At these film thickness values, the attenuation of the surface Brillouin scattering signal and the contributions of elastically scattered light from surface roughness is minimised.

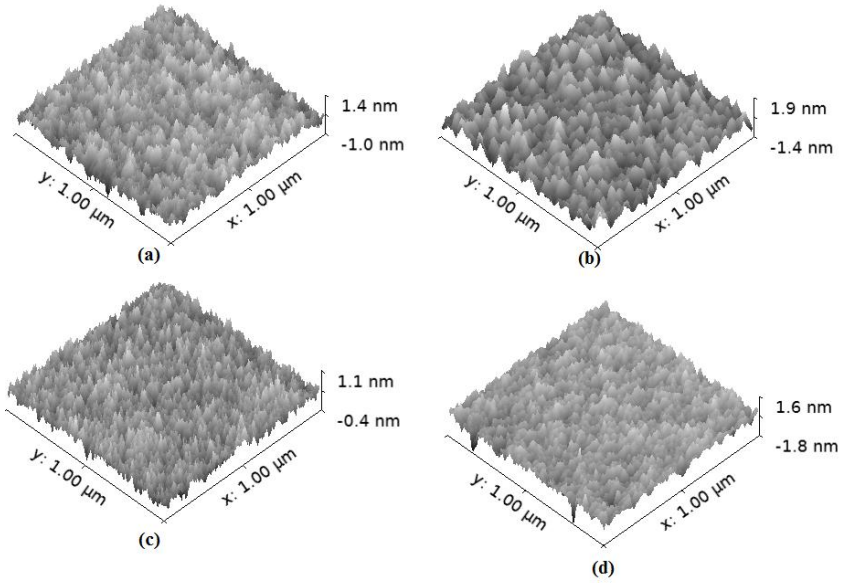

Figure 5.5: The 3D view of the morphology of the thin films of 50 nm thickness deposited at (a) 75 W, (b) 100 W, (c) 150 W, and (d) 200 W.

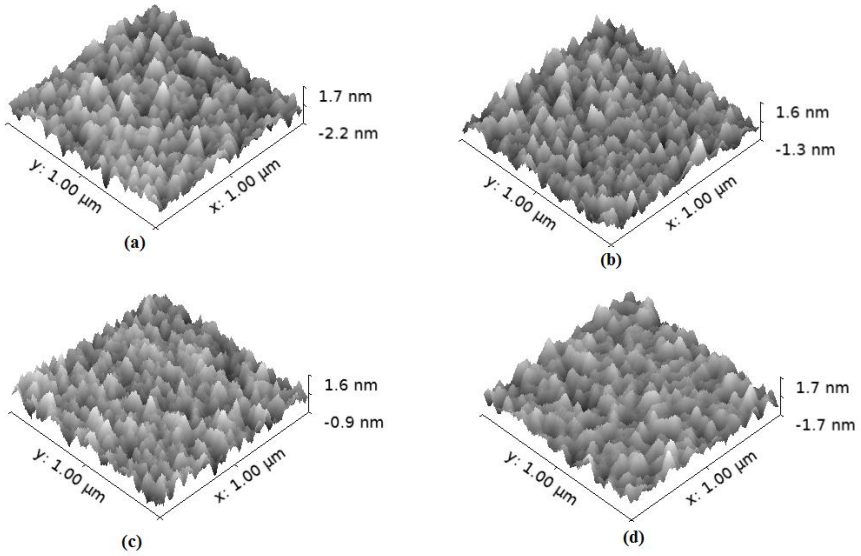

Figure 5. 6: The 3D view of the change in morphology of the thin films deposited at 250 W with thickness of (a) 100 nm, (b) 300 nm, (c) 600 nm, and (d) 800 nm.

As seen in the AFM images, there is no significant change in the surface morphology of the films with increasing deposition times (thickness). However, the values of the rms surface roughness from Table 5.4 show a decrease of roughness with increasing thickness.

Table 5. 4: The rms surface roughness of the niobium nitride films of varying thickness deposited at varying sputter powers.

Thickness (nm)	**Sputter power (W)**				
	75	**100**	**150**	**200**	**250**
50	0.26 ± 0.05	0.39 ± 0.05	0.17 ± 0.05	0.31 ± 0.05	0.46 ± 0.05
100	0.20 ± 0.05	0.39 ± 0.05	0.25 ± 0.05	0.40 ± 0.05	0.56 ± 0.05
150	0.35 ± 0.05	0.33 ± 0.05	0.28 ± 0.05	0.24 ± 0.05	0.19 ± 0.05
300	0.35 ± 0.05	0.38 ± 0.05	0.36 ± 0.05	0.33 ± 0.05	0.39 ± 0.05
450	0.64 ± 0.05	0.64 ± 0.05	1.06 ± 0.05	0.56 ± 0.05	0.48 ± 0.05
600	0.46 ± 0.05	0.50 ± 0.05	1.50 ± 0.05	0.44 ± 0.05	0.34 ± 0.05
700	0.61 ± 0.05	0.49 ± 0.05	0.70 ± 0.05	0.55 ± 0.05	0.35 ± 0.05
800	0.41 ± 0.05	0.52 ± 0.05	0.89 ± 0.05	0.60 ± 0.05	0.41 ± 0.05

5.3.5 Grazing incidence X-ray diffraction (GIXRD)

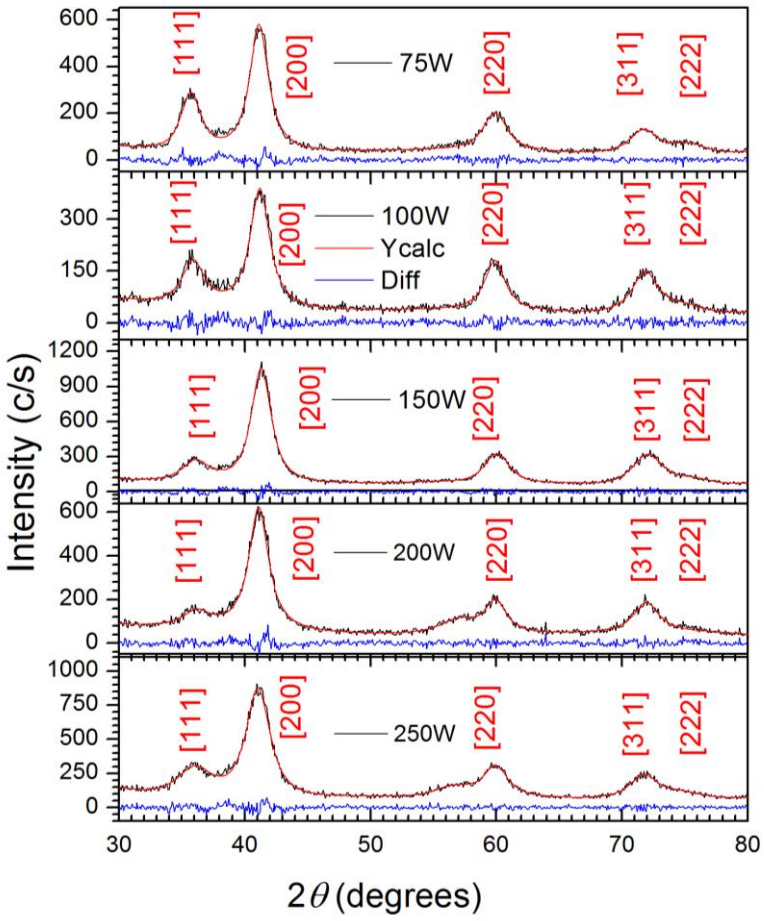

Figure 5.7: Grazing incidence XRD pattern recorded from NbN films deposited at varying sputter powers.

To determine the crystalline structure of the films, X-ray diffraction was carried out at a glancing angle of 0.7° in ω. Figure. 5.7 shows different grazing incidence XRD patterns for sample films deposited at sputter powers ranging from 75 - 250 W. It is clear from Figure. 5.7 that the films deposited at varying sputter powers present the same diffraction peaks confirming the rock salt (NaCl) polycrystalline structure of the films with a face centred cubic (FCC) lattice. For the films deposited at 75 W, 100 W, and 150W, the diffraction peaks look similar. At higher sputter powers of 200 W and 250 W, there seems to appear another peak

just before the distinctive peak (220). This could be attributed to a possible change in phase resulting in the emergence of the peak.

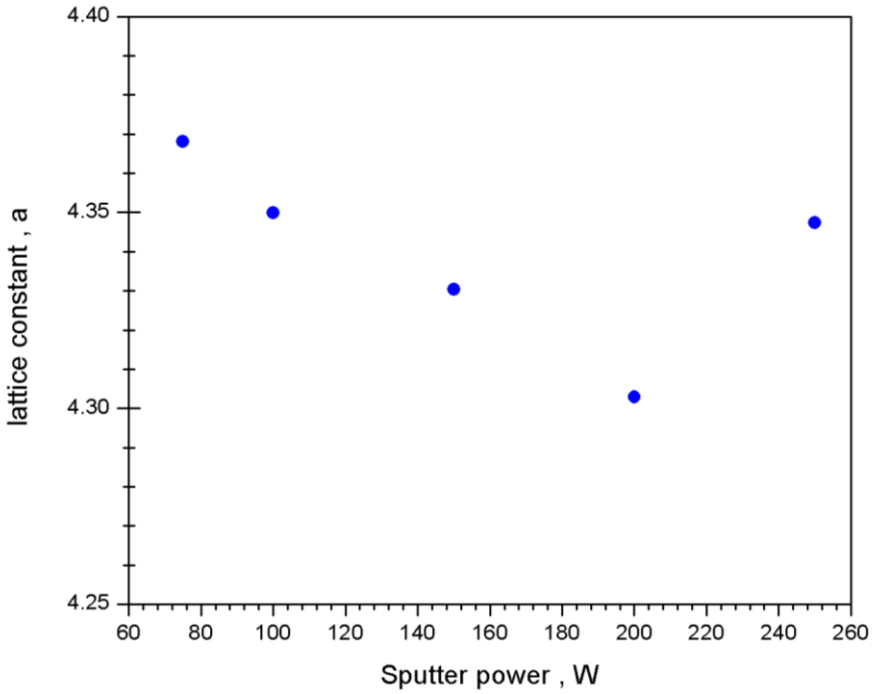

Figure 5.8: Calculated lattice constants of NbN thin films deposited at various sputter powers. After 200 W the NaCl structure increases its lattice constant owing to the appearance of the hexagonal phase.

Figure. 5.8 shows the calculated lattice constants of the films deposited at varying sputter powers. The figure shows a decrease in the lattice constants for the film samples ranging from 75 - 200 W. The lattice constants obtained for our films range between 4.30 - 4.37 Å, which is less than that of the bulk NbN (a = 4.39Å) [22]. Theoretical density values of the NbN films were calculated using the lattice constants and stoichiometry of as

$$\rho = \frac{ZM}{a^3 N_A} \tag{5.2}$$

where Z is the number of atoms per unit cell, M the molar mass, a the lattice parameter, and N_A the Avogadro's constant. The values of the calculated densities are shown in Table 5.5.

Table 5.5: The calculated and measured densities of NbN thin films as a function of sputter.

Sputter Power (W)	Calculated Density (g/cm^3)	XRR Density (g/cm^3)
75	8.02	7.74
100	6.59	7.89
150	9.52	8.22
200	8.91	7.89
250	7.75	8.14

The calculated density values were higher than those obtained from XRR measurements.

5.4 Surface Brillouin Scattering in NbN films

5.4.1 Measured Spectra for NbN thin films

A set of five NbN thin film samples were deposited using rf magnetron sputtering at sputter powers in the range 75 W - 250 W for SBS investigations. The thickness was controlled using the deposition rates calculated from XRR measurements as discussed in section 5.3. As discussed in chapter 3, the backscattering geometry enables the surface phonon conservation of momenta and energy. Therefore, the velocity V of surface acoustic waves (SAW) satisfies the following equations $k_{||} = 2k_i \sin\theta$ and $V = \omega / k_{||}$. For samples of thickness ranging from 50 - 450 nm and $\theta = 71°$, the product $k_{||}d$ for the corresponding film thickness is presented in Table 5.6 below.

Table 5.6: Showing the film thickness and the corresponding $k_{||}d$ values.

Film Thickness (nm)	50	100	150	300	450
$\boldsymbol{k_{\|\|}d}$	1.16	2.32	3.48	6.97	10.45

The SBS measurements were performed for the [110] direction in the (100) surface at room temperature using the 514.5 nm line from an argon-ion laser operating in a single axial mode and power on the sample being 70 mW. The laser beam was focused onto the sample by a lens of aperture $f/2.3$ in a back-scattering geometry to illuminate each sample. The in-elastically scattered light was resolved with a (3 +3) pass tandem Fabry-Pérot interferometer and the spectrum accumulated in a multi-channel analyzer, and its intensity was measured with a low noise photo detector.

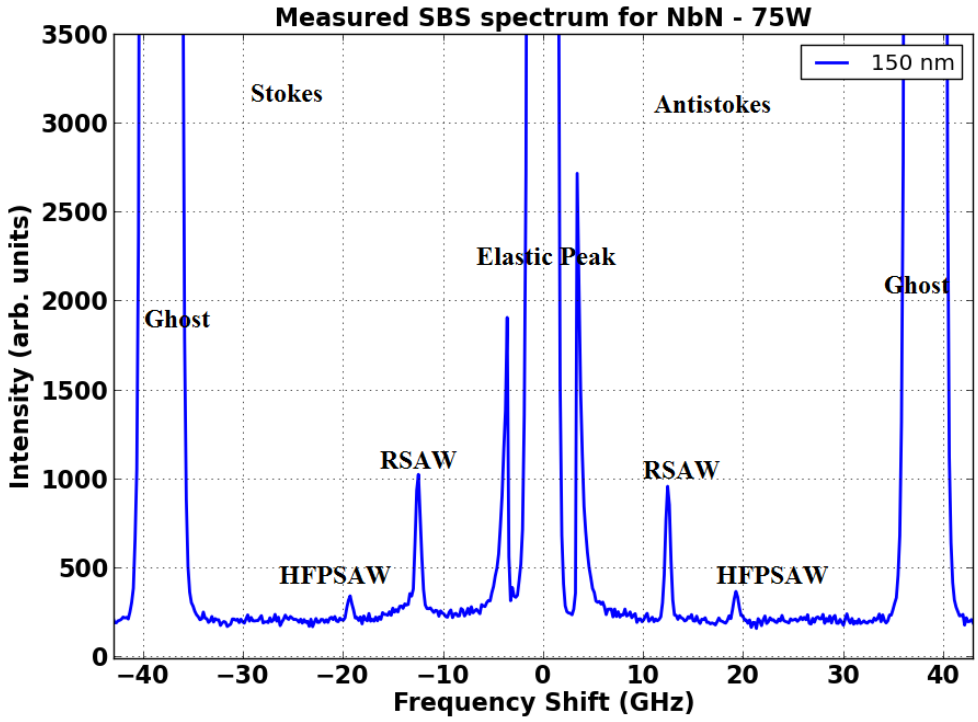

Figure 5.9: Measured SBS spectrum for a 150 nm ($k_{||}d = 3.48$) NbN/Si. Shown are the Stokes and anti-Stokes bands.

In Figure. 5.9, a representative measured SBS spectrum for NbN film of thickness 150 nm and corresponding $k_{||}d = 3.38$ is shown. The central elastic peak results from elastically scattered light which is unshifted in frequency and is injected at low intensity using an electromechanical shutter to stabilise the interferometer transmission while at the same time protecting the detector. The RSAW and other high order modes have been discussed in Chapter 3 and they represent the surface dynamics of a slow (NbN) on fast (Si-substrate) configuration confirmed due to the presence of Sezawa waves in the propagation.

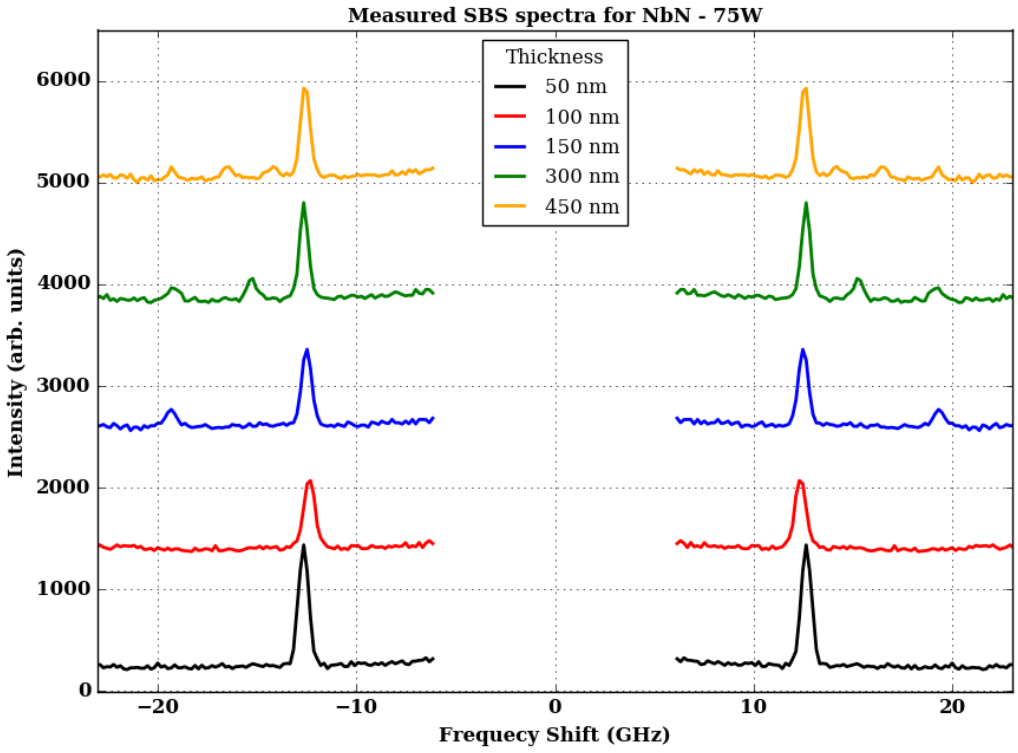

Figure 5.10: Measured Brillouin spectra at different thickness ($k_{||}d$) for NbN/Si deposited at 75 W.

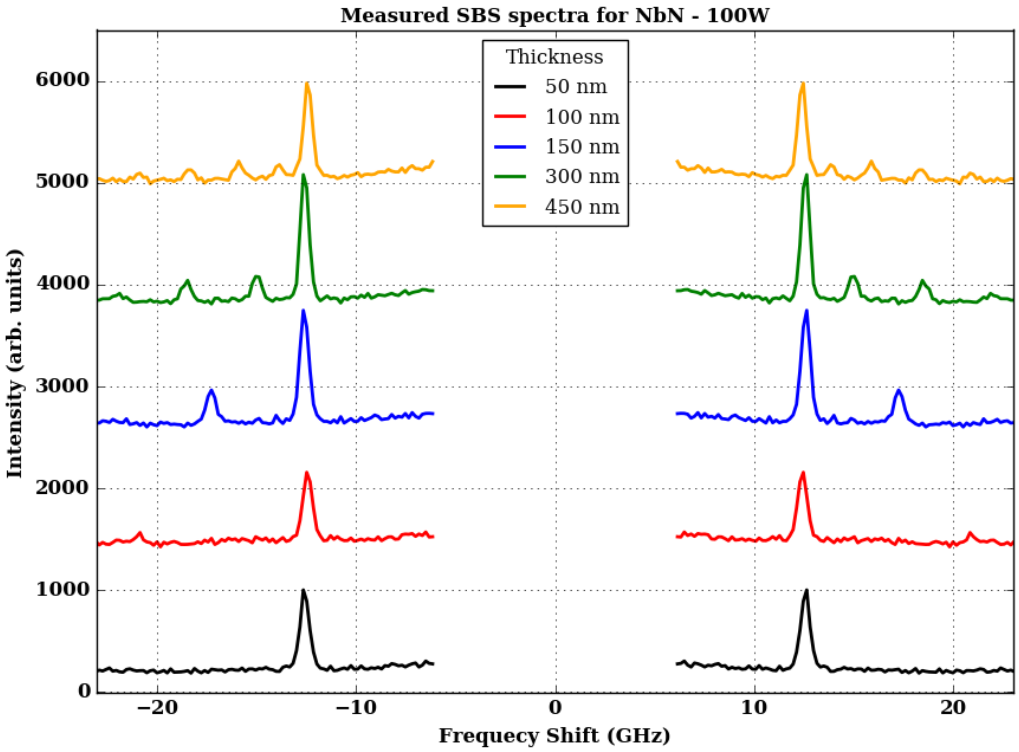

Figure 5.11: Measured Brillouin spectra at different thickness ($k_{||}d$) for NbN/Si deposited at 100 W.

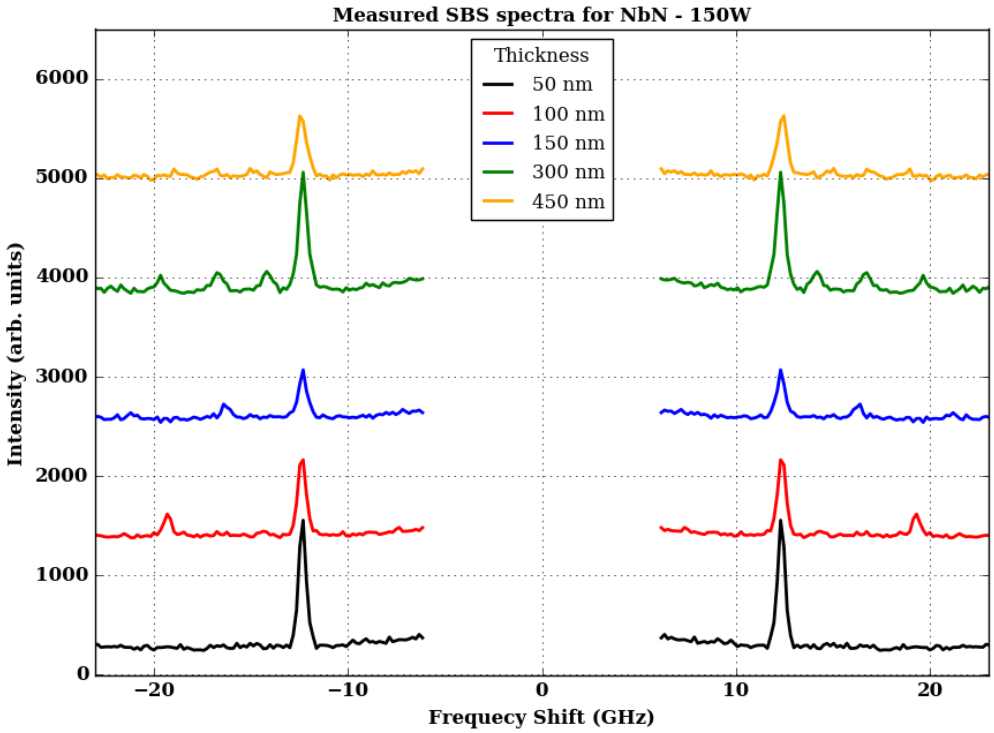

Figure 5.12: Measured Brillouin spectra at different thickness ($k_{||}d$) for NbN/Si deposited at 150 W.

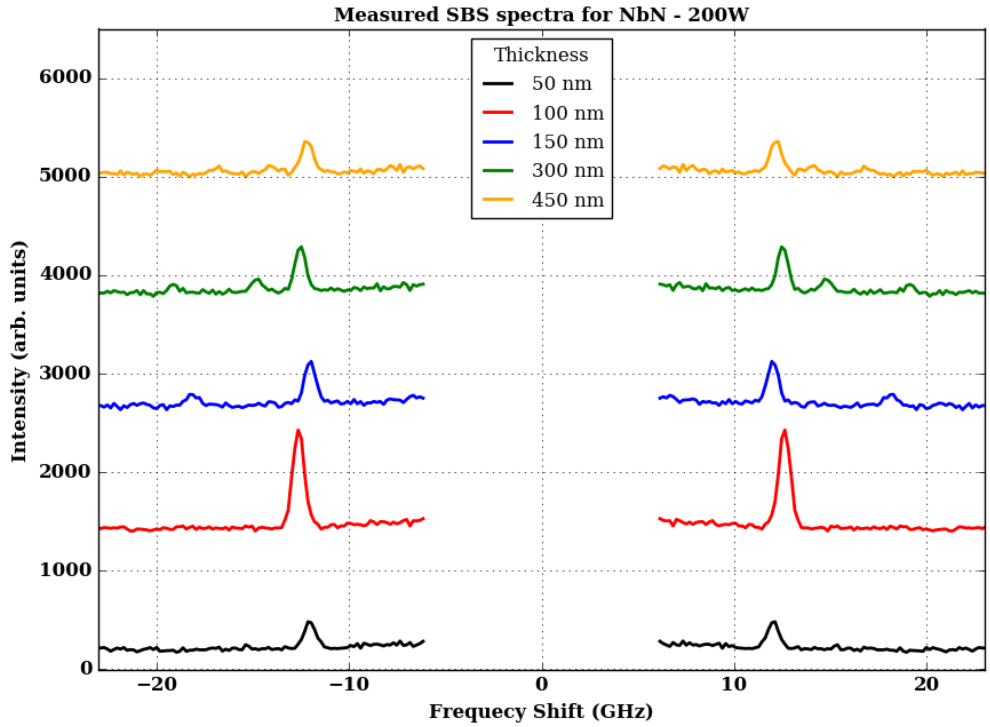

Figure 5.13: Measured Brillouin spectra at different thickness ($k_{||}d$) for NbN/Si deposited at 200 W.

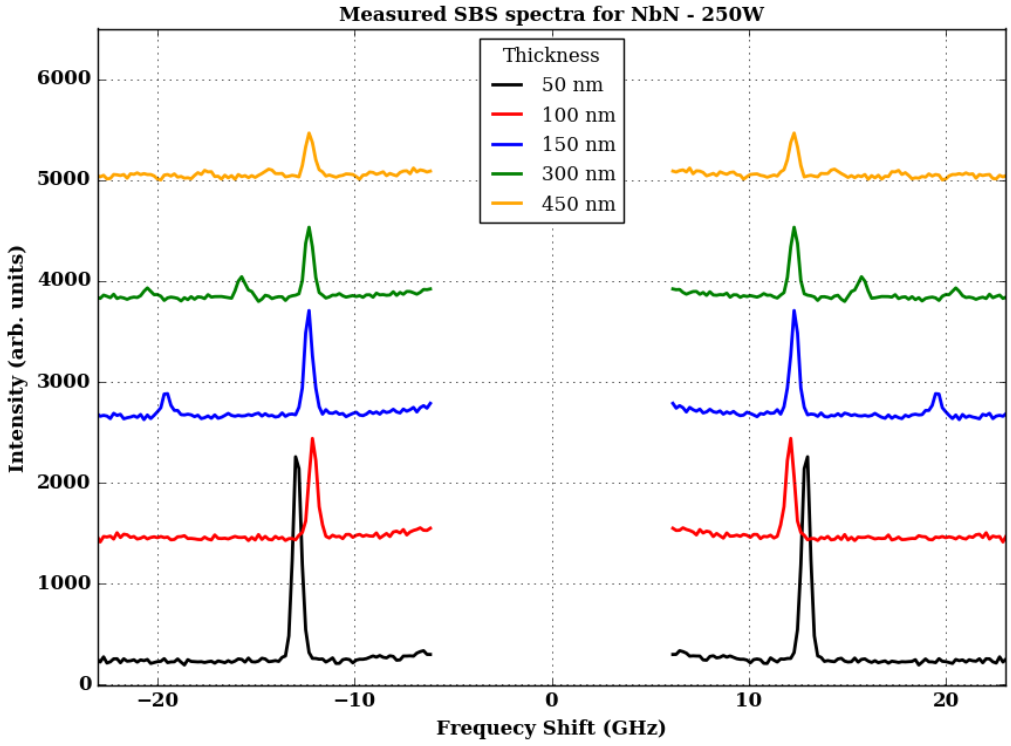

Figure 5.14: Measured Brillouin spectra at different thickness ($k_{||}d$) for NbN/Si deposited at 250 W.

In the Figures 5.10 - 5.14, measured SBS spectra for samples deposited at sputter powers ranging from 75 - 250 W at varying thickness are shown. The $k_{||}$ was kept constant by keeping θ at 71° . At 50 nm ($k_{||}d = 1.16$) and 100 nm ($k_{||}d = 2.32$), only the dominant RSAW is observed. As the thickness increases from 150 nm ($k_{||}d = 3.48$) to 450 nm ($k_{||}d = 10.45$), higher order peaks (SWs) start emerging and are more closely packed with increasing thickness. These discrete sagittal polarised guided modes are dispersive within the transonic region. With increasing rf power, a reduction of the RSAW intensity is observed for all the sample sets. In all cases it is evident that the increase in film thickness leads to stiffening of the acoustic modes.

5.4.2 SAW Velocity Dispersion and Elastic Stiffness

From the measured SBS spectra discussed in section 5.4.1 above, the SAW phase velocities were determined. Using the Green's function approach discussed in Chapter 2 theoretical SAW phase velocities were also determined. For crystalline silicon literature values: mass density $\rho = 2.332$ g/cm^3, $C_{11} = 165.7$, $C_{12} = 63.9$, and $C_{44} = 79.6$ GPa, respectively were used. By simultaneously fitting the measured and the calculated SAW phase velocities, the elastic stiffnesses of the films are extracted. The fitting of the SAW phase velocities is a procedure of inversion. From the minimisation of

$$\chi^2 = \sum_{i=1}^{n} \left(v_i^{measured} - v_i^{calculated}\right)^2 \qquad (5.3)$$

the best fit was obtained. The elastic fitness $v^{calculated}$ obtained from the Surface Green's function calculations are then considered to be the elastic stiffness of the film when χ^2 is minimum.

(a)

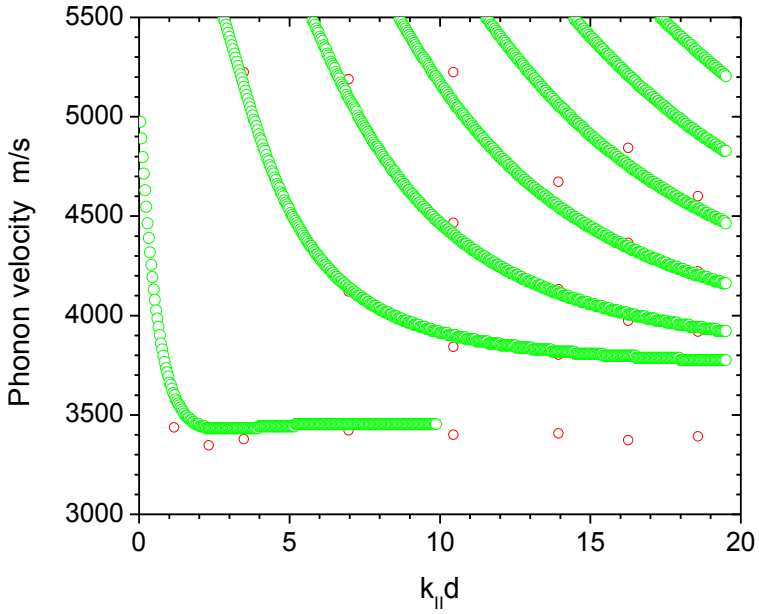

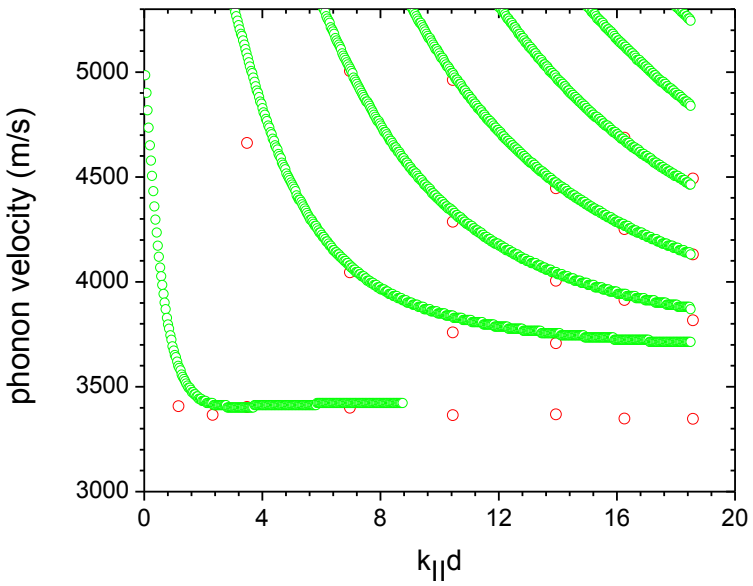

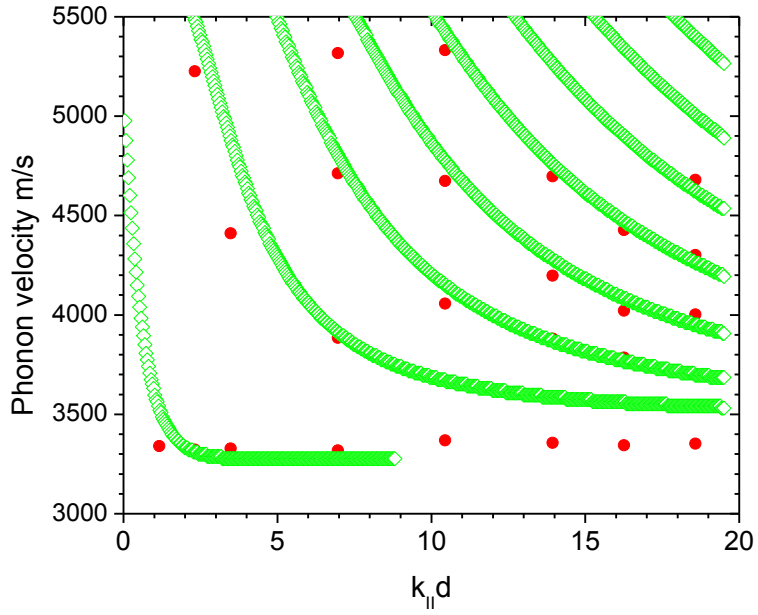
Phonon velocity m/s
5500
5000
4500
4000
3500
3000
0
5
10
15
20
k_ll d

(d)

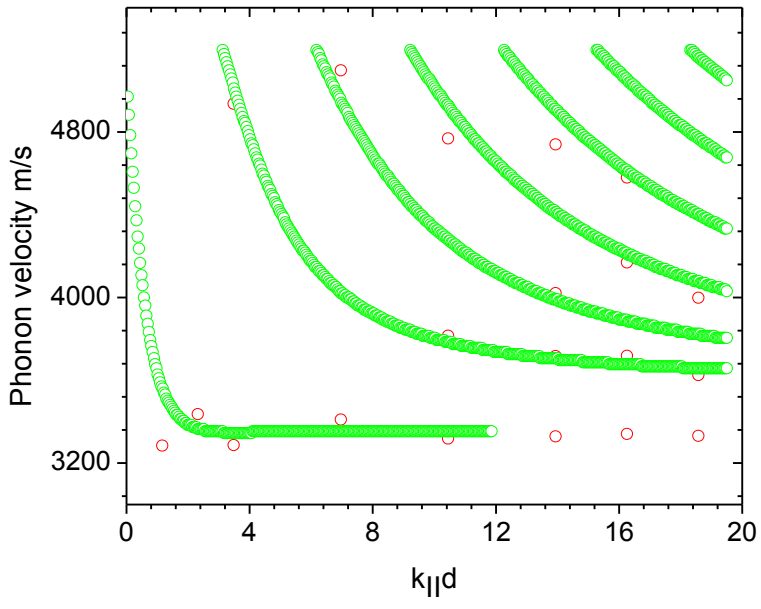
Phonon velocity m/s
4800
4000
3200
0
4
8
12
16
20
k_ll d

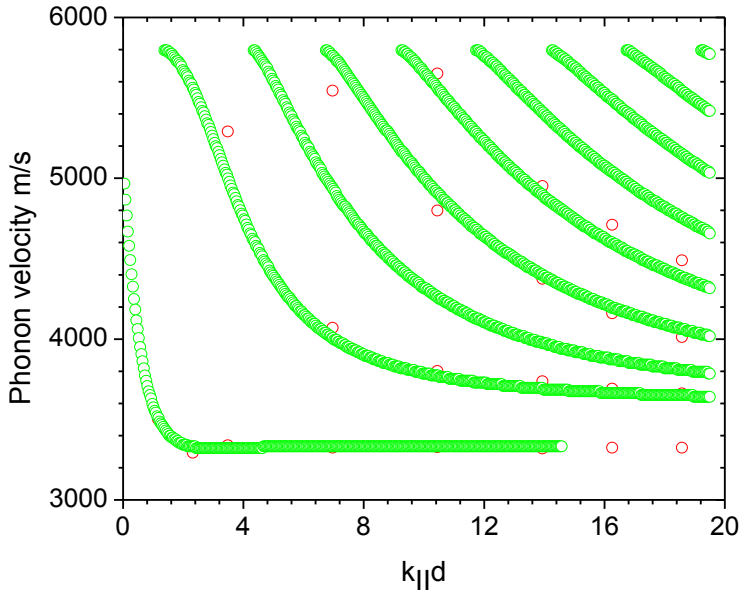

Figure 5.15: Calculated Brillouin intensities compared to the measured intensities for NbN/Si deposited at (a) 75 W, (b) 100 W, (c) 150 W, (d) 200 W and (e) 250 W as a function of $k_{||}d$. The red circles represent the measured while the green profile represent the calculated velocities. The values of the elastic stiffness resulting from the best fit are shown in the table 5.7

Since the NbN films have a polycrystalline structure, they could be considered as isotropic solids whose elastic behavior is described by C_{11} and C_{12} . The C_{44} values have been obtained from the elastic constant combination $(C_{11} - C_{12})/2$.

Table 5.7: Elastic constants of NbN in GPa deposited at varying sputter power.

Sputter Power (W)	C_{11}	C_{12}	C_{44}
75	383.3	168.5	107.4
100	386.3	171.9	107.2
150	520.5	320.7	99.9
200	394.9	190.3	102.3
250	371.5	160.9	105.3

In Table 5.7, the values of C_{11} increase for sputter powers 75 - 150 W and drop thereafter until 250 W. A similar behaviour was observed in the values of the mass density. The C_{11} and the density values for films grown at 150 W correspond significantly to those of the bulk. This could be attributed to a possible phase transition for films deposited at 200 W. To determine the self consistency of the solution, the surface elastodynamic Green's function approach was used to plot the Brillouin scattering spectra for select films for all the deposition powers (Figure. 5.16) .

(a)

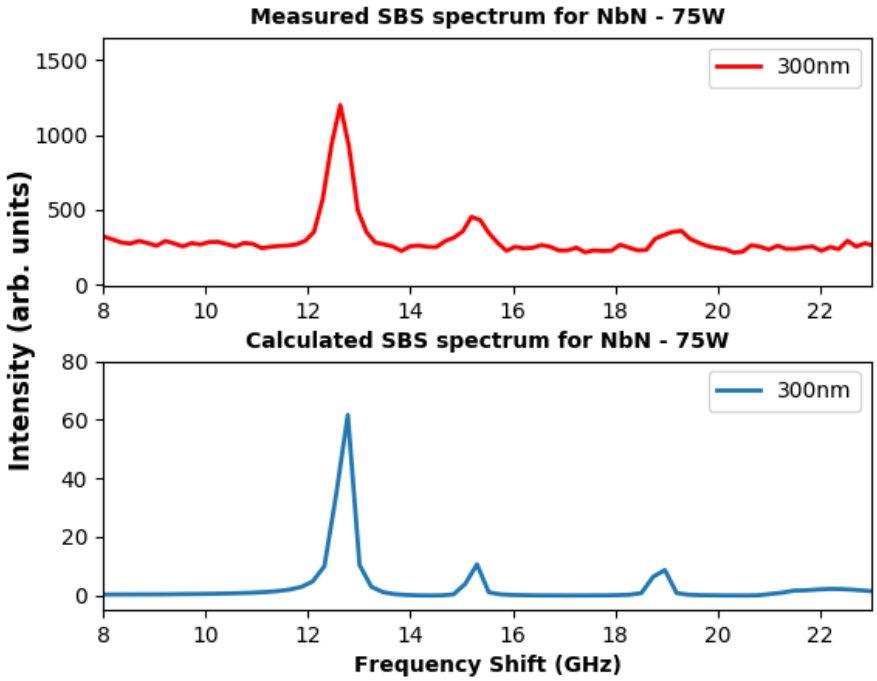

(b)

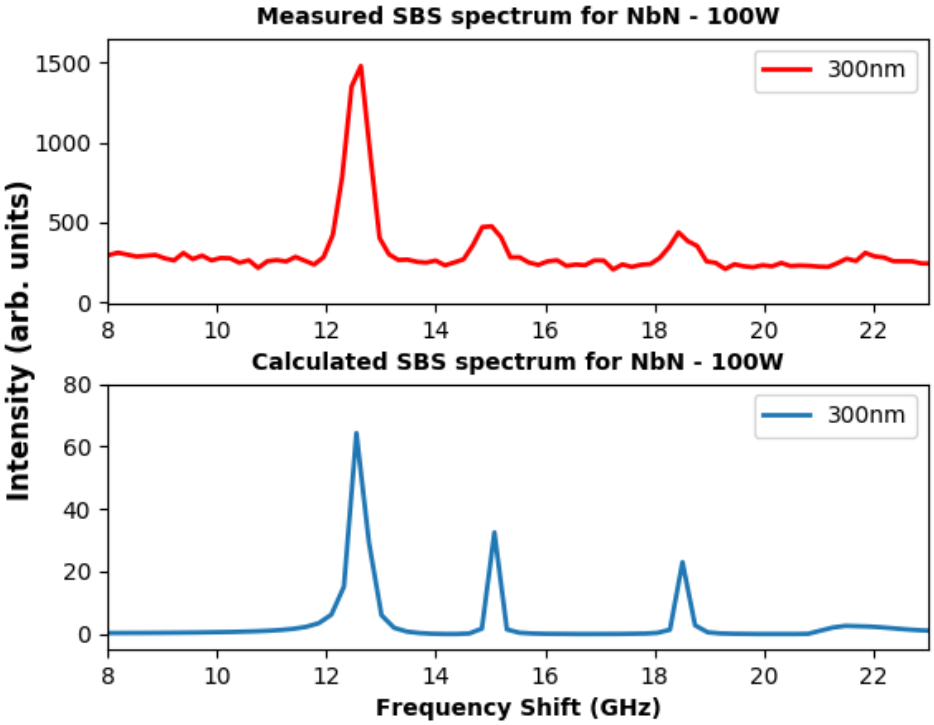
Measured SBS spectrum for NbN - 100W
300nm
Intensity (arb. units)
Calculated SBS spectrum for NbN - 100W
300nm
Frequency Shift (GHz)

(c)

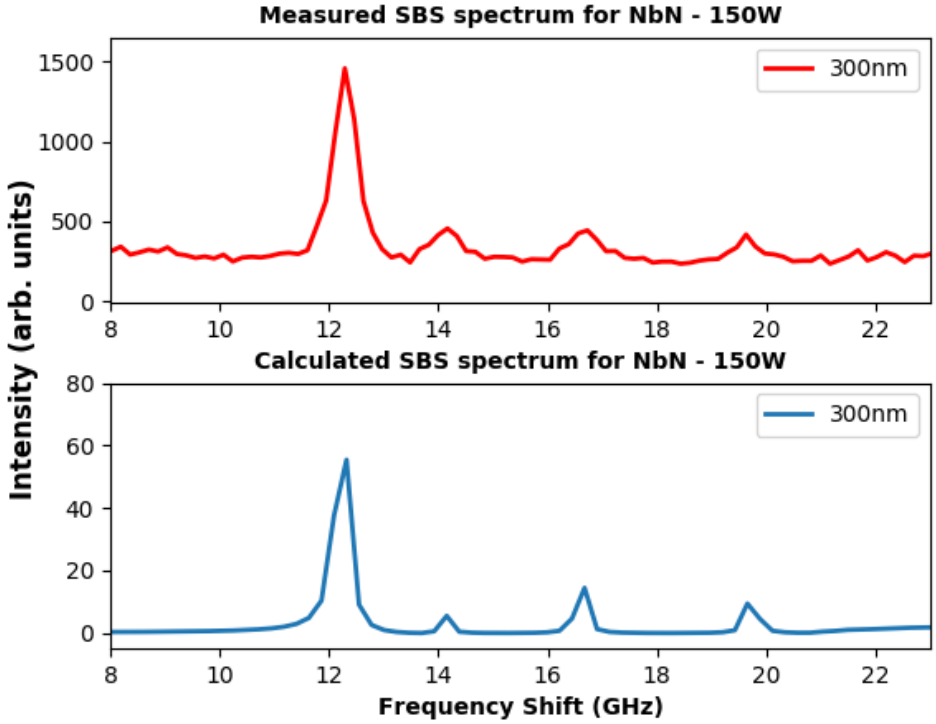
Measured SBS spectrum for NbN - 150W
300nm
Intensity (arb. units)
Calculated SBS spectrum for NbN - 150W
300nm
Frequency Shift (GHz)

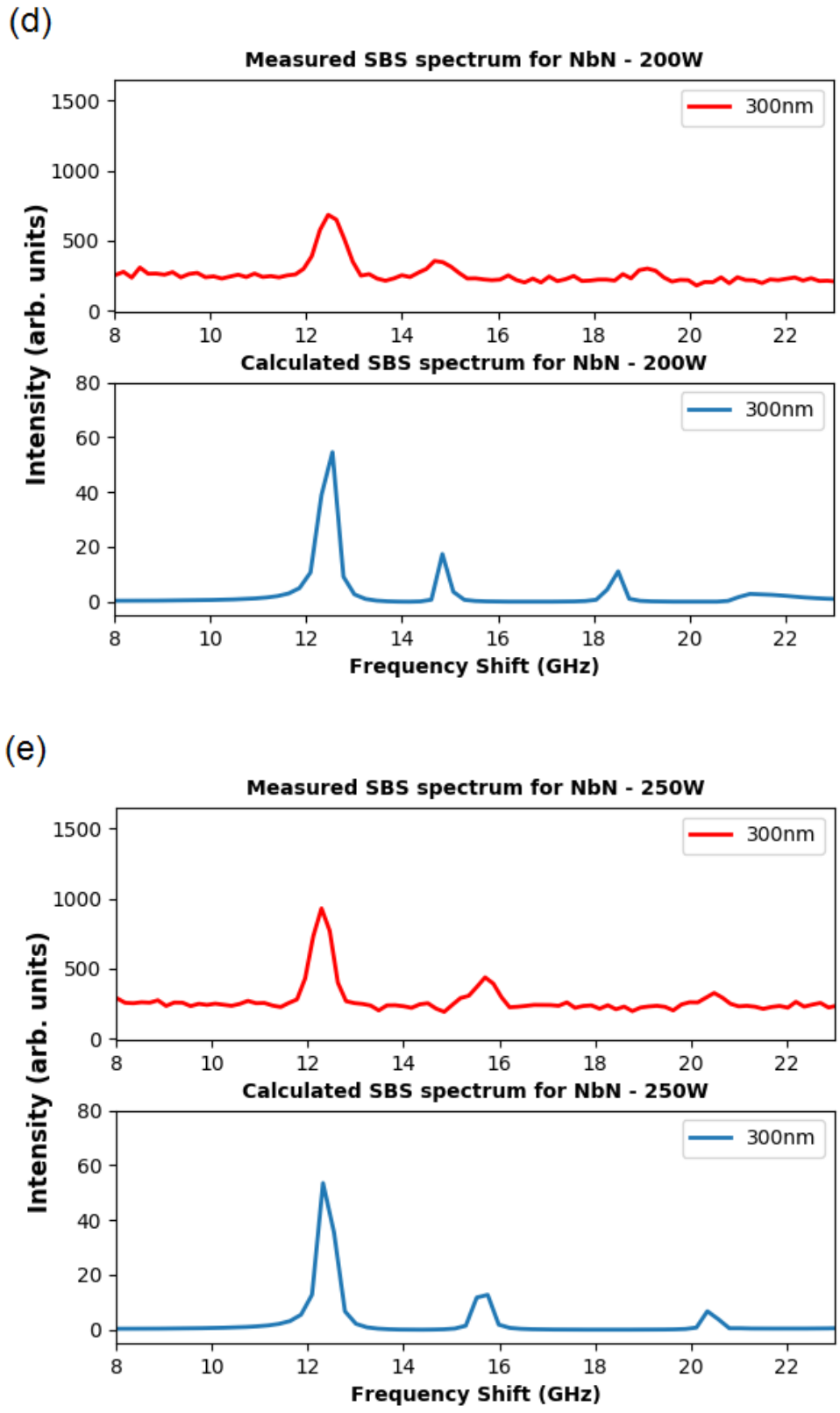

Figure 5.16: Measured and calculated anti-Stokes SBS spectra for 300 nm NbN/Si films deposited at (a) 75 W, (b) 100 W, (c) 150 W, (d) 200 W, and (e) 250 W.

The elastic constants of materials are fundamental properties that determine the existence of the solid state. The key of which is the shear modulus. As opposed to the bulk modulus, the magnitude of the shear modulus has been used to distinguish between the solid and the liquid states. If the shear modulus was not sufficiently large, all matter would be liquid [2]. Thus, the engineering moduli are essential in the classification of the strength of materials and their hardness. From the elastic stiffness obtained above, the engineering moduli have been calculated as follows,

$$B = \frac{(C_{11} + 2C_{12})}{3} \tag{5.4}$$

$$G = C_{44} \tag{5.5}$$

$$\nu = \frac{3B - 2G}{2(3B + 2G)} \tag{5.6}$$

$$k = \frac{G}{B} \tag{5.7}$$

$$P_c = C_{12} - C_{44} \tag{5.8}$$

where B, G, ν, k, P_c are Bulk modulus, shear modulus, Poisson's ratio, Pugh's ratio, and Cauchy pressure respectively. The values of the moduli are shown in the Table 5.8

Table 5.8: Moduli of NbN thin films deposited at varying sputter power

Sputter Power (W)	B (GPa)	G (GPa)	ν	k	P_c (GPa)	G_{VR} (GPa)
75	240.1	107.4	0.27	0.44	61.1	72.88
100	243.4	107.2	0.27	0.44	64.7	72.74
150	387.3	99.9	0.35	0.26	220.8	67.79
200	258.5	102.3	0.29	0.40	88	69.42
250	231.1	105.3	0.27	0.46	55.6	71.45

The shear modulus of a polycrystalline system is estimated as $G_{VR} = (G_V + G_R)/2$ where $G_V = [(C_{11} - C_{12}) + 3C_{44}]/5$ and $G_R = [5(C_{11} - C_{12})C_{44}]/4(C_{44} + 3C_{11} - 3C_{12})$ are Voigt and Reuss approximations respectively. These values are also shown in Table 5.8. A significant change in the values of the bulk modulus is observed whereas those of the shear modulus don't change significantly. The Poisson's ratio was determined to range from 0.27 – 0.35. This shows that the films are less hard than diamond which has a lower Poisson's of 0.2. Values of $C_{11} = 556$ GPa, $C_{12} = 152$ GPa and $C_{44} = 125$ GPa obtained from line-focus acoustic microscopy for single crystal NbN films have been reported in [72]. A Poisson's ratio of 0.27 calculated from the elastic stiffnesses of single crystal NbN by line-focus acoustic microscopy is in good agreement with that of the films deposited at 75 W, 100 W and 250 W.

5.5 Conclusions

NbN thin films were deposited on Si (100) substrates using rf magnetron sputtering at sputter powers ranging from 75 to 250 W and argon gas flow of 13 sccm. XRR measurements have shown an increase in mass density of films deposited at 75 W – 150 W and a decrease for the films deposited at 200 W – 250 W. Deposition rates extracted from the mass densities increased with increasing sputter power. Surface roughness of the films obtained from AFM was found to be less than 2 nm. SEM studies of the films established columnar growth. For films deposited for varying times at constant power, there were no significant changes in the microstructure. Grazing incidence X-ray diffraction revealed the presence of a polycrystalline NaCl like phase in the films. The crystallite size estimated from W-H analysis was in the range of 1 – 4 nm. HI-ERDA measurements revealed that the films were non-stoichiometric and that they contained small traces of oxygen. Elastic constants of the films have been extracted using a combination of SBS and Surface Green's functions. A decrease in C_{11} values has been observed for films deposited at 250 W. The Poisson's ratio of the films was in the range 0.27 – 0.35. The Poisson's ratio of the films deposited at 75 W, 100 W and 250 W was consistent with literature value of NbN films measured by line-focus acoustic microscopy.

Chapter 6

Elastic Properties of Tantalum Nitride Thin films

The physical and elastic properties of Tantalum nitride (TaN) thin films are discussed in this chapter. The chapter commences with the introduction on the application versatility of TaN in electronic devices and as protective coatings. Furthermore, the methods of fabrication and property investigation of TaN are presented in detail in Section 6.1. The deposition process of TaN films and sample characterisation using various analytical techniques is discussed in Section 6.2. Section 6.3 describes the analysis of the characterisation results. Surface Brillouin scattering (SBS) measurements for the extraction of elastic constants are presented in Section 6.4. Section 6.5 gives a conclusion of the chapter.

6.1 Introduction

A growing demand in electronic devices especially in the computing industry has in the recent past triggered advances in the integrated circuit industry. This has led to miniaturisation of microelectronics components which requires new technologies for manufacturing and design as well as new materials with improved performance [59]. Tantalum nitride (TaN) has attractive properties such as chemical inertness and thermal stability, corrosion resistance, and hardness making it attractive for large-scale integrated circuit applications as a structural element as well as a diffusion barrier [219]. The properties of TaN films are affected by the growth technique and growth conditions a fact that has been

exploited to fabricate films with properties required for special purposes [220]. Due to their hardness, TaN can also be used in hard, wear-resistant coatings. However, most applications of TaN layers have been focused on their use in thin film resistors and diffusion barriers. As such, much has been reported on the electrical and optical properties of TaN films as opposed to their mechanical properties [46–48,221].

TaN thin films have been deposited by physical (PVD) and chemical vapour deposition (CVD) techniques. It has however been established that PVD TaN films have higher thermal stability as compared to CVD films due to the superior microstructure of PVD based thin films [222].

Several studies on the structural and mechanical properties of TaN thin films have been reported by various authors. Most of these studies have focused on the structural and electrical properties of TaN with only a few reporting on the mechanical properties. Kim *et al.* [56] deposited TaN films on SKD11 steel using D.C. magnetron sputtering to study the influence of the N_2/Ar gas ratio of the inlet gases on the structure, hardness, adhesion and wear resistance. To determine the effect of the nitrogen partial pressure on the hardness of the films, the N_2/Ar gas ratio of the inlet was varied from 0.1 to 0.4 while target power was fixed at 200 W. It was established that the hardness of the films decreased with increase in N_2/Ar gas ratio. This was attributed to the decrease in deposition rate and the formation of the Ta_3N_5. In a comparative study on the friction performance and nano-indentation behavior of Ta-C-N and Ta-N thin films prepared using magnetron sputtering, Yan *et al*. [46] reported the hardness and elastic modulus of TaN thin films. Nano-indentation results showed that Ta-C-N had higher nano-hardness (9.45 GPa) and elastic modules (225.71 GPa) compared to Ta-N (3.16

GPa) and (108.95 GPa) respectively which was attributed to the existence of amorphous carbon in the Ta-C-N films. A study on the effect of deposition and annealing temperature on the mechanical properties of TaN films by Liu *et al*. [47] showed that the maximum value of hardness of approximately 40 GPa was attained by depositing the films at 573 K. The films were deposited by reactive sputtering a Ta target in presence of argon and nitrogen. An electron cyclotron resonance (ECR) microwave plasma source enhanced magnetron sputtering system was used in the above study and the results indicate a decrease in hardness, modulus and adhesion of TaN film with decreasing deposition temperature and increasing annealing temperature.

6.2 Sample preparation and characterisation

6.2.1 Thin film growth

TaN thin films were prepared using unbalanced rf magnetron sputtering of a 99.9% pure, 76 mm × 6 mm thick TaN target (Semiconductor Wafer) at a fixed sample-target distance of 6 cm in Ar plasma. The films were deposited on 1.5 × 1.5 cm^2 (100) Si substrates at a sputter power of 150 W. Prior to deposition, the substrates were cleaned in successive rinses in ultrasonic baths of acetone, ethanol and finally blow dried in N_2. The chamber was evacuated to a base pressure of 2.6 × 10^{-5} mbar. To remove impurities from the target surface, the TaN target was then pre-sputtered in Ar^+ at a sputter power of 100 W for 15 minutes. Four samples were each deposited on polished (100) Si substrates for 5 minutes for X-ray reflectivity (XRR) measurements. Using the deposition rate extracted from the XRR measurements, the film thickness was controlled by depositing the samples at varying times in the similar deposition conditions. The linearity of the film

thickness with deposition time was used to estimate the film thickness greater than the resolution of the X-ray reflectivity film thickness measurement. Five samples of TaN thin films of thickness ranging from ~50 nm - 450 nm were prepared for investigating the dynamics of the surface acoustic wave propagation and determination of the elastic properties by surface Brillouin scattering (SBS).

6.2.2 Structural and Chemical properties of TaN thin films

The physical properties of thin films are largely controlled by the deposition conditions; these include the total working gas pressure, the deposition power, and the presence of reactive gas species. In the present work, the physical properties of interest were the thin film thickness and density which are essential in the determination of the elastic constants of TaN films. A non-destructive procedure, X-ray reflectivity (XRR) is one of the principal characterisation technique for thickness and density determination of thin films. XRR has been used to determine the thickness and density of the TaN films for SBS measurements.

The D8 Discover high resolution X-ray diffractometer (Bruker AXS GmbH) was used for XRR measurements. A layer stack of $Si/SiO_2/TaN/Ta_2O_5$ in that order was used in the simulation to generate the simulated spectra corresponding to the measured spectra. The surface roughness of the thin films was examined by a Veeco Dimension 3100 atomic force microscope operated in tapping mode at a scan rate of 1.51 Hz for a scan size of 1 μm^2. The atomic force microscopy (AFM) data was analysed and visualised using Gwyddion software [181]. Cross-section morphology of the films was investigated using a Jeol JSM-7001F high-resolution scanning electron microscope (SEM). The phase structure of the TaN films was investigated by grazing incidence X-ray diffraction

(GIXRD) on D8 Discover X-ray diffractometer (Bruker AXS GmbH) at 0.7° incidence angle. A 2.5° Soller slit coupled with a 0.1 primary divergent slit was used to collimate the primary beam and minimise sample footprints and axial divergence of the beam. The measurements were carried out in the 2Theta geometry ranging between $20° < 2\theta < 80°$. The surface chemical composition was of the thin films was established using heavy-ion elastic recoil detection analysis (Hi-ERDA).

6.3 Results and discussion

6.3.1 Thickness, deposition rate, and mass density by XRR

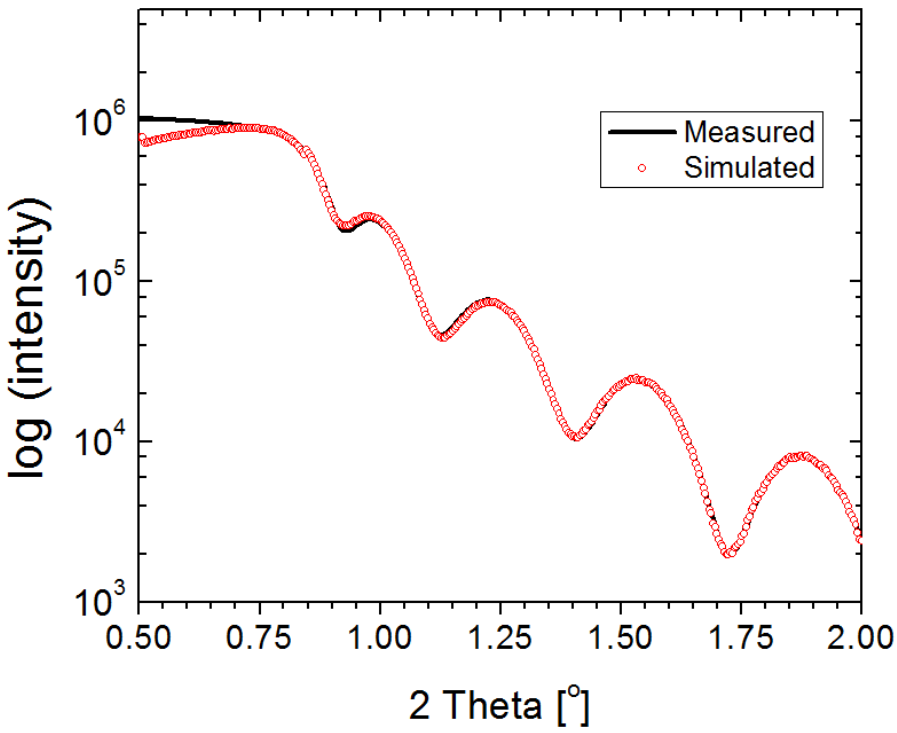

Figure 6.1: XRR measured (raw) and simulated spectra for a TaN film deposited at 150 W.

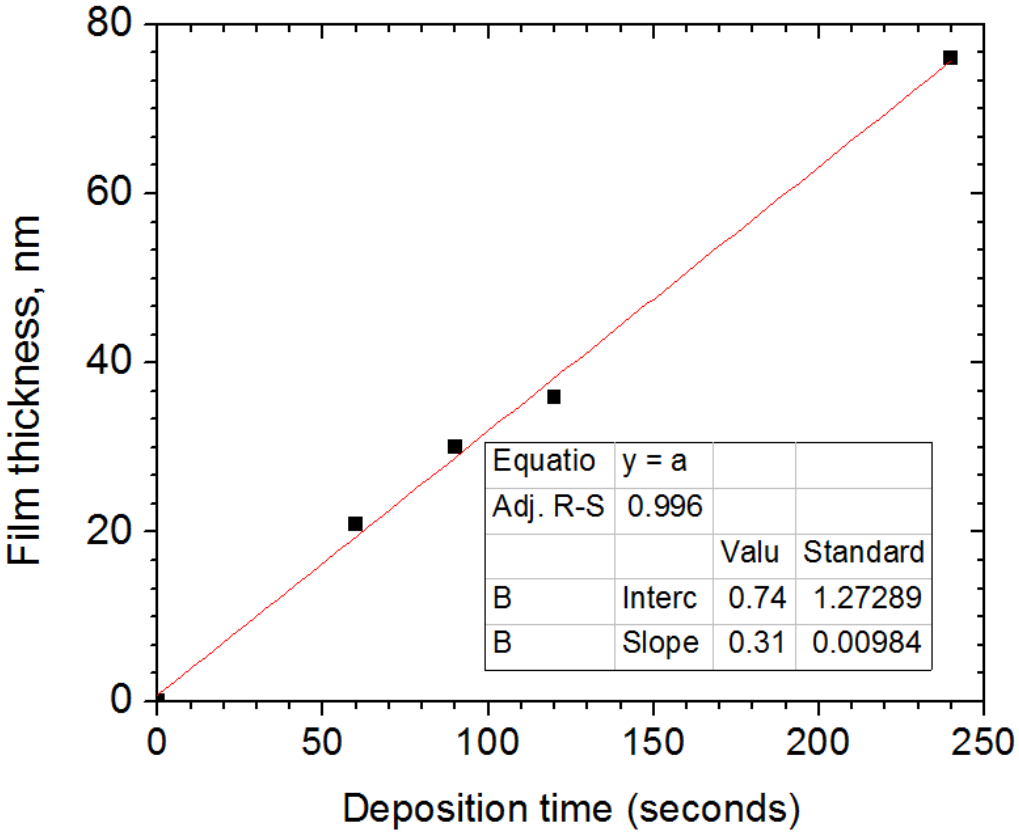

Figure 6.2: Deposition rate of TaN films deposited at 150 W.

Typical XRR spectra are shown in Figure 6.1. for TaN thin film deposited at 100 W for 3 minutes. XRR measurements were performed on a further four samples deposited at 100 W to as shown in Figure 6.2 to establish the deposition rate of 18.6 ± 0.6 nm/min. The mass density obtained from the XRR measurement was 11.09 g/cm^3 corresponding to 81 % of the bulk value (13.7 g/cm^3). The deposition rate was used to control the thickness of the samples required to determine the dispersive nature of the propagating modes in the transonic region using surface Brillouin scattering. The obtained surface phonon velocity dispersion curves were further processed using the inverse problem to determine the elastic constants based on the surface elastodynamic Green's function approach and the numerical

methods. In these simulations the mass density derived from the X-ray reflectivity measurements was used.

6.3.2 Morphology and microstructure by AFM and SEM

In the present study, eight samples of thickness ranging from ~50 nm – 800 nm were analysed using AFM. The surface morphologies of the films deposited at varying times and hence varying thickness are shown in Figure 6.3. From the figure, it can be seen that the films are smooth and homogeneous. The films are also shown to be nanostructured with the granular structure changing with increasing film thickness. The surfaces consist of fractal auto-affine symmetry and a "cauliflower morphology" where smaller grains coalesce to larger grains [223].

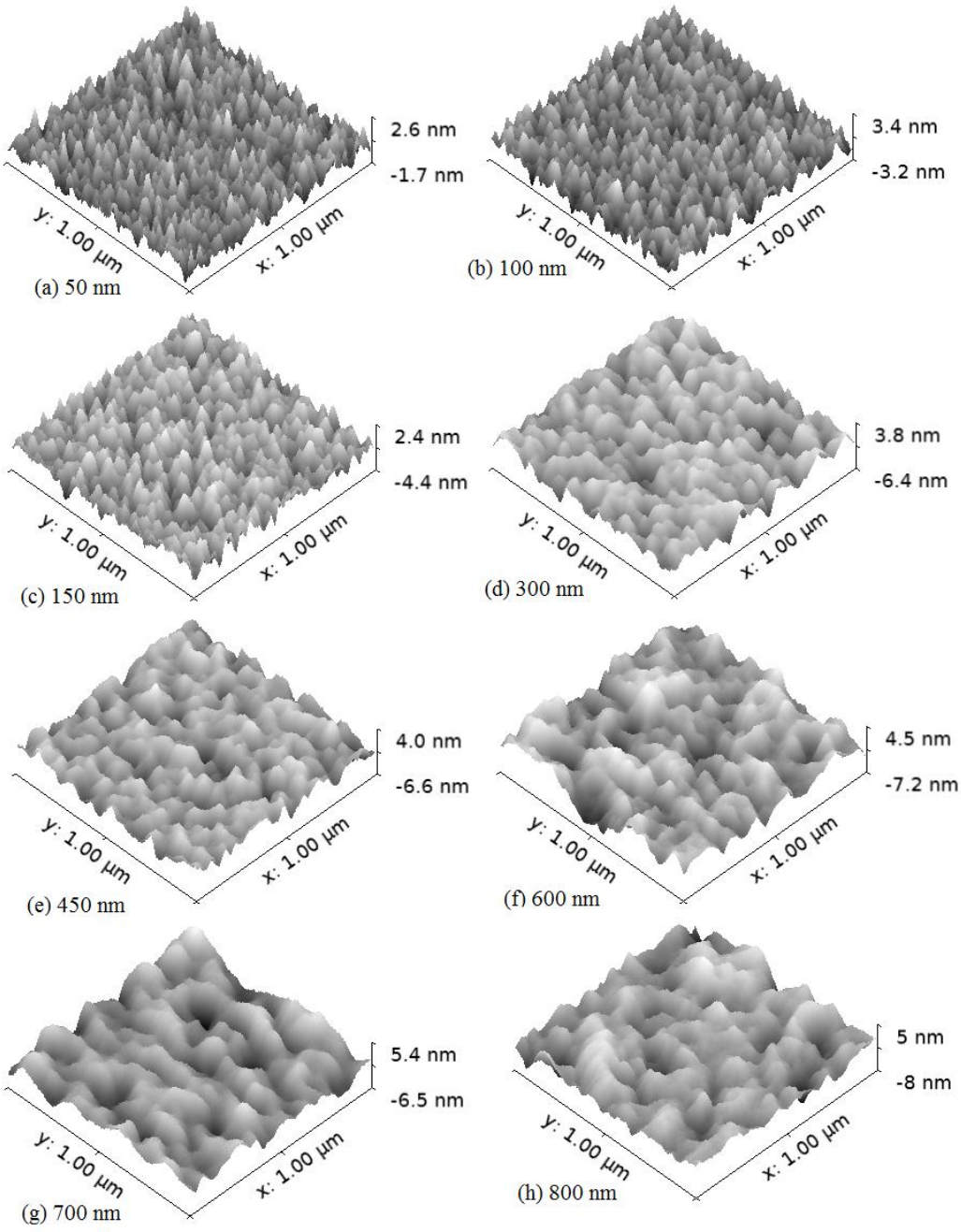

Figure 6.3: The 3D view AFM images for TaN films deposited at 150 W with thickness ranging from ~50 nm – 800 nm.

The root mean-square (rms) surface roughness of the films ranged from 0.58 nm to 1.70 nm as shown in Table 6.1 below

Table 6.1: The rms surface roughness of TaN films deposited at 150 W.

Thickness (nm)	Surface roughness (±0.05 nm)
50	0.58
100	0.86
150	0.91
300	1.23
450	1.30
600	1.70
700	1.59
800	1.66

In addition to surface roughness and morphology using AFM, cross-sectional morphology was established using SEM. The cross-sectional image of TaN sample deposited at 150 W is shown in Figure. 6.4. The SEM micrograph shows a compact columnar microstructure. As predicted by the structural zone model (SZM), the films grow under Zone I in which an under-dense structure with a fine fiber texture develops and the initial in-plain grain sizes are set by the saturation nucleation density [224]. In this zone, columns are composed of smaller more equiaxed grains or completely amorphous as opposed to single grain columns. A fractal geometry type of surface roughness develops which, due to limited diffusion, atomic shadowing, and wide angular distribution of the deposition flux, leads to extensive porosity [225].

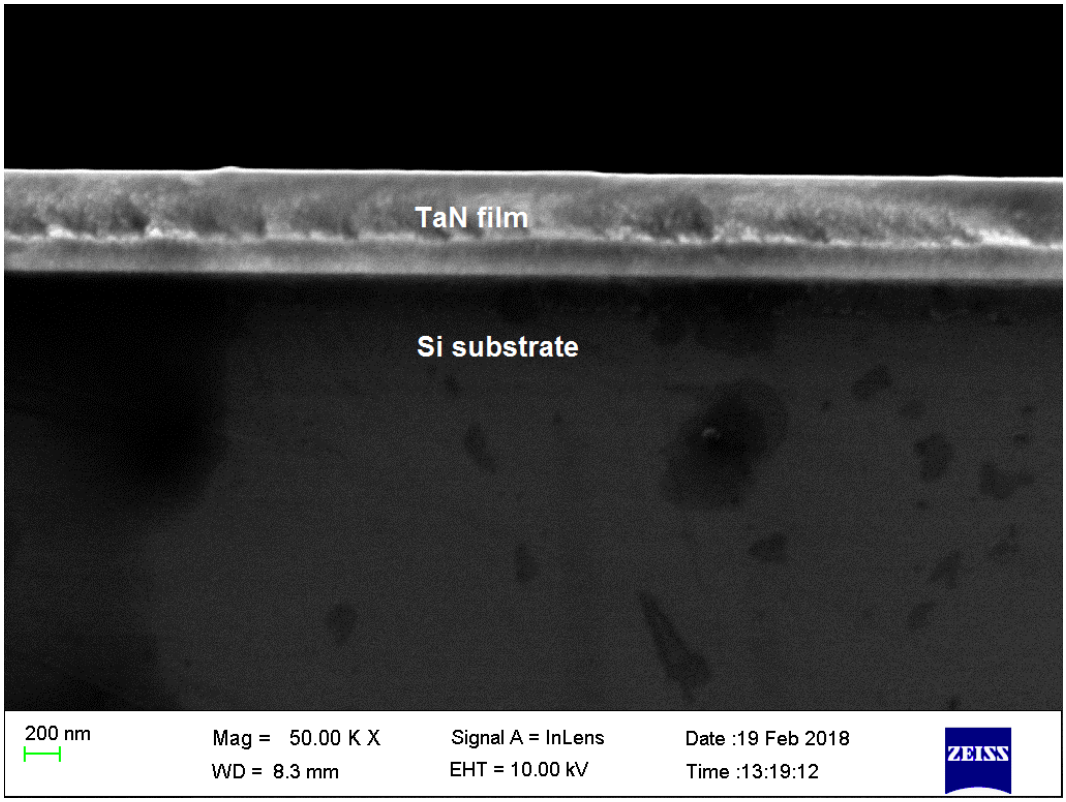

Figure 6.4: Cross-sectional field emission scanning electron microscope image of a 600 nm TaN film deposited at 150 W. The image depicts very fine grains in the film. It should be noted that the SEM image presents a continuous and homogeneous cross-section of the TaN film.

6.3.3 Crystalline structure by grazing incidence XRD

TaN exhibit many polymorphs in the crystalline phase, in this work Figure 6.5 illustrates the grazing incidence measurement of TaN thin film on Si. It is seen that the crystal structure of the TaN thin film obtained at a glancing angle of 1 degree corresponds to a cubic structure prevalent in nanocrystalline form with traces of tetragonal phases in the thin film. Formation of the tetragonal phase in reactive sputtered TaN thin films has been previously reported [57,226]. It has also been demonstrated in related studies that tantalum sputtered in pure argon on native oxide-forming substrates such as silicon wafers results in the formation of the metastable tetragonal phase [227]. The prominent NaCl like TaN has been

investigated by several authors for which the following Bragg reflexes were observed.

Table 6.2: TaN Bragg reflexes.

Miller indices	Diffraction Angle [°]
(111)	35.0
(200)	41.5
(220)	59.6

The broad peak at 41, 59, and 72° indicate the presence of a cubic symmetry with small randomly oriented grains. The presence of the cubic polycrystalline (face centred cubic (FCC) lattice) phase was thus used to simulate the elastic constant tensor for an isotropic system with no texture as confirmed by measurements of the sample in the Bragg-Brentano geometry.

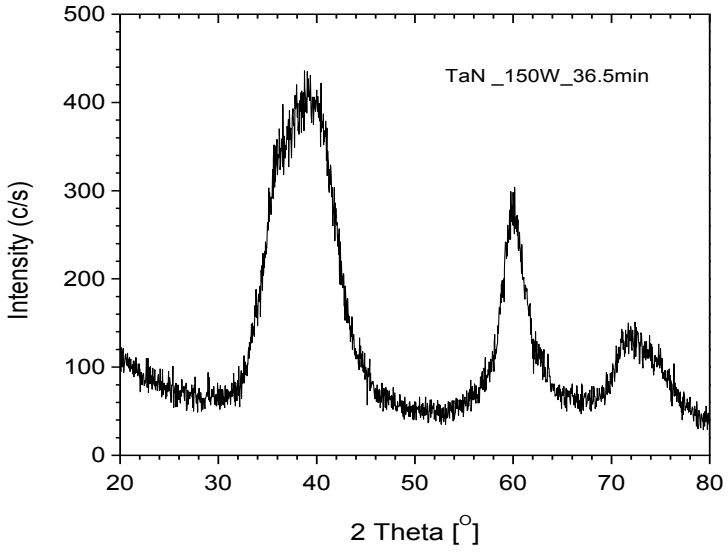

Figure 6.5: Glancing angle X-ray diffraction of TaN on (001) Si.

6.3.4 Composition determination by HI-ERDA and RBS

Heavy-ion elastic recoil detection analysis (HI-ERDA) was used to establish the surface composition of the films. HI-ERDA provides the areal density (number of atoms per unit area) as well as the atomic concentration of each constituent of the films. Figure. 6.6 shows the ERDA spectrum for TaN film deposited at 150 W as a function of the depth profile. From the profile, it was established that the films were oxygen-rich and non-stoichiometric with relative atomic fractions of 0.14 and 0.37 for Ta and N respectively.

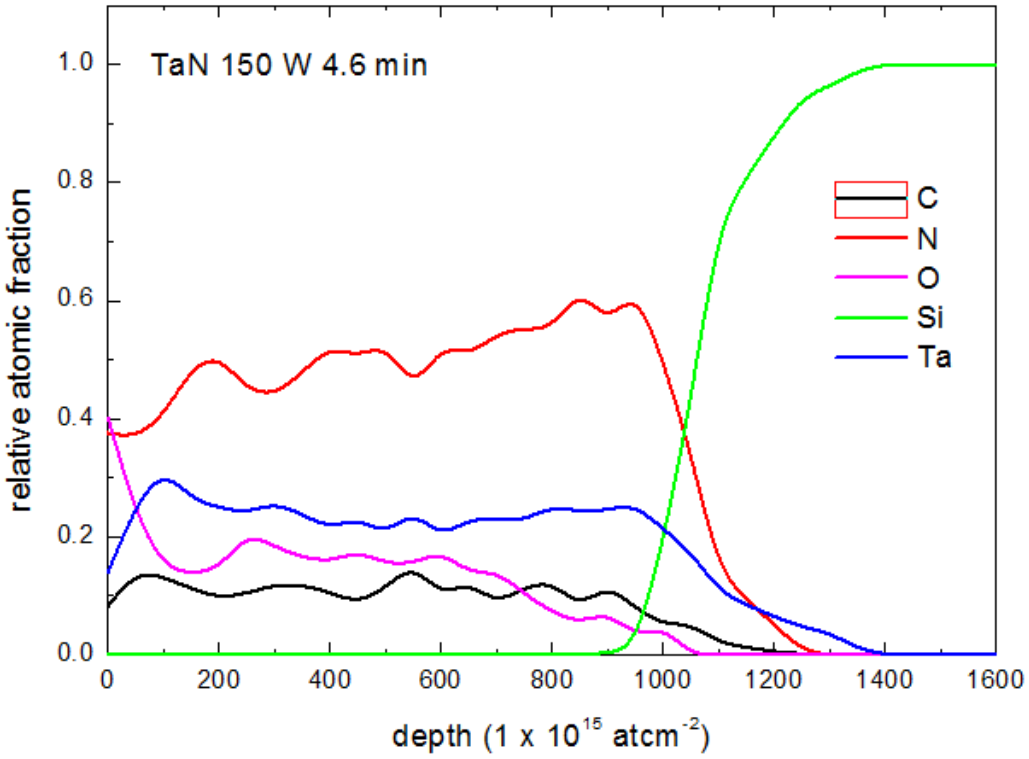

Figure 6.6: ERDA spectra of TaN deposited at 150 W showing the composition as a function of the depth profile.

6.4 Surface Brillouin scattering (SBS) in TaN thin films

6.4.1 TaN measured SBS spectra

Five TaN thin film samples deposited at 150 W and varying in thickness (~50 nm - 450 nm) were analysed for elastic constants using SBS. For scattering angle $\theta = 71°$, the corresponding $k_{||}d$ for the samples is shown in Table 5.5 (chapter 5). Brillouin spectra for the samples were collected for the [110] direction in the (100) surface at room temperature using the 514.5 nm line of an argon-ion laser operated in single axial mode and the power on the sample maintained at 70 mW. To illuminate each sample, the laser beam was focused onto the sample using a lens of f / 2.3 aperture in a back-scattering geometry. The scattered spectra were analysed using a Sandercock 3 + 3 pass tandem Fabry-Pérot interferometer. The spectra were accumulated in a multi-channel analyzer and the intensity measured using a low noise photo-detector. The detector, an SPCM-PQ, is based on a special quantum efficiency silicon avalanche photo-diode with a dark count of one per second.

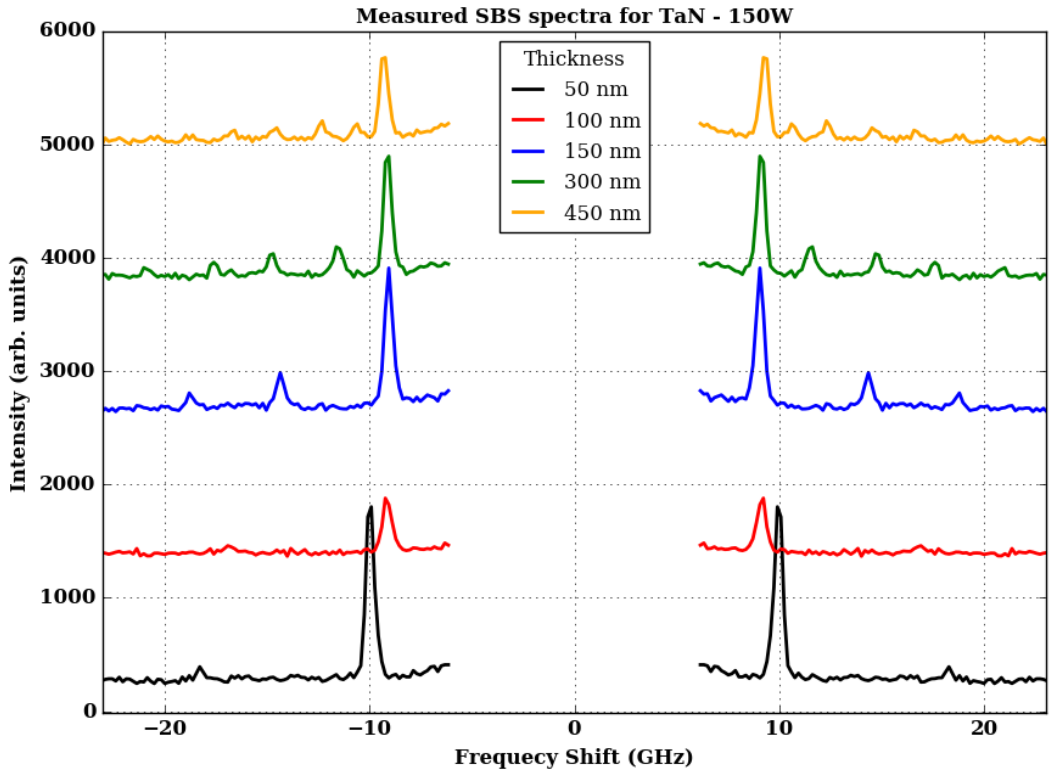

Figure 6.7: Measured SBS spectra for TaN films deposited at 150 W of varying thickness and $k_{||}d$.

In Figure. 6.7 five measured surface Brillouin spectra are shown for TaN films of thickness ranging from ~50 nm - 450 nm. The central elastic peak and the ghosts have been omitted in each spectrum for clarity. Inelastic scattering peaks corresponding to the Rayleigh doublet are present in all the spectra. However guided modes corresponding to the Sezawa wave propagate in films with thickness in the range 150 nm – 450 nm. The Sezawa modes for these films are shown to increase and grow closer with increase in thickness from 150 nm – 450 nm due to the increase in velocity.

6.4.2 SAW Velocity Dispersion and Elastic Stiffness

Theoretical and measured SAW phase velocities were determined from the surface Green's function approach and the measured spectra shown in section 6.4.1 above respectively. For crystalline silicon literature values: mass density $\rho = 2.332$ g/cm^3, $C_{11} = 165.7$, $C_{12} = 63.9$, and $C_{44} = 79.6$ GPa, respectively were used. Considering the polycrystalline TaN films as isotropic, two independent elastic constants C_{11} and C_{12} were used for fitting while C44 was obtained from the relation $(C_{11} - C_{12}) / 2$. It is noted that there are variations between the measured and simulated velocities owing to inhomogeneity in the films. The films have been grown separately at varying times as opposed to the single step growth process carried by Wittkowski *et al.* [76] in which the film inhomogeneities are reduced to a minimum.

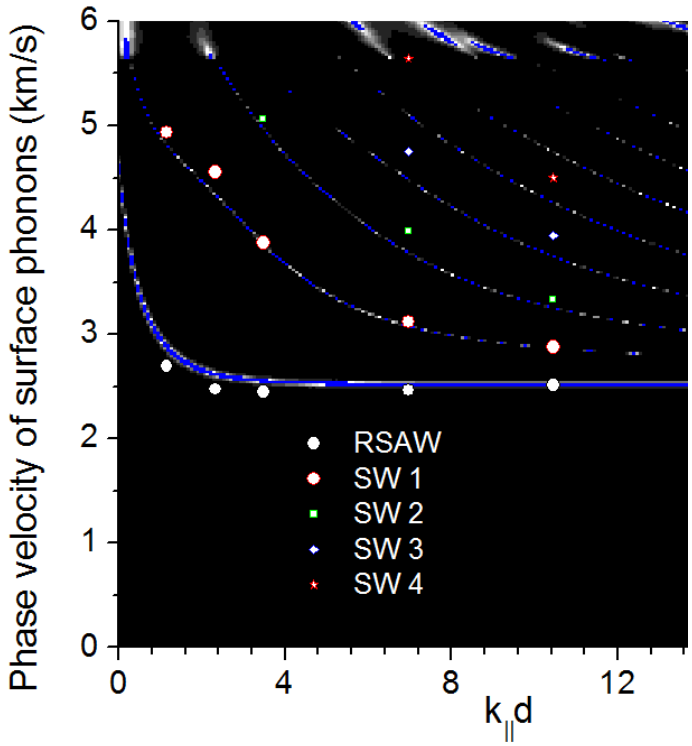

Figure 6.8: Surface Brillouin intensities compared to measured results for the TaN/Si system. Stiffnesses obtained from the best fit are $C_{11} = 288$ GPa, $C_{12} = 128$ GPa, and $C_{44} = 80$ GPa.

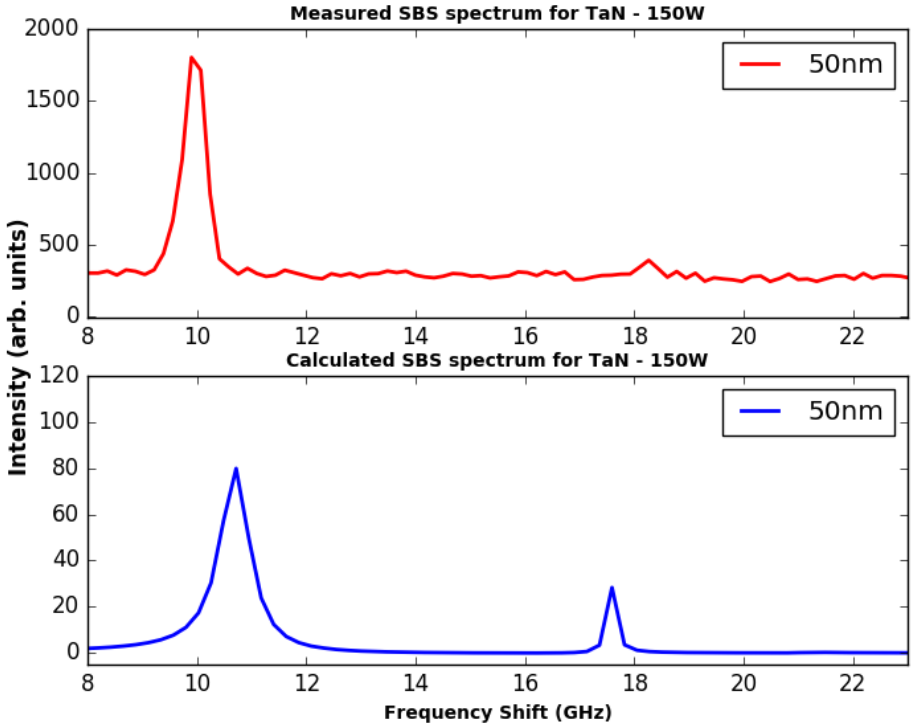

Figure 6.9: Calculated and measured SBS spectra for TaN of 50 nm thickness.

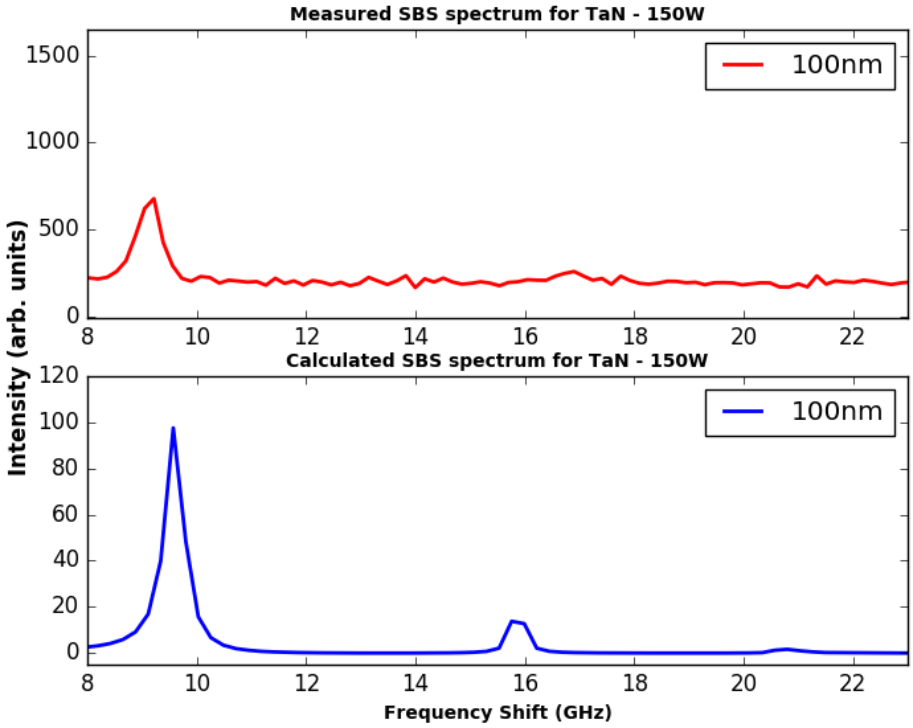

Figure 6.10: Calculated and measured SBS spectra for TaN of 100 nm thickness.

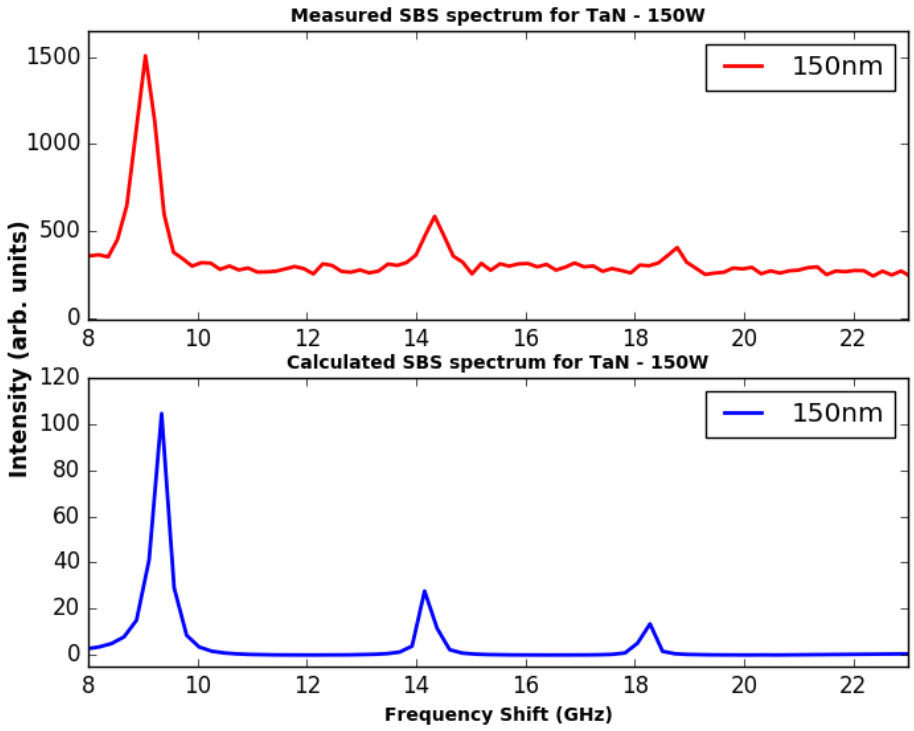

Figure 6.11: Calculated and measured spectra for a TaN film of 150 nm thickness.

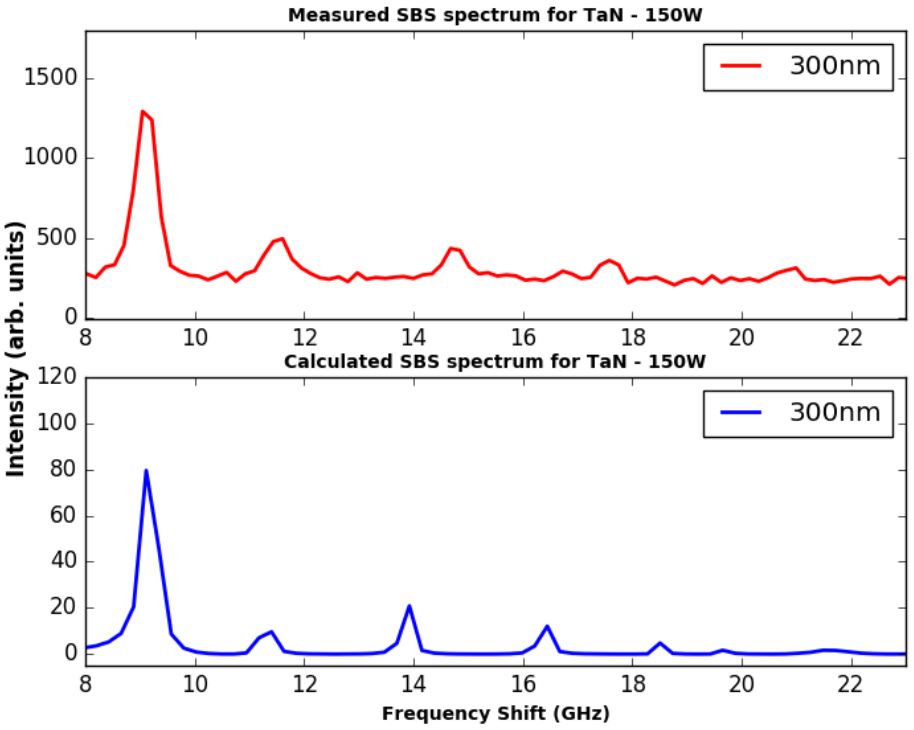

Figure 6.12: Calculated and measured spectra for a TaN film of 300 nm thickness.

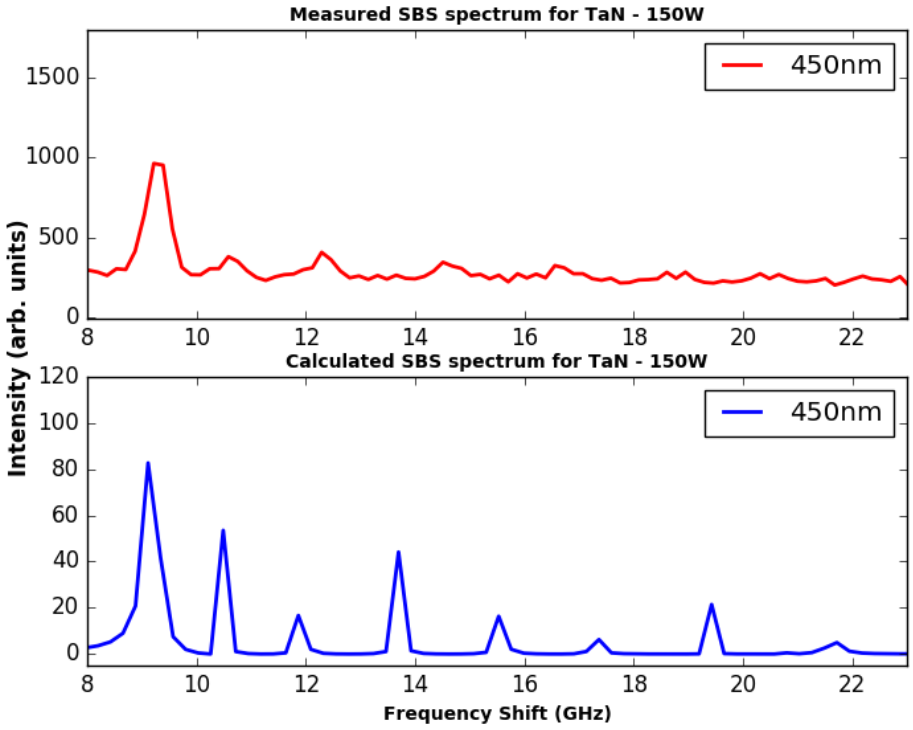

Figure 6.13: Calculated and measured spectra for a TaN film of 450nm thickness.

Using the best fit of the measured and the calculated spectra (Figure 6.8), the extracted elastic stiffnesses are $C_{11} = 288$ GPa, $C_{12} = 128$ GPa, and $C_{44} = 80$ GPa. Patil *et al*. [228] have reported elastic stiffnesses of $C_{11} = 322$GPa, $C_{12} = 224$ GPa, and $C_{44} = 60$ GPa from *ab initio* total energy calculations within the local density approximation theory (LDA) to density functional theory (DFT). Young's, bulk and shear modulus obtained from the values of the stiffnesses were $E = 250.2$ GPa, $B = 181.3$ GPa, and $G = 80$ GPa respectively. A calculated Poisson's ratio value of 0.27 was less than that of diamond (0.2). Using these figures and the mass density obtained from XRR, the Brillouin spectra were calculated and compared to the measured to assess the quality of the fit. As shown in Figure 6.9 through Figure 6.12, the measured and the calculated spectra are in good agreement.

6.5 Conclusions

High quality TaN thin films of thickness ranging from ~50nm – 800 nm were prepared on Si (100) substrates using rf magnetron sputtering at a sputter power of 150 W. The mass density obtained from XRR measurements was 11.04 g/cm^3. The root mean-square surface roughness values obtained from AFM measurements ranged between 0.58 nm and 1.70 nm. Columnar growth of the films was established from the SEM measurements. The elastic stiffnesses obtained from the best fit of the calculated and measured spectra were $C_{11} = 288$ GPa, $C_{12} = 128$ GPa, and $C_{44} = 80$ GPa. The values of the stiffnesses obtained from ab initio calculations were $C_{11} = 322$ GPa, $C_{12} = 224$ GPa, and $C_{44} = 60$ GPa. The differences in these values could be attributed to the fact the *ab initio* calculations do not take into consideration effect of deposition conditions on the elastic constants of the films.

Chapter 7

Optimisation of Elastic Constants for Isotropic NbN and TaN thin films

The elastic constants of the transition metal nitride thin films deposited on (001) Si have been derived from SBS measurements using the Green's function approach as discussed previously in this thesis. These form the starting values of the elastic constants of the transition metal nitrides to be used in the determination of the uncertainties based on the least squares fitting procedure. The elastic constants are presented in Table 1 for NbN and TaN thin films. The formalism for the determination of the elastic constant values and their uncertainties is based on the method due to Every *et al*. [229] which has been previously applied for anisotropic cubic material systems. In the present work this method is modified and applied in the optimisation of two independent elastic constants, namely C_{11} and C_{44} using the values of the Rayleigh surface acoustic and Sezawa wave velocities for various $k_{||}d$ values in the respective phonon velocity dispersion curves to minimise the χ^2 in the form;

$$\chi^2(C_{11},\, C_{44}) = \sum_{RSAW_j} \left(V_j^{meas.} - V_j^{calc.}\right)^2 + \sum_{SW_j} \left(V_j^{meas.} - V_j^{calc.}\right)^2 \tag{7.1}$$

Where $V_j^{meas.}$ and $V_j^{calc.}$ are the measured and calculated velocities corresponding to the $\left(k_{||}d\right)_j$ values, in some instances a weighting factor has been introduced to

limit the contribution of data points that are outliers in the phonon dispersion spectrum.

The uncertainties in the two independent elastic constants are determined from small deviations, (δC_j; $j = 11$ and 44). δC_{11} and δC_{44} are obtained from their optimum fits in the expression;

$$\frac{(\chi^2 - \chi_0^2)^2}{\chi_0^2} = \frac{1}{2}\left(V_{jk}\right)^{-1}\delta C_j \tag{7.2}$$

where $V_{jk} = \chi_0^2\left(\frac{\partial^2\chi^2}{\partial C_j \partial C_k}\right)^{-1}$ is the variance covariance matrix which produces ellipses in contour plots such that $\left(V_{jk}\right)^{-1}\partial C_j = 1$, the errors in the elastic constants are obtained from the extrema values (variances) of the contour plots in C_{11} and C_{44} directions as adopted in [229]. The off-diagonal elements adjust the directions of the principle axes to identify the linear combination of the most accurate values of the elastic constants [229]. The adopted procedure is based on the separate variation of C_{11} and C_{44} to establish the coefficients of the Taylor series in the linear combination of the velocity values of the RSAW and SW waves in the phonon dispersion curves. The linearised expression of the phonon velocity defined by the expression [229,230],

$$V_j(C_{11}, C_{44}) = V_j^0 + \frac{\partial V_j^0}{\partial C_{11}}(C_{11} - C_{11}^0) + \frac{\partial V_j^0}{\partial C_{44}}(C_{44} - C_{44}^0) \tag{7.3}$$

was used in the least squares fitting. The coefficients $\frac{\partial V_j^0}{\partial c_j}$ are the calculated derivatives corresponding to each data point in the velocity dispersion curve.

Following the linearisation procedure using *Mathematica*, the surface chi square values have determined by minimisation of the total χ^2 function obtained as a sum of the corresponding χ^2 values representing the linearised velocity expressions for the RSAW and SW waves for each $k_{||}d$ data, (see equation 7.3).

7.1 Elastic constants of NbN thin films deposited at various sputter powers

The determination of the optimum elastic constants and uncertainty for the isotropic NbN thin films deposited at sputter powers; 75W, 100W, 150W, 200W and 250W has been carried out using the data previously determined in chapter 5 based on the least squares fitting and the Green's function approach. These data were used as the initial values for the optimisation as shown in Table 7.1 below.

Table 7.1: Initial elastic constants values of the transition metal nitride thin films on (001) Si obtained from Green's function.

NbN thin films on (001) Si		
Sputter Power (W)	**C_{11} (GPa)**	**C_{44} (GPa)**
75	383.6	107.5
100	386.3	107.2
150	520.5	99.9
200	394.9	102.3
250	371.5	105.3
TaN thin films on (001) Si		
150	288.0	80.0

Figures 7.1 (a) - (e) represents the contour plots denoting the ellipses that yield the uncertainty of the C_{11} and C_{44} in the NbN thin films. The contour plots represent the sets of C_{11} and C_{44} values that yield χ^2 surfaces for which the colour code represents the corresponding extrema or limit of the χ^2 values. For the NbN thin films deposited at 75 W the covariance ellipse given in Figure 7.1 (a) yielded the χ^2 minimum for the optimum elastic constants and their uncertainties as;

$$C_{11} = 381.5 \pm 11.9 \quad \text{GPa}$$

$$C_{44} = 107.0 \pm 1.9 \quad \text{GPa}$$

From the optimisation procedure, it is evident that C_{11} values are the least accurate at 3.1 % while C_{44} values have a much higher accuracy at 1.8%. The corresponding contour plots for the elastic constants of NbN thin films deposited at 100W, 150W, 200W and 250W are presented below (Figure 7.1 (a) - (e)) as show with their corresponding elastic constants summarised in Table 7.2.

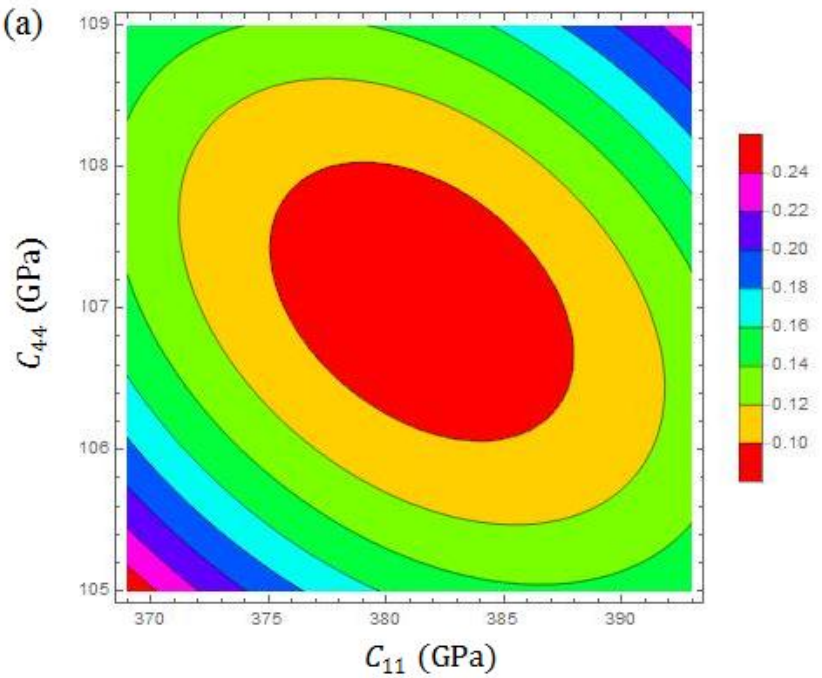

(b)

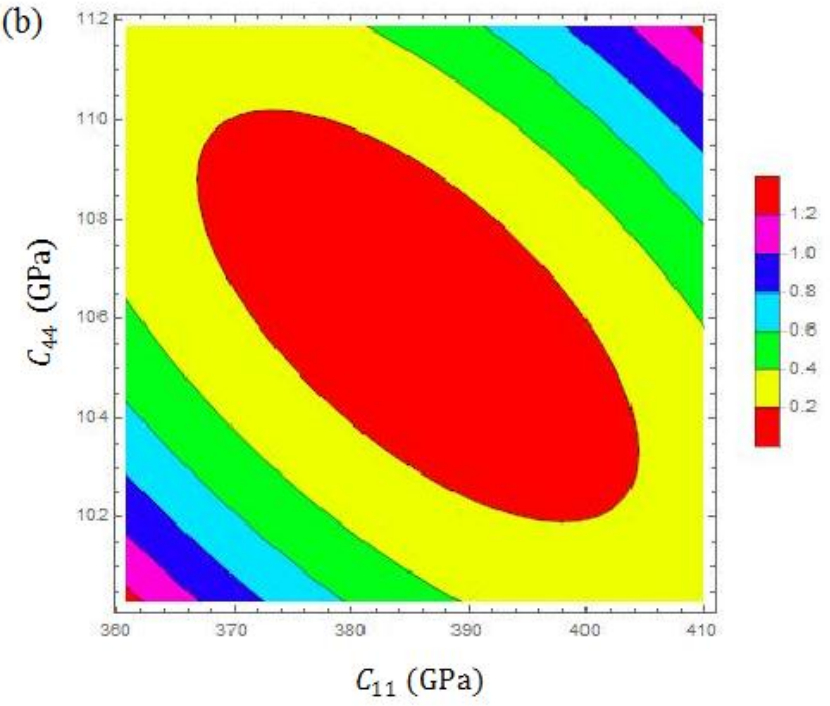
112
110
108
106
104
102
C_{44} (GPa)
360
370
380
390
400
410
C_{11} (GPa)
1.2
1.0
0.8
0.6
0.4
0.2

(c)

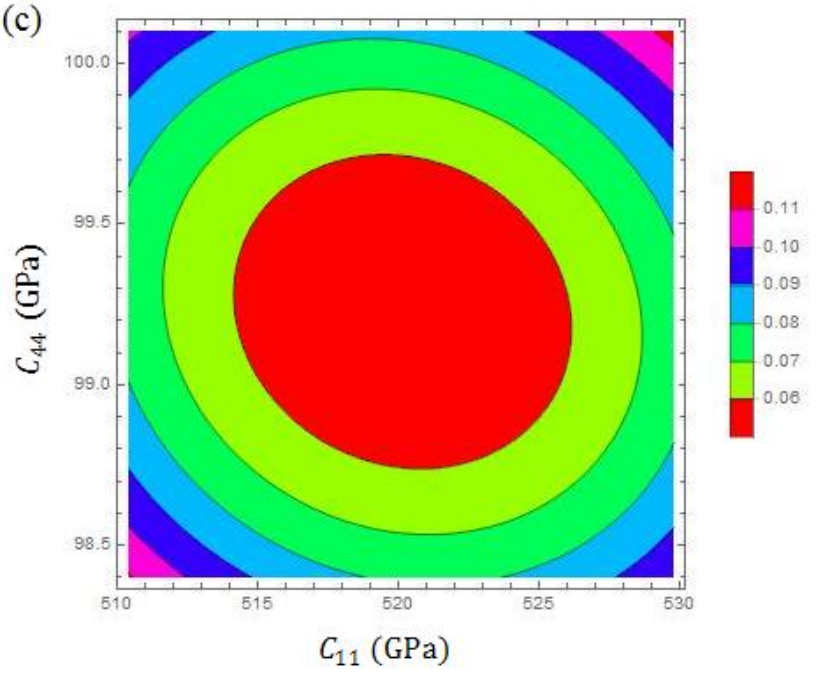
100.0
99.5
99.0
98.5
C_{44} (GPa)
510
515
520
525
530
C_{11} (GPa)
0.11
0.10
0.09
0.08
0.07
0.06

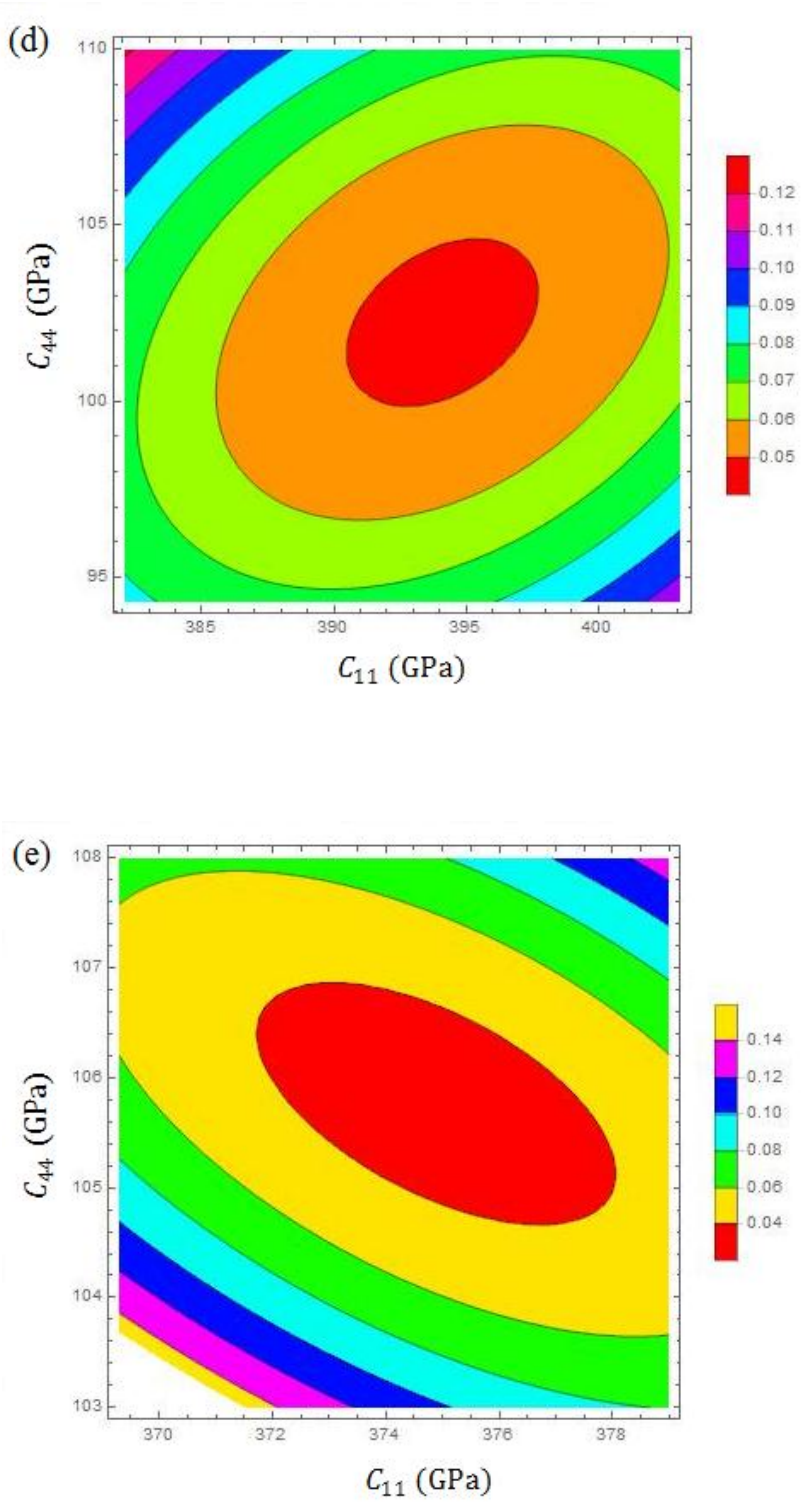

Figure 7.1: Contour plots of the minimised χ^2 values to establish the optimum elastic constants of NbN thin films deposited on (001) Si at (a) 75 W, (b) 100 W, (c) 150 W, (d) 200W, and (e) 250 W. The colour scheme corresponds to the χ^2 values for the sets of C_{11} and C_{44} values.

The optimised elastic constant values were subsequently used to generate the corresponding surface Brillouin scattering spectra based on the elastodynamic Green's function method. A presentation of selected spectra comparing the experimental and the simulated curves is presented, and it is evident that the new set of elastic constants match their corresponding measured values satisfactorily, See Figure 7.2 (a) – (e) for the NbN thin films.

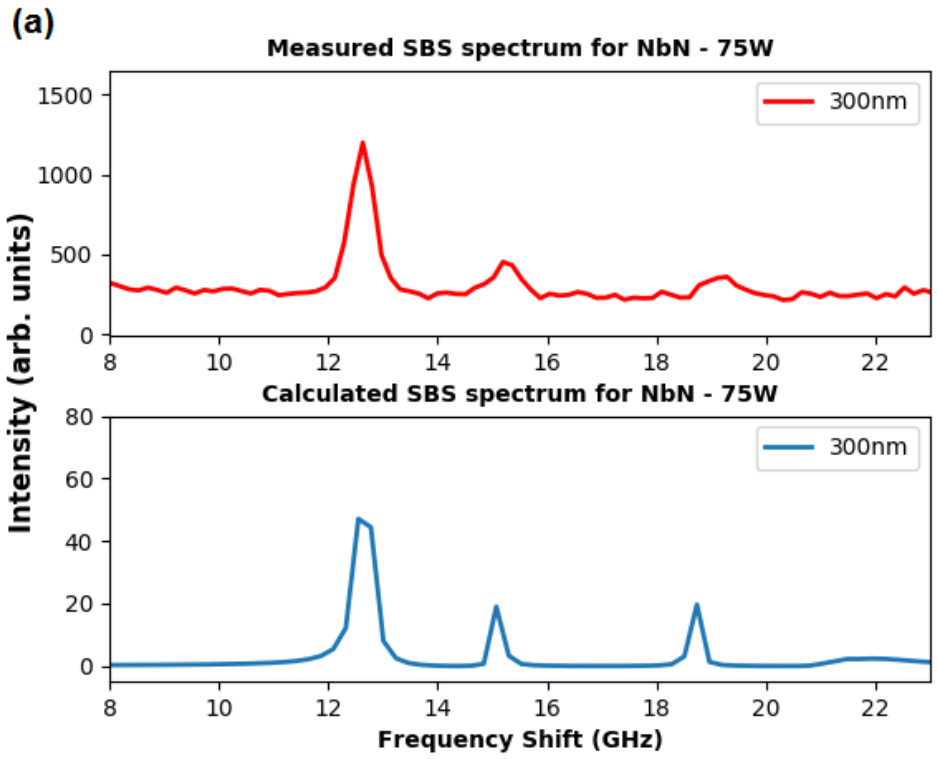

(b)

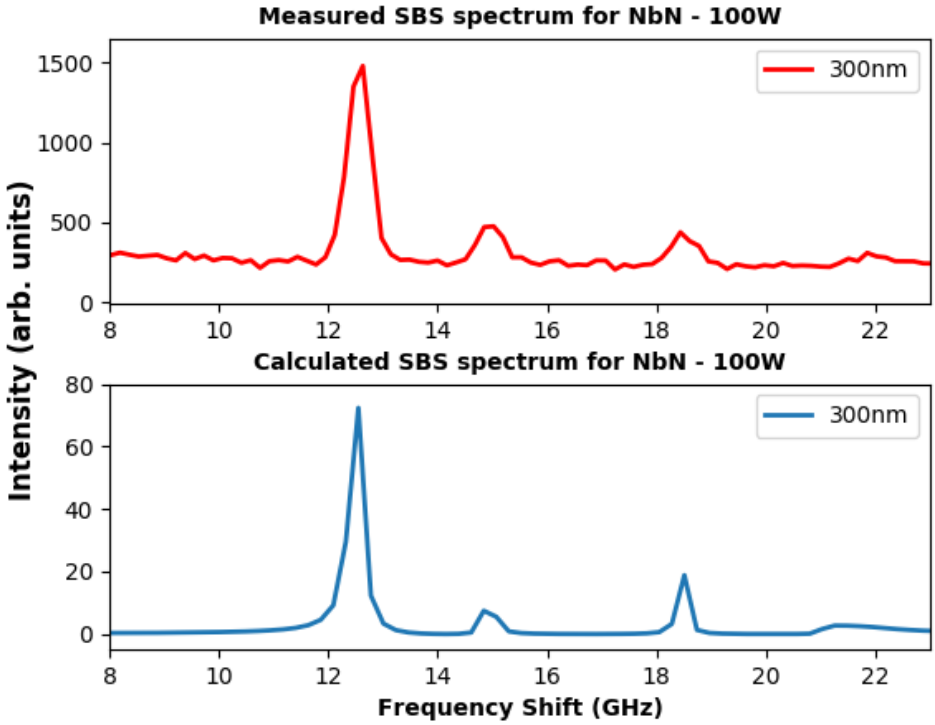
Measured SBS spectrum for NbN - 100W
300nm
1500
1000
500
0
8
10
12
14
16
18
20
22
Calculated SBS spectrum for NbN - 100W
300nm
80
60
40
20
0
Intensity (arb. units)
Frequency Shift (GHz)

(c)

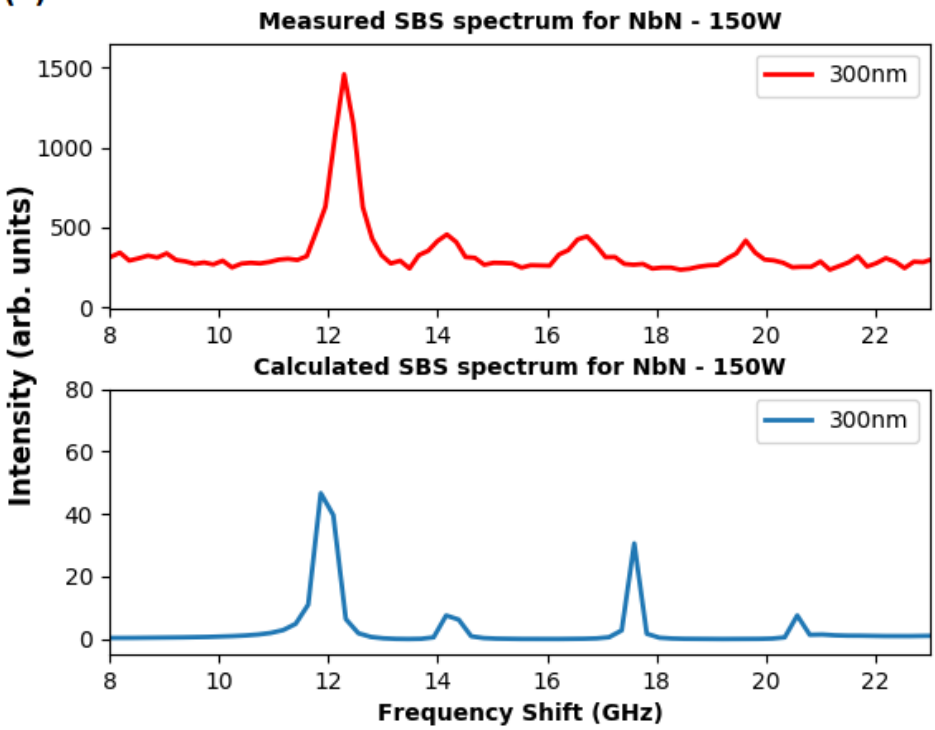
Measured SBS spectrum for NbN - 150W
300nm
1500
1000
500
0
8
10
12
14
16
18
20
22
Calculated SBS spectrum for NbN - 150W
300nm
80
60
40
20
0
Intensity (arb. units)
Frequency Shift (GHz)

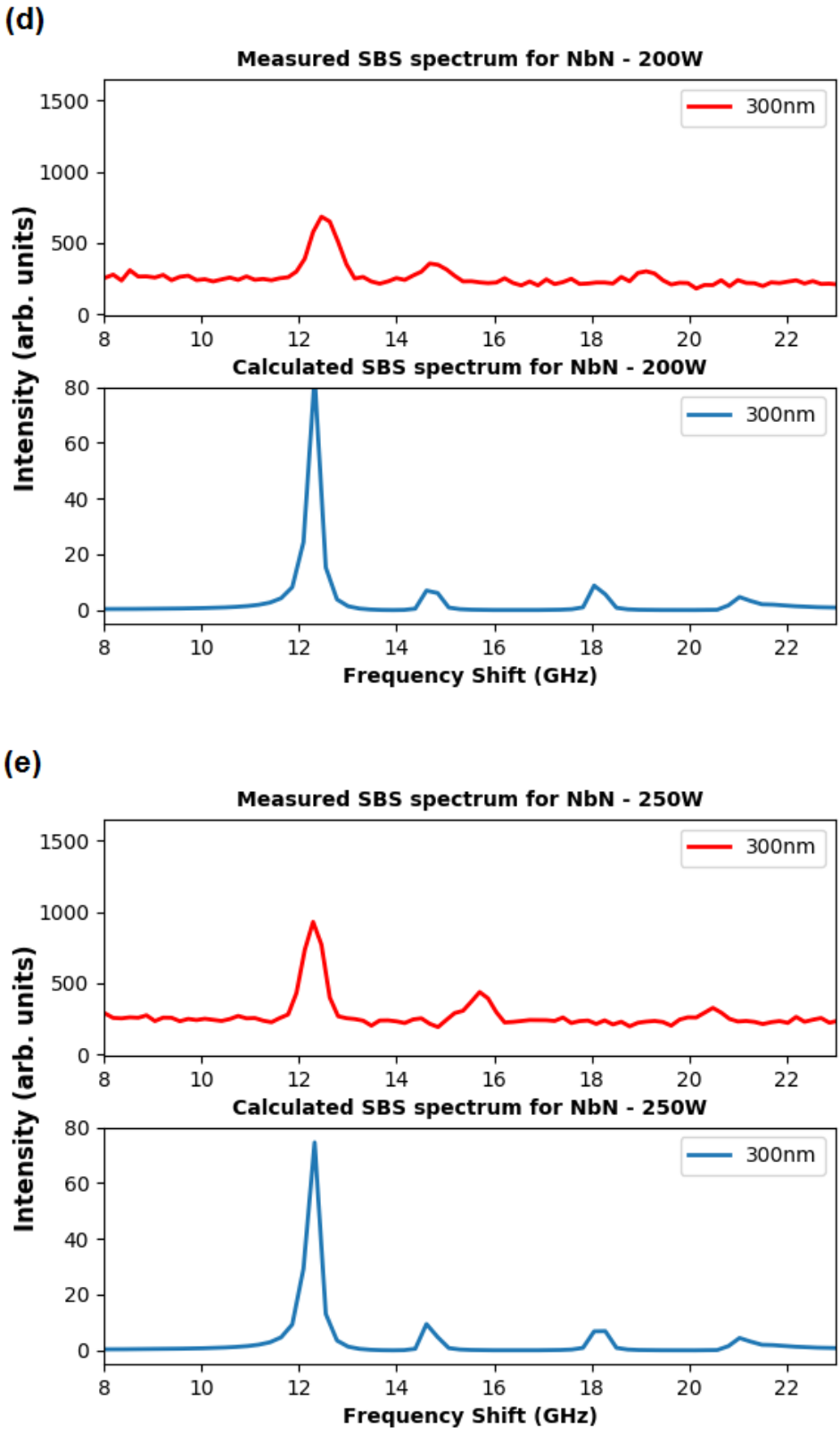

Figure 7.2: Measured and optimised calculated anti-Stokes SBS spectra for 300 nm NbN/Si films deposited at (a) 75 W, (b) 100 W, (c) 150 W, (d) 200 W, and (e) 250 W.

It is noted that the deviations in some of the films is attributed to variations in the microstructure of the films since the film deposition method is not a single step process.

7.2 Optimisation and analysis of the elastic constants of TaN thin films

A similar procedure was carried out for the initial values of the elastic constants determined for TaN thin films. The minimisation of the total χ^2 using the C_{11} and C_{44} and the velocity values of the RSAW and SW waves in the subsonic region of the velocity dispersion curve has yielded the contour plots (ellipses). These provided the optimal values of the combination of the elastic constants that produced a χ^2 minimum of 0.046 have been determined to be $C_{11} = 209.9 \pm 3.7$ GPa and $C_{44} = 81.5 \pm 2.5$ GPa, respectively. The uncertainties in these values are 1.3 % and 3.1% respectively. Using the new set of optimised elastic constants for a 300 nm thick TaN film a corresponding plot of the measured and calculated spectra is obtained (See Figure 7.4)

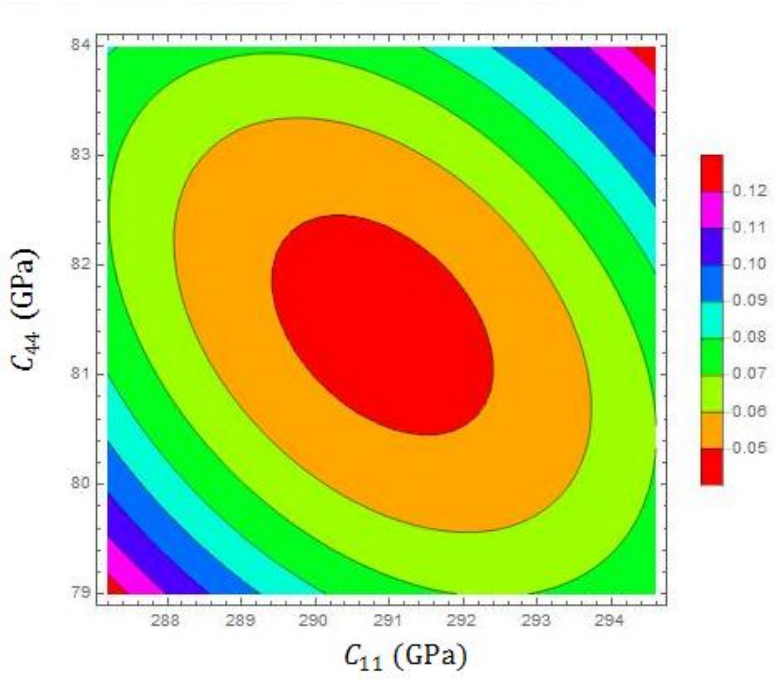

Figure 7.3: Optimised elastic constant values of isotropic TaN thin film, the color scheme represents the upper limits of χ^2 values.

Table 7.2: Summary of the optimised elastic constants of transition metal nitride thin films.

NbN thin films on (001) Si		
Sputter Power (W)	**C_{11} (GPa)**	**C_{44} (GPa)**
75	381.5 ± 11.9	107.0 ± 1.9
100	385.6 ± 12.4	107.2 ± 2.9
150	520.1 ± 9.70	99.2 ± 0.9
200	394.1 ± 12.0	102.2 ± 7.9
250	374.5 ± 5.0	105.8 ± 2.9
TaN thin films on (001) Si		
150	290.9 ± 3.7	81.5 ± 2.5

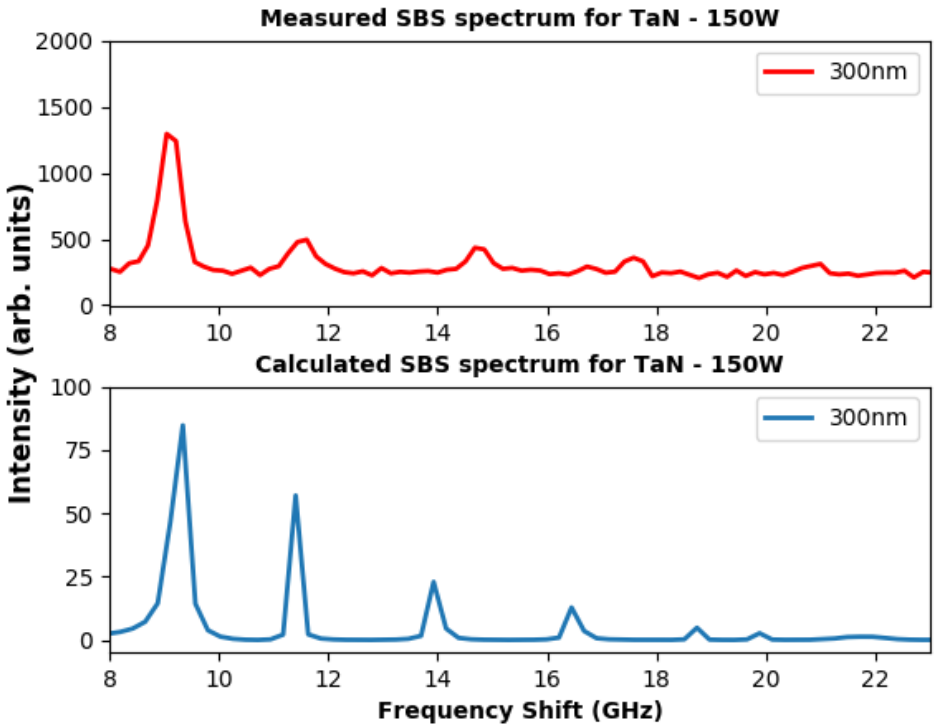

Figure 7.4: Measured and optimised calculated SBS spectra of a 300 nm TaN film on (001) Si.

7.3 Conclusions

Elastic constants of NbN and TaN thin films obtained from the Green's function approach have been optimised using a least squares fitting procedure. Uncertainties of between 1.3 % and 3.1 % for C_{11} and 0.9 % and 7.7% for C_{44} have been determined for NbN while 1.3% and 3.1% have been obtained for C_{11} and C_{44} respectively for the TaN films. A good agreement of the measured and calculated spectra from the optimised elastic constants has been achieved.

Chapter 8

Elastic Properties of Zirconium Nitride Thin films

In this chapter, a discussion of the characterisation of zirconium nitride (ZrN) thin films using various techniques as well as their elastic properties is presented. A background of the various applications of ZrN, fabrication methods and physical and elastic properties is presented in section 8.1. The fabrication and characterisation of ZrN thin films using various techniques is discussed in section 8.2. Section 8.3 gives the description of the analysis of the characterisation results. In section 8.4, a description of the extraction of elastic constants using a combination of picosecond acoustics and surface Brillouin scattering (SBS) is presented. Lastly, a conclusion of the chapter is given in section 8.5

8.1 Introduction

Recent developments in the microelectronic industry have seen the emergence of newer type of devices such as dynamic random-access memory (DRAM), switching devices, sensors among others. As such, recent studies have been devoted towards the fabrication of various materials with properties that allow for such applications. Among these, ZrN thin films have been studied extensively due to their interesting properties such as higher mechanical properties, better corrosion resistance, lower resistivity, lower work function and special optical properties [44]. Consequently, ZrN thin films have been used successfully as

hard-coatings, electrical contacts, optical application for heat mirrors, and decorative coatings.

Zirconium nitride thin films have been prepared using various techniques such as: magnetron sputtering, ion beam assisted deposition (IBAD), reactive ion beam sputtering, vacuum arc deposition, pulsed laser deposition, and chemical vapor deposition (CVD) [40]. The various deposition techniques qualitatively affect the composition, morphology and structure of the films [231].

Several authors have reported studies on the properties of ZrN thin films. Of these, there has been a focus on the optical and electrical properties of ZrN [31,38,43,232,233]. Pilloud *et al*. [234] studied the electrical, optical, structural and mechanical properties of zirconium nitride films deposited on steel and silicon substrates by magnetron sputtering of a zirconium target in reactive Ar-N_2 mixture. It was observed that unbiased films grew with a preferred orientation in the [200] direction whereas biased films exhibited a [111] preferred orientation. Cross-sectional SEM studies revealed columnar growth. Nano-indentation measurements were carried out with a load of 40 mN. A hardness of ~21.8 GPa was reported for the unbiased films. The hardness increased with increase in bias voltage (V_b) for values of up to $V_b = -100$ V where a maximum hardness value of ~39.5 GPa was reached. The hardness decreased for bias voltage values greater than -120 V to a constant value of ~33 GPa. This was attributed to an increase in films' density by an elimination of voids for low values of negative bias while higher values induced a re-sputtering phenomenon which is detrimental to the mechanical properties. In another study, Larijani *et al*. [33] deposited ZrN thin films on stainless steel 304 substrates to investigate the effect of varying N_2/Ar ratio and substrate temperature on their structural and mechanical properties. The

intensity of the (111) peak which was the preferred orientation increased for a wide range $F(N_2)(10-54\%)$ and decreased thereafter for $F(N_2)$ more than 54%. The amorphous structure was formed at $F(N_2)$ of 95%. The authors attributed this to either the absence of stable phases in the rich nitrogen zone of the ZrN system or probably due to the decrease of energy of the sputtered particles. With increasing temperature up to 400 °C, the (111) peak intensity increased with the films textured in [111] direction. A random orientation was observed for temperatures above 400 °C. It was suggested that 400 °C was the optimum temperature for atomic or molecular displacement that led to the formation of a strong configuration following the [111] direction. It was observed that the film composition remained constant from 200 - 500 °C thus the effect of film composition on the film hardness could be neglected. At the same time, an increase of micro-hardness was observed for temperature range 200 - 400 °C and a decrease from 400 - 550 °C. This could be explained using the shear-stress on the slip system which follows the (111) texture coefficient [33].

8.2 Sample preparation and characterisation

8.2.1 Thin film growth

Samples of ZrN thin films were fabricated using rf magnetron sputtering of a 99.9% pure, 76 mm diameter × 6 mm thick ZrN target (Semiconductor Wafer) at a fixed substrate-target distance of 6 cm in ambient Ar. The films were deposited on 1.5 × 1.5 cm^2 (100) Si substrates at a sputter power of 200 W. The substrates were cleaned with successive rinses in ultrasonic baths of acetone and ethanol prior to the deposition. The chamber was evacuated to a base pressure of 2.4 × 10^-

^{5} mbar prior to the deposition. To remove impurities or adsorbents from the targets surface, the ZrN target was pre-sputtered at a sputter power of 100 W for 15 minutes. Samples for X-ray reflectivity (XRR) were deposited on (100) Si substrates at a sputter power of 200 W for 3 minutes. The deposition rate extracted from the XRR measurements was used to control the film thickness of the SBS samples. At total of eight samples of thickness ranging from ~50 - 800 nm was deposited at varying times for investigation of the elastic properties of the ZrN thin films.

8.2.2 Microstructure and composition of ZrN thin films

The film thickness and mass density are important input parameters in the determination of the elastic constants of ZrN films. X-ray reflectivity (XRR), a non-destructive technique has been used to measure the film mass density and thickness as well as surface and interface roughness.

In the present work, XRR measurements on ZrN thin films were performed using a D8 Discover high resolution X-ray diffractometer (Bruker AXS GmbH). In order to generate the simulated spectra corresponding to the measured spectra, a layer stack of $Si/SiO_2/ZrN$ was used. Atomic force microscopy (AFM) measurements were carried out on a Veeco Dimension 3100 operating in tapping mode at scan rate of 1.51 Hz and a scan size of 1 μm^2. Gwyddion [181], an open source software for analysing and visualising scanning probe microscopy data was used to analyse and visualise the AFM data. A Jeol JSM-7001F high-resolution scanning electron microscope (SEM) was used to examine the cross-sectional structure of the films. Grazing incidence X-ray diffraction (GIXRD) performed on D8 Discover X-ray diffractometer (Bruker

AXS GmbH) was used to the establish the phase structure of the ZrN thin films. The measurements were performed at 0.7° incidence angle in the 2Theta geometry ranging between $20° < 2\theta < 80°$. Heavy-ion elastic recoil detection analysis (Hi-ERDA) was used to establish the stoichiometry of the thin films.

8.3 Results and discussion

8.3.1 XRR analysis

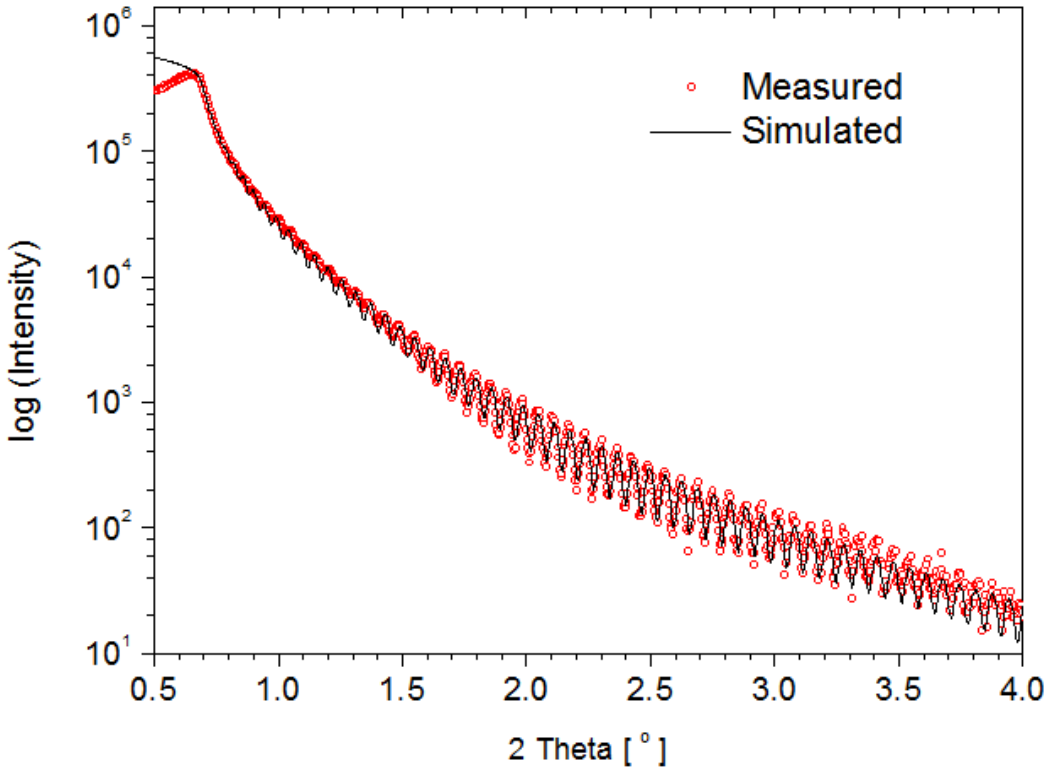

Figure 8.1: XRR measured and simulated spectra for ZrN thin film deposited at 200 W for 4 minutes. A layer stack of ZrN/SiO_2/Si was used for fitting.

Figure 8.1 shows the XRR spectrum for a 100 nm ZrN thin film deposited at 200 W for 3 minutes. The mass density obtained from the XRR measurements was 6.49 ± 0.05 g/cm^3 which corresponds to 91.5% of the bulk value of 7.09 g/cm^3. A deposition rate of 25 nm/min was calculated from a film thickness of 100 nm

deposited for 4 minutes. The deposition rate obtained was used to control the thickness of SBS samples in the range of ~50 - 800 nm.

8.3.2 Morphology and microstructure of ZrN films

The surface roughness and morphology of the ZrN films was analysed using AFM. Figure 8.2 shows the surface morphologies of the films of varying thickness deposited at 200 W. The films are smooth and homogeneous with surfaces comprising a fractal auto-affine symmetry and a "cauliflower morphology" in which larger grains are formed by the coalescence of the smaller grains [223]. The root mean-square (rms) surface roughness of the films generally increased with increasing thickness as shown in Table 8.1.

Table 8.1: Root mean-square surface roughness of ZrN films deposited at 200 W.

Thickness (nm)	**Surface roughness (±0.05 nm)**
50	0.55
100	0.75
150	0.97
300	1.19
450	1.45
600	1.62
700	1.56
800	1.31

SEM was used to establish the cross-sectional morphology of the films. Figure 8.3 shows the cross-sectional image of ZrN film deposited at 200 W. In the figure, a compact columnar microstructure is shown. This corroborates the structure zone model (SZM) prediction in which films grown under Zone 1 develop an under-dense structure with a fine fiber texture and the saturation nucleation density set the initial in-plain grain sizes [224]. This zone is

characterised by columns comprising smaller more equiaxed grains or entirely amorphous as opposed single grain columns.

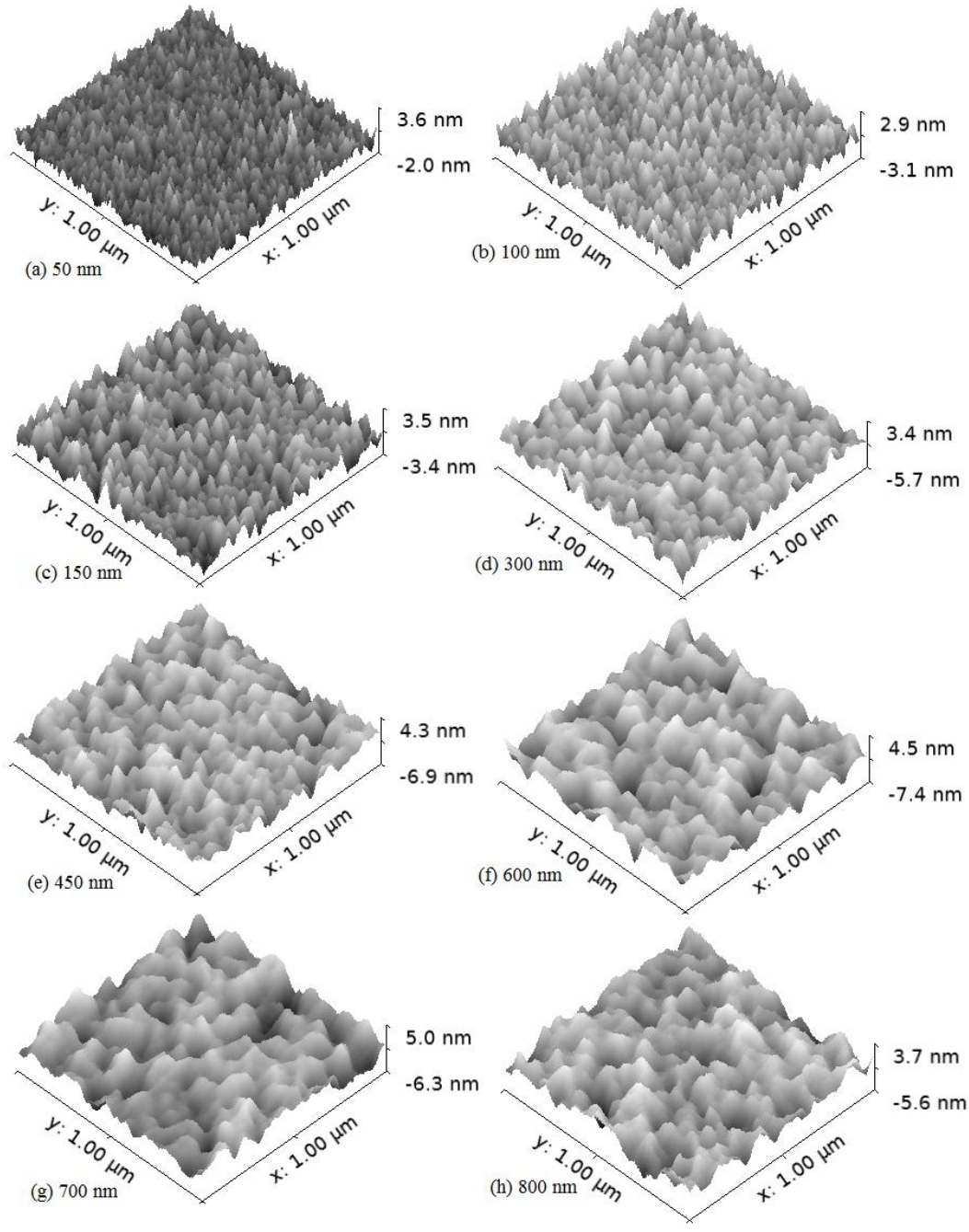

Figure 8.2: Surface morphology of ZrN films deposited at 200 W with increasing thickness ranging from ~50 nm – 800 nm. The AFM images show larger grains formed with increasing thickness.

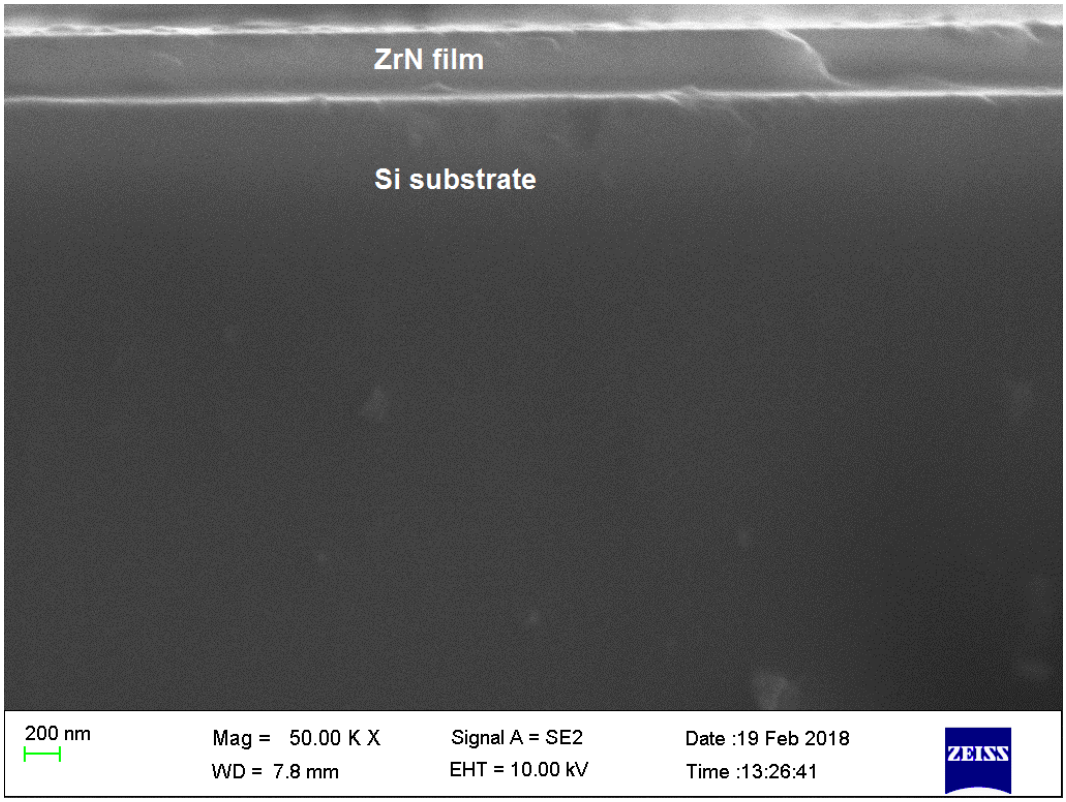

Figure 8.3: The cross-sectional SEM image of a 600 nm thick ZrN coating.

8.3.3 Grazing incidence XRD analysis

Figure 8.4 shows the grazing incidence diffraction patterns for ZrN thin films of varying thickness deposited at 200 W. As shown in the figure, all the ZrN films have similar diffraction peaks consistent with the rock salt (NaCl) polycrystalline structure which has a face centred cubic (FCC) lattice.

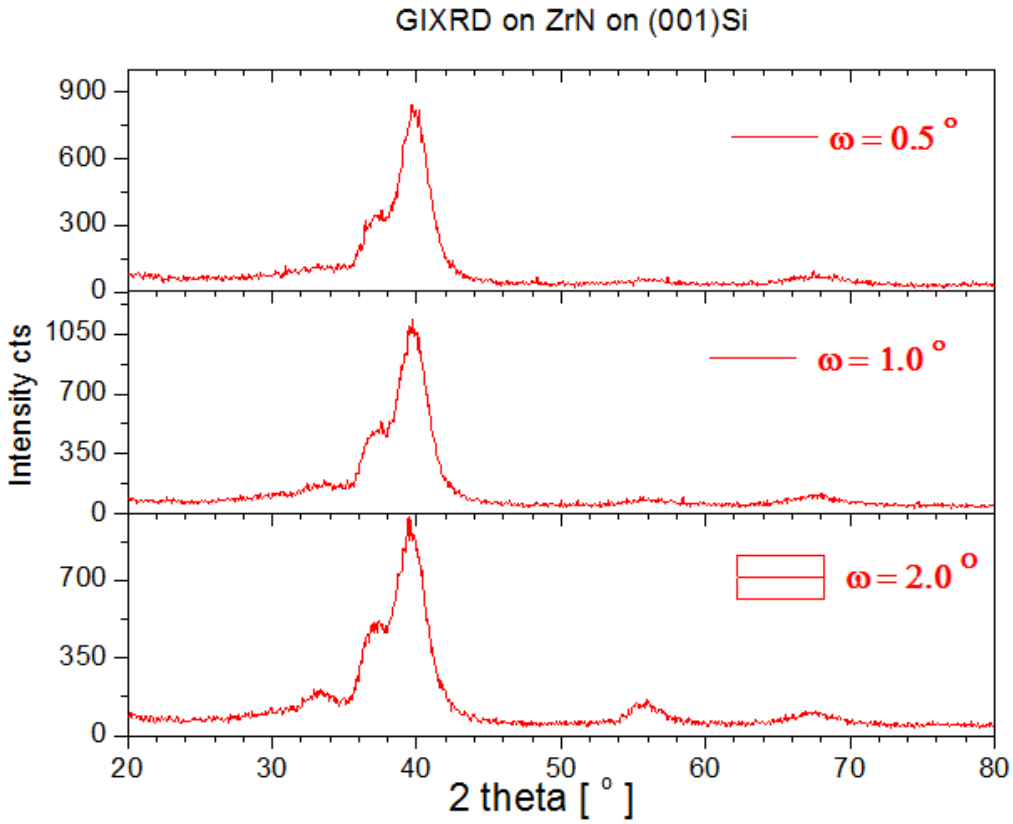

Figure 8.4: Glancing angle X-ray diffraction of ZrN on (001) Si.

8.3.4 Chemical composition using HI-ERDA

Heavy-ion elastic recoil detection analysis (HI-ERDA) was used to determine the chemical composition of the ZrN thin films. Figure 8.5 shows the ERDA spectra for ZrN thin film deposited at a sputter power of 200 W. The spectra correspond to the relative atomic fraction of each constituent element in the film. It can be seen in the figure that the films were non-stoichiometric and contained some oxygen. The relative atomic fractions were 0.28 and 0.49 for Zr and N respectively.

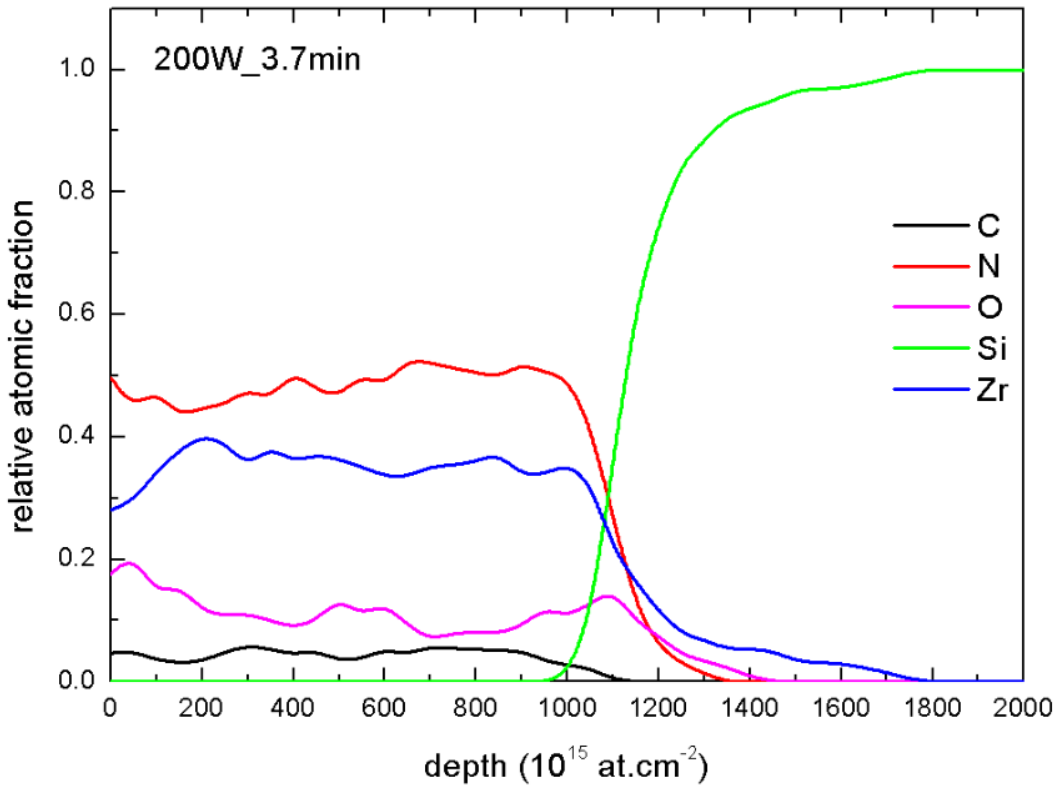

Figure 8.5: ERDA spectra of ZrN deposited at 200 W showing the relative atomic fraction as a function of depth profile.

8.4 Surface Brillouin scattering (SBS) in ZrN thin films

8.4.1 ZrN Measured SBS spectra

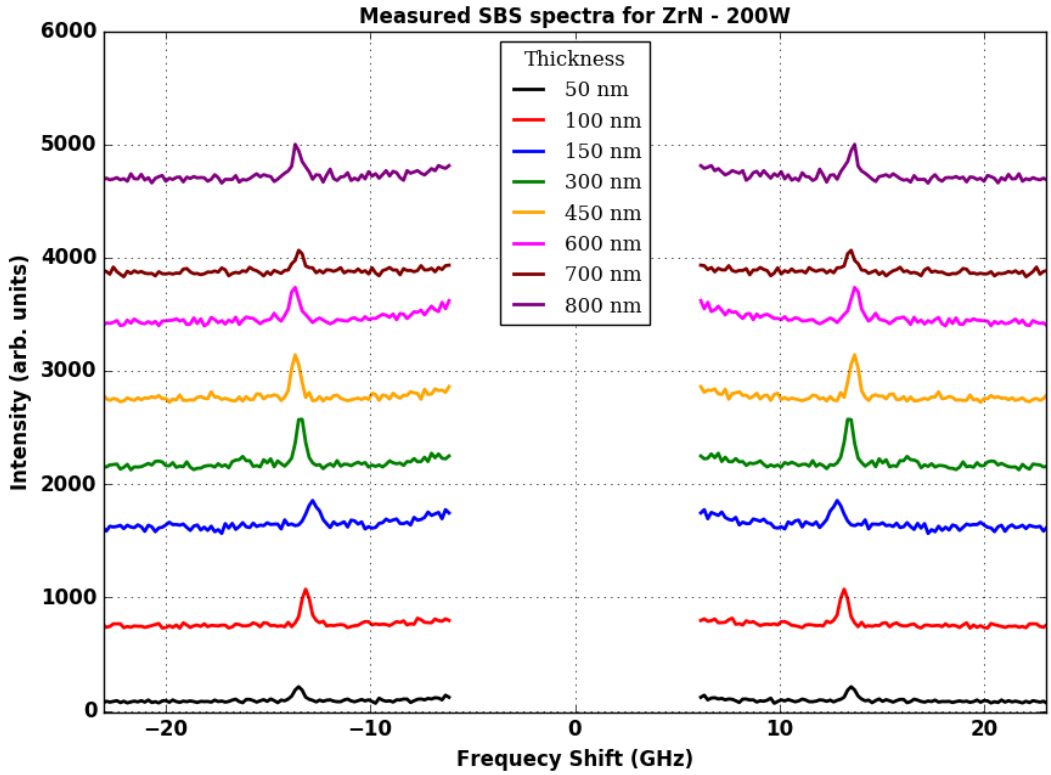

Figure 8.6: Measured SBS spectra for ZrN thin films deposited at 200 W and varying thickness and $k_{||}d$.

SBS spectra for eight samples of ZrN thin films were gathered for the [110] direction in the (100) surface at room temperature using the 514.5 nm line from an Ar^{+} laser operating in a single axial mode. For all the samples, the scattering angle $\theta = 71°$ and the power reaching the sample was 70 mW. Figure 8.6 shows the measured SBS spectra for ZrN thin films of varying thickness while the velocity dispersion curve is presented in Figure 8.7. The central elastic peak and the ghosts have been omitted for clarity.

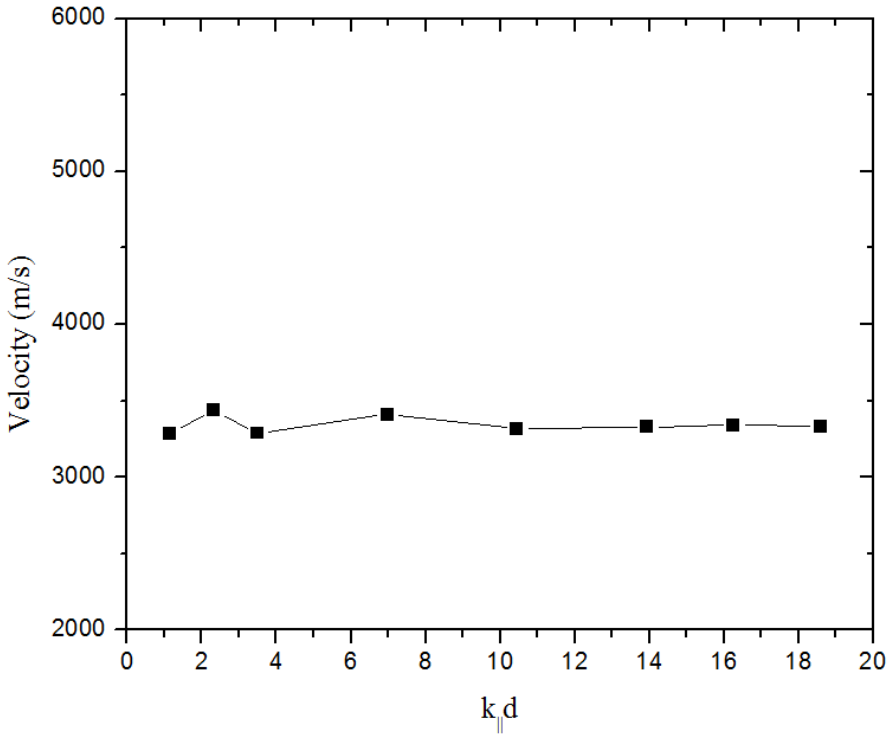

Figure 8.7: Measured velocity dispersion curve of the Rayleigh surface wave for varying $k_{||}d$ values.

Each of the spectra consists of the Rayleigh peak and no guided modes corresponding to the Sezawa wave. This is also shown in the velocity dispersion curve for which there are no guided modes corresponding to the Sezawa wave in the transonic region. This scenario is a classic case of a hard on soft film substrate configuration and can arise due to the following conditions:

(i) The transverse velocity (3330 m/s) of the film being smaller than that of the substrate Si (5800 m/s)

(ii) Film density of the film being lower than that of the substrate

In our case the transverse velocity of the film is approximated using the RSAW velocity for large $k_{||}d$ values to 3330 m/s which is lower than that of Si at 5800

m/s. The absence of the higher modes in the transonic region limits the accuracy in the extraction of the elastic constants by least squares fitting of the RSAW velocities. Indeed, the few degrees of freedom (data points) require the application of an independent method for consistent solution to the wave equation. Picosecond ultrasonics has been used as a complimentary technique. The details about this method and the subsequent results are presented in the next section.

8.4.1 Picosecond laser ultrasonics

Picosecond laser acoustics also known as picosecond ultrasonics involves the use of high frequency acoustic pulses generated and detected by ultrashort optical pulses usually less than a picosecond to probe the elastic properties of materials [235]. Some optical energy is absorbed and consequently converted to heat when such an ultrashort optical pulse, also known as the pump pulse, is incident on the surface of an opaque solid. Considering the simplest model, it is assumed that the process of heat conversion happens instantaneously, occurring within a depth approximately equal to the optical absorption depth. However, heat generation is delayed by non-equilibrium electron heating and relaxation processes while diffusion processes spatially blur the excitation region in the non-ideal case. In solids, the rise in lattice temperature results from heat production leading to thermal stress that produce a strain pulse which propagates in three dimensions. In the case of an isotropic solid, the acoustic pulse propagates normal to the surface whereby the frequency of the generated acoustic pulse is maximum and the wavelength smallest. The generated acoustic pulse can be accurately modelled as a superposition of longitudinal plane waves travelling normal to the surface when the optical spot size (typically a few microns) is much larger than the optical

absorption depth (~10 – 50 nm for example). In picosecond acoustics, the acoustic frequencies are in the range 10 - 1000 GHz compared to SBS whose surface acoustic waves have frequencies to about 150 GHz.

The picosecond ultrasonic used in this work is based on the time resolved pump and probe technique [236–238]. It is an ultrafast optical pump-probe experiment that is used to measure the elastic properties in thin film using acoustic wave (sonar) propagation. The strong optical absorption of the laser pulse (pump) in the film produces an ultra-short acoustic pulse which is further probed by another time delayed laser pulse (probe). The propagation and reflection of the acoustic pulse are time resolved and by detecting the acoustic echoes, the time of flight in the thin film layer can be measured. If the film properties such as the thickness and density are known, then the longitudinal sound velocity can be determined. The detection mechanism is based on the modification of the optical properties of the layers during the propagation of the acoustic pulse. The Elastic strain pulses propagating along the stacking axis of the film and the acoustic resonance at the surface are generated by the relaxation of the thermal stress. The acoustic waves perturb the optical reflectivity of the structure r_0. The amplitude of the the relative change of the optical reflectivity defined as $\Delta r(t)/r_0$ is measured by detecting the reflected probe pulse intensity on the surface of the film (Figure 8.8).

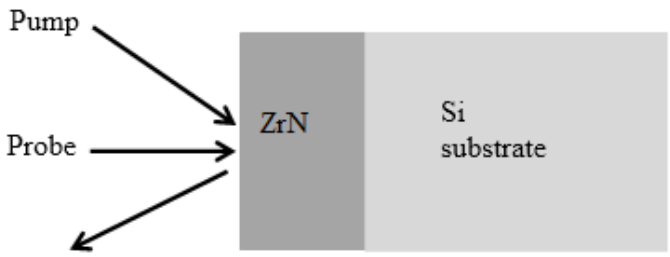

Figure 8.8: Illustration of the picosecond ultrasonic measurements on ZrN/Si thin films [239].

The time delay (ns) between the pump and the probe pulse is achieved through a variable optical path as shown in the experimental set up used in this work (Figure 8.9). A brief description of the experimental set up is given here while a detailed discussion is presented elsewhere [239].

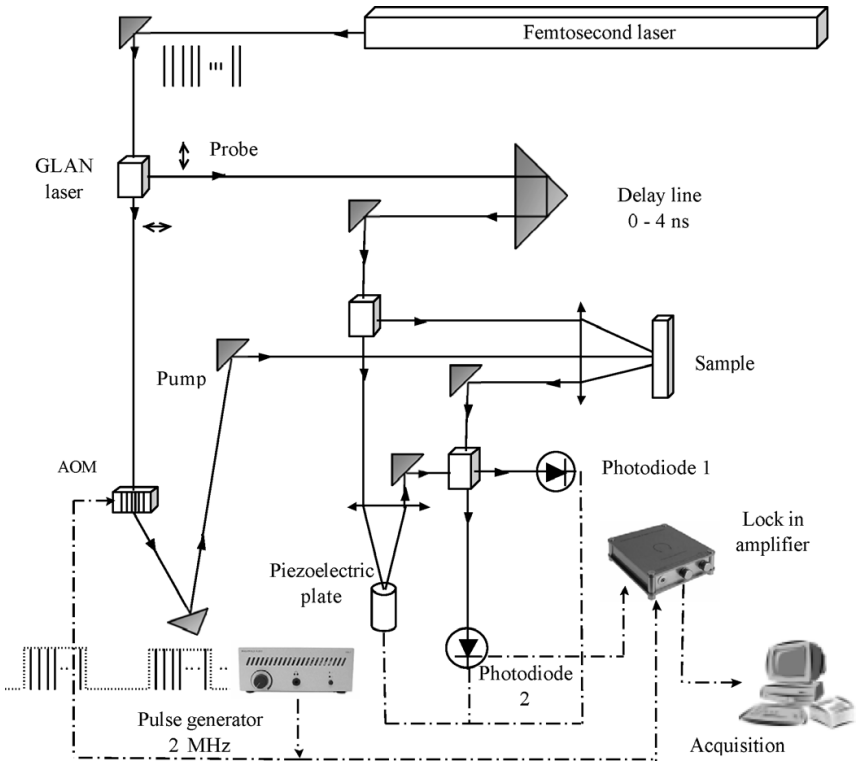

Figure 8.9: Experimental setup for the picosecond ultrasonic measurement [239].

The source of the optical pulse is a Ti:sapphire laser that provides a laser pulse of duration shorted that 100fs. These pulses can be enlarged up to 250 fs after

propagation in optical components. The laser is turned to 750 nm for a maximum power generation of up to 1.2 W. The laser beam is vertically polarized and split into 2 beams with perpendicular polarization and variable laser powers by means of the Glan laser splitter. The pump beam is chopped at 2 MHz using an AOM for lock in detection. The probe beam is delayed, up to 4 ns with respect to the pump beam by mobile mirror. Both beams are focused to arrive at the surface of the film to a spot of roughly 40 μm at near normal incidence. The intensity of the reflected probe beam is measured using a silicon photodiode and since the relative changes in the reflectivity are very small typically of the order 10^{-7} to 10^{-4}, a lock in amplifier is implemented for detection. Using the Mach-Zehnder interferometer the phase of the relative change in the optical reflectivity is measured. This is carried out by comparing the reflected probe beam with the reference beam generated from the same femtosecond laser pulse. Stability of the interferometer is achieved by means of a piezoelectric transducer [240]. Analysis of the data is carried out by simulating the experimental signals so that the relative change in reflectivity in the layers is analytically determined from the expression

$$\frac{\Delta r(t)}{r_0} = \frac{ik_0}{n_0 a_0 b_0} \sum_{l=0}^{L+1} \left\{ 2\varepsilon_l a_l b_l \left(u_l(t) - u_{l-1}(t)\right) + \frac{1}{2}\frac{\partial \varepsilon_l}{\partial \eta} \int_0^{d_l} dz \eta_l(z,t) \left[a_l e^{ik_l z} + b_l e^{-ik_l z}\right]^2 \right\} \tag{8.1}$$

Where L is the number of layers indexed by l between the cap medium ($l = 0$) and a substrate ($l = L + 1$). The thickness of the layer s denoted by d_l and z is the local coordinated defined within each layer, spanning from 0 to d_l The electromagnetic field in each layer l is given as the sum of two plane waves as

$E_l = a_l exp(ik_l Z) + b_l exp(-ik_l Z)$, where $k_l = N_l^2 k_0$, N is the complex refractive index of the layer l, k_0 is the wave vector in air. The reflection coefficient $r_0 = {}^{a_0}/_{b_0}$ at the front interface is given by the amplitudes (a_l, b_l) of the forward and back-reflected electromagnetic fields in each layer and these values are determined by the transfer matrix formalism.

Rigorous physical models for the optical and acoustic properties of the samples are used in the simulation. Foremost the amount of heat deposited in the layer is calculated from the optical constants. The heat distribution in the layer is thus used to determine the photo-thermal stress in the layer. Thereafter the acoustic field in all the layers of the sample is determined in the frequency domain while the time dependent amplitude and phase perturbations of the pulse probe reflections induced by the elastic field are derived from the fast inverse Fourier transforms. The simulations account for the following losses;

- Acoustic attenuation
- Adhesion
- Roughness of the interfaces

8.4.2 Results and discussion

In the laser ultrasonics measurement, the optical pump pulse is absorbed by the surface layer depending on the thickness of the layer, for thin films samples the heat distribution throughout the surface will be uniform leading to the creation of a broad thermal stress in the entire layer. This is the excited first acoustic resonance in the layer. The acoustic stress moves across the film at the longitudinal sound velocity of the layer and it is reflected at the interface with the

substrate to propagate to the perturbed surface *l*=0. Signals resulting from the picosecond ultrasonic measurements on ZrN/Si are presented in Figure 8.10. Figure 7.10 shows the change in optical reflectivity, $\Delta r(t)/r_0$ as a function of time for the ZrN thin film on a (001) Si-substrate. The figure comprises of the first acoustic resonance and the acoustic strain propagating normal to the film surface at a longitudinal sound velocity of the ZrN thin film. The reflection of the acoustic stress at the film-substrate interface guides the stress back to the perturbed sections of the films and it is superimposed on the thermal background due to the reduction in sample temperature as a result of heat diffusion onto the Silicon substrate. Thus, the thermal background subtraction is imperative to enable interpretation of effects attributed to the acoustic echo (Figure 8.11). Figure 8.10 also shows the real and imaginary parts of the complex reflectivity coefficients and these constitute the amplitude (black) and the phase (red) of the optical changes.

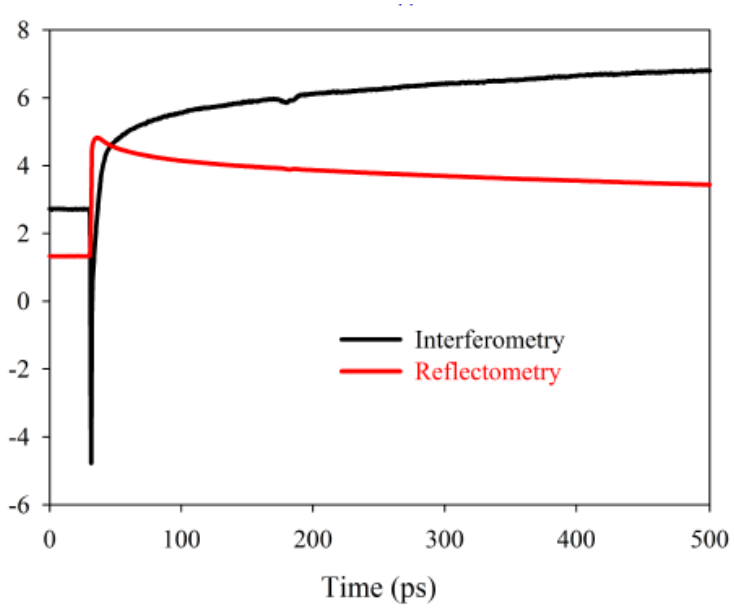

Figure 8.10: Real (reflectometry) and imaginary (interferometry) parts of the change of the complex reflectivity coefficient as a function of time.

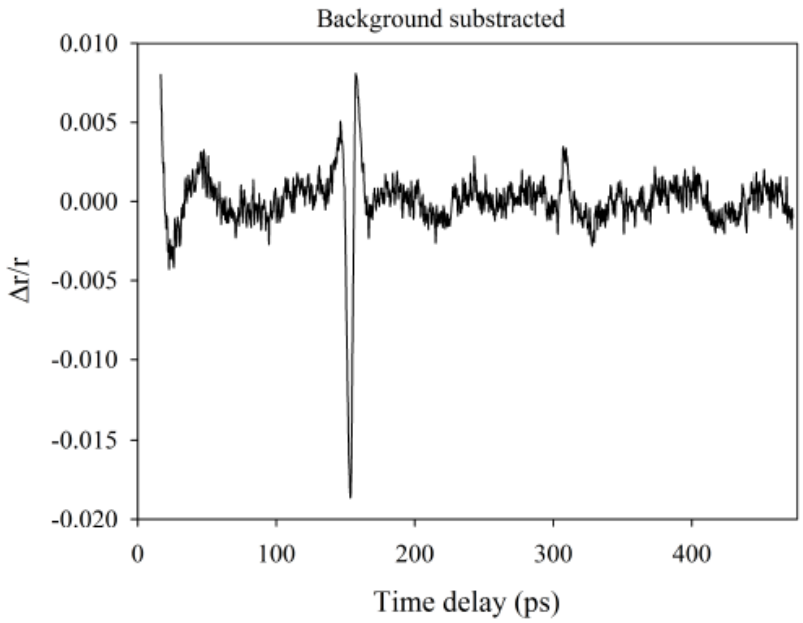

Figure 8.11: Reflectivity coefficient of ZrN on Si as a function of time after thermal background subtraction.

In the present work, picosecond laser acoustic measurements were performed on a 600 nm thick ZrN thin film. No metallic transducer was used on the top of the sample. Consequently, the acoustic echo generation occurred directly in the sample resulting in an echo duration of $\tau = 153.6$ ps. The longitudinal sound velocity v_{ZrN} of thickness d_{ZrN} is given from the expression as

$$v_{ZrN} = \frac{2d_{ZrN}}{\tau} \tag{8.2}$$

From the picoseconds acoustic measurements and X-ray reflectivity density data, the sound velocity was found to be 7.81 nm/ps and a value of $C_{11} = 402.8$ GPa was obtained. From surface Brillouin scattering at large $k_{||}d$ the Rayleigh velocity, V_R approximates to the transverse velocity in the form; $\sqrt{3}/2V_R^2\rho = C_{44}$. Thus, the value of C_{44} is estimated to be 62.3 GPa. For an isotropic film the Cauchy relation $C_{12} = C_{11} - 2C_{44}$ is valid giving $C_{12} = 278.2$ GPa for the

polycrystalline ZrN films. Hence the elastic constants of isotropic ZrN films have been evaluated to $C_{11} = 402.8$ GPa and $C_{12} = 278.2$ GPa using SBS and picosecond ultrasonics. Literature values of $C_{11} = 492$ GPa, $C_{12} = 126$ GPa and $C_{44} = 116$ GPa obtained from density functional theory (DFT) calculations have been reported in [241].

8.5 Conclusions

ZrN thin films were grown using rf magnetron sputtering on Si (100) substrates at sputter power of 200 W. A deposition rate of 25 nm/min and mass density of 6.49 g/cm^3 was determined from XRR measurements. AFM measurements indicated smooth (0.55 – 1.62 nm) and homogeneous films while columnar growth of the films has been established using SEM. A rock salt type (NaCl) polycrystalline structure of the films has been reveled using grazing incidence X-ray diffraction. The films have been shown to be non-stoichiometric using HI-ERDA. SBS measurements have revealed the absence of higher modes in the transonic region. As a result, it was not possible to extract the elastic constants of the films using the least squares fit procedure. Picosecond ultrasonics was used as a complementary technique to obtain the value of $C_{11} = 402.8$ GPa, $C_{44} = 62.3$ GPa and $C_{12} = 278.2$ GPa have been approximated from the mass density and measured C_{11} value.

Chapter 9

Conclusion

9.1 Summary

Elastic constants of hard thin coatings of NbN, TaN, and ZrN have been studied using SBS. The thin films NbN, TaN have been deposited on Si (100) substrates while for ZrN films were deposited on Si (100) and 6H-SiC substrates using rf magnetron sputtering. NbN thin films have been deposited at varying sputter powers ranging from 75 W - 250 W to establish the influence of ad-atom energy on the elastic constants. TaN and ZrN thin films have been deposited at sputter powers of 150 W and 200 W respectively.

The physical properties of the films namely composition, morphology, microstructure, and crystalline structure have been investigated using HI-ERDA, AFM, XRR, SEM, and grazing incidence X-ray diffraction. HI-ERDA results indicate the films are non-stoichiometric with the exception on NbN thin films deposited at sputter power 200 W. AFM results have shown smooth films of roughness values less than 2 nm. Mass density values obtained from XRR measurements indicate the films are less dense than the corresponding single crystal nitrides. SEM studies of the thin films have established columnar growth. For NbN thin films deposited for varying times at constant power, no significant changes in the microstructure have been observed. A polycrystalline NaCl like phase has been revealed in all the films using grazing incidence X-ray diffraction.

Surface Brillouin scattering measurements have been performed at room temperature in the back-scattering geometry. The $k_{||}$ has been kept constant at

71° while $k_{||}d$ has been varied by varying the film thickness d. RSAW and higher order peaks (SWs) have been observed in both NbN and TaN. The absence of higher order modes (SWs) in the transonic region has been revealed for ZrN thin films deposited on single crystal silicon and silicon carbide substrates. From the measured SBS spectra, SAW velocities have been determined for all the samples. Theoretical SAW velocities have also been determined using the Green's function method. The elastic stiffness of NbN and TaN thin films have been extracted by fitting the measured and calculated SAW velocities. The least squares fit has been obtained by χ^2 minimization. It has not been possible to apply the least squares procedure to the ZrN thin films due to the absence of higher order modes. Consequently, picosecond ultrasonics has been used as a complementary technique to extract the elastic constants of the films. Calculated and measured Brillouin spectra from the surface Green's function approach have been compared to determine the self-consistency of the results. An increase in C_{11} values has been observed for NbN films deposited at sputter powers 75-150 W and a decrease thereafter for 200-250 W. This has been attributed to a possible change in phase at 200 W. Elastic constants for NbN have been determined to range from $C_{11} = 371.5 - 502.5$ GPa, $C_{12} = 160.9 - 320.7$ GPa, and $C_{44} = 99.9 - 107.4$ GPa. Poisson's ratios of the NbN films has been determined to range from 0.27-0.35 indicating that the films are elastically hard but softer than diamond. The elastic constants for TaN thin films have been determined as $C_{11} = 288$ GPa, $C_{12} = 128$ GPa, and $C_{44} = 80$ GPa and a Poisson's ratio value of 0.27. A value of $C_{11} = 402.8$ GPa has been obtained from picosecond ultrasonics measurements for the ZrN thin films. $C_{44} = 62.3$ GPa and $C_{12} = 278.2$ GPa have been approximated from the mass density and measured C_{11} value for an isotropic

system. A linear fitting procedure has been used to optimise and calculate the uncertainties of the elastic constants for NbN and TaN thin films. Uncertainties of between 1.3 % and 3.1 % for C_{11} and 0.9 % and 7.7% for C_{44} have been determined for NbN while 1.3% and 3.1% have been obtained for C_{11} and C_{44} respectively for the TaN films. Finally, good agreement has been observed between the calculated and the measured Brillouin spectra of NbN and TaN thin films by the Green's function method. However, a slight discrepancy has been observed in the case of ZrN thin films. The variation has been explained by the estimation of the C_{44} and C_{12} values in chapter 8.

9.2 Suggestions for future work

Deposition parameters have been shown to affect the properties of thin films. In the present work, it has been established that SBS is sensitive to changes in the microstructure and composition of NbN thin films resulting from the variation of rf power. The change in microstructure and composition of thin films by varying other deposition conditions such as argon gas flow rate, substrate temperature, and substrate bias could be studied using SBS.

The absence of higher order modes has been observed for ZrN thin films. It has been previously established that the film-substrate configuration affects the observed acoustic excitations. As such it would be interesting to study the behavior of another configuration such as ZrN on diamond.

The HI-ERDA technique has been used to establish the composition of the films studied in the present work. Another technique such as Rutherford backscattering could be applied for self-consistency.

References

[1] R. Hübler, Surf. Coat. Technol. 158–159 (2002) 680–684.

[2] Y. Okazaki, Y. Ito, K. Kyo, T. Tateishi, Mater. Sci. Eng. A 213 (1996) 138–147.

[3] J.A. Davidson, A.K. Mishra, P. Kovacs, R.A. Poggie, Biomed. Mater. Eng. 4 (1994) 231–243.

[4] J. Probst, U. Gbureck, R. Thull, Surf. Coat. Technol. 148 (2001) 226–233.

[5] R.A. Fischer, H. Parala, in: Chem. Vap. Depos. Precursors Process. Appl., The Royal Society of Chemistry, 2009, pp. 413–450.

[6] K. Singh, N. Krishnamurthy, A.K. Suri, Tribol. Int. 50 (2012) 16–25.

[7] M.S. Wong, W.D. Sproul, X. Chu, S.A. Barnett, J. Vac. Sci. Technol. A 11 (1993) 1528–1533.

[8] I.L. Singer, R.N. Bolster, S.A. Wolf, E.F. Skelton, R.A. Jeffries, Thin Solid Films 107 (1983) 207–215.

[9] K. Baba, R. Hatada, K. Udoh, K. Yasuda, Nucl. Instrum. Methods Phys. Res. Sect. B Beam Interact. Mater. At. 127–128 (1997) 841–845.

[10] I. Hotový, J. Huran, D. Búc, R. Srnánek, Vacuum 50 (1998) 45–48.

[11] N. Rando, A. Peacock, C. Foden, A. v Dordrecht, J. Lumley, C. Pereira, J. Appl. Phys. 73 (1993) 5098–5104.

[12] G.N. Gol'tsman, A.D. Semenov, Y.P. Gousev, M.A. Zorin, I.G. Godidze, E.M. Gershenzon, P.T. Lang, W.J. Knott, K.F. Renk, Supercond. Sci. Technol. 4 (1991) 453.

[13] O. Bourgeois, E. André, C. Macovei, J. Chaussy, Rev. Sci. Instrum. 77 (2006) 126108.

[14] J.J. Olaya, S.E. Rodil, S. Muhl, Thin Solid Films 516 (2008) 8319–8326.

[15] M. Benkahoul, E. Martinez, A. Karimi, R. Sanjinés, F. Lévy, Surf. Coat. Technol. 180–181 (2004) 178–183.

[16] Y. Gotoh, M. Nagao, T. Ura, H. Tsuji, J. Ishikawa, Nucl. Instrum. Methods Phys. Res. Sect. B Beam Interact. Mater. At. 148 (1999) 925–929.

[17] V.N. Zhitomirsky, Surf. Coat. Technol. 201 (2007) 6122–6130.

[18] V.N. Zhitomirsky, I. Grimberg, L. Rapoport, N.A. Travitzky, R.L. Boxman, S. Goldsmith, A. Raihel, I. Lapsker, B.Z. Weiss, Thin Solid Films 326 (1998) 134–142.

[19] A. Kawakami, S. Miki, Z. Wang, Phys. C Supercond. 378–381, Part 2 (2002) 1295–1300.

[20] J.E. Alfonso, J. Buitrago, J. Torres, J.F. Marco, B. Santos, J. Mater. Sci. 45 (2010) 5528–5533.

[21] S.K. Kim, B.C. Cha, J.S. Yoo, Surf. Coat. Technol. 177–178 (2004) 434–440.

[22] D. Xin-Kang, W. Tian-min, W. Cong, B. CHEN, L. ZHOU, Chin. J. Aeronaut. 20 (2007) 140–144.

[23] K.S. Havey, J.S. Zabinski, S.D. Walck, Thin Solid Films 303 (1997) 238–245.

[24] N. Cansever, Thin Solid Films 515 (2007) 3670–3674.

[25] C.S. Sandu, M. Benkahoul, M. Parlinska-Wojtan, R. Sanjinés, F. Lévy, Surf. Coat. Technol. 200 (2006) 6544–6548.

[26] R. Krishnan, C. David, P.K. Ajikumar, S. Dash, A.K. Tyagi, V. Jayaram, B. Raj, Surf. Coat. Technol. 206 (2011) 1196–1202.

[27] M. Wen, C.Q. Hu, Q.N. Meng, Z.D. Zhao, T. An, Y.D. Su, W.X. Yu, W.T. Zheng, J. Phys. Appl. Phys. 42 (2009) 035304.

[28] G. Ramírez, S.E. Rodil, H. Arzate, S. Muhl, J.J. Olaya, Appl. Surf. Sci. 257 (2011) 2555–2559.

[29] M. Benkahoul, C.S. Sandu, N. Tabet, M. Parlinska-Wojtan, A. Karimi, F. Lévy, Surf. Coat. Technol. 188–189 (2004) 435–439.

[30] Y. Ufuktepe, A.H. Farha, S.I. Kimura, T. Hajiri, K. Imura, M.A. Mamun, F. Karadag, A.A. Elmustafa, H.E. Elsayed-Ali, Thin Solid Films 545 (2013) 601–607.

[31] S. Niyomsoan, W. Grant, D.L. Olson, B. Mishra, Thin Solid Films 415 (2002) 187–194.

[32] W.-J. Chou, G.-P. Yu, J.-H. Huang, Thin Solid Films 405 (2002) 162–169.

[33] M.M. Larijani, N. Tabrizi, S. Norouzian, A. Jafari, S. Lahouti, H. Haj Hosseini, N. Afshari, Vacuum 81 (2006) 550–555.

[34] J.-H. Huang, C.-Y. Hsu, S.-S. Chen, G.-P. Yu, Mater. Chem. Phys. 77 (2003) 14–21.

[35] N. Farkas, G. Zhang, K.M. Donnelly, E.A. Evans, R.D. Ramsier, J.A. Dagata, Thin Solid Films 447–448 (2004) 468–473.

[36] L. Pichon, T. Girardeau, A. Straboni, F. Lignou, P. Guérin, J. Perrière, Appl. Surf. Sci. 150 (1999) 115–124.

[37] C.-H. Ma, J.-H. Huang, H. Chen, Surf. Coat. Technol. 133–134 (2000) 289–294.

[38] H.B. Bhuvaneswari, I. Nithiya Priya, R. Chandramani, V. Rajagopal Reddy, G. Mohan Rao, Cryst. Res. Technol. 38 (2003) 1047–1051.

[39] J.S. Becker, E. Kim, R.G. Gordon, Chem. Mater. 16 (2004) 3497–3501.

[40] H.M. Benia, M. Guemmaz, G. Schmerber, A. Mosser, J.-C. Parlebas, Appl. Surf. Sci. 200 (2002) 231–238.

[41] H. Wiame, M.-A. Centeno, S. Picard, P. Bastians, P. Grange, J. Eur. Ceram. Soc. 18 (1998) 1293–1299.

[42] K.A. Gruss, T. Zheleva, R.F. Davis, T.R. Watkins, Surf. Coat. Technol. 107 (1998) 115–124.

[43] H.M. Benia, M. Guemmaz, G. Schmerber, A. Mosser, J.C. Parlebas, Appl. Surf. Sci. 211 (2003) 146–155.

[44] L. Hu, D. Li, G. Fang, Appl. Surf. Sci. 220 (2003) 367–371.

[45] H.J. Ramos, N.B. Valmoria, Vacuum 73 (2004) 549–554.

[46] X.H. Yan, J. Yin, X.N. Cheng, J.Q. Liu, Mater. Werkst. 44 (2013) 79–83.

[47] X. Liu, G.J. Ma, G. Sun, Y.P. Duan, S.H. Liu, Appl. Surf. Sci. 258 (2011) 1033–1037.

[48] M. Stavrev, D. Fischer, C. Wenzel, K. Drescher, N. Mattern, Thin Solid Films 307 (1997) 79–88.

[49] K. Holloway, P.M. Fryer, C.C. Jr, J.M.E. Harper, P.J. Bailey, K.H. Kelleher, J. Appl. Phys. 71 (1992) 5433–5444.

[50] M. Takeyama, A. Noya, T. Sase, A. Ohta, K. Sasaki, J. Vac. Sci. Technol. B 14 (1996) 674–678.

[51] K.-H. Min, K.-C. Chun, K.-B. Kim, J. Vac. Sci. Technol. B 14 (1996) 3263–3269.

[52] J.O. Olowolafe, C.J. Mogab, R.B. Gregory, M. Kottke, J. Appl. Phys. 72 (1992) 4099–4103.

[53] H. Shen, R. Ramanathan, Microelectron. Eng. 83 (2006) 206–212.

[54] M.L. Lovejoy, G.A. Patrizi, D.J. Roger, J.C. Barbour, Thin Solid Films 290–291 (1996) 513–517.

[55] M.H. Tsai, S.C. Sun, C.E. Tsai, S.H. Chuang, H.T. Chiu, J. Appl. Phys. 79 (1996) 6932–6938.

[56] S.K. Kim, B.C. Cha, Thin Solid Films 475 (2005) 202–207.

[57] D. Kim, H. Lee, D. Kim, Y. Keun Kim, J. Cryst. Growth 283 (2005) 404–408.

[58] N.D. Cuong, D.-J. Kim, B.-D. Kang, C.S. Kim, K.-M. Yu, S.-G. Yoon, J. Electrochem. Soc. 153 (2006) G164–G167.

[59] T. Riekkinen, J. Molarius, T. Laurila, A. Nurmela, I. Suni, J.K. Kivilahti, Microelectron. Eng. 64 (2002) 289–297.

[60] N. Dalili, Q. Liu, D.G. Ivey, J. Mater. Sci. 48 (2012) 489–501.

[61] A. Aryasomayajula, K. Valleti, S. Aryasomayajula, D.G. Bhat, Surf. Coat. Technol. 201 (2006) 4401–4405.

[62] A.O. Ibidunni, Oxid. Met. 40 (1993) 5–20.

[63] C. Palacio, J.M. Sanz, J.M. Martínez-Duart, Thin Solid Films 124 (1985) 243–247.

[64] A.C. Anacleto, A. Zauner, D. Cany-Canian, J. Gatineau, M.-C. Hugon, Thin Solid Films 519 (2010) 367–372.

[65] X. Sun, E. Kolawa, J.-S. Chen, J.S. Reid, M.-A. Nicolet, Thin Solid Films 236 (1993) 347–351.

[66] A.G. Every, W. Pang, J.D. Comins, P.R. Stoddart, Ultrasonics 36 (1998) 223–227.

[67] E. Török, A.J. Perry, L. Chollet, W.D. Sproul, Thin Solid Films 153 (1987) 37–43.

[68] A.J. Perry, Thin Solid Films 193–194, Part 1 (1990) 463–471.

[69] A.J. Perry, Thin Solid Films 170 (1989) 63–70.

[70] A.G. Every, Meas. Sci. Technol. 13 (2002) R21–R39.

[71] J.O. Kim, J.D. Achenbach, Thin Solid Films 214 (1992) 25–34.

[72] J.O. Kim, J.D. Achenbach, P.B. Mirkarimi, M. Shinn, S.A. Barnett, J. Appl. Phys. 72 (1992) 1805.

[73] B. Hillebrands, P. Baumgart, R. Mock, G. Güntherodt, P.S. Bechthold, J. Appl. Phys. 58 (1985) 3166.

[74] G. Carlotti, D. Fioretto, L. Palmieri, G. Socino, L. Verdini, E. Verona, IEEE Trans. Ultrason. Ferroelectr. Freq. Control 38 (1991) 56–61.

[75] W. Pang, P.R. Stoddart, J.D. Comins, A.G. Every, D. Pietersen, P.J. Marais, Int. J. Refract. Met. Hard Mater. 15 (1997) 179–185.

[76] T. Wittkowski, V. Wiehn, J. Jorzick, K. Jung, B. Hillebrands, Thin Solid Films 368 (2000) 216–221.

[77] A.M. Marvin, V. Bortolani, F. Nizzoli, J. Phys. C Solid State Phys. 13 (1980) 299.

[78] X. Zhang, J.D. Comins, A.G. Every, P.R. Stoddart, Int. J. Refract. Met. Hard Mater. 16 (1998) 303–308.

[79] J.D. Comins, A.G. Every, P.R. Stoddart, X. Zhang, J.C. Crowhurst, G.R. Hearne, Ultrasonics 38 (2000) 450–458.

[80] M. Montagna, Phys. Rev. B 77 (2008) 045418.

[81] L. Sui, L. Huang, P. Podsiadlo, N.A. Kotov, J. Kieffer, Macromolecules 43 (2010) 9541–9548.

[82] H.T. Nguyen, G. Gubbiotti, M. Madami, S. Tacchi, M.G. Cottam, Microelectron. J. 40 (2009) 598–600.

[83] E. Salas, R.J. Jiménez-Riobóo, A. de Andrés, C. Prieto, Eur. Phys. J. B 75 (2010) 151–155.

[84] N. Lou, J. Groenen, G. Benassayag, A. Zwick, Appl. Phys. Lett. 97 (2010) 141908.

[85] G. Gubbiotti, S. Tacchi, M. Madami, G. Carlotti, A.O. Adeyeye, M. Kostylev, J. Phys. Appl. Phys. 43 (2010) 264003.

[86] M. Pochylski, J. Gapiński, J. Phys. Chem. B 114 (2010) 2644–2649.

[87] Q. Zhao, M. Guerette, L. Huang, J. Non-Cryst. Solids 358 (2012) 652–657.

[88] L.M. Kotane, J.D. Comins, A.G. Every, J.R. Botha, J. Phys. Conf. Ser. 278 (2011) 012001.

[89] R.J. Jiménez-Riobóo, R. Cuscó, R. Oliva, N. Domènech-Amador, C. Prieto, J. Ibáñez, C. Boney, A. Bensaoula, L. Artús, Appl. Phys. Lett. 101 (2012) 062103.

[90] S. Speziale, H. Marquardt, T.S. Duffy, Rev. Mineral. Geochem. 78 (2014) 543–603.

[91] V. Bortolani, A.M. Marvin, F. Nizzoli, G. Santoro, J. Phys. C Solid State Phys. 16 (1983) 1757.

[92] R. Loudon, Phys. Rev. Lett. 40 (1978) 581–583.

[93] E.L. Albuquerque, N.S. Almeida, Solid State Commun. 70 (1989) 107–109.

[94] E.L. Albuquerque, Phys. Status Solidi B 118 (1983) 223–227.

[95] M.W. Elmiger, J. Henz, H.V. Känel, M. Ospelt, P. Wachter, Surf. Interface Anal. 14 (1989) 18–22.

[96] T. Wittkowski, P. Cortina, J. Jorzick, K. Jung, B. Hillebrands, Diam. Relat. Mater. 9 (2000) 1957–1964.

[97] V. Chandrasekharan, Proc. Indian Acad. Sci. Sect. A 32 (1950) 379.

[98] J. Gump, H. Xia, M. Chirita, R. Sooryakumar, M.A. Tomaz, G.R. Harp, J. Appl. Phys. 86 (1999) 6005–6009.

[99] P. Zinin, M.H. Manghnani, X. Zhang, H. Feldermann, C. Ronning, H. Hofsäss, J. Appl. Phys. 91 (2002) 4196–4204.

[100] M.G. Beghi, C.E. Bottani, P.M. Ossi, T.A. Lafford, B.K. Tanner, J. Appl. Phys. 81 (1997) 672–678.

[101] P.B. Mirkarimi, M. Shinn, S.A. Barnett, S. Kumar, M. Grimsditch, J. Appl. Phys. 71 (1992) 4955–4958.

[102] L. Brillouin, Ann. Phys. 17 (1922) 88–122.

[103] L.I. Mandelstam, Zh. Russ. Fiz.Khim.Ova. 58 (1926) 381.

[104] E. Gross, Nature 126 (1930) 400.

[105] E. Gross, Z. Phys. 63 (1930) 685.

[106] R. Krishnan, in: Anderson A (ed) Dekker, New York, 1972, pp. 343–404.

[107] G.B. Benedek, K. Fritsch, Phys. Rev. 149 (1966) 647–662.

[108] R.W. Gammon, H.Z. Cummins, Phys. Rev. Lett. 17 (1966) 193–195.

[109] E.M. Brody, H.Z. Cummins, Phys. Rev. Lett. 21 (1968) 1263–1266.

[110] J.D. Comins, in: Handb. Elastic Prop. Solids Liq. Gases Ed. Levy Bass Stern Vol. 1 Dyn. Methods Meas. Elastic Prop. Solids, Academic Press, 2001, pp. 349–378.

[111] J.R. Sandercock, in: M. Cardona, G. Güntherodt (Eds.), Light Scatt. Solids III, Springer Berlin Heidelberg, Berlin, Heidelberg, 1982, pp. 173–206.

[112] P. Mutti, C.E. Bottani, G. Ghislotti, M. Beghi, G.A.D. Briggs, J.R. Sandercock, in: A. Briggs (Ed.), Adv. Acoust. Microsc., Springer US, Boston, MA, 1995, pp. 249–300.

[113] S.M. Lindsay, M.W. Anderson, J.R. Sandercock, Rev. Sci. Instrum. 52 (1981) 1478–1486.

[114] B. Hillebrands, Rev. Sci. Instrum. 70 (1999) 1589–1598.

[115] X. Zhang, J.D. Comins, A.G. Every, P.R. Stoddart, W. Pang, T.E. Derry, Phys Rev B 58 (1998) 13677–13685.

[116] R. Loudon, J. Phys. C Solid State Phys. 11 (1978) 403.

[117] K.R. Subbaswamy, A.A. Maradudin, Phys Rev B 18 (1978) 4181–4199.

[118] V.R. Velasco, F. Garcia-Moliner, J. Phys. C Solid State Phys. 13 (1980) 2237.

[119] N.L. Rowell, G.I. Stegeman, Phys Rev B 18 (1978) 2598–2615.

[120] A.M. Marvin, V. Bortolani, F. Nizzoli, G. Santoro, J. Phys. C Solid State Phys. 13 (1980) 1607.

[121] R. Loudon, J.R. Sandercock, J. Phys. C Solid State Phys. 13 (1980) 2609.

[122] D.L. Mills, K.R. Subbaswamy, in: E. Wolf (Ed.), Elsevier, 1981, pp. 45–137.

[123] M. Grimsditch, in: Handb. Elastic Prop. Solids Liq. Gases Ed. Levy Bass Stern Vol. 1 Dyn. Methods Meas. Elastic Prop. Solids, Academic Press, 2001.

[124] V. Bortolani, F. Nizzoli, G. Santoro, J.R. Sandercock, Phys Rev B 25 (1982) 3442–3445.

[125] V. Bortolani, F. Nizzoli, G. Santoro, Phys Rev Lett 41 (1978) 39–42.

[126] V. Bortolani, F. Nizzoli, G. Santoro, Phys. Lett. A 68 (1978) 342–344.

[127] J.R. Sandercock, Phys Rev Lett 28 (1972) 237–240.

[128] M. Mendik, S. Sathish, A. Kulik, G. Gremaud, P. Wachter, J. Appl. Phys. 71 (1992) 2830–2834.

[129] X. Zhang, P.R. Stoddart, J.D. Comins, A.G. Every, J. Phys. Condens. Matter 13 (2001) 2281.

[130] B. Graczykowski, B. Mroz, S. Mielcarek, T. Breczewski, M.L. Nó, J.S. Juan, J. Phys. Appl. Phys. 44 (2011) 455307.

[131] D. Visser, N.C.J.A. van Hijningen, J.G. Dil, J. Phys. Colloq. 45 (1984) C5-83-C5-91.

[132] J.C. Crowhurst, G.R. Hearne, J.D. Comins, A.G. Every, P.R. Stoddart, Phys. Rev. B 60 (1999) R14990–R14993.

[133] B.A. Auld, Acoustic Fields and Waves in Solids. Vol. 1: [...], Wiley, New York, NY, 1973.

[134] A.E.H. Love, Some Problems of Geodynamics, 1911.

[135] A.L. Bassi, C.E. Bottani, C. Casari, M. Beghi, Appl. Surf. Sci. 226 (2004) 271–281.

[136] E.L. Albuquerque, R. Loudon, D.R. Tilley, J. Phys. C Solid State Phys. 13 (1980) 1775.

[137] X. Zhang, M.H. Manghnani, A.G. Every, Phys Rev B 62 (2000) R2271–R2274.

[138] J.A. Bell, R.J. Zanoni, C.T. Seaton, G.I. Stegeman, W.R. Bennett, C.M. Falco, Appl. Phys. Lett. 51 (1987) 652–654.

[139] M. Beghi, A. Every, P. Zinin, in: T. Kundu (Ed.), Ultrason. Nondestruct. Eval., CRC Press, 2003.

[140] J.R. Sanderocock, Solid State Commun. 26 (1978) 547–551.

[141] G.W. FARNELL, E.L. ADLER, in: W.P. MASON, R.N. THURSTON (Eds.), Academic Press, 1972, pp. 35–127.

[142] C. Sumanya, Surface Brillouin Scattering in Opaque Thin Films and Bulk Materials, University of the Witwatersrand, 2012.

[143] W.-J. Chou, C.-H. Sun, G.-P. Yu, J.-H. Huang, Mater. Chem. Phys. 82 (2003) 228–236.

[144] D.L. Smith, Thin Film Deposition: Principles and Practice, 1st ed., McGraw-Hill Education, New York, 1995.

[145] W.R. Grove, Philos. Trans. R. Soc. Lond. 142 (1852) 87–101.

[146] K. Seshan, ed., Handbook of Thin-Film Deposition Processes and Techniques: Principles, Methods, Equipment, and Applications, 2nd ed, Noyes Publications, Norwich, N.Y, 2002.

[147] Ist. Fis. Plasma Piero Caldirola (n.d.).

[148] B.N. Chapman, Glow Discharge Processes: Sputtering and Plasma Etching, Wiley, New York, 1980.

[149] K. Wasa, M. Kitabatake, H. Adachi, Thin Film Materials Technology: Sputtering of Compound Materials, William Andrew Pub.; Springer, Norwich, NY: Heidelberg, 2004.

[150] P. Sigmund, Phys. Rev. 184 (1969) 383–416.

[151] J.A. Thornton, J. Vac. Sci. Technol. 11 (1974) 666–670.

[152] K.S. SreeHarsha, Principles of Physical Vapor Deposition of Thin Films, 1st ed, Elsevier, Amsterdam; Boston, 2006.

[153] G. Ceriola, F. Iacona, F. La Via, V. Raineri, E. Bontempi, L.E. Depero, J. Electrochem. Soc. 148 (2001) F221.

[154] H. Kiessig, Ann. Phys. 402 (1931) 769–788.

[155] M. Yasaka, Rigaku J. 26 (2010).

[156] V. Holý, A.A. Darhuber, J. Stangl, G. Bauer, J. Nützel, G. Abstreiter, Phys. Rev. B 57 (1998) 12435–12442.

[157] E. Bontempi, L.E. Depero, L. Sanagaletti, Philos. Mag. Part B 80 (2000) 623–633.

[158] S. Kohli, C.D. Rithner, P.K. Dorhout, J. Appl. Phys. 91 (2002) 1149–1154.

[159] M. Brunel, L. Ortega, Y. Cros, S. Viscaino, Appl. Surf. Sci. 65–66 (1993) 289–292.

[160] M. Tolan, X-Ray Scattering from Soft-Matter Thin Films, Springer Berlin Heidelberg, Berlin, Heidelberg, 1999.

[161] V. Holý, U. Pietsch, T. Baumbach, High-Resolution X-Ray Scattering from Thin Films and Multilayers, Springer, Berlin; New York, 1999.

[162] J. Als-Nielsen, D. McMorrow, Elements of Modern X-Ray Physics, 2. ed, Wiley, Chichester, 2011.

[163] L. Névot, P. Croce, Rev. Phys. Appliquée 15 (1980) 761–779.

[164] D. Simeone, G. Baldinozzi, D. Gosset, S. Le Caer, J.-F. Bérar, Thin Solid Films 530 (2013) 9–13.

[165] G.H. Vineyard, Phys. Rev. B 26 (1982) 4146–4159.
[166] J. Daillant, A. Gibaud, eds., X-Ray and Neutron Reflectivity, Springer Berlin Heidelberg, Berlin, Heidelberg, 2009.
[167] D.T. Cromer, D. Liberman, J. Chem. Phys. 53 (1970) 1891.
[168] S.-L. Chang, J. Phys. Chem. Solids 62 (2001) 1765–1775.
[169] M. Laue, Naturwissenschaften 39 (1952) 361–363.
[170] W.H. Bragg, W.L. Bragg, Proc. R. Soc. Math. Phys. Eng. Sci. 88 (1913) 428–438.
[171] R.D. Tarey, R.S. Rastogi, K.L. Chopra, Rigaku J. 4 (1987) 11–15.
[172] M. Bouroushian, T. Kosanovic, Cryst. Struct. Theory Appl. 01 (2012) 35–39.
[173] T.C. Huang, P.K. Predecki, JCPDS-Int. Cent. Diffr. Data (1997).
[174] B. Lengeler, Adv X-Ray Anal 35 (1992) 127.
[175] T.C. Huang, W. Parrish, Adv X-Ray Anal 35 (192AD) 137.
[176] M. Neuschitzer, A. Moser, A. Neuhold, J. Kraxner, B. Stadlober, M. Oehzelt, I. Salzmann, R. Resel, J. Novák, J. Appl. Crystallogr. 45 (2012) 367–370.
[177] G. Solookinejad, A.S.H. Rozatian, M.H. Habibi, Exp. Tech. 38 (2014) 21–27.
[178] I. Schmitz, M. Schreiner, G. Friedbacher, M. Grasserbauer, Anal. Chem. 69 (1997) 1012–1018.
[179] Askewmind, (2006).
[180] K.L. Westra, D.J. Thomson, Thin Solid Films 257 (1995) 15–21.
[181] D. Nečas, P. Klapetek, Cent. Eur. J. Phys. 10 (2011) 181–188.
[182] (2006).
[183] D.R. Baer, S. Thevuthasan, in: Handb. Depos. Technol. Films Coat., Elsevier, 2010, pp. 749–864.
[184] Y. Wang, M.A. Nastasi, eds., Handbook of Modern Ion Beam Materials Analysis. Vol. [1]: [...], 2. ed, Materials Research Soc, Warrendale, Pa, 2009.
[185] J. L'Ecuyer, C. Brassard, C. Cardinal, J. Chabbal, L. Deschênes, J.P. Labrie, B. Terreault, J.G. Martel, R. St.-Jacques, J. Appl. Phys. 47 (1976) 381–382.

[186] J. Jokinen, J. Keinonen, P. Tikkanen, A. Kuronen, T. Ahlgren, K. Nordlund, Nucl. Instrum. Methods Phys. Res. Sect. B Beam Interact. Mater. At. 119 (1996) 533–542.

[187] M. Msimanga, D. Wamwangi, C.M. Comrie, C.A. Pineda-Vargas, M. Nkosi, T. Hlatshwayo, Nucl. Instrum. Methods Phys. Res. Sect. B Beam Interact. Mater. At. 296 (2013) 54–60.

[188] (2018).

[189] S.C. Singh, H. Zeng, C. Guo, W. Cai, in: S.C. Singh, H. Zeng, C. Guo, W. Cai (Eds.), Nanomaterials, Wiley-VCH Verlag GmbH & Co. KGaA, Weinheim, Germany, 2012, pp. 1–34.

[190] T. Wittkowski, Brillouin-Lichtstreuuntersuchungen an Bornitridschichten, University of Kaiserslautern, 2002.

[191] J.R. Sandercock, (n.d.).

[192] J. Musil, Surf. Coat. Technol. 125 (2000) 322–330.

[193] H. Randhawa, J. Vac. Sci. Technol. Vac. Surf. Films 4 (1986) 2755–2758.

[194] O. Knotek, W.D. Münz, T. Leyendecker, J. Vac. Sci. Technol. Vac. Surf. Films 5 (1987) 2173–2179.

[195] P. Roquiny, F. Bodart, G. Terwagne, Surf. Coat. Technol. 116–119 (1999) 278–283.

[196] M.J. Deen, Thin Solid Films 152 (1987) 535–544.

[197] D.F. Dawson-Elli, C.A. Fung, J.E. Nordman, IEEE Trans. Magn. 27 (1991) 1592–1595.

[198] W.N. Maung, D.P. Butler, C.-L. Huang, J. Vac. Sci. Technol. Vac. Surf. Films 11 (1993) 615–620.

[199] E.I. Alessandrini, J. Vac. Sci. Technol. 8 (1971) 188.

[200] M. Fenker, M. Balzer, R.V. Büchi, H.A. Jehn, H. Kappl, J.-J. Lee, Surf. Coat. Technol. 163–164 (2003) 169–175.

[201] Y. Ufuktepe, A.H. Farha, S. Kimura, T. Hajiri, F. Karadağ, M.A. Al Mamun, A.A. Elmustafa, G. Myneni, H.E. Elsayed-Ali, Mater. Chem. Phys. 141 (2013) 393–400.

[202] N. Cansever, M. Danışman, K. Kazmanlı, Surf. Coat. Technol. 202 (2008) 5919–5923.

[203] P.M. Martin, ed., in: Handb. Depos. Technol. Films Coat. Third Ed., Third Edition, William Andrew Publishing, Boston, 2010, pp. 1–31.

[204] S. Makarov, E. Chilla, H. -J. Fröhlich, J. Appl. Phys. 78 (1995) 5028–5034.

[205] A.C. Ferrari, J. Robertson, M.G. Beghi, C.E. Bottani, R. Ferulano, R. Pastorelli, Appl. Phys. Lett. 75 (1999) 1893–1895.

[206] D. Faurie, P. Djemia, E. Le Bourhis, P.-O. Renault, Y. Roussigné, S.M. Chérif, R. Brenner, O. Castelnau, G. Patriarche, P. Goudeau, Acta Mater. 58 (2010) 4998–5008.

[207] D. Faurie, P.-O. Renault, E. Le Bourhis, P. Villain, P. Goudeau, F. Badawi, Thin Solid Films 469–470 (2004) 201–205.

[208] T.Y. Tsui, G.M. Pharr, J. Mater. Res. 14 (1999) 292–301.

[209] N. Nakamura, H. Ogi, M. Hirao, Jpn. J. Appl. Phys. 43 (2004) 3115–3118.

[210] C.M. Flannery, C. Murray, I. Streiter, S.E. Schulz, Thin Solid Films 388 (2001) 1–4.

[211] T.C. Huang, R. Gilles, G. Will, Thin Solid Films 230 (1993) 99–101.

[212] E. Chason, C.M. Falco, A. Ourmazd, E.F. Schubert, J.M. Slaughter, R.S. Williams, MRS Proc. 280 (1992).

[213] D. Pelliccia, S. Kandasamy, M. James, Phys. Status Solidi A 210 (2013) 2416–2422.

[214] S. Junfei, D. Chengyuan, D. Wenjun, W. Jie, C. Yuting, Z. Runze, J. Semicond. 34 (2013) 084003.

[215] M.-T. Le, Y.-U. Sohn, J.-W. Lim, G.-S. Choi, Mater. Trans. 51 (2010) 116–120.

[216] D.B. Beringer, W.M. Roach, C. Clavero, C.E. Reece, R.A. Lukaszew, Phys. Rev. Spec. Top. - Accel. Beams 16 (2013).

[217] K. Srinivas, M. Manivel Raja, D.V. Sridhara Rao, S.V. Kamat, Thin Solid Films 558 (2014) 349–355.

[218] O. Cevher, M.O. Guler, U. Tocoglu, T. Cetinkaya, H. Akbulut, S.C. Okumus, Acta Phys. Pol. A 125 (2014) 293–295.

[219] T. Hashizume, A. Saiki, K. Terayama, IOP Conf. Ser. Mater. Sci. Eng. 18 (2011) 092032.

[220] M.R. Hantehzadeh, S.H. Mortazavi, S. Faryadras, M. Ghoranneviss, J. Fusion Energy 31 (2011) 84–88.

[221] R. Westergård, M. Bromark, M. Larsson, P. Hedenqvist, S. Hogmark, Surf. Coat. Technol. 97 (1997) 779–784.

[222] K. Radhakrishnan, N. Geok Ing, R. Gopalakrishnan, Mater. Sci. Eng. B 57 (1999) 224–227.

[223] Z. Xin, S. Xiao-Hui, Z. Dian-Lin, Chin. Phys. B 19 (2010) 086802.

[224] I. Petrov, P.B. Barna, L. Hultman, J.E. Greene, J. Vac. Sci. Technol. Vac. Surf. Films 21 (2003) S117–S128.

[225] R. Messier, J. Vac. Sci. Technol. Vac. Surf. Films 4 (1986) 490–495.

[226] D. Bernoulli, U. Müller, M. Schwarzenberger, R. Hauert, R. Spolenak, Thin Solid Films 548 (2013) 157–161.

[227] G.S. Chen, P.Y. Lee, S.T. Chen, Thin Solid Films 353 (1999) 264–273.

[228] S.K.R. Patil, N.S. Mangale, S.V. Khare, S. Marsillac, Thin Solid Films 517 (2008) 824–827.

[229] A.G. Every, C. Sumanya, B.A. Mathe, X. Zhang, J.D. Comins, Ultrasonics 69 (2016) 273–278.

[230] W.H. Press, ed., Numerical Recipes: The Art of Scientific Computing, Cambridge University Press, Cambridge [Cambridgeshire]; New York, 1986.

[231] J.V. Ramana, S. Kumar, C. David, A.K. Ray, V.S. Raju, Mater. Lett. 43 (2000) 73–76.

[232] H.B. Bhuvaneswari, V. Rajagopal Reddy, R. Chandramani, G. Mohan Rao, Appl. Surf. Sci. 230 (2004) 88–93.

[233] H.M. Benia, M. Guemmaz, G. Schmerber, A. Mosser, J.C. Parlebas, Catal. Today 89 (2004) 307–312.

[234] D. Pilloud, A.S. Dehlinger, J.F. Pierson, A. Roman, L. Pichon, Surf. Coat. Technol. 174–175 (2003) 338–344.

[235] O. Matsuda, M.C. Larciprete, R. Li Voti, O.B. Wright, Ultrasonics 56 (2015) 3–20.

[236] C. Thomsen, J. Strait, Z. Vardeny, H.J. Maris, J. Tauc, J.J. Hauser, Phys. Rev. Lett. 53 (1984) 989–992.

[237] C. Thomsen, H.T. Grahn, H.J. Maris, J. Tauc, Phys. Rev. B 34 (1986) 4129–4138.

[238] H.T. Grahn, H.J. Maris, J. Tauc, IEEE J. Quantum Electron. 25 (1989) 2562–2569.

[239] C. Rossignol, B. Perrin, IEEE Trans. Ultrason. Ferroelectr. Freq. Control 52 (2005) 1354–1359.

[240] L. Sarger, P. Segonds, L. Canioni, F. Adamietz, A. Ducasse, C. Duchesne, E. Fargin, R. Olazcuaga, G.L. Flem, J. Opt. Soc. Am. B 11 (1994) 995.

[241] D. Holec, M. Friák, J. Neugebauer, P.H. Mayrhofer, Phys. Rev. B 85 (2012) 064101.

Publications

1. Adatom Effects on The Film growth and Surface Phonon Propagation in Niobium Nitride (NbN) Thin Films I,

J.M. Kuria, D. M. Wamwangi, J. D. Comins, M. Msimanga, and D. G. Billing, *In preparation*.

2. Elastic constants of Niobium Nitride (NbN) Thin Films Using Surface Brillouin Scattering II,

J.M. Kuria, D. M. Wamwangi, J. D. Comins, M. Msimanga, and D. G. Billing, *In preparation*.

3. Surface Brillouin Scattering Study of TaN Thin Films,

J.M. Kuria, D. M. Wamwangi, J. D. Comins, M. Msimanga, and D. G. Billing, *In preparation*.

4. Elastic Constants of ZrN Films Using Surface Brillouin Scattering and Picoscond Acoustics,

J.M. Kuria, D. M. Wamwangi, J. D. Comins, M. Msimanga, and D. G. Billing, *In preparation*.

Conference presentations

1. Synthesis of Hard Films of ZrN and NbN using RF Magnetron Sputtering (Poster) Student Presentation Workshop, May 2012, Student Presentation Workshop, DST/NRF Centre of Excellence in Strong Materials, University of the Witwatersrand, Johannesburg, South Africa.

2. Synthesis and Characterisation of Hard Thin Films of NbN and ZrN (Poster), October 2012, 4th Cross-Faculty Graduate Symposium, University of the Witwatersrand, Johannesburg

3. Growth and Characterisation of RF Magnetron Sputtered NbN and ZrN Thin Films (Poster), November 2012, 5th African Laser Centre Student Workshop, University of Namibia, Windhoek Namibia. Awarded the Best Poster Presentation in The PhD student category.

4. Characterisation of Transition Metal Nitrides Thin Films Deposited Using RF Magnetron Sputtering (Poster), May 2013, Student Presentation Workshop, DST/NRF Centre of Excellence in Strong Materials, University of the Witwatersrand, Johannesburg, South Africa.

5. Surface Brillouin Scattering in NbN Thin Films (Oral), November 2013, 6th African Laser Centre Student Workshop, Zeewenwacht, Stellenbosch, South Africa.

6. Surface Brillouin Scattering Studies of NbN thin films (Oral) Student Presentation Workshop, May 2015, Student Presentation Workshop, DST/NRF Centre of Excellence in Strong Materials, University of the Witwatersrand, Johannesburg, South Africa.